# Thrust-Reverser Flow Investigation on a Twin-Engine Transport

Christopher M. Catlin
and
Frank Quinto

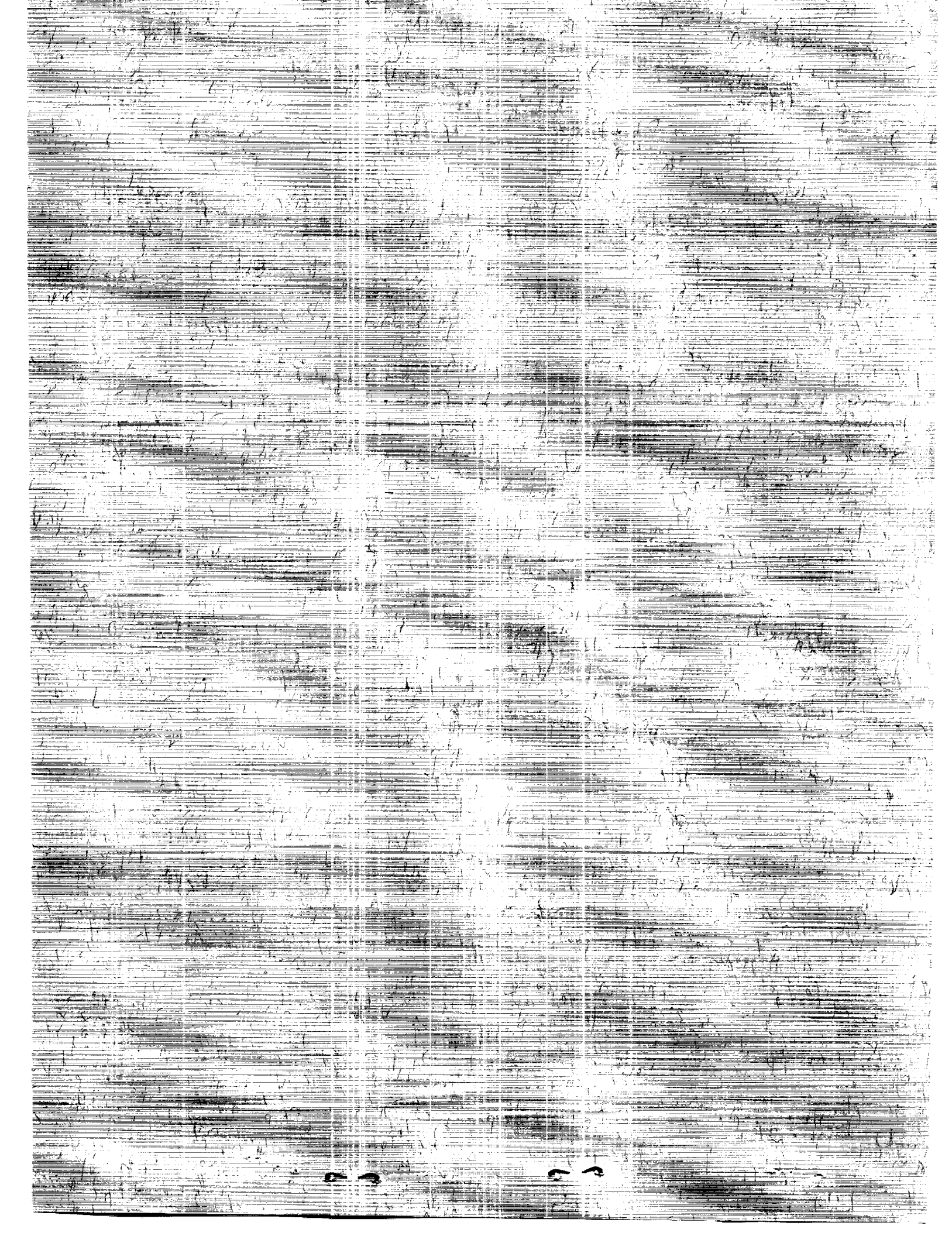

**NASA Technical Paper 2856**

1988

# Thrust-Reverser Flow Investigation on a Twin-Engine Transport

Gregory M. Gatlin
and P. Frank Quinto
*Langley Research Center*
*Hampton, Virginia*

NASA
National Aeronautics
and Space Administration

Scientific and Technical
Information Division

## Summary

An investigation was conducted in the Langley 14- by 22-Foot Subsonic Tunnel to study the effects of engine thrust reversing on an aft-mounted twin-engine transport and to develop effective testing techniques. Testing was done over a fixed and a moving-belt ground plane and over a pressure-instrumented ground board. Free-stream dynamic pressure was set at values up to 12.2 psf, which corresponded to a maximum Reynolds number based on mean aerodynamic chord of $7.65 \times 10^5$. The thrust reversers examined included cascade, target, and four-door configurations. The investigation focused on the range of free-stream velocities and engine thrust-reverser flow rates that would be typical for landing ground-roll conditions. Flow visualization techniques were investigated, and the use of water or smoke injected into the reverser flow proved effective for determining the forward progression of the reversed-flow and reingestion limits. When testing over a moving-belt ground plane, as opposed to a fixed ground plane, forward penetration of the reversed flow was reduced. The use of a pressure-instrumented ground board enabled reversed-flow ground velocities to be obtained, and it provided a means by which to identify the reversed-flow impingement point on the ground. Finally, longitudinal aerodynamic data and forward progression of the reversed flow were found to be only mildly sensitive to reductions in inlet mass flow rate.

## Introduction

The development and use of engine thrust reversers have become widely accepted on transport aircraft and are rapidly gaining acceptance on high performance fighter/attack aircraft as well, as discussed in reference 1. Lowering the operating costs of transport aircraft has always been a major concern for the airline industry, and one area of consideration to reduce costs is through the use of engine thrust reversers to decrease ground roll following aircraft touchdown. The use of thrust reversers can lower operating costs by significantly reducing wear on the aircraft brakes and tires. The decreased ground roll can also lower operating costs by reducing the amount of fuel needed to taxi back to the terminal. In addition to these reduced cost benefits, thrust reversers provide a very effective means of slowing an aircraft operating on a wet or icy runway when wheel braking effectiveness is reduced (refs. 2 and 3). These advantages from the use of thrust reversers apply to high performance military aircraft as well. A significant additional benefit for military aircraft is the resulting decreased ground roll which will allow operations from airfields with reduced runway lengths (refs. 1 and 4).

Thrust reversers have already been shown to be very effective in stopping aircraft after touchdown; however, a factor of major concern is the matter of foreign object ingestion and hot gas reingestion by the engine (refs. 5 through 11). The extent of foreign object damage on current aircraft varies with each configuration but generally appears more severe for aircraft with the newer higher bypass-ratio turbofan engines. The exhaust flow pattern and the extent to which the reversed flow progresses forward must be fully defined so that exhaust gases and runway debris are not ingested into the engine inlet. Accordingly, a simulation and study of the engine inlet conditions are very important to the design of any thrust reverser.

When investigating a thrust-reverser configuration in ground effect in a wind tunnel, the accuracy of engine simulation is particularly important. The forward progression of the reversed flow and any exhaust flow ingested into the inlet will depend heavily on both the reverser and inlet flow simulators.

Simultaneously matching engine inlet and exhaust mass flows and exhaust pressure ratio with model engine simulators is usually very difficult on powered wind-tunnel models. For example, if a flow-through engine simulator is equipped with an ejector to increase the inlet mass flow, the resulting exhaust pressure ratio is too low to properly simulate the correct nozzle pressure ratio and the exhaust mass flow is increased over that of the inlet by the added ejector mass flow. If a high-pressure system is used to accurately simulate true engine exhaust mass flow and pressure ratio, then a separate simulation system must be used to simulate the inlet mass flow. If this inlet simulation is accomplished with a lower pressure ejector, the additional low-pressure inlet flow must be removed from the model separately from the engine exhaust nozzle. This removal is usually accomplished with large-diameter piping which can interfere substantially with accurate force and moment measurements (refs. 3, 9, and 10). Even when a turbine-powered engine simulator is used, the expense and the difficulties arising from the complexity of the device must be overcome, and the problem of removing the drive air from the model in order to match inlet and exhaust mass flow still exists. Historically, the most common method of powered testing for high-pressure-ratio engine configurations (such as on fighter aircraft) has been to simulate only the exhaust flow and to fair over the closed inlet (ref. 4). This approach has the obvious drawback of providing no inlet flow at all as well as introducing the physical interference of the inlet fairing.

At the present time, the sensitivity of thrust-reverser characteristics to the inlet and exhaust simulation is not well understood. In addition, techniques used to investigate thrust-reversing configurations have not been well developed.

In order to develop techniques with which to fully test thrust-reversing configurations, an investigation has been carried out in the Langley 14- by 22-Foot Subsonic Tunnel. A modern twin-engine jet transport model with a separate engine simulation incorporating individual reverser and inlet flow simulators was used in the tests, and three different thrust-reverser designs representing cascade, target, and four-door configurations were studied. Several flow visualization techniques were investigated, force and moment data were obtained, and pressure data were obtained on a pressure-instrumented ground board. A comparison of a fixed and a moving ground plane was conducted, investigations were done both in and out of ground effect, and an investigation was carried out to determine the sensitivity of a thrust-reversing configuration to variations in the ratio of inlet to exit flow.

Data were obtained at free-stream dynamic pressures up to 12.2 psf while the model attitude was held constant at an angle of attack of $-1^\circ$ and zero sideslip. Flaps and spoilers were tested undeflected and at deflection angles of 40° and 60°, respectively. The reverse-thrust flow rates (for each engine simulator) were set at values from 0.80 up to 5.12 lb/sec while the inlet flow rates were set from a minimum of free-stream flow through conditions up to a maximum of 6 lb/sec.

## Symbols

All data have been reduced to standard coefficient form and are presented in the stability axis system.

| | |
|---|---|
| $A$ | aspect ratio, $\frac{b^2}{S}$ |
| $b$ | wing span, ft |
| $C_D$ | drag coefficient, $\frac{\text{Drag}}{q_\infty S}$ |
| $C_L$ | lift coefficient, $\frac{\text{Lift}}{q_\infty S}$ |
| $C_m$ | pitching-moment coefficient, $\frac{\text{Pitching moment}}{q_\infty S \bar{c}}$ |
| $C_p$ | pressure coefficient, $\frac{p_{s,\text{local}} - p_\infty}{q_\infty}$ |
| $c_{\text{local}}$ | chord at local spanwise station, in. |
| $\bar{c}$ | mean aerodynamic chord, ft |
| $\bar{c}_{ht}$ | mean aerodynamic chord of horizontal tail, ft |
| $\bar{c}_{vt}$ | mean aerodynamic chord of vertical tail, ft |
| $h$ | height of horizontal laser light sheet above ground, in. |
| $\dot{m}_I$ | inlet flow rate for one engine simulator (weight flow), lb/sec |
| $\dot{m}_R$ | reverser exhaust flow rate for one engine simulator (weight flow), lb/sec |
| $p_{s,\text{local}}$ | pressure measured at local static-pressure orifice on pressure-instrumented ground board, psf |
| $p_\infty$ | free-stream static pressure, psf |
| $q_\infty$ | free-stream dynamic pressure, psf |
| $S$ | wing reference area, $\text{ft}^2$ |
| $V_l$ | local velocity of reversed flow, ft/sec |
| $\Delta C_p$ | increment in pressure coefficient between pressure contours |
| $\delta_f$ | flap deflection angle, deg |
| $\delta_s$ | spoiler deflection angle, deg |
| $\eta$ | wing spanwise location nondimensionalized by $b/2$ |

Abbreviations:

| | |
|---|---|
| IGE | in ground effect |
| INBD | inboard |
| FRP | fuselage reference plane |
| F.T. | flow through |
| OGE | out of ground effect |
| T.S. | tunnel station (T.S. = 0 at beginning of test section), ft |

## Model Description

The configuration used in this investigation was a 9-percent-scale model of a McDonnell Douglas MD-89 twin-engine jet transport. It was installed on a six-component internal balance and was supported by a top-entry blade sting support. A three-view sketch of the model is presented in figure 1, and the model support system is shown in figure 2. Additional model dimensional data are presented in

table I. Engine inlet and reverser exhaust flows were provided by nonmetric engine simulators which were supported separately from the sting as shown in figure 2. A photograph of the entire test setup is presented in figure 3. Three different engine thrust-reverser designs representing cascade, target, and four-door configurations were tested. Installation of the cascade and four-door reversers is shown in figure 2(a). The top view shown in figure 2(b) shows the slightly modified pylon used when the target thrust reversers were investigated. A foam rubber spacer, shown in figure 2(b), separates the metric pylon from the nonmetric engine simulator for all three thrust-reversing configurations. The engine inlet remained the same for each of the thrust-reversing configurations.

The engine simulation system is approximately 10.5 ft long and contains separately driven inlet and reverser systems. The inlet simulator is driven by an ejector-type system which exhausts high-pressure air down the center of an 8-in-diameter tube. (See fig. 2.) This high-pressure air flow rate can be adjusted to regulate the amount of free-stream air entrained into the inlet. If no high-pressure air is flowing, this system simulates a flow-through inlet.

The thrust-reverser simulators consist of arc-shaped plenums which fit circumferentially around the 6-in-diameter inlet tube as shown in the sketches in figure 4 and the photographs in figure 5. Each plenum is fed by a high-pressure air supply line. The cascade reverser consists of three reverser sections and three wood filler blocks as shown in figure 4(a), the target reverser consists of two reverser sections and two wood filler blocks as shown in figure 4(b), and the four-door reverser consists of four reverser sections alone as shown in figure 4(c).

The cascade reverser has been tailored to reduce exhaust gas interactions with the fuselage, wing, and tail surfaces (ref. 8). The upper and lower outboard reverser sections deflect reversed flow 45°, whereas the lower inboard reverser section performs more like a spoiler with a 75° deflection angle. These angles are based on 0° deflection being for reversed flow that directly opposes the free stream.

The target reverser has two reverser sections that are 180° apart. This reverser was tested in a vertical orientation and was then rotated 15° and 22.5° (with the lower reverser section being moved outboard) in an attempt to minimize exhaust gas reingestion.

The four-door reverser consists of four separate reverser sections, and an example of this type of thrust-reversing configuration is discussed in reference 12. The configuration tested contains two sections that have a folding door with side fences, one section that has a folding door with 30° turning vanes and one section that has a nonfolding door. The folding doors are set at a 30° angle as shown in figure 4(c) and deflect the exhaust flow forward, whereas the nonfolding door allows the exhaust flow to progress outward perpendicular to the free-stream flow. Each reverser section is one quarter of an annulus; therefore, the four-door plenums can be configured several different ways. Three configurations were studied in this investigation and their orientations are shown in figure 4(d). The sketch presented in figure 4(c) is configuration II.

The engine simulators were driven by the 14- by 22-Foot Subsonic Tunnel high-pressure air system. A sketch showing the air system used to supply high-pressure air to all reverser plenums and both inlet ejectors is presented in figure 6. There was a hand control valve on each individual line so that flow rates to each reverser plenum or inlet ejector could be varied and balanced. When the cascade or target reversers were tested, the unused air lines were capped off. Flowmeters were used to monitor the flow rates to the reverser system and to the inlet ejector system.

Instrumentation was required in the engine inlets and at each reverser (fig. 7) in order to adjust the control valves correctly for the proper individual flow rates and to balance the mass flow to each engine simulator. Each inlet had three static-pressure orifices (120° apart and manifolded together) and one total-pressure probe at the center. From this instrumentation, inlet flow rate could be determined. Each reverser section had a total-pressure probe in the reverser exhaust jet, and reverser calibration data provided a correlation between jet total pressure and flow rate. In addition, as shown in figure 7, each reverser section had both plenum screens and exit screens so as to produce a uniform exhaust flow.

## Test Conditions

This thrust-reversing investigation was carried out in the Langley 14- by 22-Foot Subsonic Tunnel. A description of this facility can be found in reference 13 under the previous name of Langley V/STOL Tunnel and in reference 14 under the name of Langley 4- by 7-Meter Tunnel.

Primary emphasis during this investigation was placed on obtaining data with the model at a height and attitude representing roll-out on the runway following aircraft touchdown. To simulate these conditions, angle of attack was held constant at −1° and sideslip was fixed at 0°. For most of the testing, the model height was fixed such that the landing gear was 1 in. above the tunnel floor. This 1-in. space was provided to ensure that there would be no contact of the model with the floor during

testing. When the model was in this position, the centerline of the inlet was 14 in. above the floor. All data in ground effect (IGE) were obtained with the tunnel boundary-layer-removal system in operation. In a few instances, when data were obtained out of ground effect (OGE), the model was raised such that the landing gear was 4 ft above the floor. This height corresponds to 82 percent of $b/2$ and was thought to be adequate such that any downwash or reversed-flow ground effects would be minimal and therefore negligible. Unless otherwise noted, data were taken with the model in ground effect, the engine simulators were simulating full inlet flow, and the flaps and spoilers were set for landing conditions ($\delta_f = 40°$ and $\delta_s = 60°$).

Under normal conditions, a transport aircraft of this type would touch down at approximately 130 knots, shortly thereafter the thrust reverser would be deployed and would operate until the aircraft slowed to approximately 60 knots. Finally, wheel braking alone would be used to slow the aircraft for the remainder of the ground roll. Thrust reversing presents foreign object damage and reingestion problems at 60 knots ($q_\infty = 12.2$ psf) and below; therefore, the wind-tunnel investigation focused on free-stream dynamic pressure values of 12.2 psf and below.

Data were obtained at free-stream dynamic pressures up to 12.2 psf with corresponding Reynolds numbers (based on $\bar{c}$) up to $7.65 \times 10^5$. The effects of flap and spoiler deflections were investigated for deflection angles of 40° and 60°, respectively.

For each engine simulator, the flow rate was varied up to 5.12 lb/sec for the reverser and up to 6 lb/sec for the inlet. An engine flow rate of 6 lb/sec is representative (in terms of flow rate/unit area) of the maximum power at which the engine thrust reverser can be operated; therefore, all testing was conducted at or below this value. The engine simulators were tested in a fashion representative of a 6-to-1 bypass-ratio engine. The cascade and four-door type thrust reversers had reverser flow rates lower than the inlet flow rates because the cascade and four-door thrust reversers reverse only the engine fan flow. During full inlet flow simulation, inlet flow and reverser flow were matched for the target reverser configuration because a target thrust reverser reverses the entire engine flow (both fan and core).

The wind-tunnel investigation was divided into three major phases. The first phase consisted of investigating flow visualization techniques over a fixed ground plane. This tunnel test section configuration is presented in figure 3. In the second phase, the effects of a moving-belt ground plane were investigated. The moving-belt surface was 14 ft wide and 20 ft long, and the model was centered over it as shown by the tunnel test section configuration presented in figure 8. The third phase consisted of obtaining pressure measurements in the ground plane of the reverser flow field to determine the reversed-flow–ground impingement point, the extent of the forward progression of the reversed flow, and its velocity on the tunnel floor. This testing was conducted over a pressure-instrumented ground board as shown in figure 9(a). Only the left side of the ground board was instrumented. Dimensions of the instrumented portion of the ground board and details of the pressure ports are shown in figure 9(b). All pressure orifices had an inner diameter of 0.040 in. A 3/4-in. plywood dummy ground plane was used on the right side so that the entire flow field would be exposed to a uniform ground plane, and a 5-in. wood fairing was placed around the entire ground board to minimize edge effects. (See fig. 9(a).) A photograph of the model over the pressure-instrumented ground board is presented in figure 10. The model was raised 0.75 in. during this phase of testing to compensate for the thickness of the ground board. During each phase of the investigation, force and moment data were obtained, and each of the three reverser configurations was tested.

The longitudinal forces and moment were measured with an internal strain-gauge balance capable of supporting loads of up to 2000 lb of normal force, 600 lb of axial force, and 17 000 in-lb of pitching moment. The error of these balance measurements is, at worst case, ±0.5 percent of the maximum loadings. The pressures measured on the pressure-instrumented ground board were obtained through a scanivalve system capable of measuring a maximum pressure of 10 lb/in$^2$. The error of the pressure measurements is, at worst case, ±0.1 percent of the 10 lb/in$^2$ maximum.

## Presentation of Results

The results of this investigation are presented in the following figures:

## Results and Discussion

### Flow Visualization Techniques and Conditions for Exhaust Gas Reingestion

Several different flow visualization techniques were tested throughout the wind-tunnel investigation with initial testing being carried out over a fixed ground plane as shown in figure 3. Since the interactions of the engine reverser flow with the model

were of prime importance in this investigation, visualization of the reverser plumes was necessary to produce a descriptive picture of what was happening in the entire flow field.

When testing over a fixed ground plane, the reverser exhaust plumes were made visible by injecting water into the reversed flow. A spotlight was used to illuminate the water particles in the reversed flow, and a 6-in. square grid pattern, as identified in figure 10(b), was painted on the wind-tunnel floor to aid in determining the shape and position of the reverser exhaust plumes. This water injection technique would hinder the operation of a moving-belt ground plane due to the water-absorbing characteristics of the moving belt. Therefore, a technique in which smoke was injected into the reversed flow was developed for use when testing over a moving-belt ground plane.

All flow conditions investigated were representative of reverser flow rates that the actual aircraft could produce as its ground-roll velocity was reduced below 60 knots ($q_\infty$ = 12.2 psf). When simulating these conditions it was necessary to identify which reverser exhaust flow patterns would be unacceptable during landing ground-roll operations. A flow condition was deemed unacceptable if (1) a reverser exhaust jet was impinging directly on a model surface or (2) the reversed flow progressed upstream far enough to be in the inlet plane. Examples of these unacceptable flow conditions are noted as the flow visualization techniques are discussed. Flow visualization photographs are presented for each of the thrust-reverser configurations in figures 12 through 29, and a graphical summary illustrating the onset of exhaust gas reingestion is presented in figure 30.

***Water injection flow visualization.*** The first technique to be tested was one in which the reverser flow was visualized by injecting water into the reverser air-supply lines so that the reverser exhaust plume consisted of a spray mist. If enough water was injected and the lighting was correct, the reverser exhaust plumes could easily be seen. Because of model symmetry, flow visualization was only necessary in one reverser flow field; therefore, the water injection flow visualization technique was only performed on the right engine simulator.

In order to get the spray mist in the reverser exhaust plume, water was injected into the air-supply line upstream of the reverser plenum as shown in figure 11(a). The water was most evenly distributed in the reverser exhaust plume if the water-supply line was attached vertically to the air-supply line so that the water entered the flow of air from the top of the tube. This attachment is illustrated in both figure 11(a) and the photograph presented in figure 11(b). For all configurations and reverser flow rates tested, a standard 60-psi water-supply system provided enough pressure to inject the water into the air line at the connections discussed previously. The shape and position of the reverser exhaust plumes were well-defined when the flow rate of the injected water was set at approximately one sixth the flow rate of the reverser exhaust flow. When the water injection technique was used, the reverser flow rate was increased due to the addition of the water.

Water injection flow visualization techniques have been successfully applied to thrust-reversing configurations in the past as discussed in references 7 and 9. However, in order to ensure that the addition of water into the reversed flow did not affect the shape or position of the reverser exhaust plumes, comparisons were made in the present investigation for configurations both with and without water injection. A flow visualization comparison is presented at the end of this section which shows good agreement between the water injection flow visualization technique and a smoke injection technique. A comparison of longitudinal aerodynamic data for configurations both with and without water injection is also presented and shows minimal effect.

Photographs of the water injection flow visualization technique are presented for the cascade reverser configuration in figure 12. In each case, full inlet flow was being simulated. As can be seen from these figures, the spotlight and 6-in. square grid pattern on the wind-tunnel floor aid in determining the shape and position of the reverser exhaust plumes. A reverser flow rate of 2.55 lb/sec is shown in figures 12(a)–(c) while free-stream dynamic pressure is lowered from 12.2 to 1.4 psf. The forward progression of the reversed flow is easily seen as free-stream dynamic pressure is reduced. At this reverser flow rate there appears to be little danger of exhaust gas reingestion until the free-stream dynamic pressure is reduced to 1.4 psf at which point the possibility of reingestion does exist (fig. 12(c)). The vertical tail was wet; therefore, the reverser exhaust flow was having an interaction there at all free-stream speeds.

A reverser flow rate of 1.15 lb/sec is shown in figures 12(d)–(f) while free-stream dynamic pressure is again lowered from 12.2 to 1.4 psf. The reverser plumes are much less visible in the photographs of figures 12(d)–(f) than in those of figures 12(a)–(c) because not enough water was being injected into the reverser supply lines. The forward progression of the reversed flow can again be seen as the free-stream dynamic pressure is reduced; now there is little danger of reingestion even at the lowest free-stream velocity. However, reverser exhaust flow was

contacting the vertical tail. The location where the reversed flow contacts the tunnel floor can be seen as a darker "wet spot" on the floor when the spotlight is directed at the reverser flow field from the side as shown in figures 12(d)–(f).

Photographs showing the reverser exhaust plumes for the 15° rotated target configuration are presented in figure 13. Both the inlet and reverser flow rates are 3.2 lb/sec. The reverser flow rate is equal to the inlet flow rate because a target thrust reverser reverses the entire engine flow (both fan and core). The free-stream dynamic pressure is 5.4 psf in figure 13(a) and 1.4 psf in figure 13(b).

A possible reingestion problem may exist under these conditions; however, the forward progression of the lower reverser exhaust flow cannot be clearly seen. The fact that the lower target exhaust jet is angled outboard 15° will minimize both reverser flow interactions with the airframe and reingestion from the lower exhaust plume. However, the upper target exhaust jet is angled inboard 15°, and this can be seen to promote interactions with the tail surfaces.

A more complete series of flow visualization photographs is presented in figure 14 for the 22.5° rotated target configuration. The possibility of reingestion exists as the free-stream dynamic pressure is reduced below 12.2 psf when $\dot{m}_R = 3.2$ lb/sec. When $\dot{m}_R = 2.25$ lb/sec, the onset of reingestion is shown to occur as $q_\infty$ is reduced below 5.4 psf (fig. 14(f)). It is at these conditions that the reverser exhaust plume progresses forward to the vicinity of the engine inlet. When the exhaust flow rate is reduced to 1.35 lb/sec, a potential reingestion problem does not begin to appear until $q_\infty$ is reduced to 1.4 psf (fig. 14(j)). These flow visualization photographs suggest that, for the 22.5° rotated target thrust reverser, the maximum amount of usable reverse thrust without reingestion would be obtained by throttling back the engines as the aircraft slows to keep the reversed flow out of the inlet plane. In all cases, the flow from the upper reverser appears to interact with the tail surfaces.

One method of improving the quality of the flow visualization is illustrated in the top-view photographs presented in figures 14(c) and (d). Lighting for the model and the reverser plume came from the sides in figure 14(c). However, in figure 14(d) additional lighting came from directly above the model, and many more details are clearly seen. It was found that the water spray in the reverser exhaust flow was much more visible in photographs where the lighting and the camera were in the same location as can be seen by comparing the side-view and top-view flow visualization photographs that have been presented so far. In each case, the spotlight was directed at the reversed flow from the side, and in each case, the side-view photograph captured more detail than the top-view photograph.

Photographs of the water injection flow visualization technique are presented for all three configurations of the four-door reverser in figures 15 through 17. For each configuration, reverser flow rates of 5.12, 3.0, and 1.15 lb/sec are shown as $q_\infty$ is reduced from 12.2 psf. In all cases, full inlet flow is being simulated. Photographs for configuration I of the four-door thrust reverser (fig. 4(d)) are presented in figure 15. When $\dot{m}_R = 5.12$ lb/sec and $q_\infty = 12.2$ psf, the wet spot on the fuselage reveals that the upper inboard reversed flow is grazing the side of the fuselage for configuration I as shown in figure 15(a), and as $q_\infty$ is reduced, this unacceptable direct contact of the reversed flow with the fuselage becomes even greater. In figures 15(a)–(c), the water valve to the upper inboard reverser plenum was not set properly, and therefore very little of that reverser plume is visible in the photograph.

When $\dot{m}_R$ is reduced to 3.0 lb/sec and $q_\infty$ is reduced to 5.4 psf, there is again contact of the reversed flow with the fuselage (fig. 15(e)). For all photographs where $\dot{m}_R = 3.0$ lb/sec or greater, the reversed flow progresses well upstream on the tunnel floor; this indicates a potential reingestion problem. The nonfolding door on the upper outboard section effectively deflects the exhaust flow outboard and away from the fuselage to eliminate any possibility of its reingestion.

When $\dot{m}_R = 1.15$ lb/sec, there is a small amount of contact of the reversed flow with the upper rear section of the fuselage. Since there is some reversed flow contact in this area for each flow condition, it appears that the reverser plenum with the folding door and 30° turning vanes should have the turning vane angle increased when used in the upper inboard location.

Flow visualization for configuration II of the four-door thrust reverser is presented in figure 16. When $\dot{m}_R = 5.12$ lb/sec and $q_\infty = 5.4$ psf or below, the reversed flow comes in contact with the wing. These conditions illustrate the potential for both reingestion problems and foreign object damage. When $\dot{m}_R$ is reduced to 3.0 lb/sec, reingestion does not appear to be present until $q_\infty$ is reduced below 5.4 psf. (See figs. 16(e) and (f).) When $\dot{m}_R$ is reduced to 1.15 lb/sec, there is no reingestion problem, even when $q_\infty = 1.4$ psf.

The effects of the nonfolding door reverser being located in the lower inboard position can be seen by comparing figure 15(g) with figure 16(h). The folding door with side fences reverser plenum is in

the lower inboard position in figure 15(g) and the reverser flow field is shown to be well forward on the tunnel floor. This is because the lower inboard reversed flows from each engine come together and move upstream. When the nonfolding door reverser plenum is in the lower inboard position, the lower inboard reversed flows do not move nearly as far upstream as shown in figure 16(h).

Photographs for configuration III of the four-door thrust reverser (fig. 4(d)) are presented in figure 17. When $\dot{m}_R = 5.12$ lb/sec and $q_\infty = 5.4$ psf or less, the reversed flow disrupts the normal free-stream flow over the wing and conditions suitable for reingestion and foreign object damage are present as shown in figures 17(b) and (c). When $\dot{m}_R$ is decreased to 3.0 lb/sec, the reversed flow does not progress up to the wing until $q_\infty$ is lowered to 1.4 psf. When $\dot{m}_R = 1.15$ lb/sec (figs. 17(g)–(i)), there would be no danger of reingestion, even when $q_\infty$ is lowered to 1.4 psf.

One problem noted on configuration III of the four-door thrust reverser is that the upper inboard plenum with a folding door and side fences directs the reversed flow directly into the fuselage. This is shown in every top-view photograph in figure 17. Therefore, the reverser plenum with a folding door and side fences would be unacceptable in the upper inboard location.

As previously noted, the reverser plenum with a folding door and 30° turning vanes also directed reversed flow into the fuselage when it was located in the upper inboard location. However, when figures 16(a)–(i) are compared with figures 17(a)–(i), the beneficial effects of the turning vanes are clearly seen as the 30° vanes greatly reduce the amount of reversed flow coming in contact with the fuselage.

When all three of the four-door reverser configurations are compared, configuration II has the least disruptive reverse flow pattern. As an illustration of this, compare configuration I in figure 15(d) with configuration II in figure 16(d) and configuration III in figure 17(d). Each of these figures presents the same conditions where $\dot{m}_R = 3.0$ lb/sec and $q_\infty = 12.2$ psf. When configuration II (fig. 16(d)) is compared with configuration I (fig. 15(d)), the plenum with the nonfolding door on the lower inboard location on configuration II significantly reduces the amount of forward progression of the reversed flow on the tunnel floor. The exhaust flow from the plenum with the folding door and side fences in that same location on configuration I directs the reversed flow farther forward on the tunnel floor. When configuration II (fig. 16(d), top view) is compared with configuration III (fig. 17(d), top view), the upper inboard reversed flow on configuration II has less contact with the fuselage. The influence of the turning vanes in configuration II effectively reduced reversed flow interactions with the fuselage.

***Laser light sheet with water injection flow visualization.*** Flow visualization was also investigated by using a laser light sheet in combination with water injection into the reversed flow. The laser light sheet was used in a horizontal and a vertical orientation and provided a picture of one cross-sectional "slice" of the reverser flow field.

The horizontal laser light sheet was developed by directing a laser beam (produced by a 12-W argon-ion laser) through an optics package as illustrated in figure 18(a). The laser beam, directed by two small mirrors, first passed through a spinning glass block which swept it back and forth over a 1-in. distance. This sweeping beam then passed through a lens which focused it, and finally it passed through a cylindrical lens which created the laser light sheet. Figure 18(b) illustrates the position of both the horizontal and vertical laser light sheets with respect to the model. For all laser light sheet flow visualization, water was injected into the reversed flow only on the right engine simulator. The horizontal light sheet was directed parallel to the floor, and it spanned an area wide enough to cover the entire reversed flow region. The light sheet could be set at any height at or above 1.5 in. above the floor.

To generate the vertical laser light sheet, the laser beam was initially passed through a lens that focused it to keep it thin and was then directed to an optics package on the tunnel ceiling. This optics package directed the laser beam vertically downward and through a cylindrical lens to produce a vertical light sheet parallel to the free-stream flow. The light sheet was centered over the right simulator inlet and spanned an area wide enough to cover the entire reversed flow region.

Photographs showing the horizontal laser light sheet used with water injected into the reversed flow are presented in figure 19 for the cascade thrust reverser out of ground effect. In these photographs, the laser light sheet is at the height where the ground would be if the model were on the tunnel floor, and $\dot{m}_R = 2.55$ lb/sec while $q_\infty$ is reduced from 12.2 psf. In each of the figures, the light sheet is more easily seen in the side view than the top view due to Mie scattering. The light from the laser light sheet scatters back toward the source better than it scatters upward at a 90° angle. These figures show that there is no danger of reingestion when $q_\infty = 12.2$ psf or less when the cascade configuration is out of ground effect. The ground effects can be seen by comparing the intersection of the reverser

plume and the laser light sheet in figures 19(a)–(c) (out of ground effect) to the forward extent of the wet region on the tunnel floor in figures 12(a)–(c) (in ground effect). As expected, evidence can be seen that the reversed flow progresses farther forward when in ground effect than when it is in free air.

Photographs showing the vertical laser light sheet used with water injected into the reversed flow are presented in figure 20. In each side-view photograph, the upper reverser exhaust plume is more visible than the side exhaust plumes due to the presence of the laser light sheet. The thick line that cuts across each top-view photograph perpendicular to the model is the laser beam being directed to the ceiling before it is turned vertically downward and converted into the laser light sheet. The effects of the intensity of the vertical laser light sheet can be seen by comparing figures 20(b) and (c). Both these figures have identical flow conditions; however, the intensity of the laser light sheet was lower in figure 20(c). When the side-view photographs are compared, the higher intensity laser light sheet is seen to produce a much better view of the upper and side reverser exhaust plumes. When the top-view photographs are compared, the lower intensity laser light sheet provides a better visualization of the upper reverser plume. The intensity of the laser light sheet is too high in the top view of figure 20(b) and, therefore, details of the reversed flow are lost. The effects of the location of the light sheet with respect to the camera are demonstrated in these photographs. As stated before, the light from the laser light sheet scatters back toward the source better than it scatters outward at a 90° angle. It is for this reason that the best flow visualization is produced by having an intense vertical laser light sheet when viewed from the side and a reduced intensity vertical laser light sheet when viewed from the top.

Photographs showing the horizontal laser light sheet used with water injected into the reversed flow are presented in figure 21 for the 15° rotated target configuration in ground effect. The horizontal laser light sheet is 1.5 in. above the floor, and $\dot{m}_R$ = 2.55 lb/sec as $q_\infty$ is reduced from 12.2 psf. The forward progression of the reversed flow is clearly shown in the laser light sheet. Many more details are visible in the reverser exhaust plume when the laser light sheet is used to illuminate the water particles than when the spotlight is used.

Photographs obtained with the vertical laser light sheet used with water injected into the reverser flow are presented in figures 22(a) and (b) for the 15° rotated target configuration. In both photographs, $\dot{m}_R$ equals 2.55 lb/sec; however, $q_\infty$ equals 12.2 psf in figure 22(a) and 5.4 psf in figure 22(b). Due to the rearward location of the target thrust reverser with respect to the inlet, the lower reverser exhaust plume is shielded from the vertical laser light sheet by the engine nacelle. Therefore the vertical laser light sheet is only able to make contact with the reverser plume from the upper target thrust reverser. Since the upper target reverser is rotated inboard 15° and the light sheet is vertical, the upper exhaust plume is not fully illuminated by the laser light sheet. This is why the upper reverser exhaust plume is easy to see as it leaves the target nozzle and then fades as it progresses upward. Even though the flow visualization showed few details in figures 22(a) and (b), there are still two flow phenomena that can be seen. First, the upper reverser plume is influencing flow over the tail surfaces, and second, the water on the tunnel floor is being illuminated by the laser light sheet in a manner similar to that observed in figure 14(d). The degree to which the lower target reverser flow is turned outboard is illustrated in the top view of figure 22(b). This figure shows that the outward deflection of the lower target exhaust plume helps to reduce the possibility of reingestion, but it does not eliminate the problem. This flow phenomenon is completely undetectable in the top view of figure 13(b) due to the absence of any lighting from above.

Flow fields observed with the horizontal laser light sheet used with water injected into the reversed flow are presented in figures 23 through 25 for configuration I of the four-door thrust reverser. The light sheet is positioned 7 in. off the floor (halfway between the floor and the center of the inlet) in each of these photographs. The horizontal laser light sheet was not positioned any higher because it would then strike the side of the fuselage or nacelle, and the bright reflection caused by the light sheet illuminating the model made flow details within the light sheet virtually impossible to see. Extensive forward progression of the reversed flow is seen in the laser light sheet at all free-stream dynamic pressures presented. Photographs of the laser light sheet with tunnel lights on and off are presented in figures 24 and 25. When the tunnel lights were turned on, a slight amount of reverser flow detail was lost in the outer fringes of the portion of the reversed flow in the laser light sheet; however, the obvious benefit of the tunnel lights being on is that the reverser flow from all the reverser plenums can be seen.

The fact that the reversed flow appears in the horizontal light sheet when it is positioned halfway between the floor and the center of the nacelle reveals that the forward progression of the reversed flow is not restricted to just near the ground. Therefore,

reingestion would be likely under the flow conditions presented in figures 23 through 25 for configuration I of the four-door thrust reverser.

***Laser light sheet with smoke injection flow visualization.*** Tests were conducted in which smoke was injected into the free-stream flow upstream of the model so as to make the free-stream flow differentiable from the clean reverser flow. A smoke generator that emitted an alcohol vapor smoke from a 2-in-diameter flexible hose was used to inject the smoke at floor level directly in front of the engine simulator upstream of the model. Even at the slowest free-stream speeds, the smoke dissipated very rapidly and the reversed flow was never distinguishable from the free stream. The smoke system used was not able to generate enough smoke in the free-stream flow to provide sufficient contrast against the reversed flow. Since this technique was not successful, no flow visualization photographs are presented for it.

The use of smoke for flow visualization was more successful when smoke was injected into the reversed flow right at the reverser nozzle. Smoke in the reversed flow made the reverser exhaust plumes visible against the free stream, but contrast was very poor with the basic tunnel lighting. Additional contrast was obtained by using the laser light sheet in combination with smoke in the reversed flow. The laser light sheet was directed across the reversed flow region and illuminated the smoke particles to provide a clear picture of one slice of the reverser flow field. The light sheet was only operated in the horizontal orientation when used in combination with smoke in the reversed flow. The horizontal laser light sheet was generated the same way and produced the same type of flow visualization as it did when it was used with the water injection technique. The limiting conditions for which the smoke technique was successful were that the reverser flow rate should be no greater than 2.55 lb/sec and $q_\infty$ should be no greater than 1.4 psf. If either the reverser flow or the free-stream flow exceeded these values, the smoke quickly dissipated and flow visualization was poor.

Photographs showing the horizontal laser light sheet used with smoke injected into the reversed flow are presented in figures 26 through 29. In each of these photographs the laser light sheet was 1.5 in. above the floor, and smoke was only injected into the lower reverser exhaust nozzles since that is the only exhaust flow that would be visible in the laser light sheet. The limit of the forward progression of the reversed flow is rather well-defined in each photograph except those in figures 27(a), 28(a), and 28(b). In these photographs the exhaust flow rate was so high that the smoke was rapidly dispersed and the boundary of reverser flow influence was difficult to detect.

The effects of the 22.5° rotation angle on the target reverser configuration can be clearly seen by comparing figures 27(a)–(e) with figures 28(a)–(f). The 22.5° rotation angle is shown to delay the onset of reingestion since it directs the reversed flow farther outboard than forward as the free-stream velocity is reduced. Configuration III of the four-door thrust reverser is presented in figure 29, and even though smoke was being injected into both of the lower reverser ports, only the inboard exhaust plume is seen in the laser light sheet. This illustrates the effectiveness of the turning vanes on the lower outboard exhaust nozzle because this reversed flow was deflected outboard and never progressed low enough to appear in the laser light sheet.

Even though the free-stream velocity and the exhaust flow rate had to be reduced to produce effective flow visualization when using smoke, an accurate reverser flow field could still be produced if the correct ratio of exhaust jet dynamic pressure to free-stream dynamic pressure was obtained. This is illustrated by comparing the cascade reverser flow in figure 26 with that shown in figure 12(b). In figure 26, $\dot{m}_R$ equals 1.15 lb/sec and $q_\infty$ equals 0.7 psf, whereas in figure 12(b) $\dot{m}_R$ equals 2.55 lb/sec and $q_\infty$ equals 5.4 psf. Even though the reverser flow rates and the free-stream dynamic pressures are different, the ratio of the dynamic pressure of the lower outboard reverser jet to the free-stream dynamic pressure is 10 in both cases. As a result, the forward progression of the reversed flow is essentially the same in both photographs. A similar set of matching flow patterns can be seen for the 22.5° rotated target configuration when figures 28(c) and 14(f) are compared. In this case, the ratio of the dynamic pressure of the lower reverser jet to the free-stream dynamic pressure is 16 in both photographs. The fact that the smoke injection flow visualization is in good agreement with the water injection flow visualization is further evidence that the water in the exhaust flow is not significantly affecting the shape or position of the reverser exhaust plumes.

The cascade, target, and four-door thrust reversers were not all tested at the same flow rates; therefore, direct comparisons of each reverser is difficult. Identical reverser flow rates were not tested for each configuration due to a partial failure in the high-pressure air-supply system. This resulted in a reduction in the flow rate of high-pressure air available to the model. In general, however, one conclusion that can be drawn from all the flow visualization photographs for all the configurations investigated is that the maximum deceleration from reverse thrust

without reingestion would be obtained by reducing the reverse thrust flow rate (throttling back the engines) as the aircraft slows.

The limit at which exhaust flow from the reversers progresses forward to the plane of the engine inlet as based on $\dot{m}_R$ and $q_\infty$ is presented in figure 30. The boundaries presented indicate the conditions at which reingestion is likely to begin based on flow visualization photographs. Therefore, in order to get the maximum amount of thrust reversing without reingestion, the engines would have to be throttled back as $q_\infty$ is reduced such that conditions remain just below the exhaust gas reingestion boundaries presented. Configurations II and III of the four-door thrust reverser would, in general, allow higher reverse thrust flow rates without reingestion than the other configurations. Configurations II and III of the four-door thrust reverser would also require a more abrupt throttling back of the engines as the aircraft slows to prevent reingestion than the other configurations. However, in order to make an overall comparison of the thrust-reverser configurations the net reverse thrust force for each configuration, as well as the reingestion characteristics, would have to be considered as discussed in reference 15.

## Longitudinal Force and Moment Data Over a Fixed Ground Plane

Longitudinal force and moment data were obtained for each of the reverser configurations over the fixed ground plane. Data for the cascade configuration with $\dot{m}_R$ from 2.55 to 1.15 lb/sec are presented in figure 31. When the free-stream dynamic pressure is low ($q_\infty$ = 1.4 psf), lift increases with increasing $\dot{m}_R$. By referring to figure 12(c) it can be seen that, at $\dot{m}_R$ = 2.55 lb/sec, the reversed flow progresses forward far enough to produce a stagnation region under the outboard portion of the wing. This high-pressure area creates a cushioning effect leading to higher lift accompanied by a nose-down increment in pitching moment. When $\dot{m}_R$ is low, the reverser flow field does not extend far enough forward to affect the wing. (See fig. 12(f).) The increased lift which develops as $\dot{m}_R$ is increased is not desirable as it decreases the normal force on the wheels, which in turn reduces the effectiveness of the wheel brakes. There may be an additional effect on pitching moment due to the reversed flow from the upper exhaust nozzle passing over the horizontal tail.

The effects of water injection into the reversed flow on the longitudinal force and moment data for the cascade thrust reverser are presented in figure 32. The flow rate of the water was approximately one sixth that of the flow rate of air used for the exhaust-flow simulation. The effects of the water injection are small.

Longitudinal aerodynamic data for the target configuration are presented in figures 33 to 35. The effects of decreasing $\dot{m}_R$ for the 22.5° rotated target configuration are presented in figure 33 and can be compared directly to the flow visualization photographs presented in figures 14(a)–(j). The results are similar to those observed for the cascade configuration in that reductions in $\dot{m}_R$ at low speed lead to reductions in lift. At the reverser flow rates of 3.2 lb/sec and 2.25 lb/sec (figs. 14(c) and (g), respectively), the reverser flow moves far enough forward on the ground plane to produce a stagnation region under the wing; thereby, lift is produced. As $\dot{m}_R$ is reduced, however, this effect is lost and lift decreases.

The effects of rotating the target thrust reverser are presented in figure 34 as a function of $\dot{m}_R$ at $q_\infty$ = 1.4 psf. The 0° rotated target configuration produces minimum lift and drag at the highest reverser flow rate. This overall reduction in lift and drag occurs because of the high velocity reversed flow moving forward along the ground near the fuselage. In this position, the reduced static pressure in the reversed flow created a suck-down effect (ref. 16) on the fuselage to reduce lift and produced a forward-directed scrubbing effect along the lower surface of the fuselage to reduce the net drag. Both these flow phenomena disappeared as the target thrust reverser was rotated and the lower reverser exhaust plume moved outboard. As the reversed flow was rotated for the higher values of $\dot{m}_R$, a larger stagnation region was created under the wing, and lift increased. Water injected into the reversed flow on the 15° rotated target configuration at $\dot{m}_R$ = 3.2 lb/sec had a minimal effect on the longitudinal aerodynamics as shown in figure 35.

Longitudinal data both in and out of ground effect for the 15° rotated target configuration with $\dot{m}_R$ = 2.55 lb/sec are presented together for comparison in figure 36. Only when the free-stream dynamic pressure was reduced to 1.4 psf was there any noticeable difference in the data. Therefore, the major influence in ground effect for the 15° rotated target configuration occurs when the free stream is reduced enough such that the reversed flow progresses far enough forward to influence flow over the wing. There may be an additional effect on pitching moment due to the reversed flow from the upper exhaust nozzle passing over the horizontal tail.

Longitudinal aerodynamic data for each of the four-door reverser configurations are presented in figures 37 through 39. As $\dot{m}_R$ is reduced at the lowest free-stream dynamic pressure, configurations I and II show increases in lift and all configurations

show increased drag and decreased pitching moment. A comparison of the three configurations at $\dot{m}_R$ = 5.12 lb/sec (fig. 40) shows that configuration I has the greatest loss in lift as the free-stream dynamic pressure is reduced. This result was generally as expected because the folding door with side fences in the lower inboard location on configuration I directed the reversed flow much farther forward between the floor and the model than did the nonfolding door in the same location on the other two configurations. The aerodynamic effects of the nonfolding door in the lower inboard location also help to explain the nose-up pitching moment at $q_\infty$ = 1.4 psf observed on configurations II and III. For these cases, the inboard section of the wing was undisturbed by the reversed flow and continued to produce lift. This was not true however for configuration I because the free-stream flow over the wing was disrupted by the reversed flow. The largest decrease in drag as $q_\infty$ was reduced occurred for configuration III. This was primarily because of the folding door with turning vanes in the lower outboard location. As illustrated in figure 17(c), this high velocity flow from the lower outboard location was directed right at the wing into the back of the deflected flaps and spoilers. The reversed flow overpowered the free-stream energy and impinged on the deflected flaps and spoilers to produce a large negative drag on the model.

The effects of flap and spoiler deflection were investigated and longitudinal data are presented for configuration I of the four-door thrust reverser in figure 41. The deflection of flaps and spoilers at low values of $q_\infty$ resulted in a net loss in lift which was proportional to $\dot{m}_R$. When the reverser flow rate was at its highest value of 5.12 lb/sec, the effect of deflected flaps and spoilers on drag was directly related to free-stream dynamic pressure. With $\dot{m}_R$ = 5.12 lb/sec and $q_\infty$ = 12.2 psf, the free stream had the dominant effect on the wing, and the deflected flaps and spoilers increased the drag on the model. However, as $q_\infty$ was decreased below 8 psf, the trend reversed, the reversed flow had the dominant effect on the wing, and the effect of deflected flaps and spoilers was a reduction in drag. At the low reverser flow rate ($\dot{m}_R$ = 1.15 lb/sec), the free-stream flow had the dominant effect on the wing over the range of $q_\infty$ tested.

## Effects of a Moving-Belt Ground Plane

As was previously mentioned, all testing in ground effect was conducted with the tunnel boundary-layer removal system in operation. This, however, still allowed a boundary layer approximately 1.6 in. thick to form on the tunnel floor under the model. In order to simulate more accurately actual landing conditions, the floor boundary layer under the model was completely eliminated by using a moving-belt ground plane operating at a velocity equal to the test section free-stream velocity (ref. 7). (A sketch of the test section with the model over the moving-belt ground plane is shown in fig. 8.) Both flow visualization photographs and longitudinal aerodynamic data are presented for the fixed ground plane and the moving-belt ground plane. Because the moving belt is constructed of a water-absorbing woolen fabric, the water injection flow visualization technique could not be used. All flow visualization comparisons therefore consist of configurations with smoke injected into the reversed flow in combination with the horizontal laser light sheet.

Photographs for the reverser flow fields over a fixed and a moving-belt ground plane are presented for the cascade configuration with $\dot{m}_R$ = 1.15 lb/sec and $q_\infty$ = 0.7 psf in figure 42. These photographs illustrate how the presence of the boundary layer over a fixed ground plane provides conditions under which the reversed flow can progress farther forward than when over a moving-belt ground plane. The low energy flow in the boundary layer over a fixed ground plane presents less resistance to the reversed flow than does the high energy flow over a moving-belt ground plane where no boundary layer exists.

Longitudinal aerodynamic data are presented as functions of reverser flow rate in figure 43 for the cascade configuration over both a fixed and a moving-belt ground plane for $q_\infty$ = 1.4 psf. The most substantial difference between the fixed and the moving-belt data occurs in lift coefficient at the highest reverser flow rate. When the ground belt was moving, the forward progression of the reversed flow was reduced, as compared with operation over the fixed ground plane. The fixed ground plane allowed the exhaust plume to move farther forward (ref. 17), and the stagnation region, which forms as a result of the free stream and the reversed flow interacting, occurred under the wing. This stagnation region under the wing resulted in additional lift, and its presence is further illustrated by the water injection flow visualization over the fixed ground plane presented in figure 12(c).

A similar comparison is made of longitudinal data presented for $q_\infty$ = 12.2 psf in figure 44. Under these conditions there is still additional lift over the fixed ground plane at the highest reverser flow rate compared with that over the moving ground plane; however, the magnitude of this additional lift has been reduced due to the higher velocity free-stream flow. In figure 43 more lift was generated over the fixed ground plane when $\dot{m}_R$ was increased above approximately 1 lb/sec; however, in figure 44

the reverser flow rate must be increased above approximately 1.6 lb/sec before the configuration over the fixed ground plane begins to produce more lift. This is because when the higher velocity free stream in figure 44 comes in contact with the reversed flow the stagnation region forms farther downstream and therefore has less effect on the wing.

Photographs for the reverser flow fields over a fixed and a moving-belt ground plane are presented for the 0° rotated target thrust reverser with $\dot{m}_R = 0.80$ lb/sec and $q_\infty = 0.7$ psf in figure 45. As seen previously, the reversed flow does not progress as far forward over a moving-belt ground plane as it does over a fixed ground plane. In addition, the reversed flow from the 0° rotated target thrust reverser spreads outboard farther when over a fixed ground plane than when over a moving-belt ground plane.

Longitudinal aerodynamic data are presented versus reverser flow rate in figure 46 for the 0° rotated target thrust reverser over both fixed and moving-belt ground planes with $q_\infty = 1.4$ psf. In general both lift and drag are higher for the configuration over the moving-belt ground plane. This is because the forward penetration of the reversed flow was reduced by the moving ground belt, which reduced the suck-down effect on the back of the fuselage. The reduced forward progress of the reversed flow also reduced the skin friction on the fuselage from the exhaust flow resulting in an overall increase in drag.

Flow visualization photographs were not obtained for the 15° rotated target thrust reverser over both fixed and moving-belt ground planes; however, longitudinal aerodynamic data were taken and are presented for both conditions in figure 47. The results from the 15° rotated target thrust reverser are similar to those for the cascade thrust reverser in that the 15° rotated target thrust reverser produced more lift at the highest value of $\dot{m}_R$ when over the fixed ground plane. The fixed ground plane allowed the reversed flow to progress farther forward so that the stagnation region forms under the wing as already discussed.

Flow visualization photographs for the flow fields over a fixed and moving-belt ground plane are presented for the 22.5° rotated target thrust reverser with $\dot{m}_R = 1.15$ lb/sec and $q_\infty = 1.4$ psf in figure 48. These photographs are similar to those for the 0° rotated target thrust reverser in that the reversed flow does not progress as far forward or outboard when over the moving-belt ground plane.

Longitudinal aerodynamic data are presented against reverser flow rate in figure 49 for the 22.5° rotated target thrust reverser over both fixed and moving-belt ground planes with $q_\infty = 1.4$ psf. These data, like those for the 15° rotated target thrust reverser, show that more lift is generated at the highest value of $\dot{m}_R$ when over the fixed ground plane. The photographs in figures 14(c) and (d) illustrate how high velocity reversed flow from the 22.5° rotated target thrust reverser progresses forward over a fixed ground plane and forms a stagnation region under the wing; thus, additional lift results.

These results, from both flow visualization and longitudinal force and moment data, indicate that when investigating a thrust-reversing configuration in ground effect, a moving-belt ground plane is necessary to simulate landing conditions correctly. A fixed ground plane results in incorrect forces and moments on the model due to incorrect interaction of the free stream and reversed flows. In addition, since the fixed ground plane allows the reversed flow to progress farther forward on the tunnel floor, exhaust gas reingestion can occur at a higher free-stream velocity or a lower reverser flow rate than when over a moving-belt ground plane. Based on this information, the boundaries for the onset of reingestion presented in figure 30 would be conservative since a moving-belt ground plane would allow a lower free-stream velocity or a higher reverser flow rate before the reverser flow would move upstream to the vicinity of the inlet.

### Reversed Flow Contours From a Pressure-Instrumented Ground Board

Pressure measurements were obtained on the ground as a means to identify the reversed-flow ground impingement point (ref. 18) and to provide reversed-flow velocity data. Both static and total pressures were obtained on a pressure-instrumented ground board as illustrated in figures 9 and 10. Static-pressure measurements were obtained from the static-pressure orifices illustrated in figure 9(a), while total-pressure measurements were obtained from the total-pressure orifices identified in figure 9(b).

The total-pressure orifices were all pointed to a spot directly below the reverser nozzle for the target thrust-reverser configurations. This positioning of the total-pressure probes was based on flow patterns seen in the flow visualization study. However, this alignment was not suitable for the cascade or four-door thrust-reverser configurations since the reversed flow from these configurations did not impinge and moved forward on the ground in the same location as reversed flow from the target reversers. Therefore, reversed-flow velocity contours, which are derived from the static- and total-pressure data, are only presented for the target thrust-reversing configurations. Static-pressure contours and velocity

contours are presented in figures 50 through 54. To aid in comparisons, vertical and horizontal rows of tick marks which correspond to the position of the grid presented in figure 10(b) have been added to each figure.

Static-pressure contours, which are presented in terms of pressure coefficient $C_p$, show the position at which the reverser exhaust flows come in contact with the ground and are presented for the cascade thrust reverser in figure 50. The dashed-line contours represent $C_p = 0$, contours inside the dashed line represent positive values of $C_p$, and contours outside the dashed line represent negative values of $C_p$. The increment between contours is identified as $\Delta C_p$ in each figure. The horizontal line on the nacelle marks the location of the center of the reverser exhaust nozzles. (See fig. 50(a).) This description holds true for all static-pressure contours presented in this paper.

The effects of decreased reverser flow rate can be seen by comparing figure 50(a) with 50(b). The higher reverser flow rate produces a more expansive set of pressure contours. The highest pressures sensed by the static-pressure orifices are from those in the area where the reverser exhaust jet impinges on the ground. This is illustrated in the contours where $\dot{m}_R = 2.55$ lb/sec because positive values of $C_p$ are recorded where the exhaust jet impinges on the ground. When the reverser flow rate is reduced to 2.15 lb/sec, the pressure measured at the center of the flow impingement point is reduced due to the lower velocity of the exhaust flow. For both conditions presented in figure 50, pressure decreases and exhaust flow velocity parallel to the floor increases as the exhaust flow moves away from the point of impingement.

The water injection flow visualization photographs presented in figure 12(c) were taken under the same flow conditions as those which generated the pressure contours in figure 50(a). When these figures are compared, the point of impingement identified by the pressure contours shows very good agreement with the flow visualization. In addition, the pressure contours reveal a potential reingestion problem that could develop as the exhaust from the two reverser jets move toward one another on the ground. As these flows come together they will lift off the ground to produce a fountain effect (refs. 16 and 19), and the combined exhaust flow will rise right under the engine inlet.

The pressure contours also provide a further explanation as to why lift increases and a nose-down pitching moment is produced as $\dot{m}_R$ is increased at $q_\infty = 1.4$. (See longitudinal data in fig. 31.) Additional lift is generated on the rear of the fuselage as the inboard reverser jets from each engine simulator come together on the ground under the center of the fuselage. As these jets come together they produce a fountain effect and, thus, increase lift on the rear of the fuselage which in turn adds to a nose-down pitching moment.

As the free-stream dynamic pressure was increased above $q_\infty = 1.4$ psf, the wake from the wing and landing gear produced enough influence on the static-pressure orifices such that the resulting pressure contours were not adequate to accurately identify the point of reversed-flow impingement on the ground. For this reason, pressure contours are presented only for $q_\infty = 1.4$ psf.

Both pressure and velocity contours are presented for the 15° rotated target thrust reverser in figure 51 as $\dot{m}_R$ is reduced from 3.2 to 1.35 lb/sec. The velocity contours are bounded by lines that show the most rearward location of total-pressure probes on the pressure-instrumented ground board. (See fig. 51(a).) In each case, the point at which the reversed flow impinges on the ground is clearly identified by the pressure contours. In addition, the strength of the reversed flow is illustrated by the number of pressure contours and the position of the velocity contours. As the reverser exhaust flow rate is reduced from 3.2 to 2.25 lb/sec, there is no change in the location of the reversed-flow impingement point (fig. 51(b)); however, when the reverser exhaust flow rate is further reduced to 1.35 lb/sec, the reversed-flow impingement point moves inboard slightly (fig. 51(c)).

The water injection flow visualization photographs presented in figure 13(b) were taken under the same conditions as those for the contours in figure 51(a) and when compared show good agreement in relative location of reversed-flow ground impingement.

The 22.5° rotated target thrust reverser was also investigated over the pressure-instrumented ground board and both pressure and velocity contours are presented for that configuration in figure 52. The effects of the increased rotation angle are clearly seen as the point of impingement (identified by the pressure contours) is clearly located farther outboard in all cases presented in figure 52 as compared with those in figure 51. The pressure contours for the configuration with the higher rotation angle reveal that the exhaust jet is weaker when it impinges on the ground, as would be expected, because of the greater distance between the exhaust nozzle and the ground. The velocity contours also show the effects of the increased rotation angle, and when parts (a) and (b) of figures 52 and 51 are compared, it can be seen that the increased rotation angle decreased

the potential for reingestion in that it reduced the amount of reversed flow directed on the ground in front of the engine inlet.

When the four-door thrust-reverser configurations were investigated over the pressure-instrumented ground board, only the reverser jets from the nonfolding door exhaust nozzles contacted the ground board with sufficient magnitude to identify the point of impingement in the pressure contours. Since configuration I of the four-door thrust reverser had no nonfolding door exhaust nozzles in either of the lower positions, the pressure-instrumented ground board was not effective in providing information as to where the reversed exhaust flow came in contact with the ground. When configurations II and III were investigated over the pressure-instrumented ground board, the point of impingement of the lower outboard exhaust jets could not be clearly identified, and the points of impingement of the lower inboard exhaust jets were identical since both configurations had a nonfolding door exhaust nozzle in that location. For this reason, pressure contour data are only presented for configuration II of the four-door thrust reverser. These data, presented in figure 53, show the point of impingement and the intensity of the reversed flow from the lower inboard exhaust jet as $\dot{m}_R$ is reduced from 2.55 to 1.15 lb/sec. At $\dot{m}_R = 1.15$ lb/sec, the point of impingement is farther downstream due to the free-stream flow having a stronger effect on the weaker exhaust jet. This is further supported by the water injection flow visualization for these same flow conditions as presented in figure 16(i).

As was mentioned previously, when the free-stream dynamic pressure was increased above 1.4 psf, the pressure contours which resulted from the static-pressure orifices did not clearly show the reverser impingement location due to interference from the landing gear wake. It was, however, possible to obtain velocity contours since they were primarily located outboard of the area of the landing gear wake. Therefore, the effects of reducing the free-stream dynamic pressure from 12.2 to 1.4 psf could be illustrated by developing velocity contours from static and total pressures measured on the pressure-instrumented ground board. This is shown in figure 54 for the 15° rotated target thrust reverser. The velocity of the reversed flow on the ground is rapidly reduced when opposed by the highest free-stream dynamic pressure of 12.2 psf; however, as the free-stream dynamic pressure is lowered, the velocity contours clearly illustrate the increased forward progression of the reversed flow. Thus, when both static and total pressures are measured in the reverser flow field, a representation of the effects of variations in the free-stream dynamic pressure can be obtained.

### Effects of Reduced Inlet Flow

In this investigation, the engine simulators provided the correct inlet flow rate for each reverse thrust flow rate on each of the thrust-reverser configurations. In addition, the inlet simulation system was equipped with a flow rate control so that the inlet flow rate $\dot{m}_I$ could be set anywhere from full inlet flow to free-stream, flow-through conditions. This inlet flow control enabled the investigation of the effects of reduced inlet flow.

Investigations of full inlet flow versus flow-through inlet flow were conducted by using the water injection flow visualization technique. Photographs showing the results of these investigations are presented for the cascade thrust reverser at $\dot{m}_R = 1.15$ lb/sec with $q_\infty = 12.2$ psf in figure 55. Similar photographs for the 22.5° rotated target thrust reverser are presented in figure 56 with $\dot{m}_R = 3.2$ lb/sec and $q_\infty = 1.4$ psf. In both cases, the reversed flow progresses farther forward on the ground when the engine simulators are operating at full inlet flow conditions. This occurs because during full inlet flow conditions the free-stream flow is accelerated in the vicinity of the inlet, as compared with the flow-through case; thus, the local pressure is reduced and more forward penetration of the reversed flow is allowed.

Additional investigations were performed where inlet flow was reduced from the full engine flow to the flow-through case, and longitudinal force and moment data were obtained at each extreme as well as at intermediate conditions. Longitudinal aerodynamic data are presented versus $q_\infty$ for the cascade thrust reverser with reduced inlet flows both in and out of ground effect in figure 57. In both cases, the configuration was insensitive to reductions in inlet flow rate except possibly at the lowest free-stream dynamic pressure. When the free stream was reduced to $q_\infty = 1.4$ psf, variations appear in the data; however, no trends which correspond to reductions in $\dot{m}_I$ can be identified. Longitudinal aerodynamic data for full inlet flow versus a flow-through inlet are presented for several values of $\dot{m}_R$ in figure 58. One trend that can be observed here is that when $q_\infty = 1.4$ psf the full inlet flow condition produces slightly more lift than the flow-through inlet condition for each of the values of $\dot{m}_R$ presented.

Longitudinal aerodynamic data are presented for the 15° rotated target thrust reverser with reduced inlet flows both in and out of ground effect in figure 59. These data are similar to those presented for the cascade configuration in figure 57 in that they

are insensitive to reductions in inlet flow except when $q_\infty = 1.4$ psf; however, at that condition no trends based on the reduced inlet flow rate can be identified. Longitudinal aerodynamic data for full inlet flow versus a flow-through inlet are presented for both the 15° and 22.5° rotated target configuration for several values of $\dot{m}_R$ in figure 60. As was the case for the cascade configuration, both these target configurations produce slightly more lift under the full inlet flow condition. This holds true for each value of $\dot{m}_R$ when $q_\infty = 1.4$ psf.

Longitudinal aerodynamic data were obtained for both configurations I and III of the four-door thrust reverser under reduced inlet flow conditions and are presented in figure 61. The initial reduction of $\dot{m}_I$ below full inlet flow conditions acts to reduce lift on configuration I of the four-door thrust reverser; however, further inlet flow reductions do not produce a clear trend. When the longitudinal aerodynamic data for configuration III of the four-door thrust reverser are observed, no trends based on the reduction of $\dot{m}_I$ can be identified. Both configurations, however, show an increased sensitivity to reduced inlet flow as free-stream dynamic pressure is reduced.

The investigation of the effects of full inlet flow versus a flow-through inlet also included acquiring pressure-instrumented ground board data for the target thrust-reverser configuration. These data are presented in the form of velocity contours for both the 15° and 22.5° rotated target thrust reversers in figure 62. The contours for both rotation angles show that the reversed flow did not progress as far forward on the ground in front of the inlet for the flow-through inlet condition as it did for the full inlet flow condition. The full inlet flow condition effectively reduced the free-stream flow in the vicinity of the inlet; thus, increased forward progression of the reversed flow was allowed. This increased forward penetration of the reversed flow is most pronounced in the area in front of the inlet as would be expected and is in agreement with the flow visualization photographs presented in figures 55 and 56.

## Summary of Results

A wind-tunnel investigation has been conducted to study the effects of engine thrust reversing on an aft-mounted twin-engine transport. The thrust reversers examined included cascade, target, and four-door configurations. Testing was done over a fixed ground plane, a moving-belt ground plane, and a pressure-instrumented ground board. Longitudinal aerodynamic data have been obtained both in and out of ground effect and the effects of flap and spoiler deflections have been determined. Several flow visualization techniques have been examined to determine the forward progression of the reverser flow. The results of this investigation as well as the testing techniques developed are summarized as follows:

1. Injection of water or smoke into the thrust reverser exhaust flow provided a very effective means of visualizing the reversed flow and had little effect on longitudinal force and moment data. The use of a laser light sheet in combination with water or smoke injected into the reversed flow was effective for highlighting a slice of the reverser exhaust plume.

2. Measured pressures from a pressure-instrumented ground board corroborate flow visualization results and provide a means by which to obtain reverser flow velocities on the ground.

3. Conditions under which exhaust gas reingestion occurred were configuration dependent. Maximum deceleration from reverse thrust without reingestion would be obtained by continually reducing the reverse thrust flow rate, just enough to prevent reingestion, as the aircraft slows. Configurations II and III of the four-door thrust reverser would, in general, allow higher reverse thrust flow rates without reingestion than the other configurations.

4. When a high velocity reversed flow progressed upstream under the fuselage, as for the 0° rotated target configuration or configuration I of the four-door thrust reverser, a loss in lift occurred resulting from a suck-down effect.

5. For configurations and free-stream dynamic pressures where a high velocity reversed flow impinged on deflected flaps and spoilers, a decrease in drag resulted.

6. A significant difference in forward progression of the reversed exhaust flow and the resulting longitudinal aerodynamic data results when testing over a fixed versus a moving-belt ground plane. A fixed ground plane produces conservative results in terms of reingestion; a moving-belt ground plane improves conditions for testing thrust reversing configurations in ground effect.

7. All configurations showed an increased sensitivity to reductions in inlet flow rate as free-stream dynamic pressure $q_\infty$ was reduced to 1.4 psf. In general, configurations with a flow-through inlet generated less forward progression of the reversed flow and less lift than configurations with full inlet flow when $q_\infty = 1.4$ psf.

NASA Langley Research Center
Hampton, VA 23665-5225
September 16, 1988

## References


1. Harford, James J.: Thrust Reversing Too Complex for Computers. *Aerosp. America*, vol. 22, no. 11, Nov. 1984, pp. 30–33.
2. Eagles, David: Development of the Tornado Thrust Reverser. *J. Soc. Environ. Eng.*, vol. 22–3, no. 98, Sept. 1983, pp. 3–9.
3. Lotter, Kurt; and Kurz, Wolfgang: Aerodynamic Aspects and Optimization of Thrust Reverser Systems. *Airframe/Propulsion Interference*, AGARD-CP-150, Mar. 1975, pp. 27-1–27-22.
4. Glezer, A.; Hughes, R. V.; and Hunt, B. L.: Thrust Reverser Effects on Fighter Aircraft Aerodynamics. *J. Aircr.*, vol. 22, no. 6, June 1985, pp. 455–461.
5. Colehour, J. L.: *A Study of Foreign Particle Ingestion for a 747 Type Inlet.* D6-23238, Commercial Airplane Div., Boeing Co., Aug. 1969. (Available from DTIC as AD B073 428L.)
6. Adams, J. D.: *Study of Requirements for B-1 Engine Foreign Object Damage Protection.* TFD-71-1012A, North American Rockwell Corp., June 1972. (Supersedes TFD-71-1012.) (Available from DTIC as AD B027 506L.)
7. Kurz, Wolfgang: Comparisons of Model and Flight Testing With Respect to Hot Gas Reingestion and Debris Ingestion During Thrust Reversal. *Proceedings of the Fifth International Symposium on Airbreathing Engines*, National Aeronautical Lab. (Bangalore, India), Feb. 1981, pp. 13-1–13-9.
8. Jackson, John: Development of the Boeing 767 Thrust Reverser. AIAA-86-1536, June 1986.
9. Amin, Nasim F.; and Richards, Clifford J.: Thrust Reverser Exhaust Plume Reingestion Model Tests. *J. Aircr.*, vol. 21, no. 6, June 1984, pp. 401–407.
10. Willmer, A. C.; and Scotland, R. L.: Reverse Thrust Experience on the Concorde. *Airframe/Propulsion Interference*, AGARD-CP-150, Mar. 1975, pp. 11-1–11-15.
11. Petit, John E.; and Scholey, Michael B.: Analysis, Design and Test of Thrust Reverser and Thrust Vectoring Systems for STOL Transport Aircraft. AIAA-73-1218, Nov. 1973.
12. Lenorovitz, Jeffrey M.: CFM Plans No Ultrahigh Bypass Competitor to IAE's Superfan. *Aviation Week & Space Technol.*, vol. 126, no. 5, Feb. 2, 1987, pp. 28–30.
13. Baals, Donald D.; and Corliss, William R.: *Wind Tunnels of NASA.* NASA SP-440, 1981.
14. Applin, Zachary T.: *Flow Improvements in the Circuit of the Langley 4- by 7-Meter Tunnel.* NASA TM-85662, 1983.
15. Gatlin, Gregory M.; Banks, Daniel W.; and Paulson, John W., Jr.: *Low-Speed Longitudinal Aerodynamics and Directional-Control Effectiveness of an Advanced Fighter Configuration With Multifunction Nozzles.* NASA TP-2794, 1988.
16. Campbell, John Paul.: *Vertical Takeoff and Landing Aircraft.* Macmillan Co., c.1962.
17. Stewart, V. R.; Kuhn, R. E.; and Walters, M. M.: Characteristics of the Ground Vortex Developed by Various V/STOL Jets at Forward Speed. AIAA-83-2494, Oct. 1983.
18. Dudley, Michael R.; Eshleman, James E.; and Schell, Charles J.: Full-Scale Ground Effects of Twin Impinging Jets Beneath a Subsonic Tactical V/STOL Aircraft. AIAA-86-2704, Oct. 1986.
19. Kind, R. J.; and Suthanthiran, K.: The Interaction of Two Opposing Plane Turbulent Wall Jets. AIAA Paper No. 72-211, Jan. 1972.

Table I. Model Dimensional Data

[Model moment reference center is 93.385 in. aft of model nose and 3.500 in. above FRP]

| | |
|---|---|
| Wing: | |
| Area, $S$, ft$^2$ | 9.795 |
| Span, $b$, ft | 9.707 |
| Root chord, ft | 1.746 |
| Tip chord, ft | 0.272 |
| Mean aerodynamic chord, $\bar{c}$, ft | 1.188 |
| Aspect ratio, $A$ | 9.619 |
| Taper ratio | 0.156 |
| Sweep ($0.25c_{\text{local}}$), deg | 24.5 |
| Twist, deg | 5.04 |
| Incidence, deg, at — | |
| $\eta = 0.1881$ | 4.04 |
| $\eta = 0.3031$ | 3.35 |
| $\eta = 0.3859$ | 2.65 |
| $\eta = 0.5276$ | 1.73 |
| $\eta = 0.89$ | −1.0 |
| Dihedral, deg | 4.0 |
| Main landing gear: | |
| Wheel diameter, in. | 3.780 |
| Wheel width, in. | 1.359 |
| Nose gear: | |
| Wheel diameter, in. | 2.340 |
| Wheel width, in. | 0.630 |
| Horizontal tail: | |
| Area, ft$^2$ | 2.864 |
| Span, ft | 3.916 |
| Root chord, ft | 1.112 |
| Tip chord, ft | 0.351 |
| Mean aerodynamic chord, $\bar{c}_{ht}$, ft | 0.797 |
| Aspect ratio | 5.357 |
| Taper ratio | 0.316 |
| Sweep ($0.25c_{\text{local}}$), deg | 31.6 |
| Twist, deg | 0 |
| Incidence, deg | 0 |
| Dihedral, deg | −3.0 |
| Tail length, $0.25\bar{c}$ to $0.25\bar{c}_{ht}$, ft | 5.785 |
| Vertical tail: | |
| Area, ft$^2$ | 1.305 |
| Span, ft | 1.036 |
| Root chord, ft | 1.399 |
| Tip chord, ft | 1.119 |
| Mean aerodynamic chord, $\bar{c}_{vt}$, ft | 1.265 |
| Aspect ratio | 0.82 |
| Taper ratio | 0.800 |
| Sweep ($0.25c_{\text{local}}$), deg | 43.5 |
| Tail length, $0.25\bar{c}$ to $0.25\bar{c}_{vt}$, ft | 4.898 |

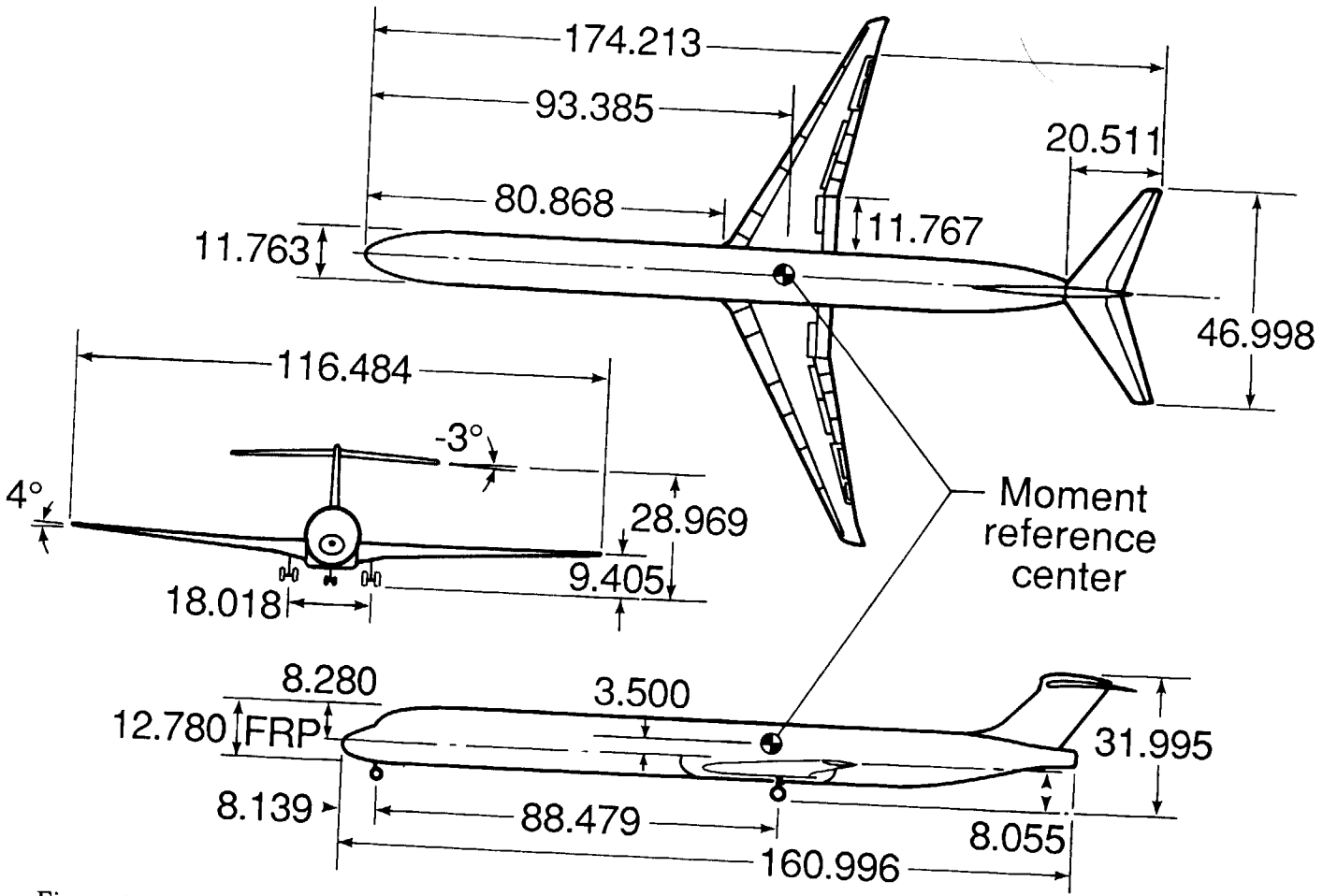


Figure 1. Three-view sketch of MD-89 twin engine jet transport model. Linear dimensions are in inches.

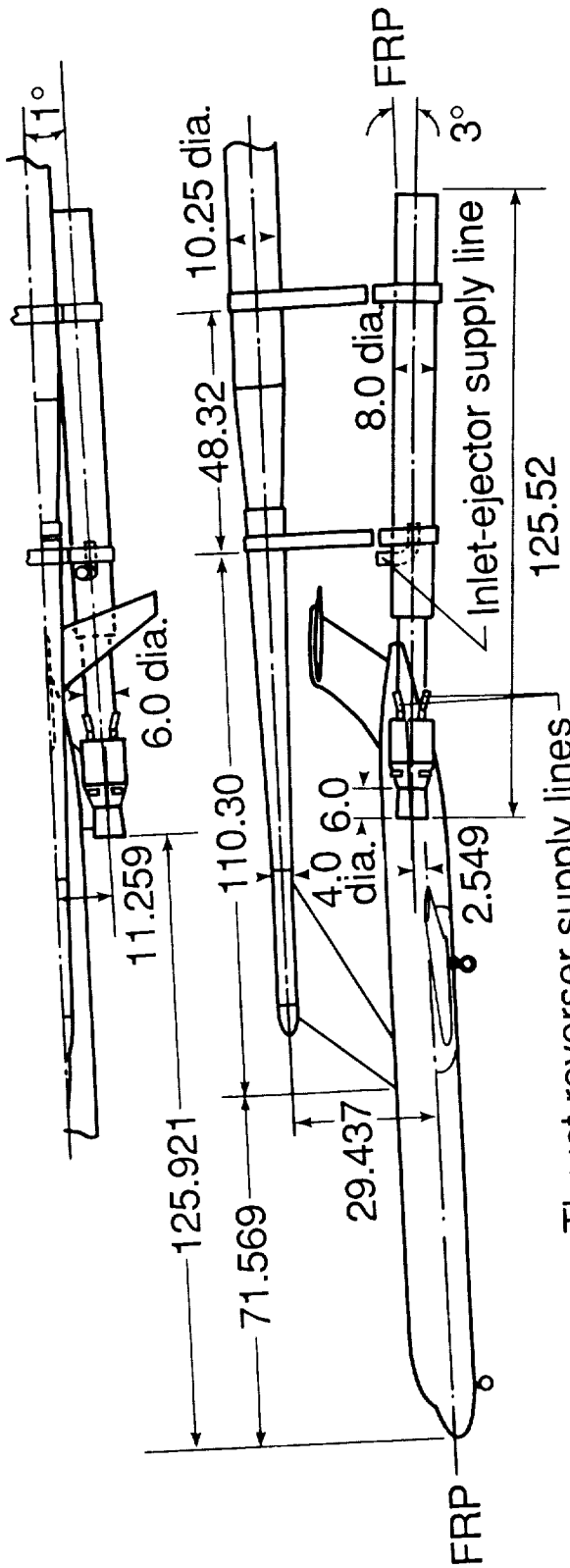


(a) Test setup used for cascade and four-door thrust-reverser simulation.

Figure 2. Model support and engine simulation system. Linear dimensions are in inches.

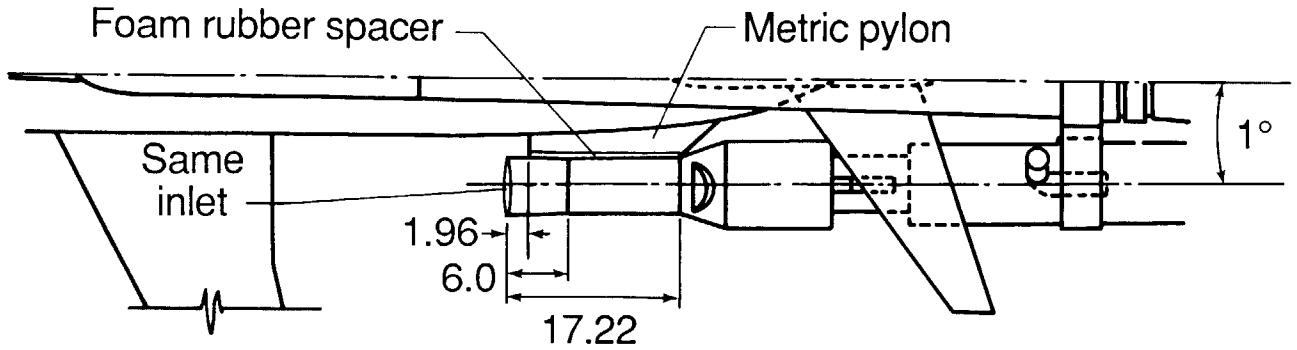


(b) Test setup used for target thrust-reverser simulation.

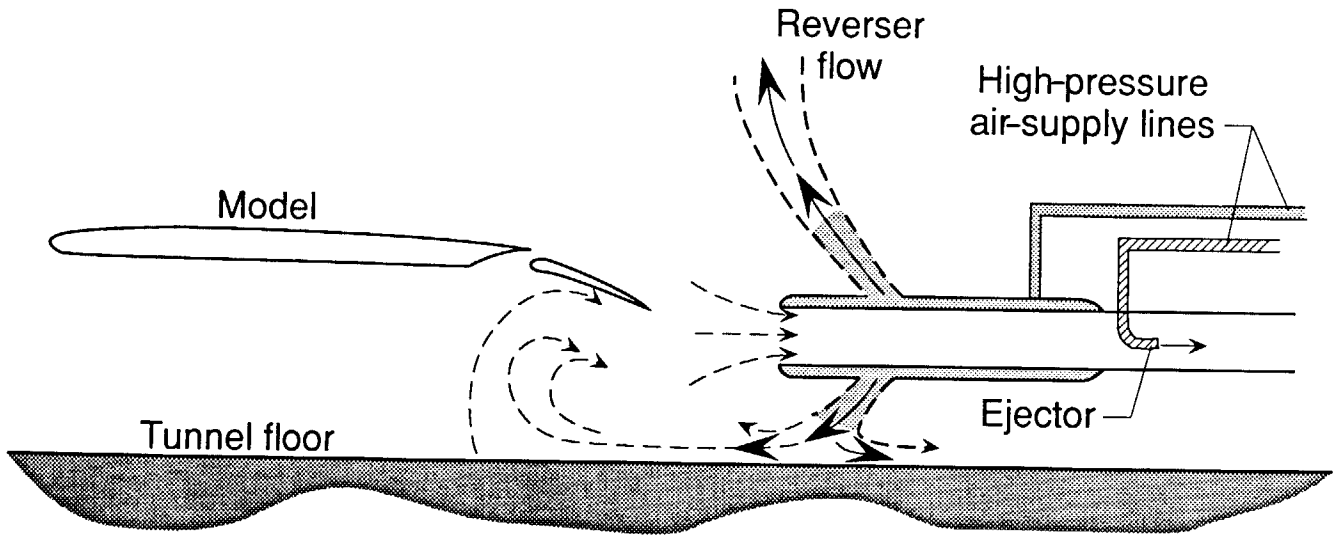


(c) Schematic diagram of engine simulation system.

Figure 2. Concluded.

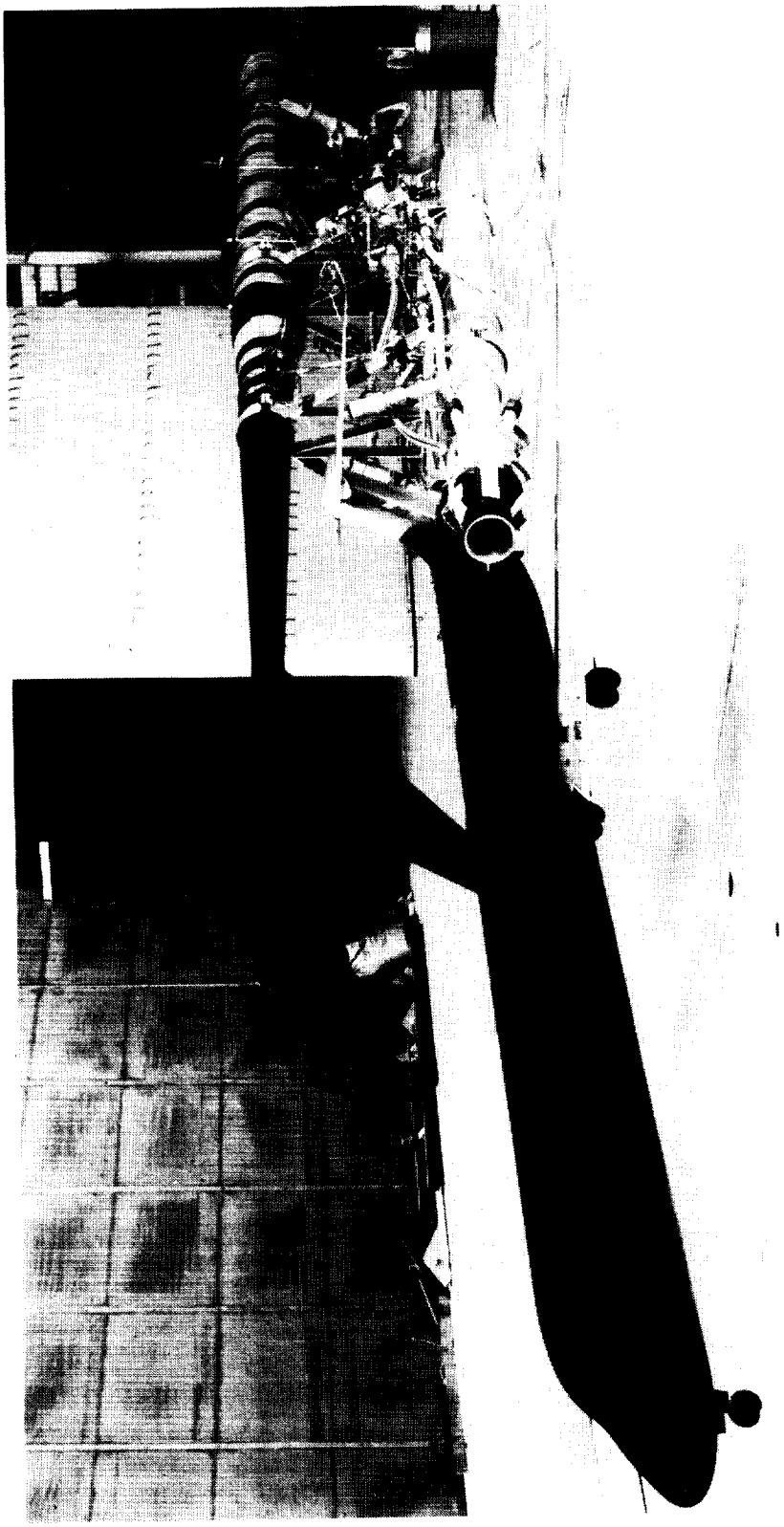

L-86-5370

Figure 3. Photograph of McDonnell Douglas MD-89 jet transport model with engine simulators as mounted in test section of Langley 14- by 22-Foot Subsonic Tunnel.

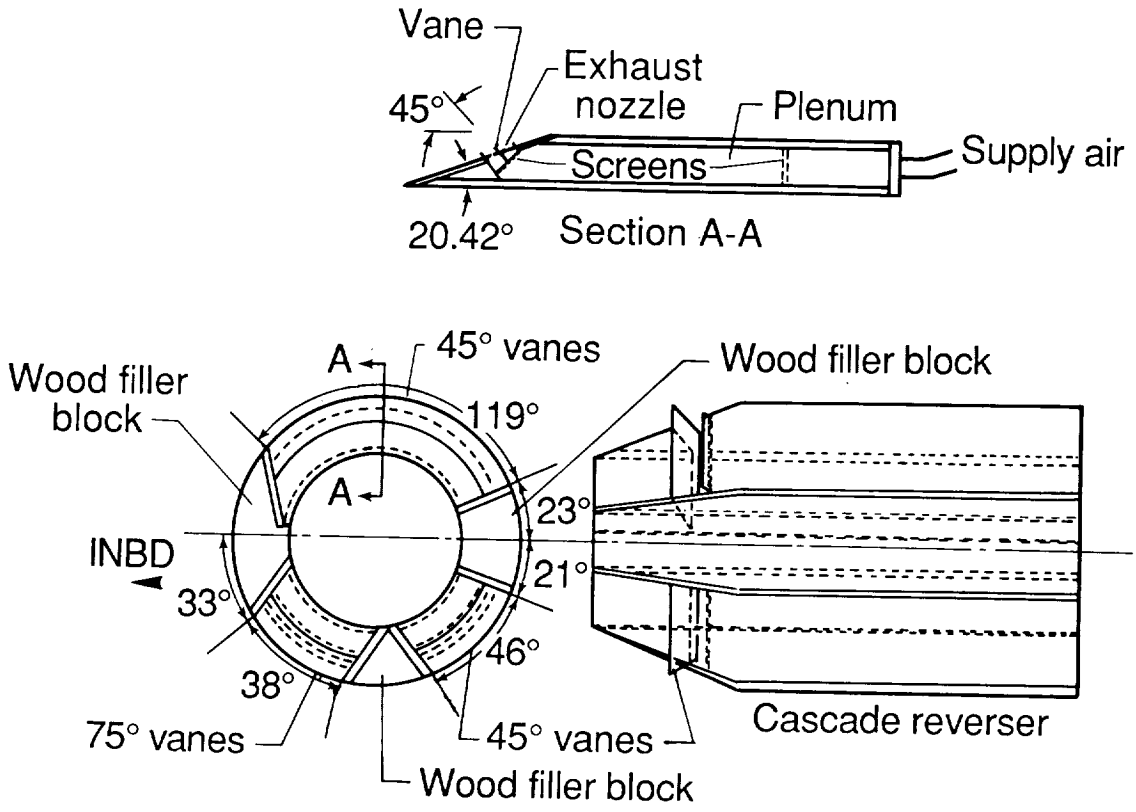


(a) Cascade thrust reverser.

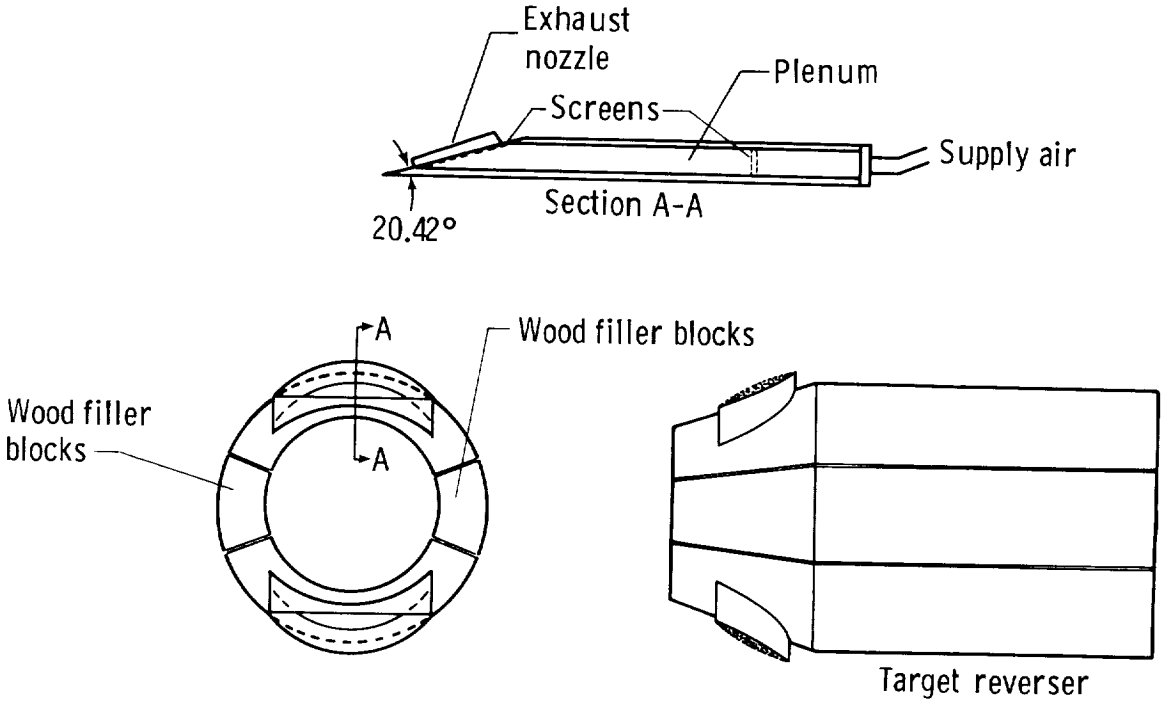


(b) Target thrust reverser.

Figure 4. Sketches of thrust-reverser simulators.

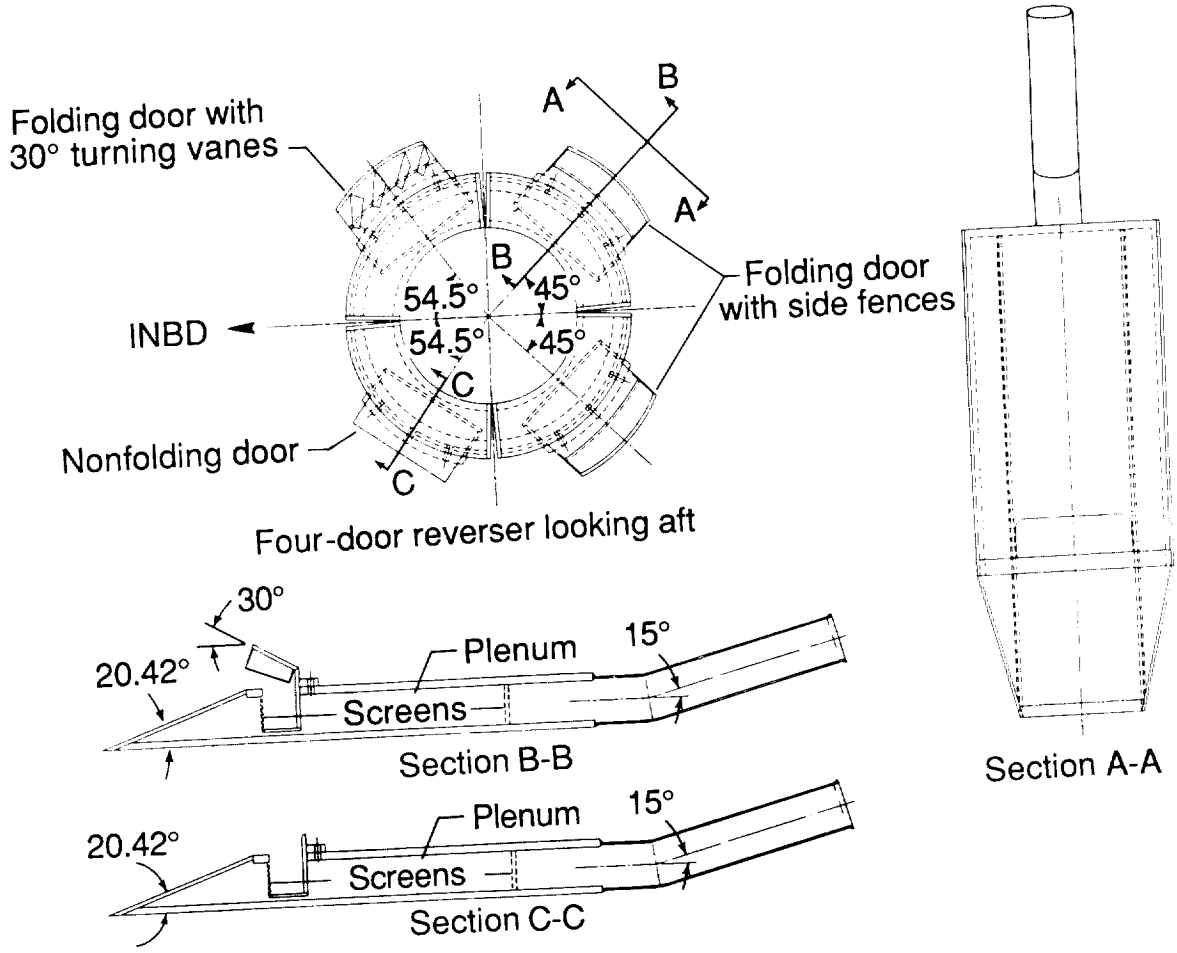


(c) Four-door thrust reverser.

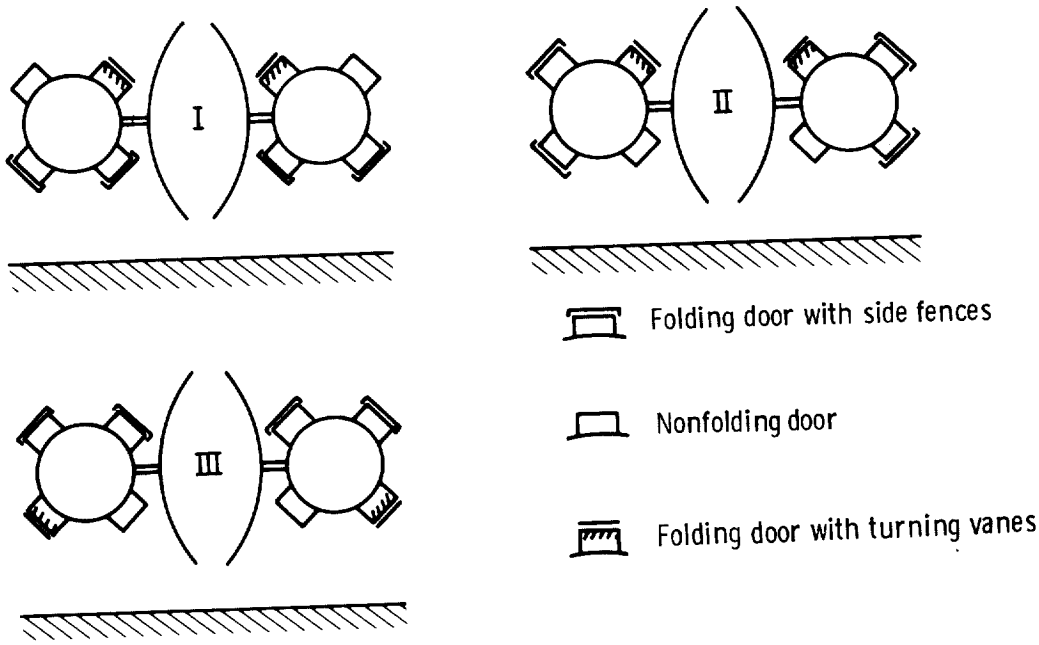


(d) Three configurations tested of four-door thrust reverser.

Figure 4. Concluded.

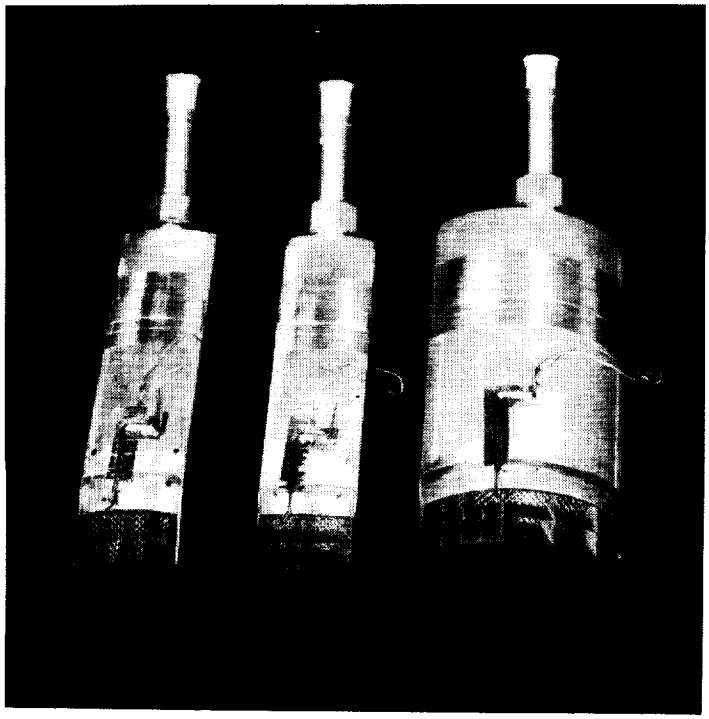


L-88-118

(a) Cascade thrust-reverser plenums.

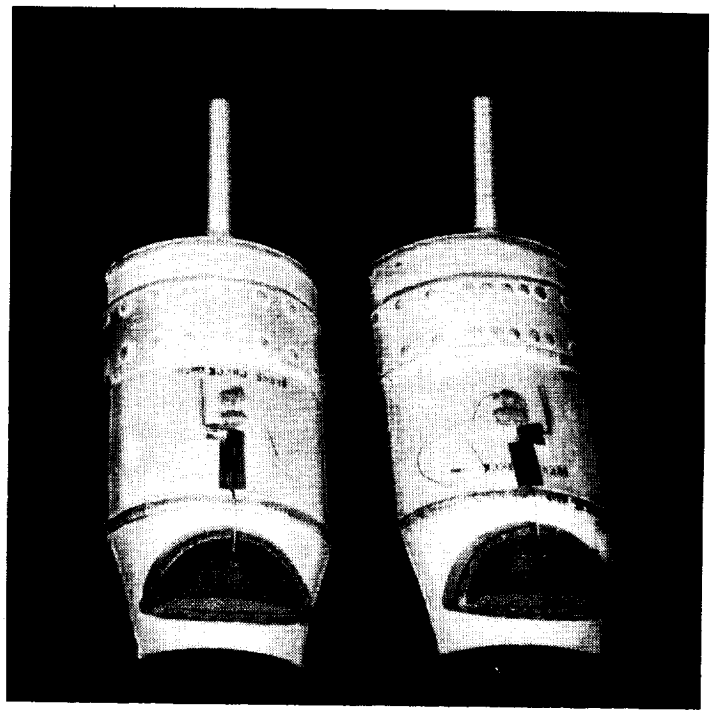

L-88-119

(b) Target thrust-reverser plenums.

Figure 5. Photographs of reverser plenums.


(c) Four-door thrust-reverser plenums.

Figure 5. Concluded.

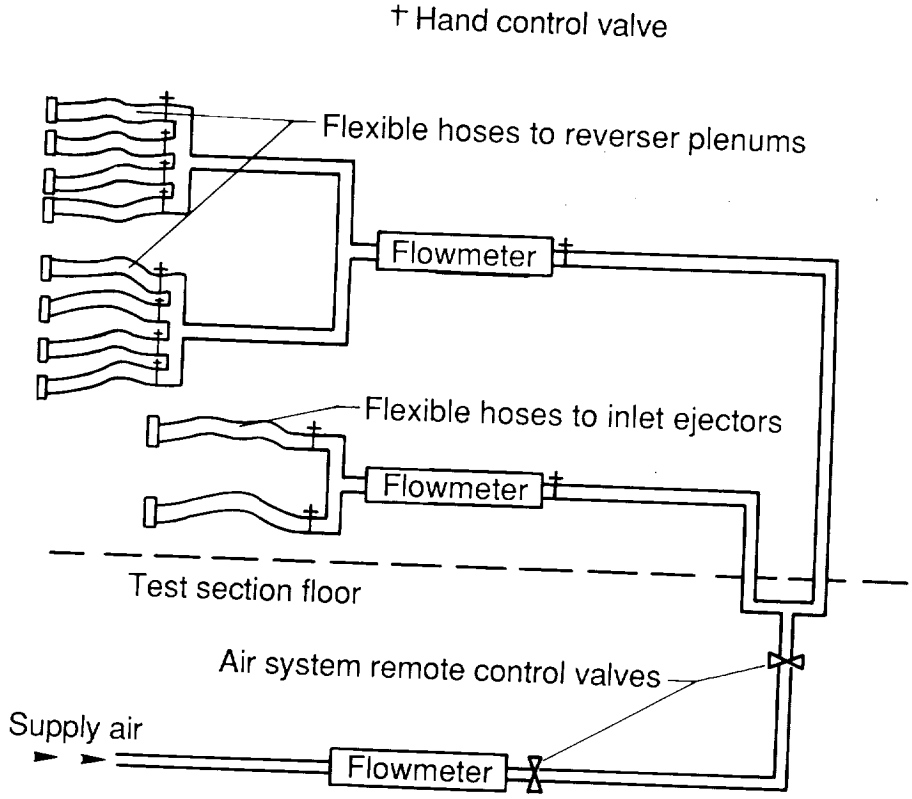


Figure 6. High-pressure air-supply system to engine simulators.

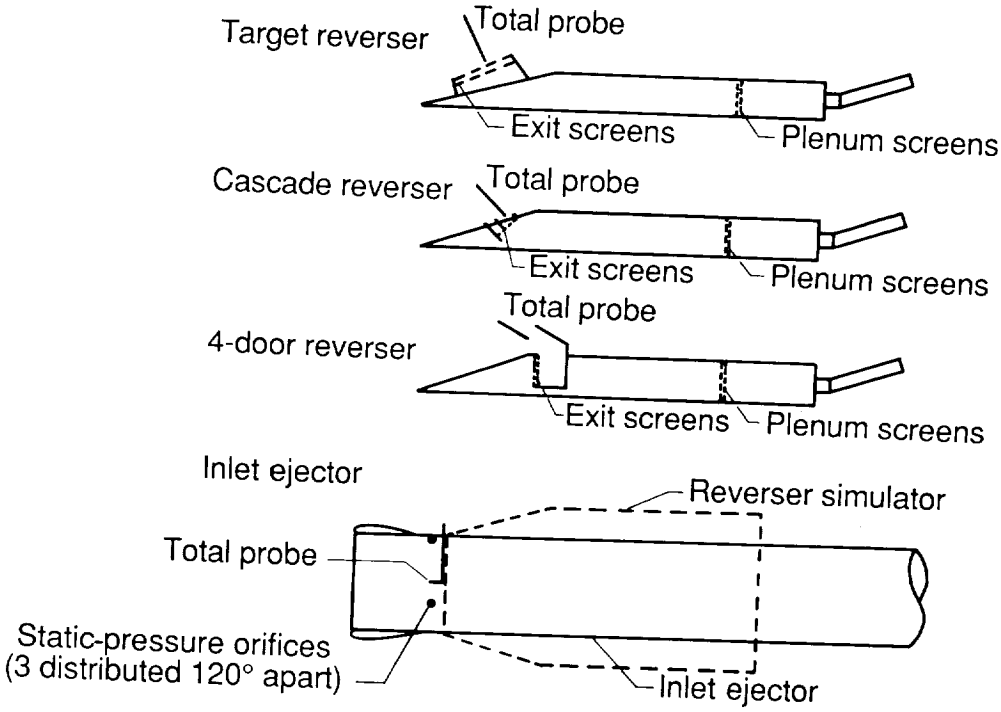


Figure 7. Pressure instrumentation used in engine simulators.

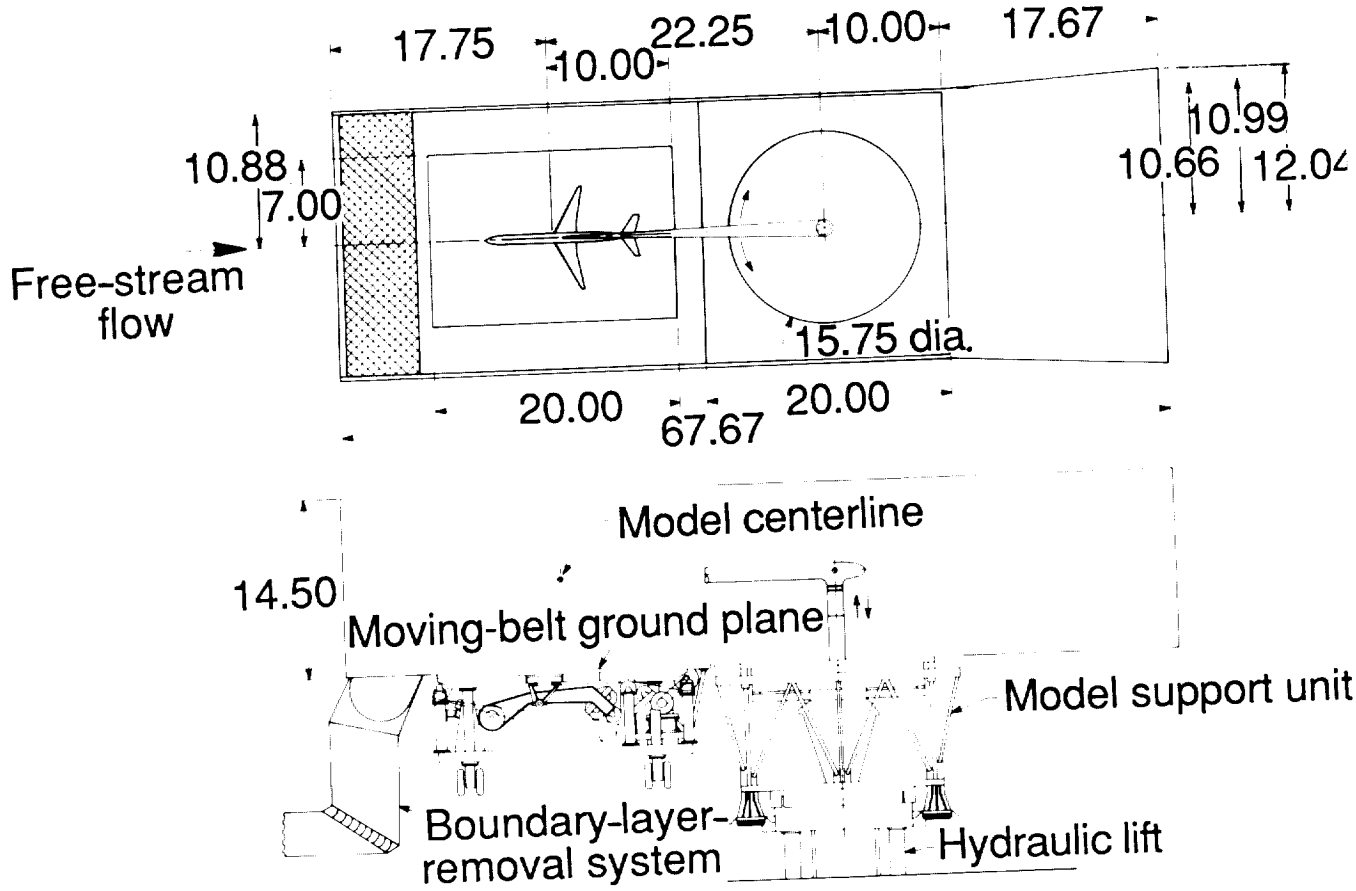


Figure 8. Test section configuration when investigating effects of moving-belt ground plane. All dimensions are in feet.

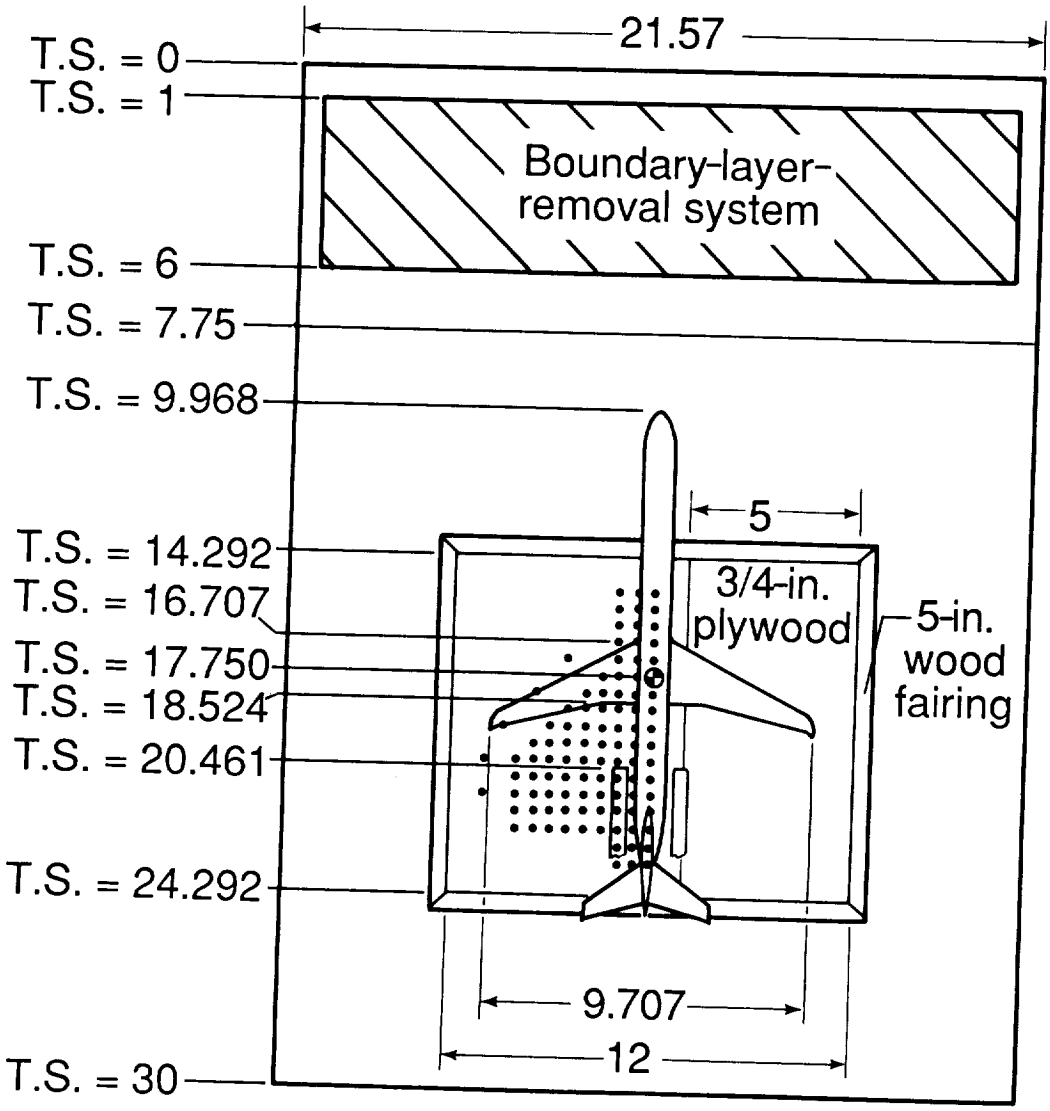


(a) Position of pressure-instrumented ground board with respect to model. All dimensions are in feet unless otherwise noted.

Figure 9. Sketches of pressure-instrumented ground board showing location of pressure orifices.

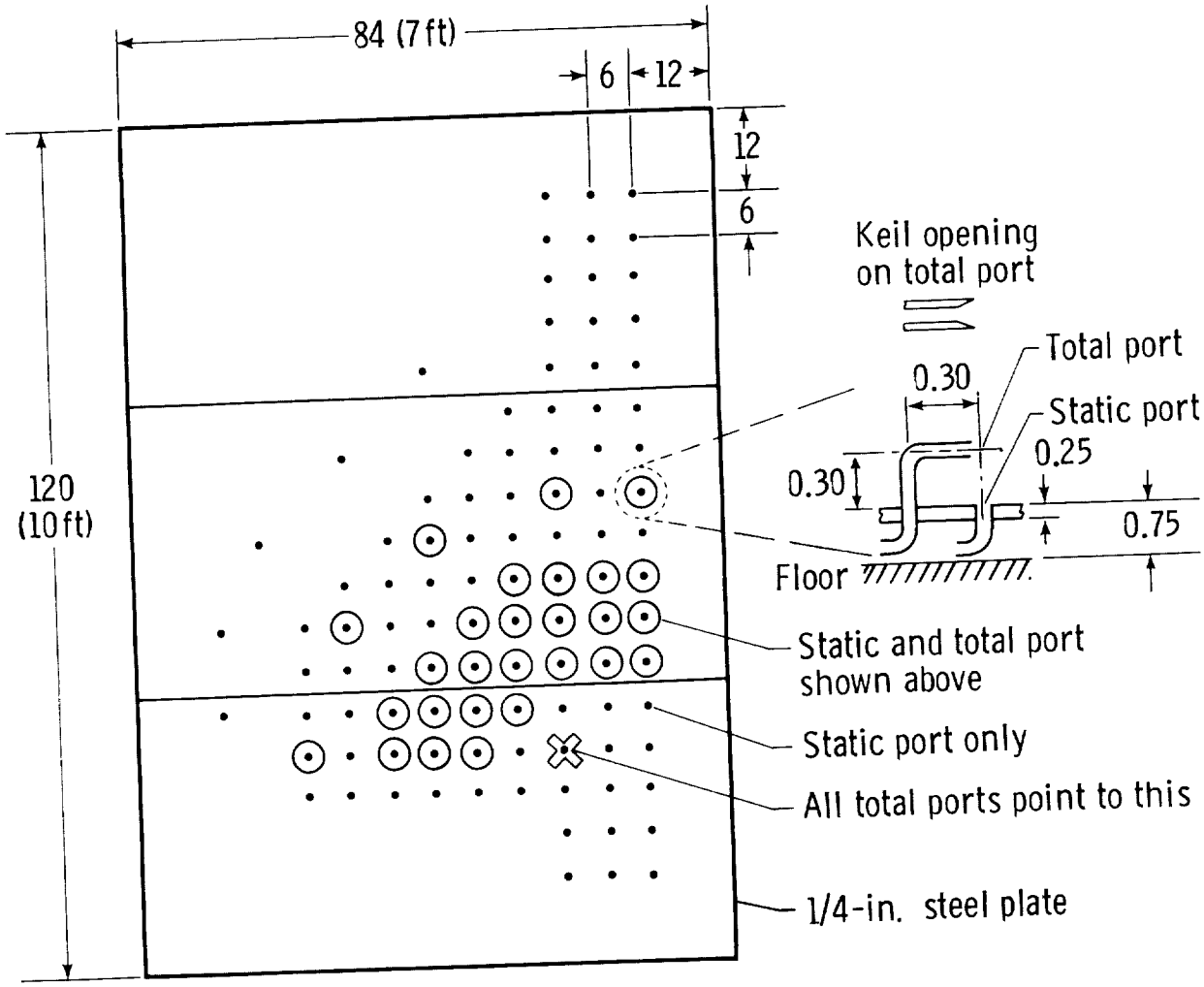


(b) Detailed sketch of pressure-instrumented ground board. All dimensions are in inches unless otherwise noted.

Figure 9. Concluded.

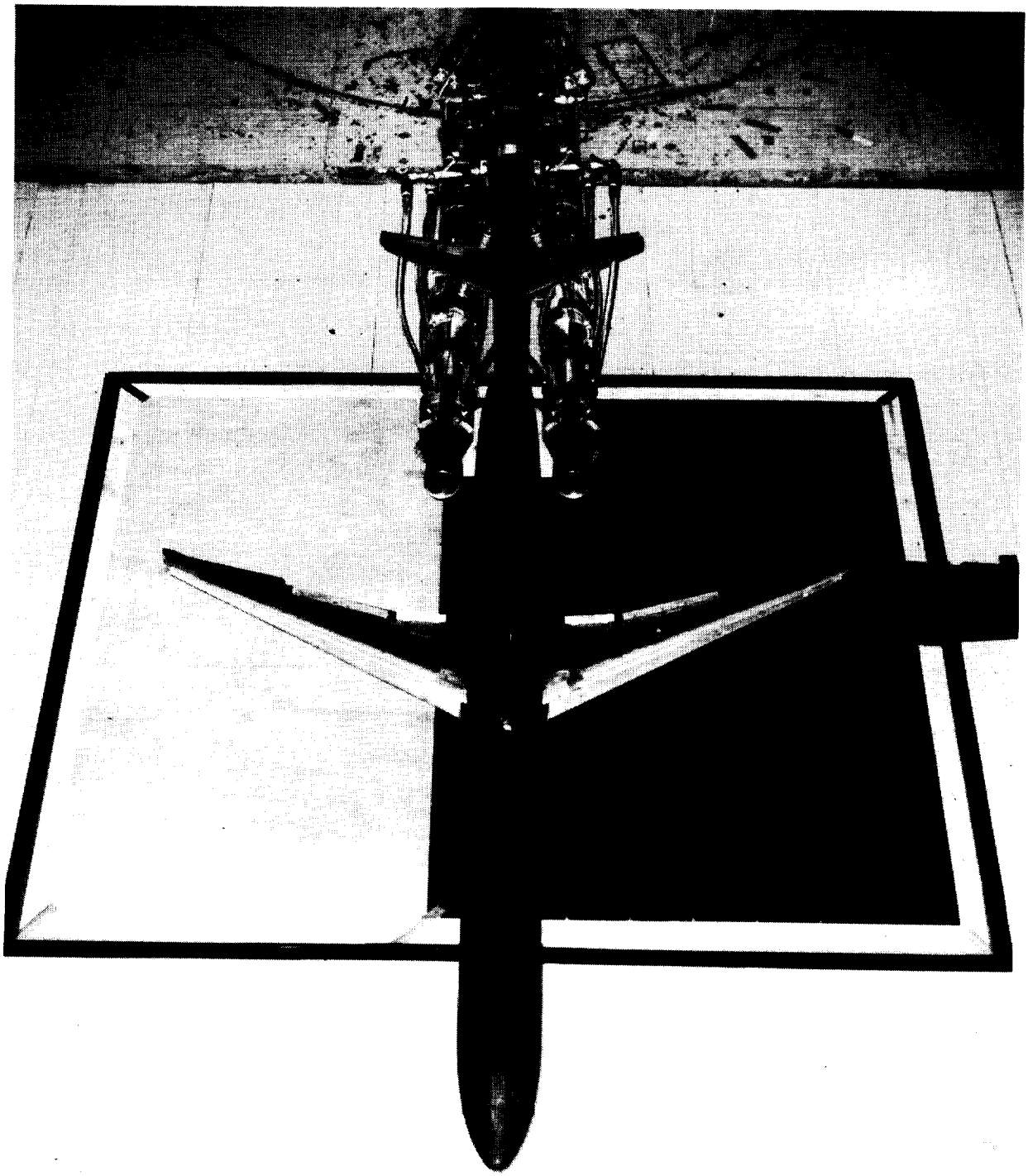

L-86-6114

(a) Photograph of model over pressure-instrumented ground board.

Figure 10. Illustrations of model orientation.

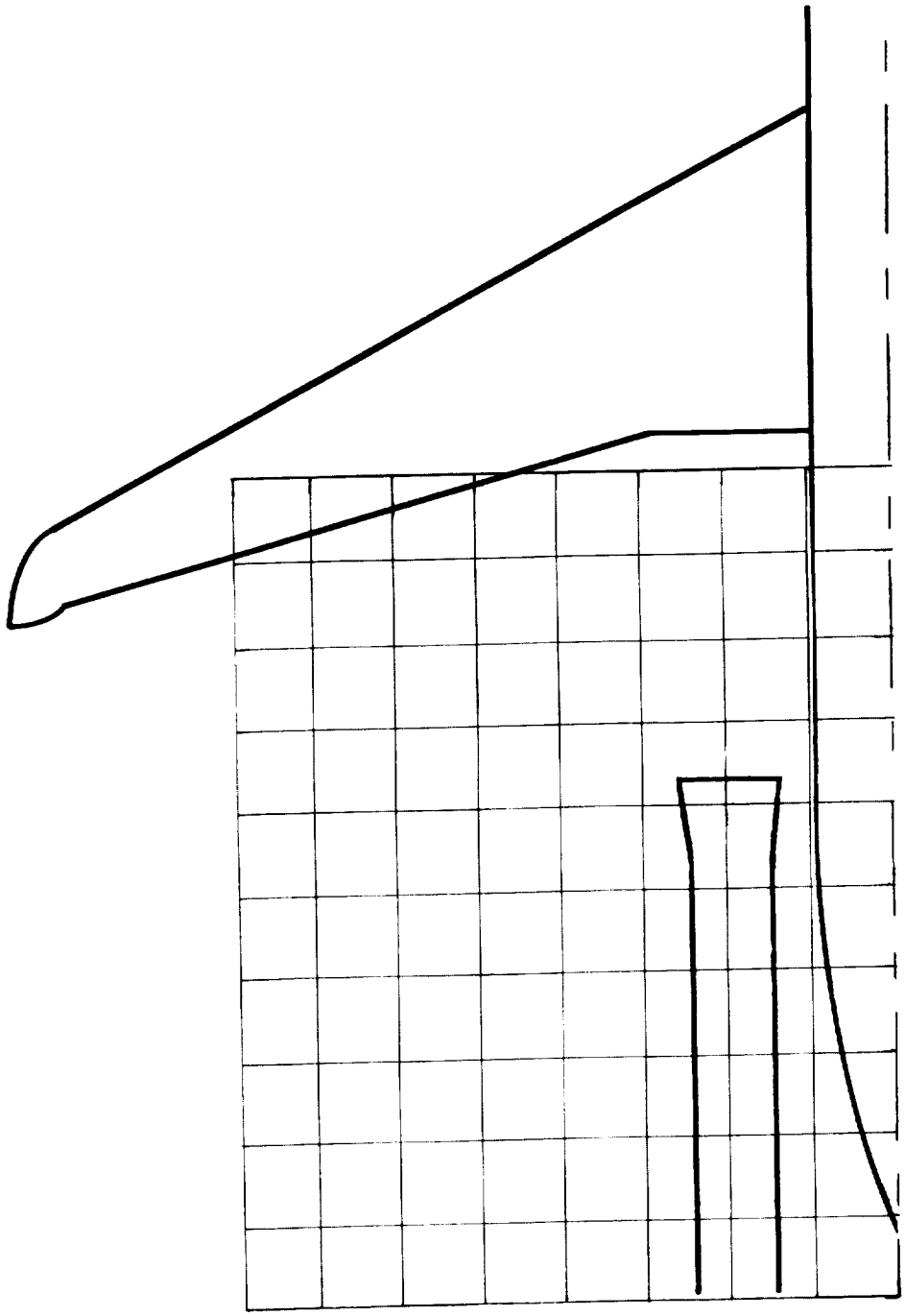

(b) Position of model with respect to 6-in. square grid pattern on floor.

Figure 10. Concluded.

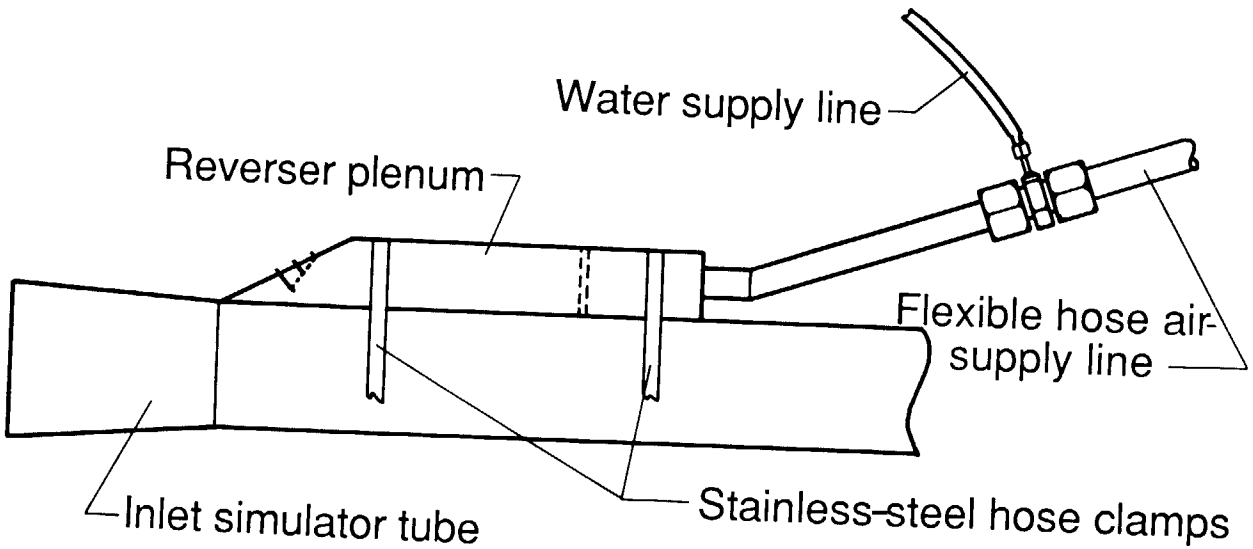


(a) Sketch showing location of water injection.

Figure 11. Water injection system used for flow visualization.

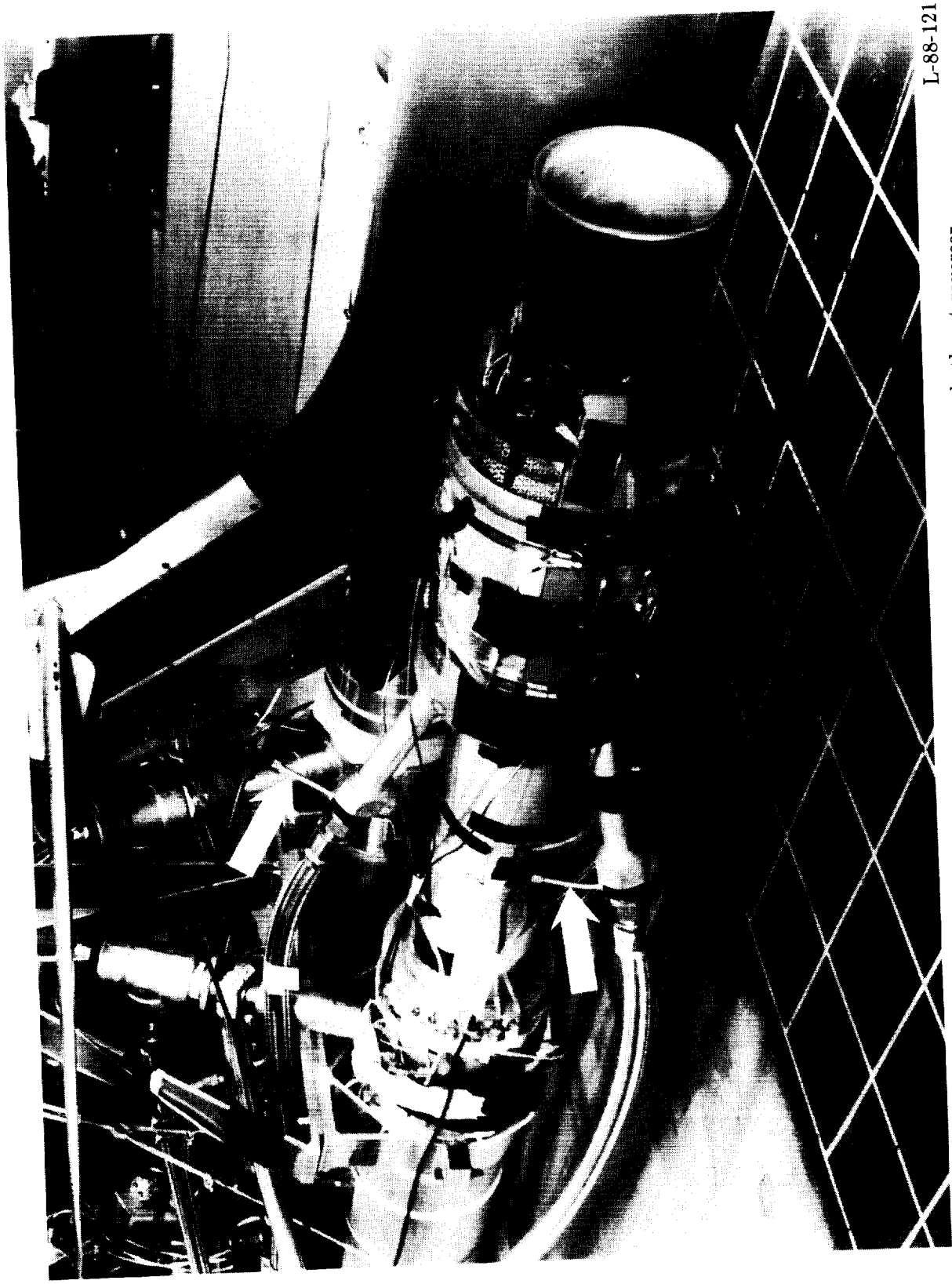

L-88-121

(b) Photograph with arrows showing water supply lines for cascade thrust reverser.

Figure 11. Concluded.

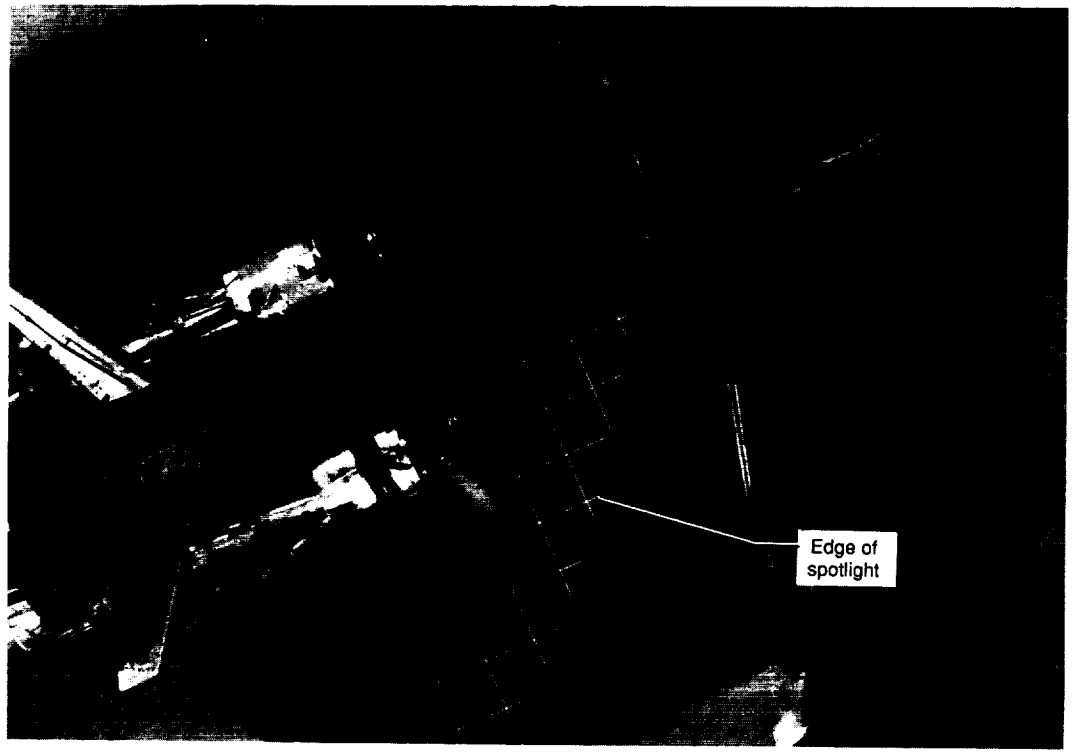


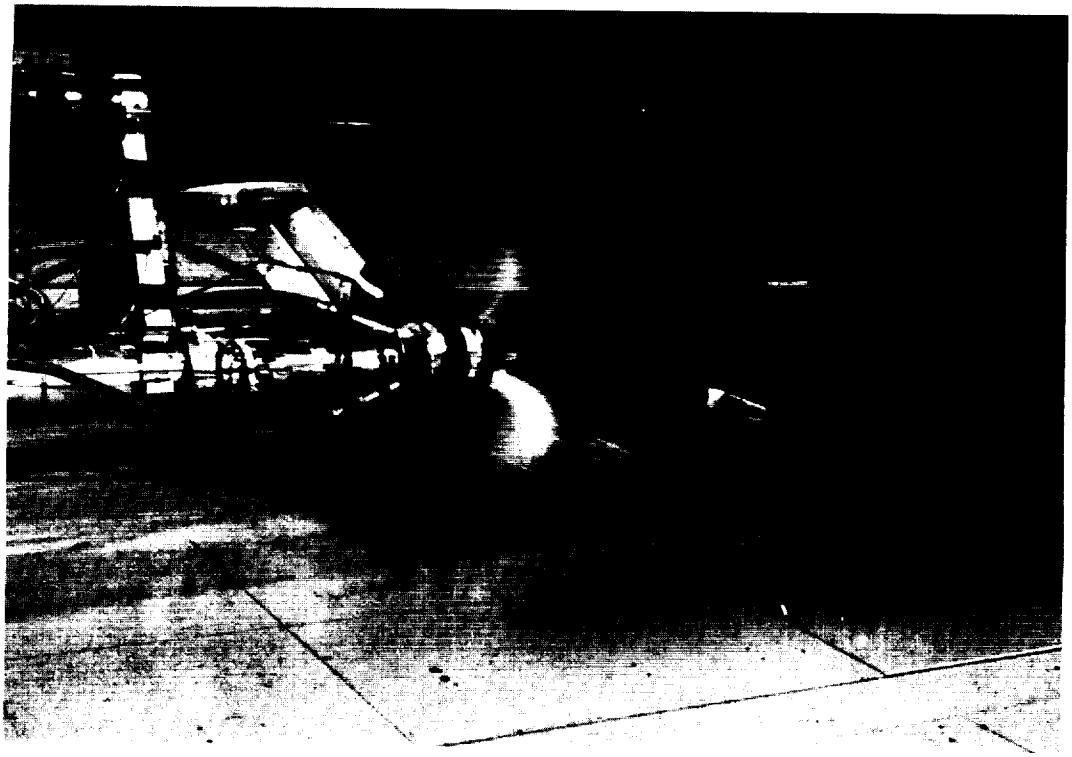

L-88-122

(a) $\dot{m}_R = 2.55$ lb/sec; $q_\infty = 12.2$ psf.

Figure 12. Water injection flow visualization for cascade thrust reverser. $\delta_f = 40°; \delta_s = 60°$; IGE.

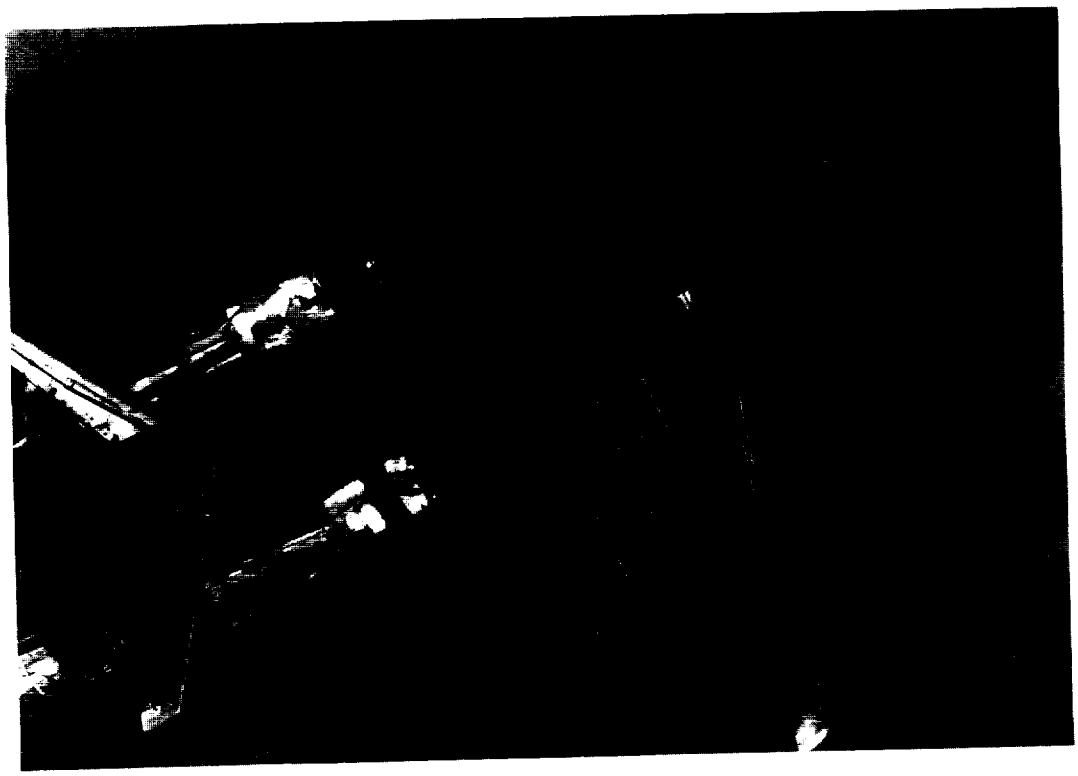

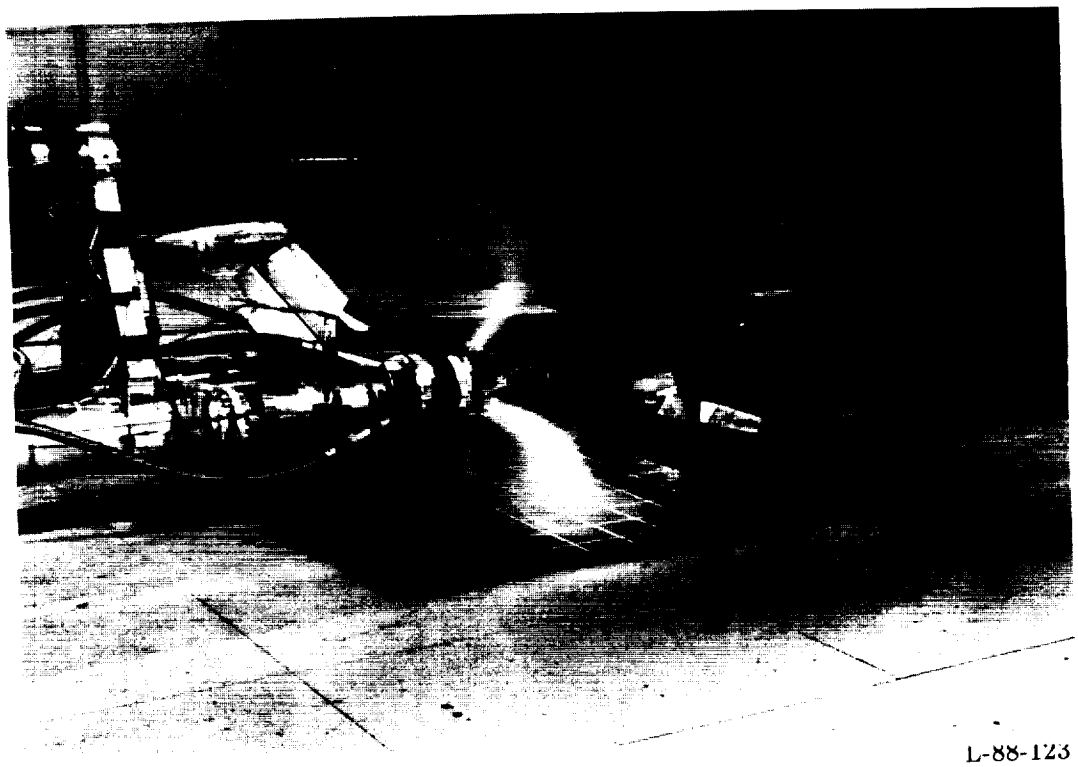

L-88-123

(b) $\dot{m}_R = 2.55$ lb/sec; $q_\infty = 5.4$ psf.

Figure 12. Continued.

L-88-124

(c) $\dot{m}_R = 2.55$ lb/sec; $q_\infty = 1.4$ psf.

Figure 12. Continued.

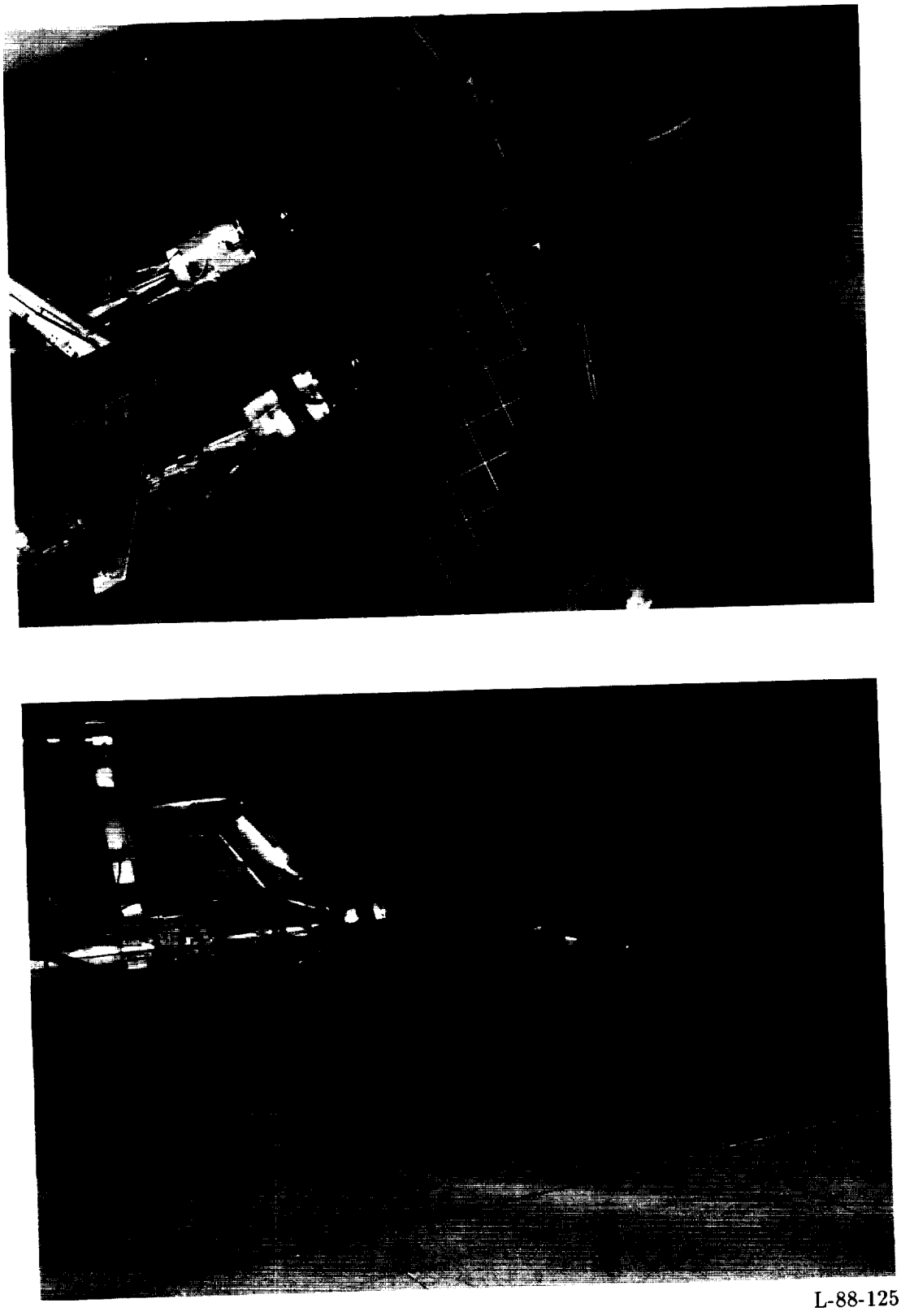

L-88-125

(d) $\dot{m}_R = 1.15$ lb/sec; $q_\infty = 12.2$ psf.

Figure 12. Continued.

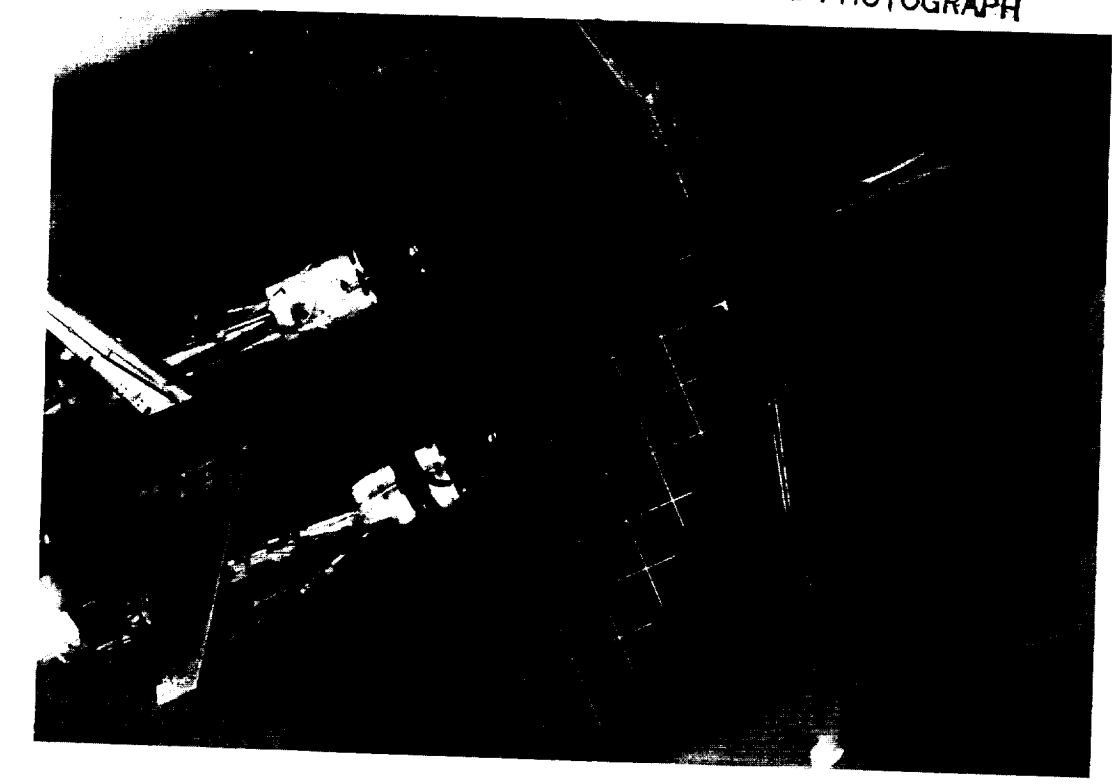

L-88-126

(e) $\dot{m}_R = 1.15$ lb/sec; $q_\infty = 5.4$ psf.

Figure 12. Continued.

L-88-127

(f) $\dot{m}_R = 1.15$ lb/sec; $q_\infty = 1.4$ psf.

Figure 12. Concluded.

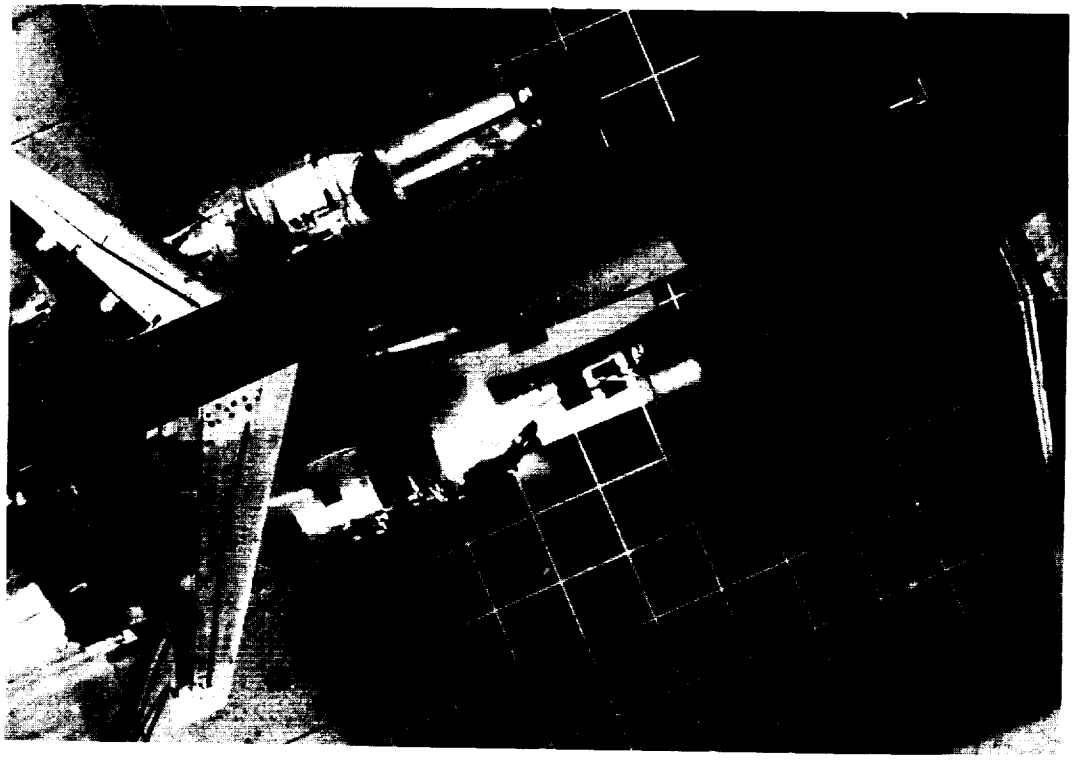

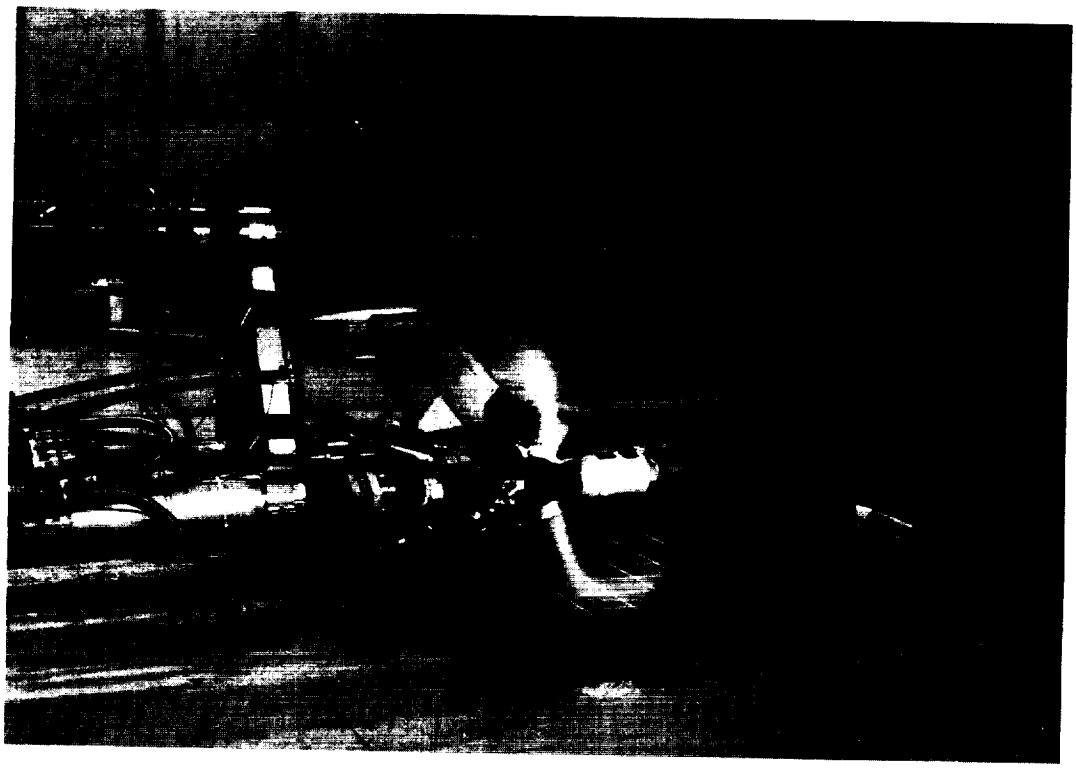

L-88-128

(a) $q_\infty = 5.4$ psf.

Figure 13. Water injection flow visualization for 15° rotated target thrust reverser. $\dot{m}_R = 3.2$ lb/sec; $\delta_f = 40°$; $\delta_s = 60°$; IGE.

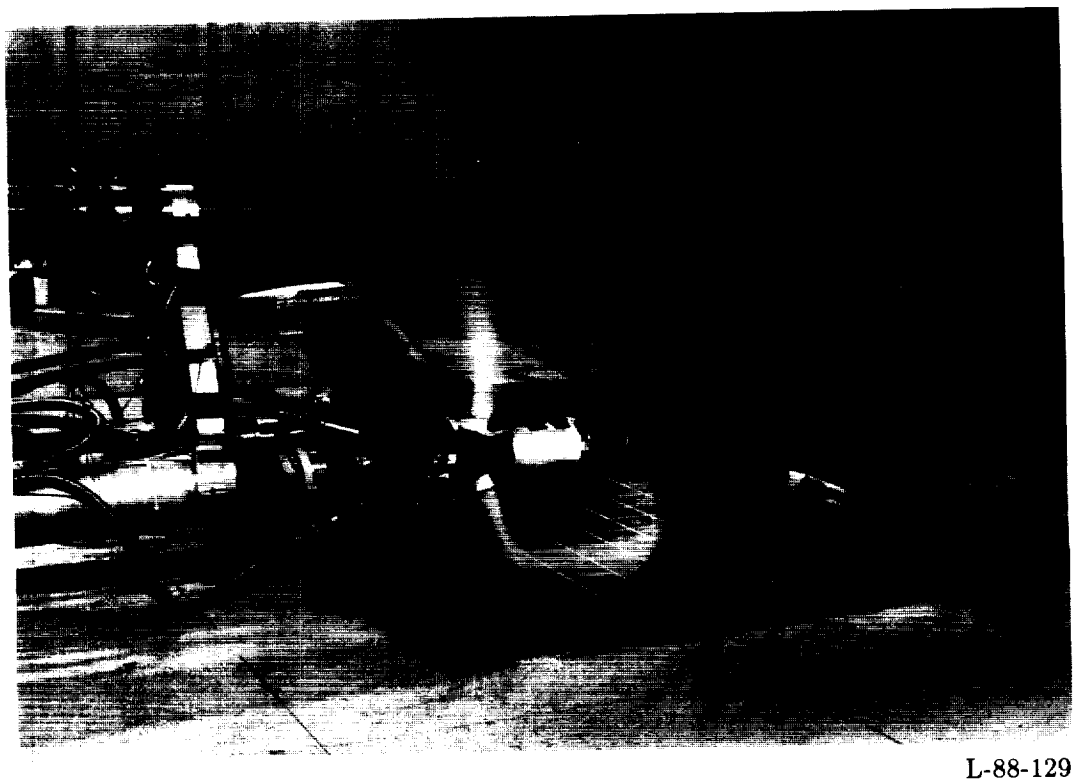

L-88-129

(b) $q_\infty = 1.4$ psf.

Figure 13. Concluded.

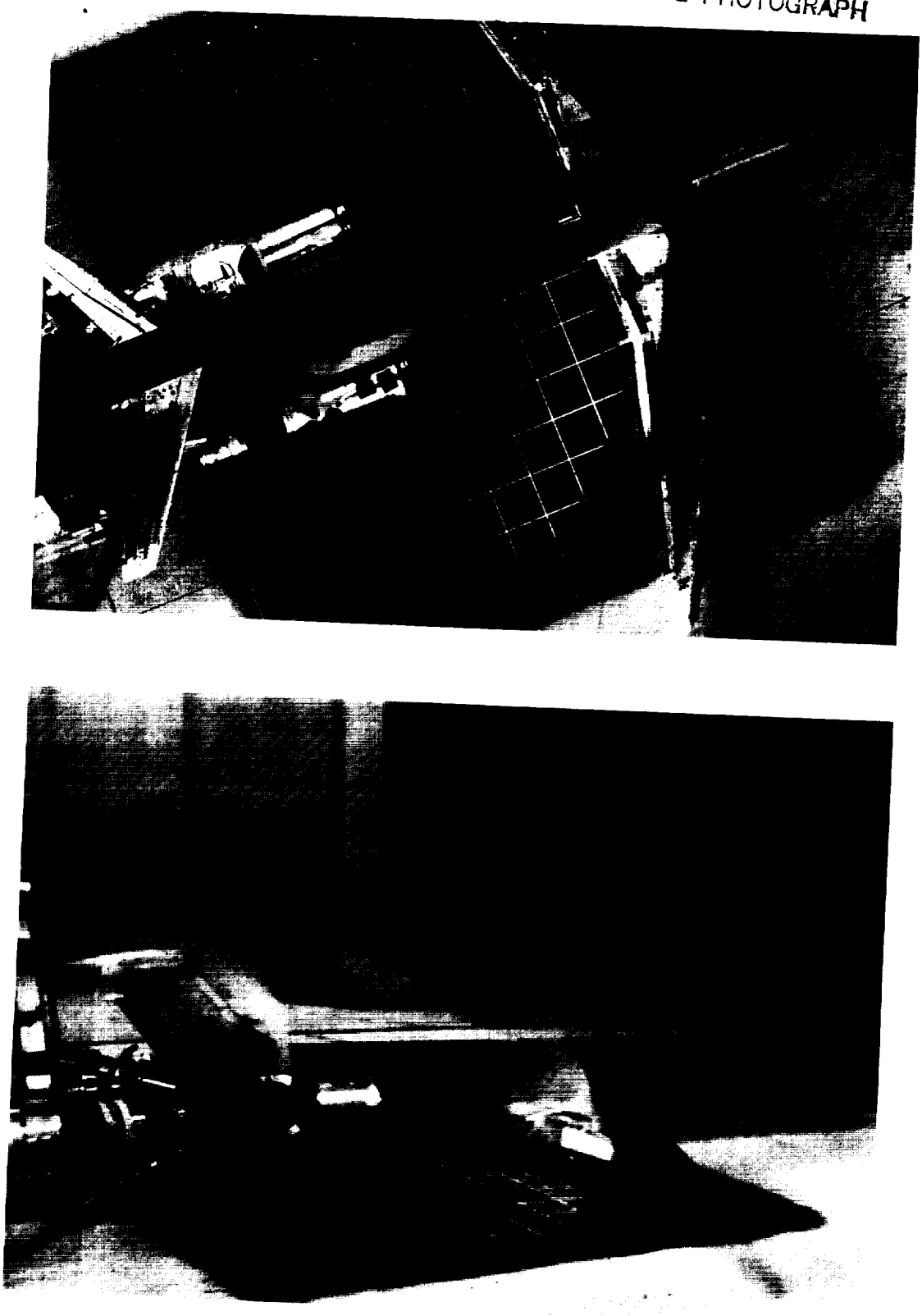

(a) $\dot{m}_R = 3.2$ lb/sec; $q_\infty = 12.2$ psf. L-88-130

Figure 14. Water injection flow visualization for 22.5° rotated target thrust reverser. $\delta_f = 40°$; $\delta_s = 60°$; IGE.

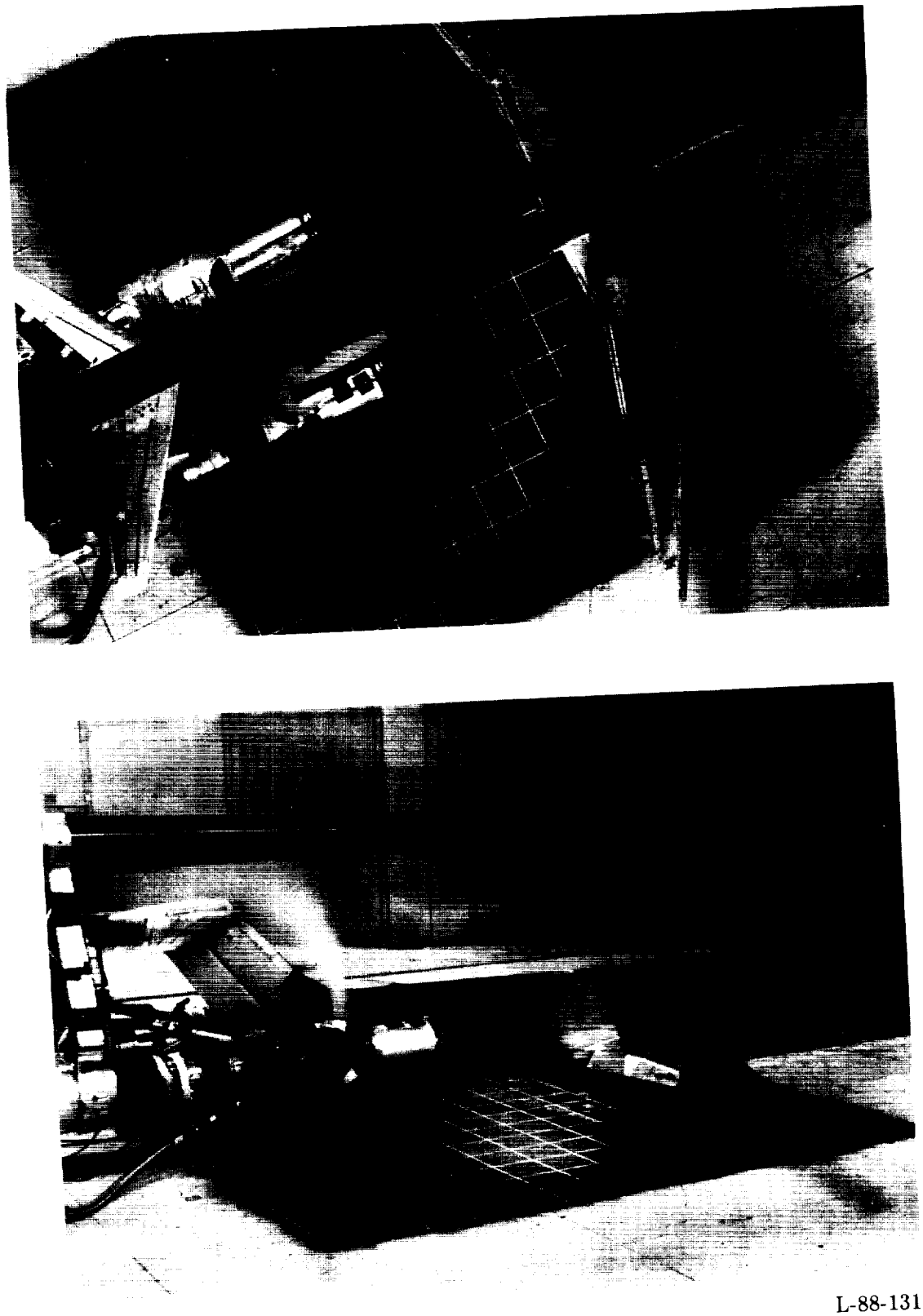

L-88-131

(b) $\dot{m}_R = 3.2$ lb/sec; $q_\infty = 5.4$ psf.

Figure 14. Continued.

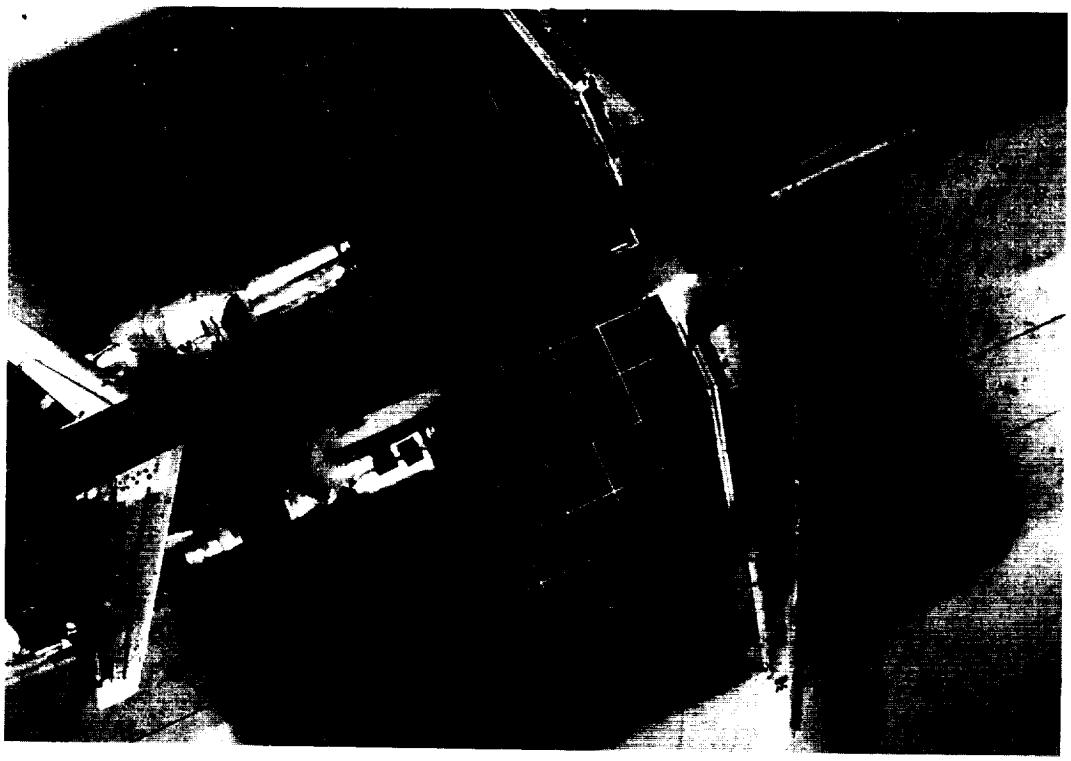

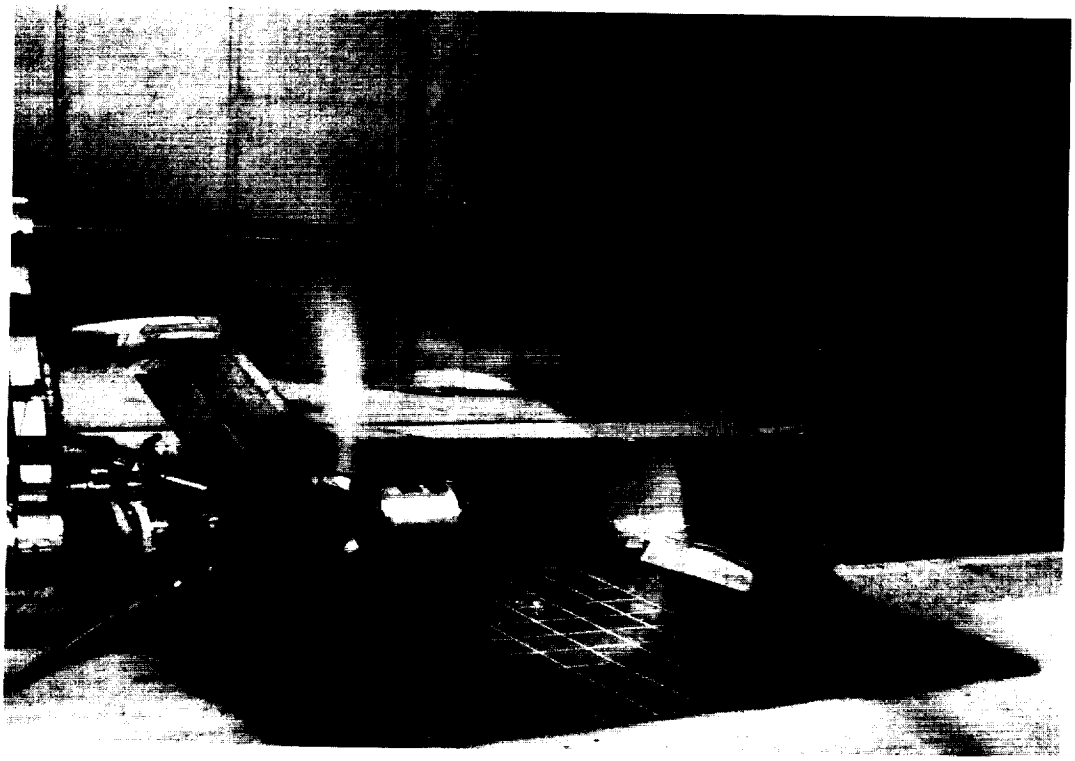

L-88-132

(c) $\dot{m}_R = 3.2$ lb/sec; $q_\infty = 1.4$ psf.

Figure 14. Continued.

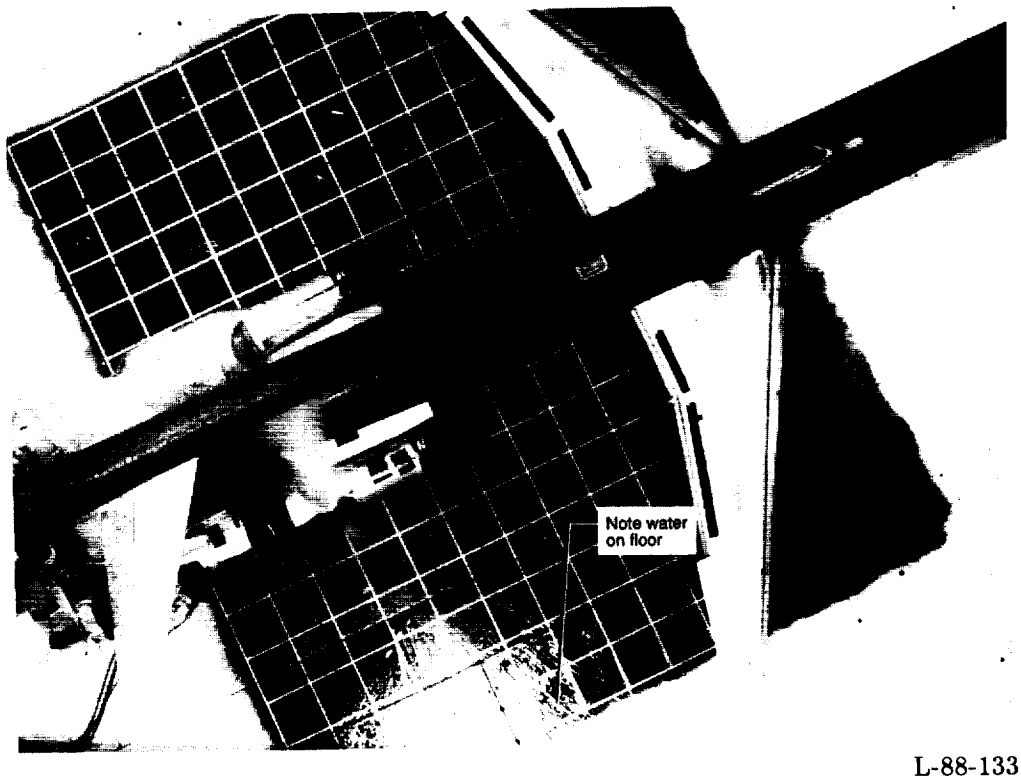


L-88-133

(d) Top view with additional overhead lighting. $\dot{m}_R = 3.2$ lb/sec; $q_\infty = 1.4$ psf.

Figure 14. Continued.

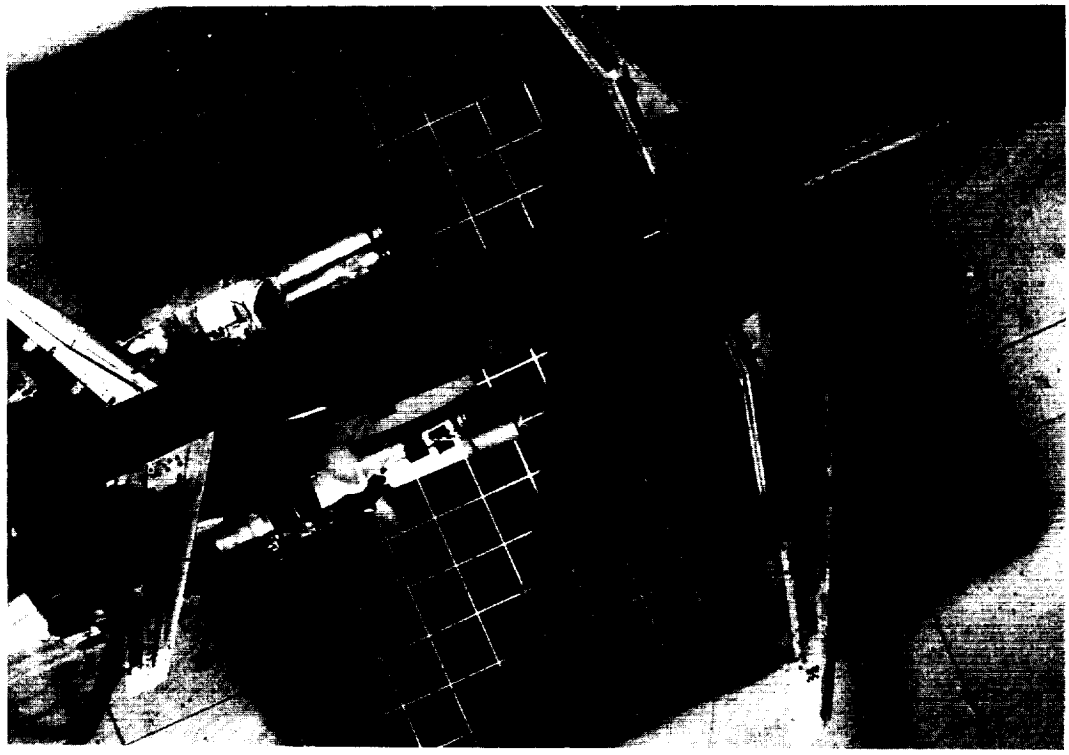

L-88-134

(e) $\dot{m}_R = 2.25$ lb/sec; $q_\infty = 12.2$ psf.

Figure 14. Continued.

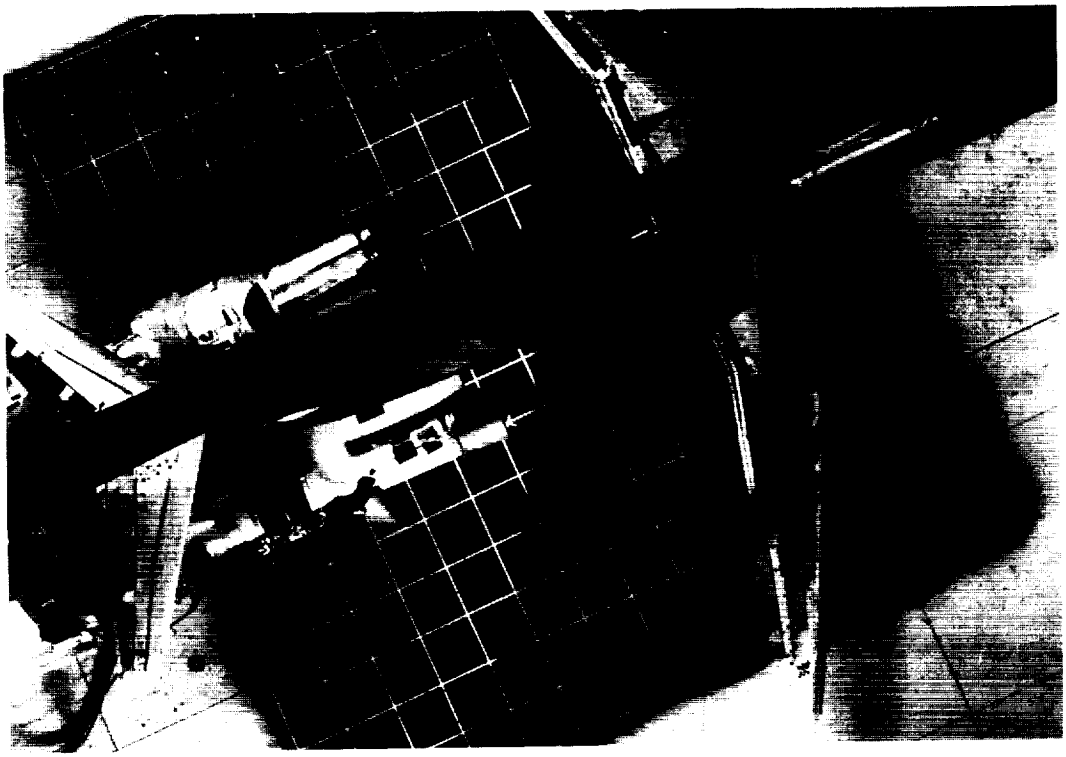

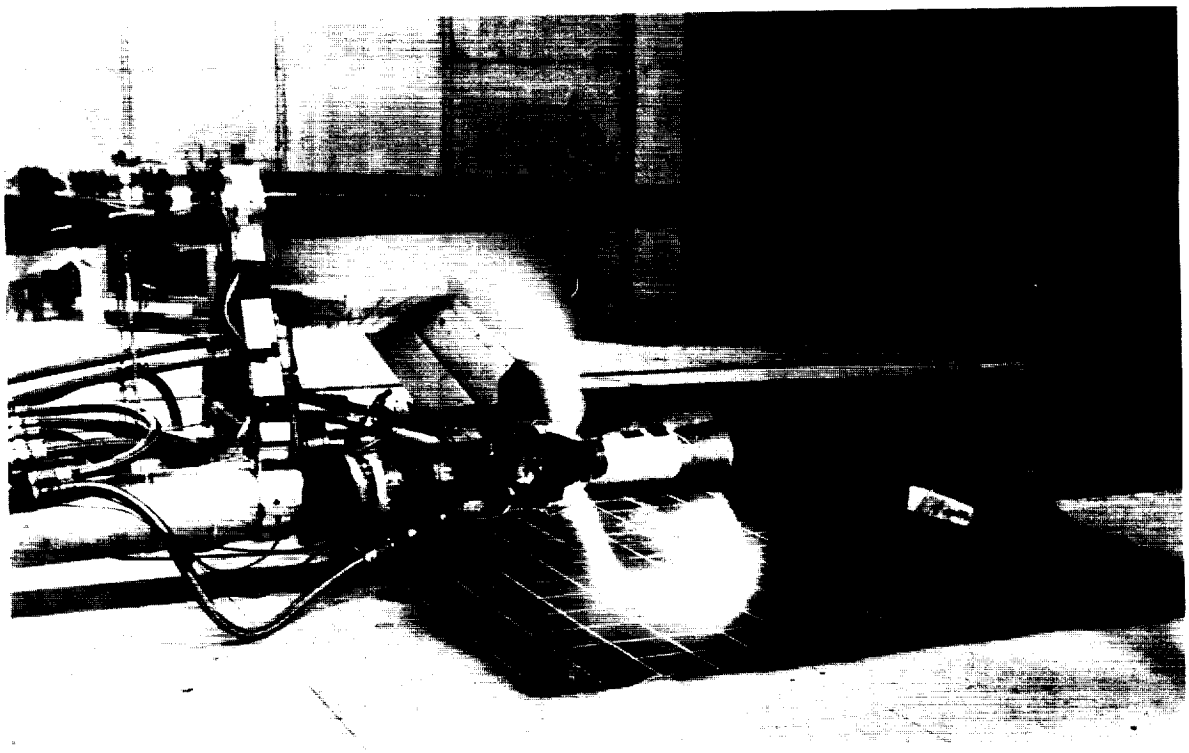

L-88-135

(f) $\dot{m}_R = 2.25$ lb/sec; $q_\infty = 5.4$ psf.

Figure 14. Continued.

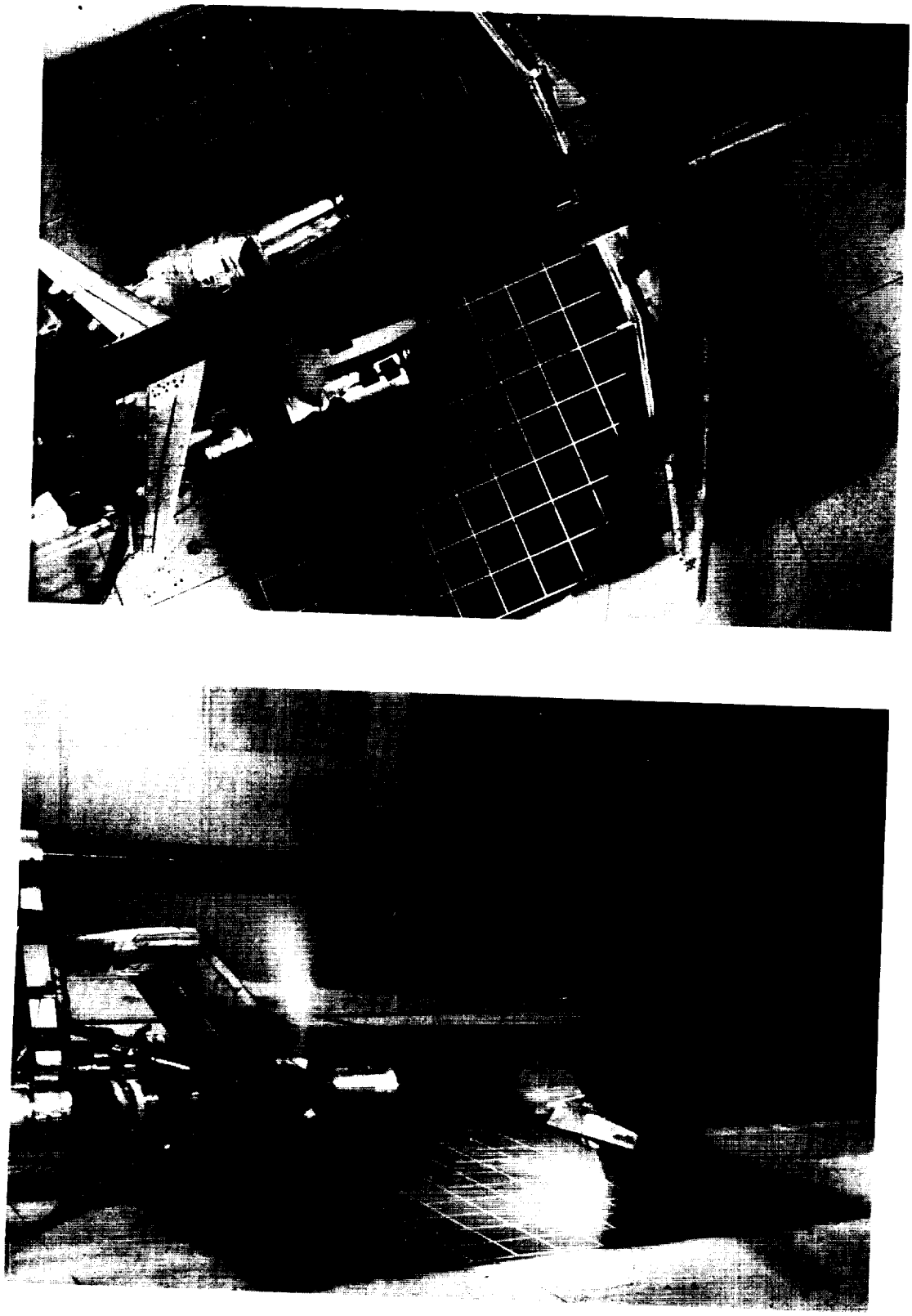

L-88-136

(g) $\dot{m}_R = 2.25$ lb/sec; $q_\infty = 1.4$ psf.

Figure 14. Continued.

L-88-137

(h) $\dot{m}_R = 1.35$ lb/sec; $q_\infty = 12.2$ psf.

Figure 14. Continued.

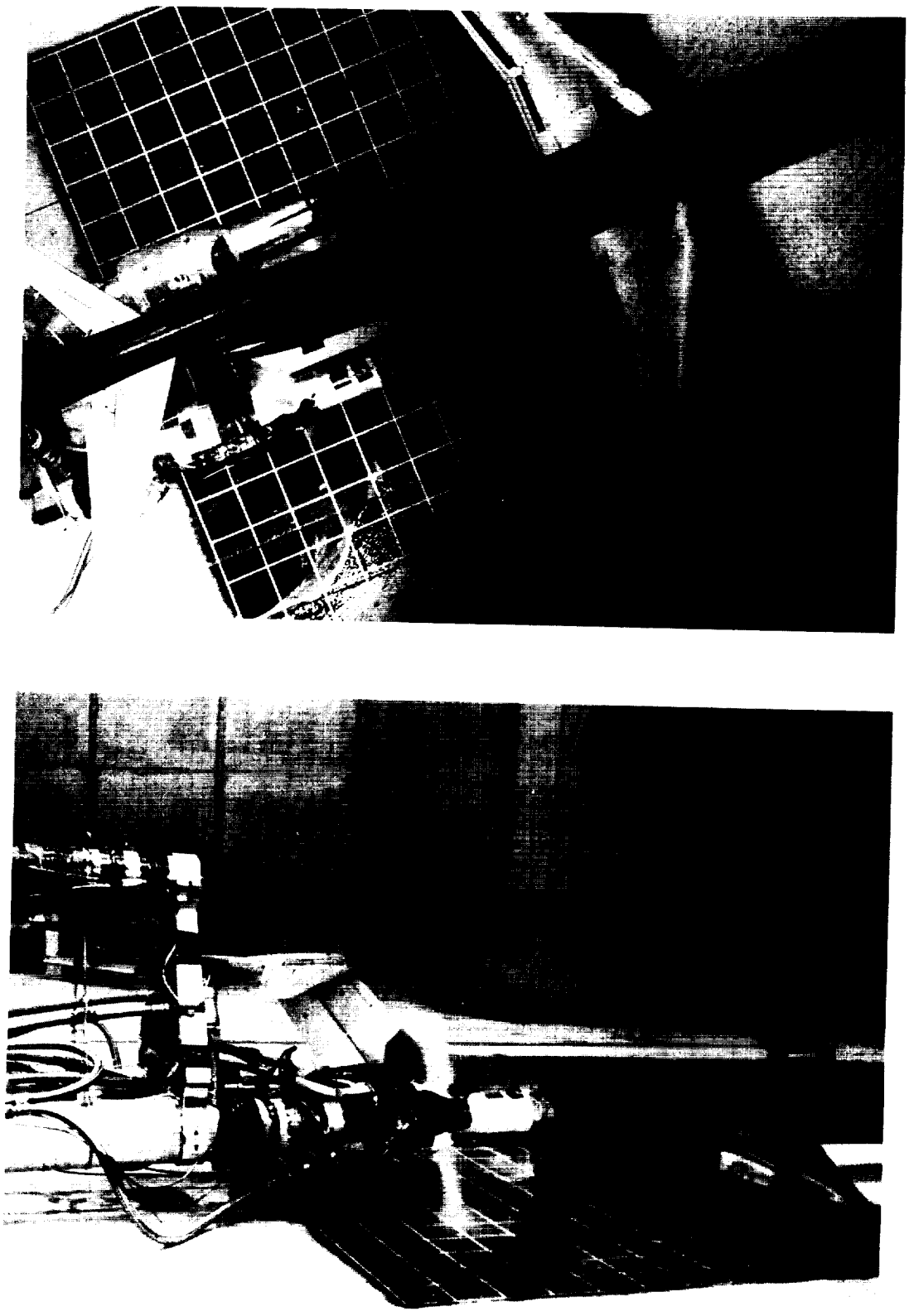

L-88-138

(i) $\dot{m}_R = 1.35$ lb/sec; $q_\infty = 5.4$ psf.

Figure 14. Continued.

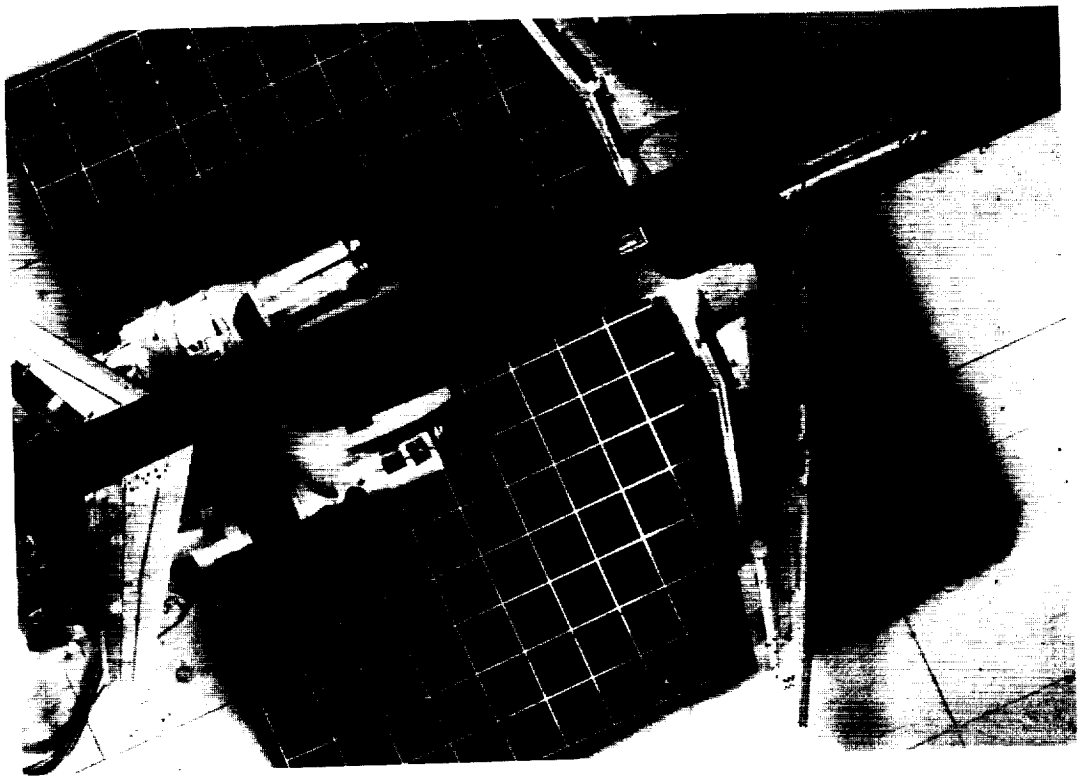

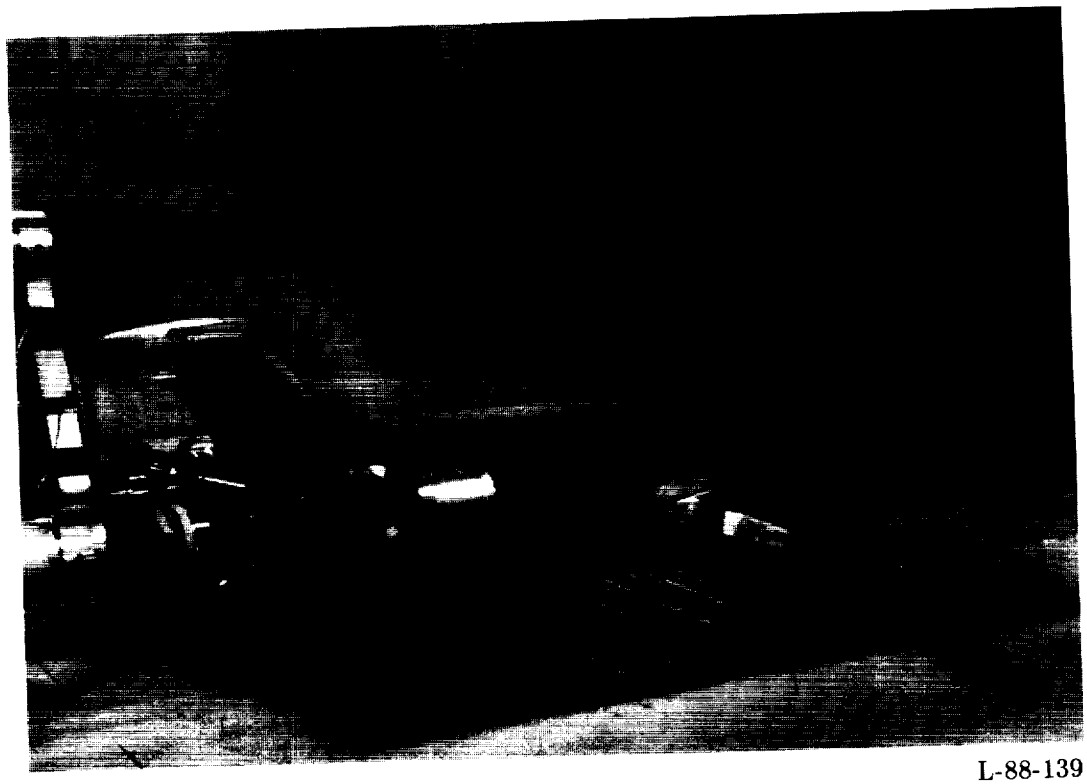

L-88-139

(j) $\dot{m}_R = 1.35$ lb/sec; $q_\infty = 1.4$ psf.

Figure 14. Concluded.

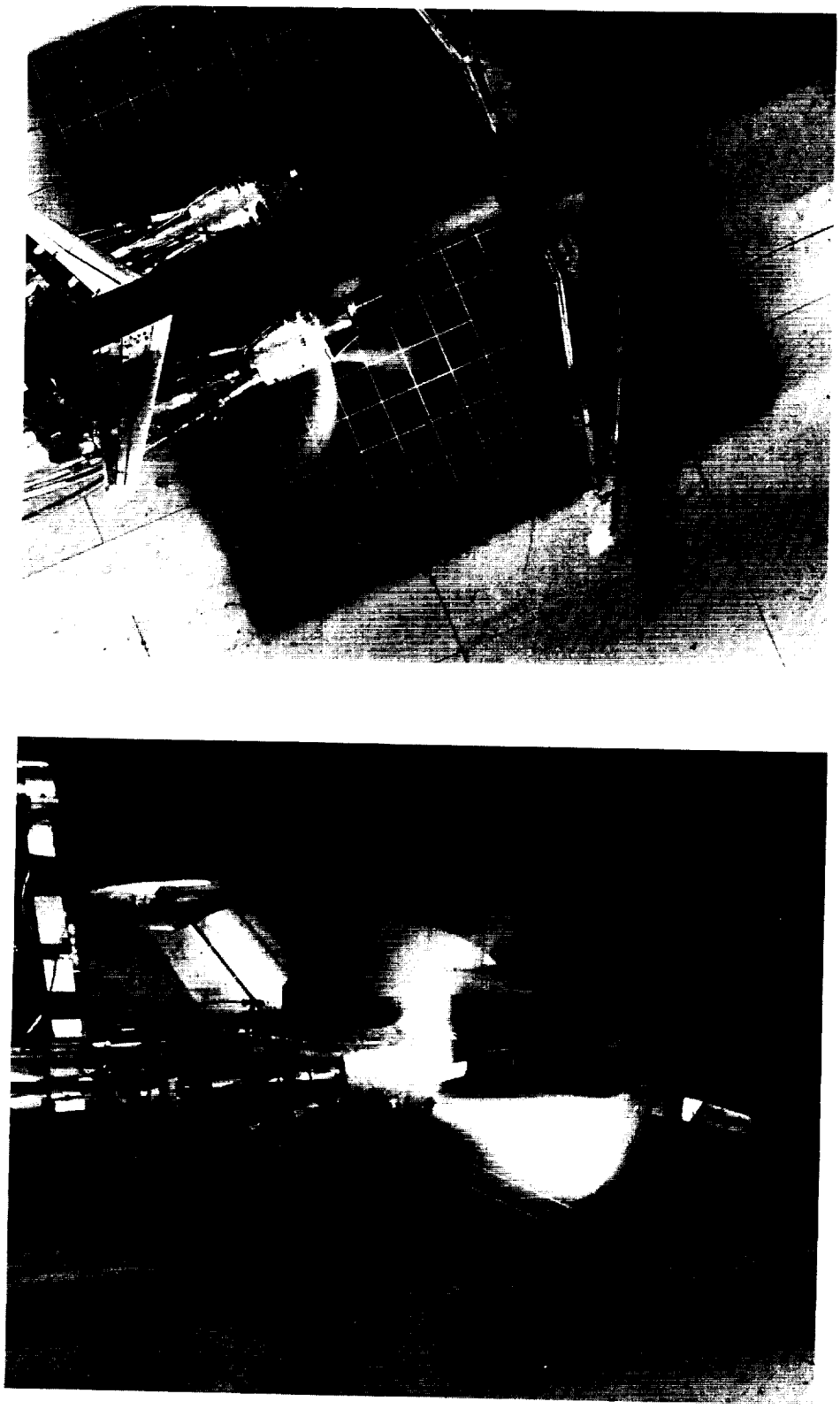

L-88-140

(a) $\dot{m}_R = 5.12$ lb/sec; $q_\infty = 12.2$ psf.

Figure 15. Water injection flow visualization for configuration I of four-door thrust reverser. $\delta_f = 40°$; $\delta_s = 60°$; IGE.

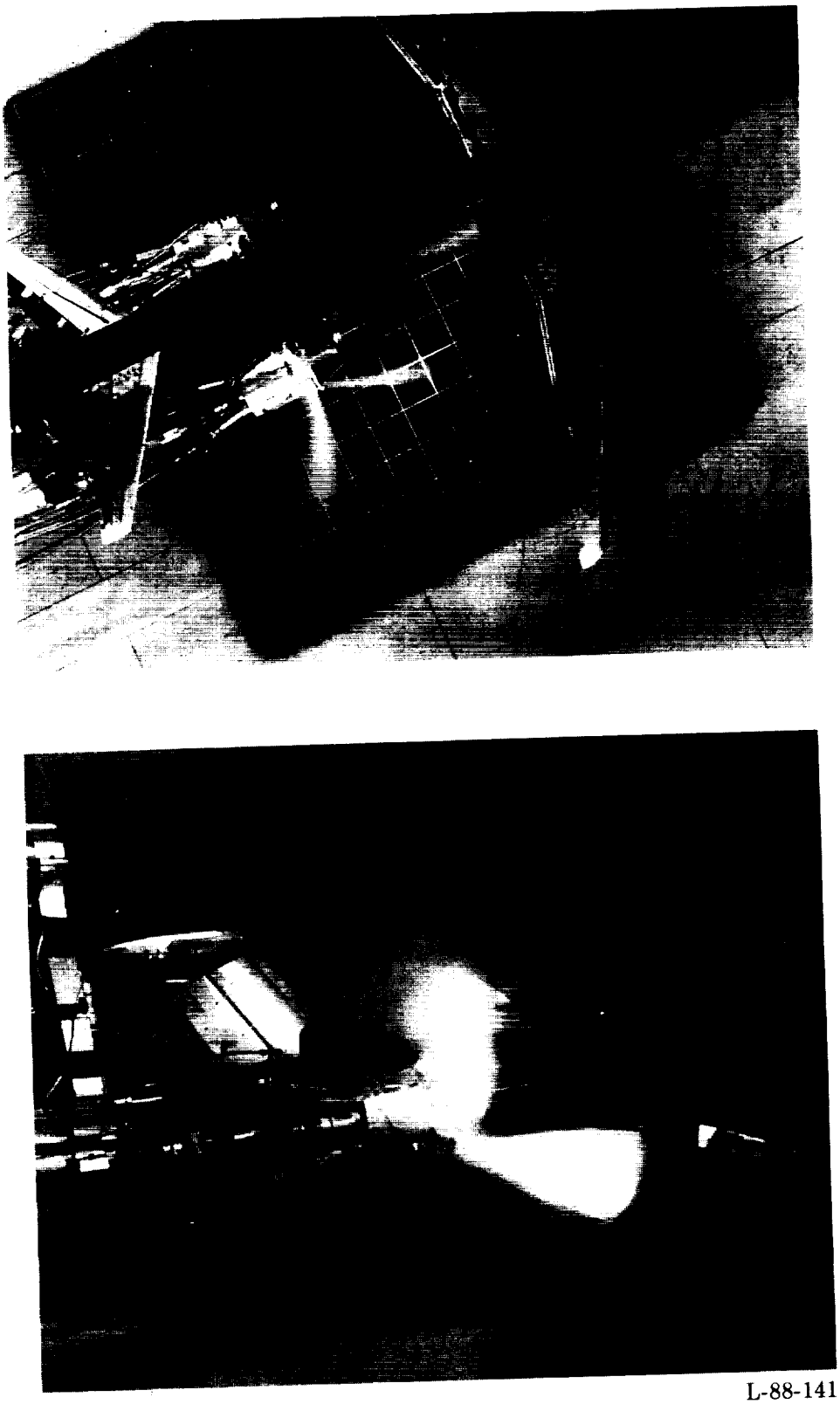

L-88-141

(b) $\dot{m}_R = 5.12$ lb/sec; $q_\infty = 5.4$ psf.

Figure 15. Continued.

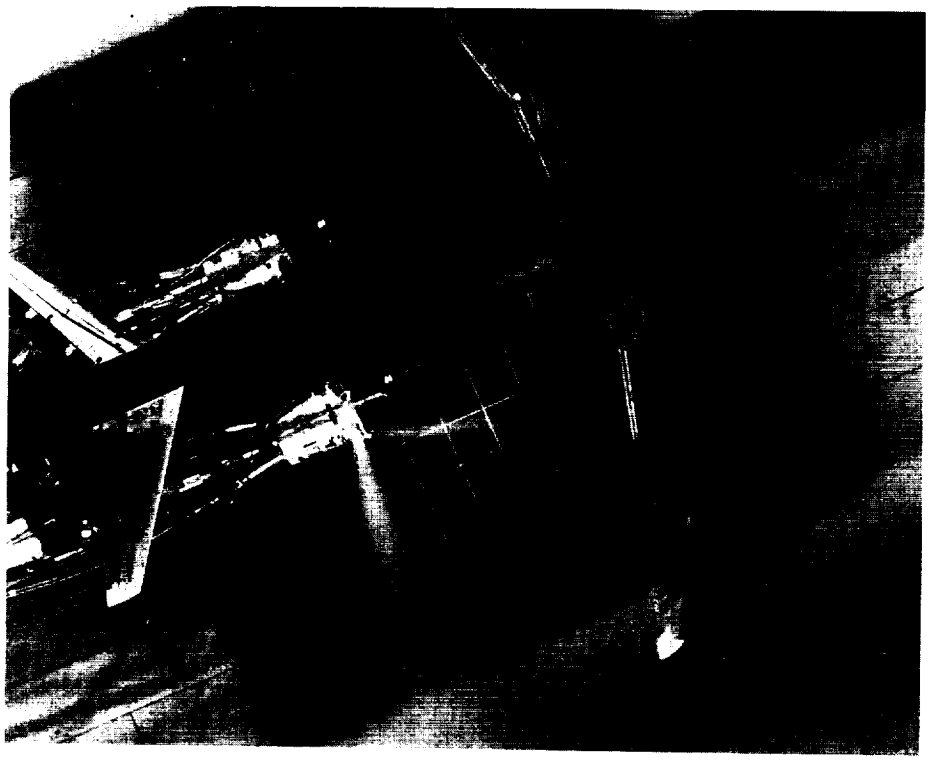

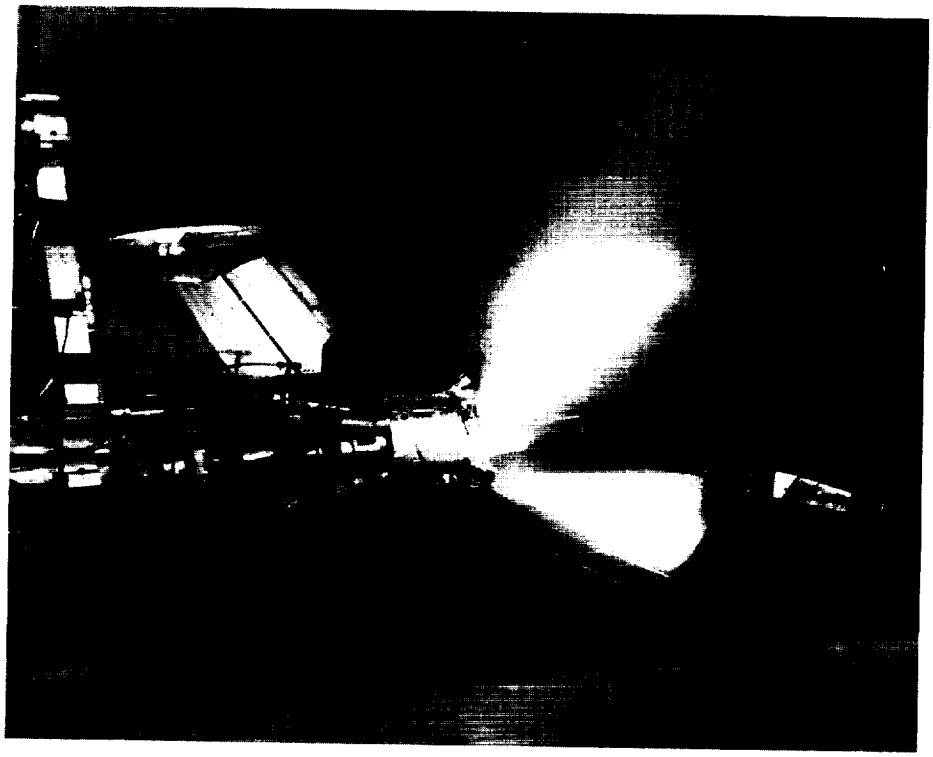

L-88-142

(c) $\dot{m}_R = 5.12$ lb/sec; $q_\infty = 1.4$ psf.

Figure 15. Continued.

L-88-143

(d) $\dot{m}_R = 3.0$ lb/sec; $q_\infty = 12.2$ psf.

Figure 15. Continued.

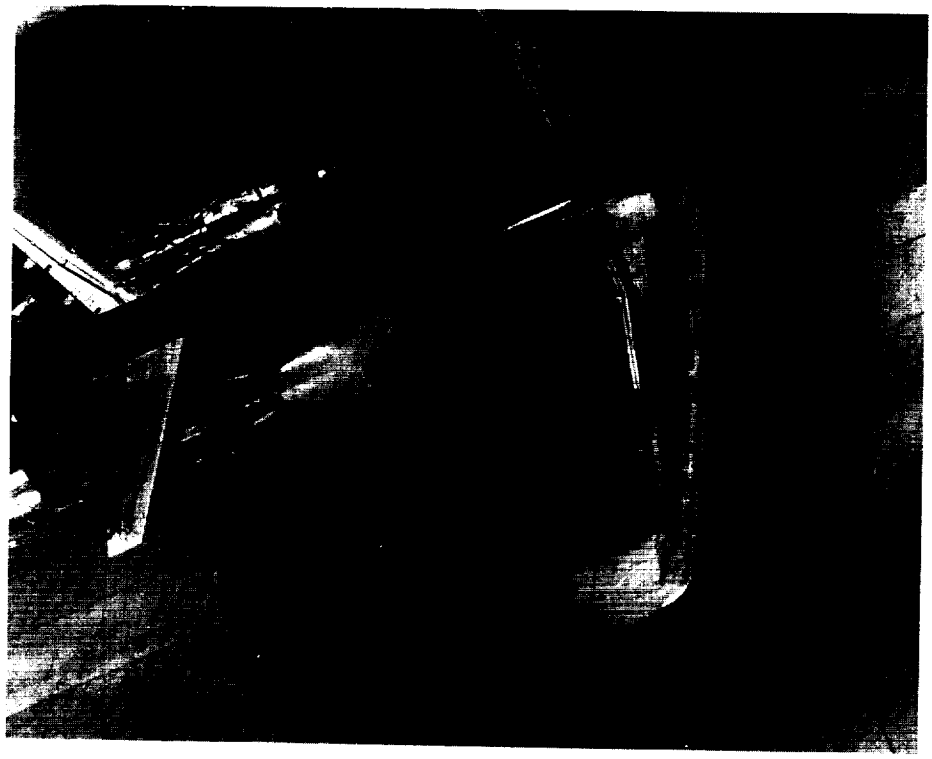

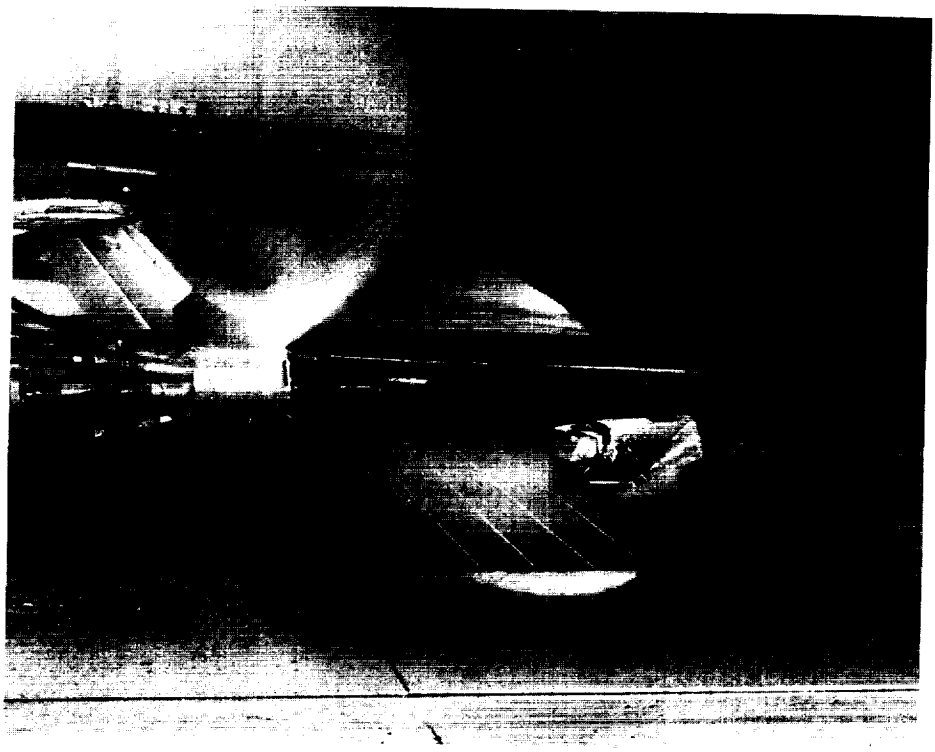

L-88-144

(e) $\dot{m}_R = 3.0$ lb/sec; $q_\infty = 5.4$ psf.

Figure 15. Continued.

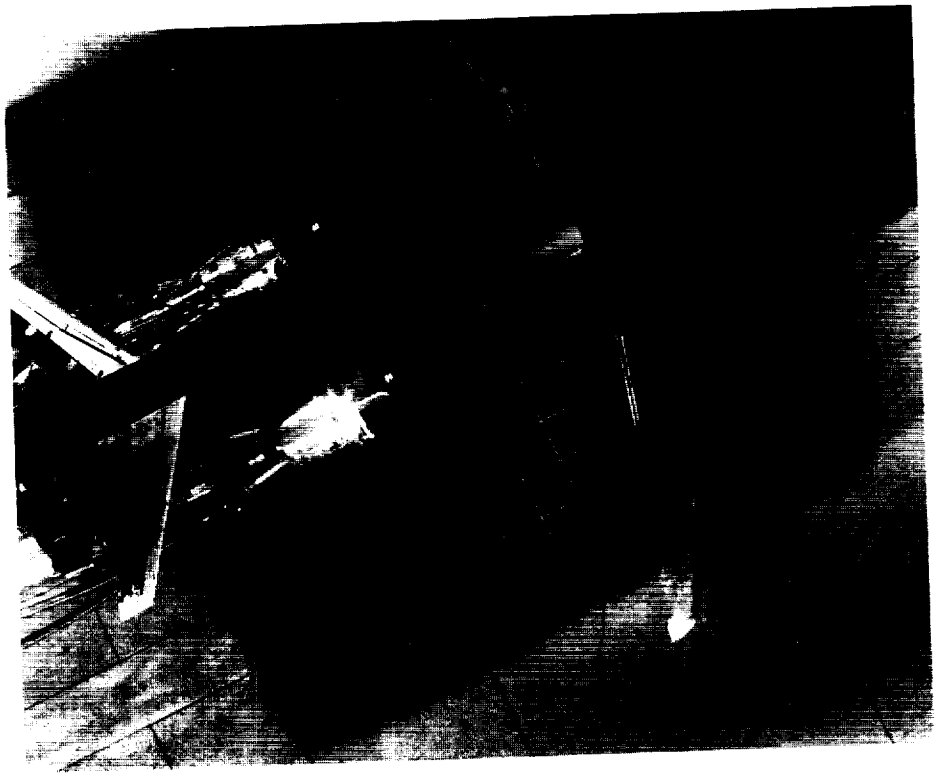

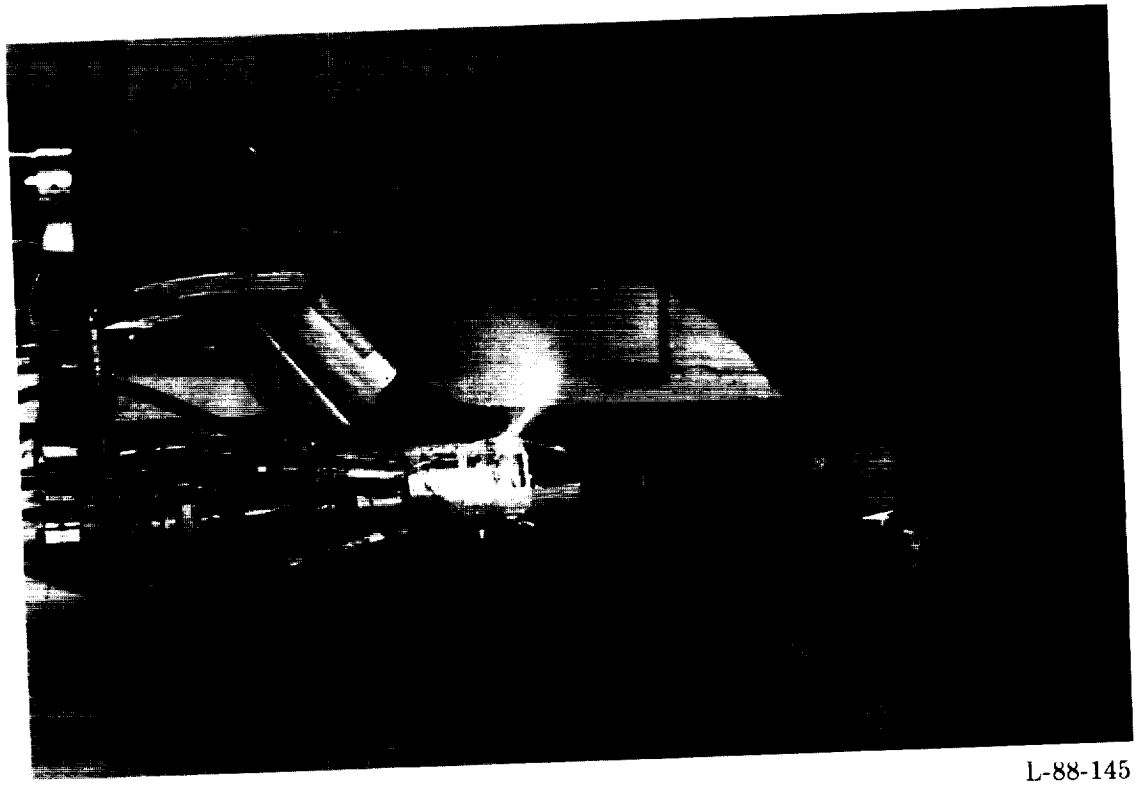

L-88-145

(f) $\dot{m}_R = 1.15$ lb/sec; $q_\infty = 12.2$ psf.

Figure 15. Continued.

(g) $\dot{m}_R = 1.15$ lb/sec; $q_\infty = 5.4$ psf. L-88-146

Figure 15. Continued.

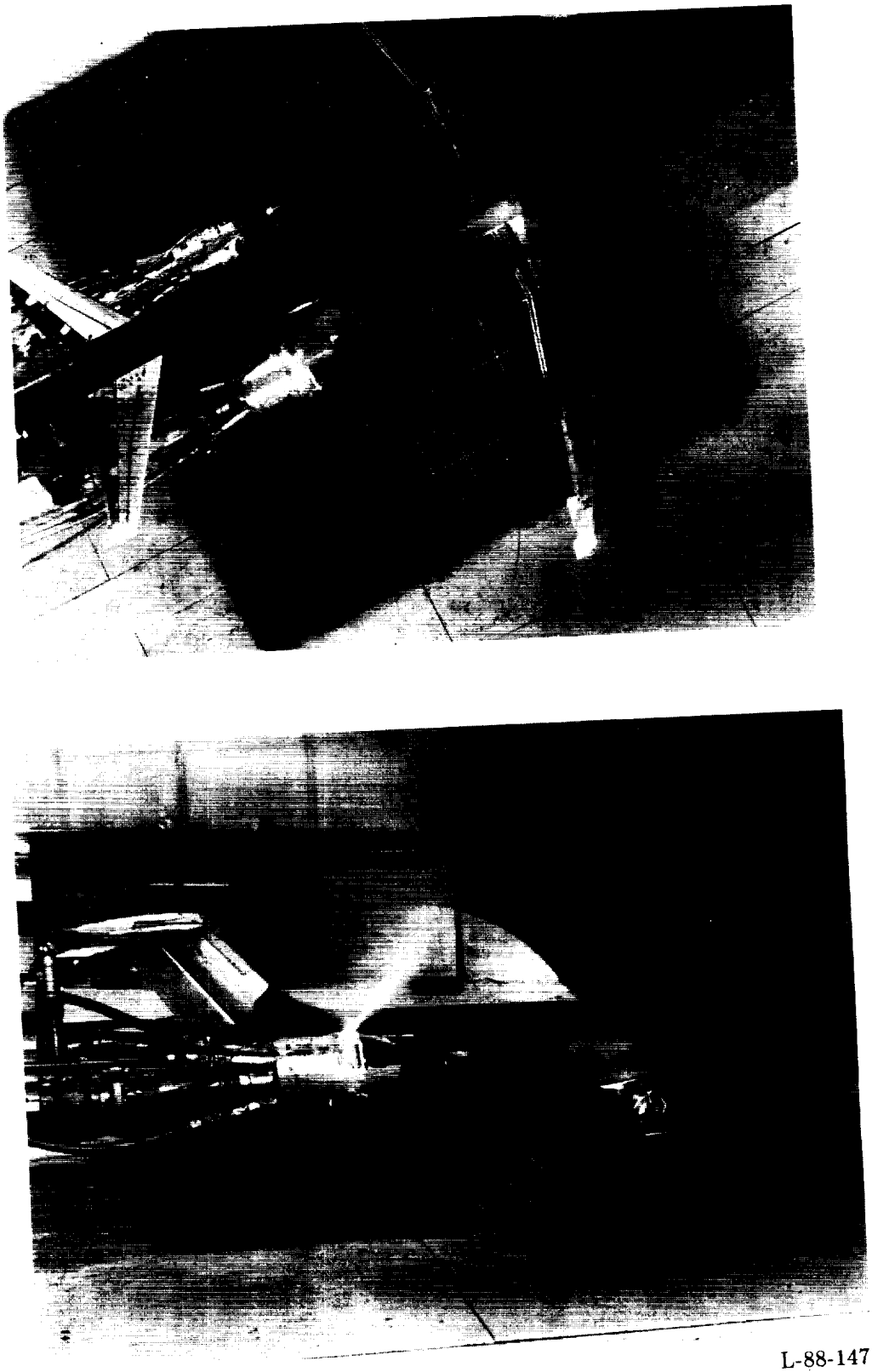

L-88-147

(h) $\dot{m}_R = 1.15$ lb/sec; $q_\infty = 1.4$ psf.

Figure 15. Concluded.

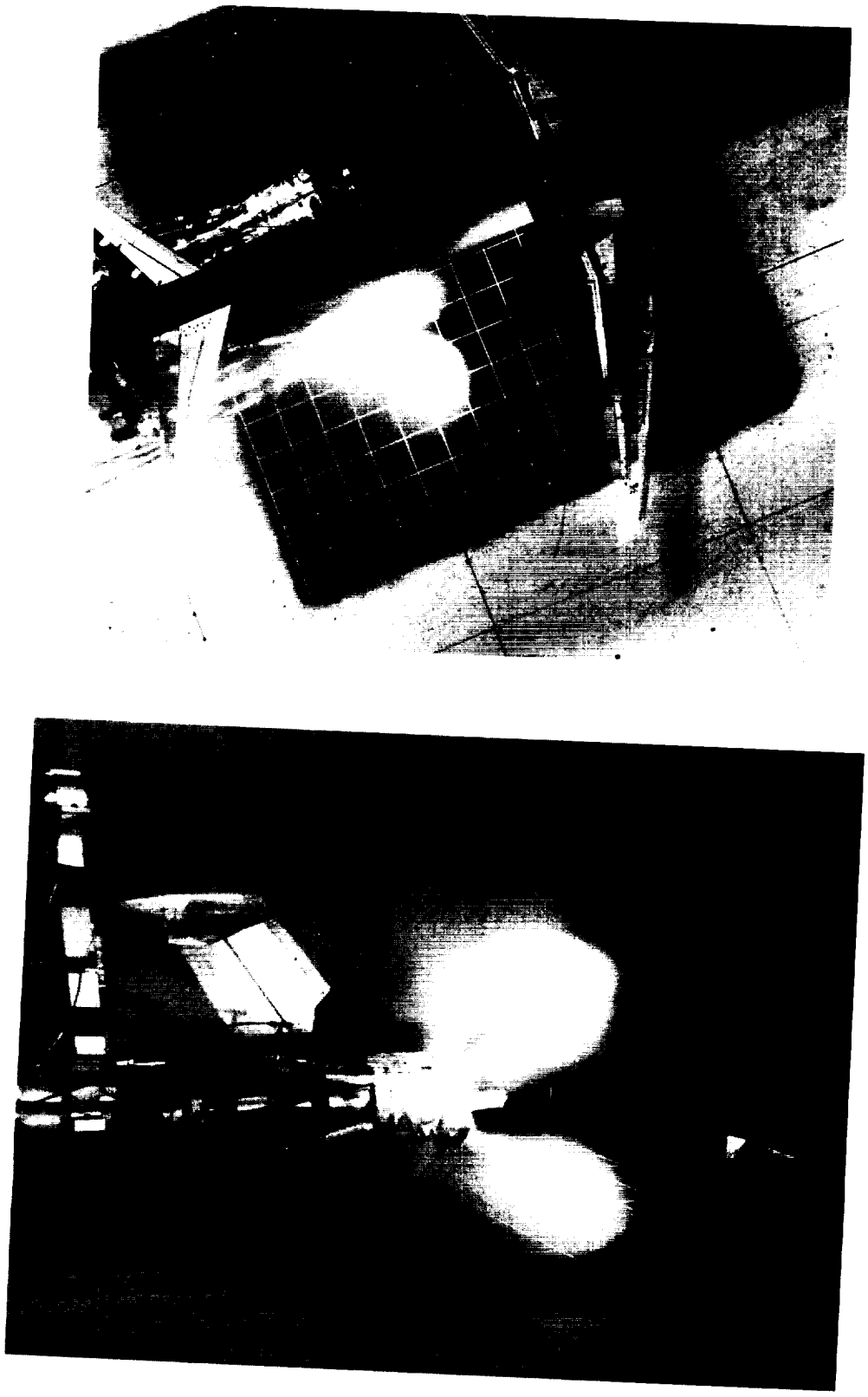

(a) $\dot{m}_R = 5.12$ lb/sec; $q_\infty = 12.2$ psf.

L-88-148

igure 16. Water injection flow visualization for configuration II of four-door thrust reverser. $\delta_f = 40°$; $\delta_s = 60°$; IGE.

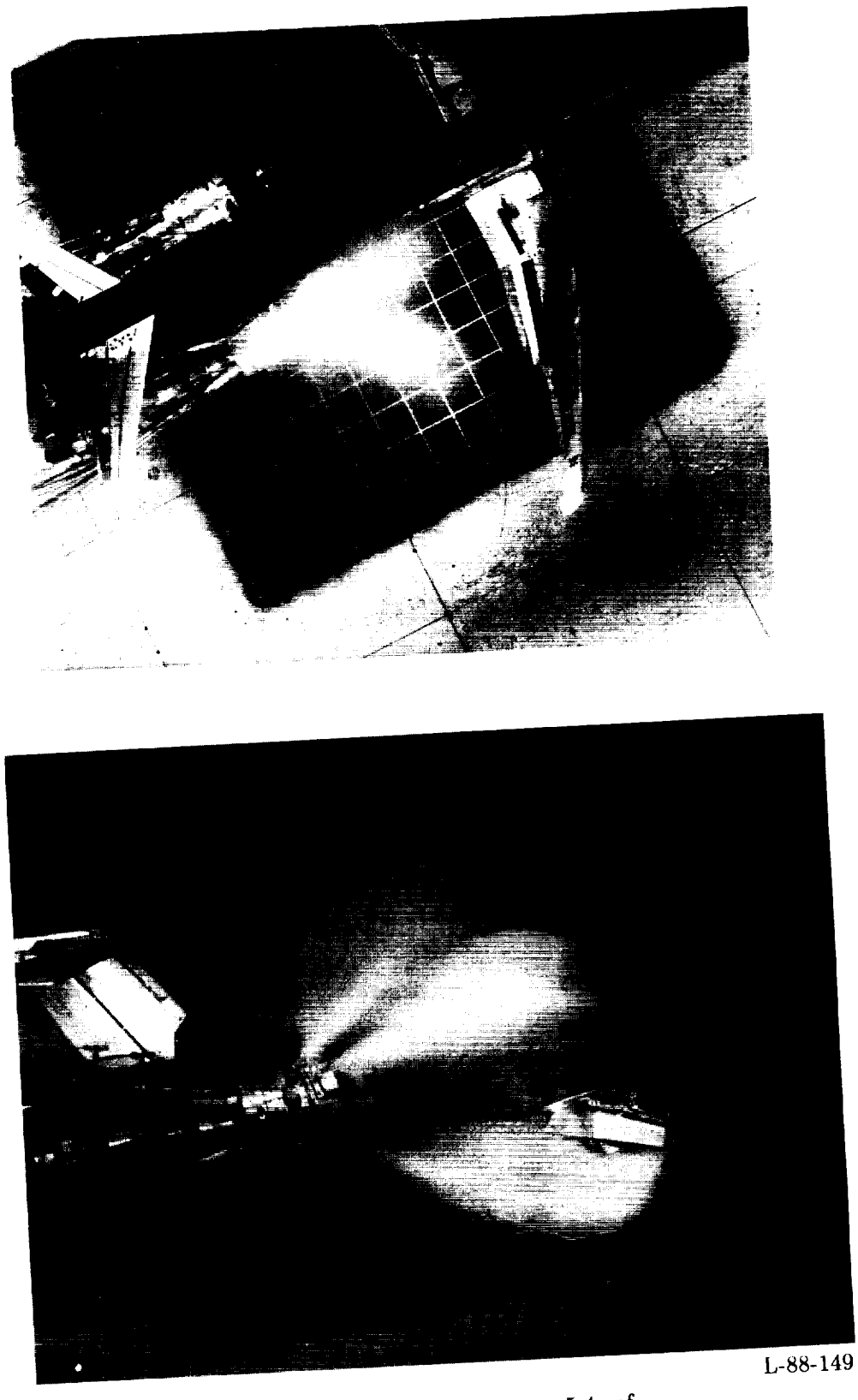

L-88-149

(b) $\dot{m}_R = 5.12$ lb/sec; $q_\infty = 5.4$ psf.

Figure 16. Continued.

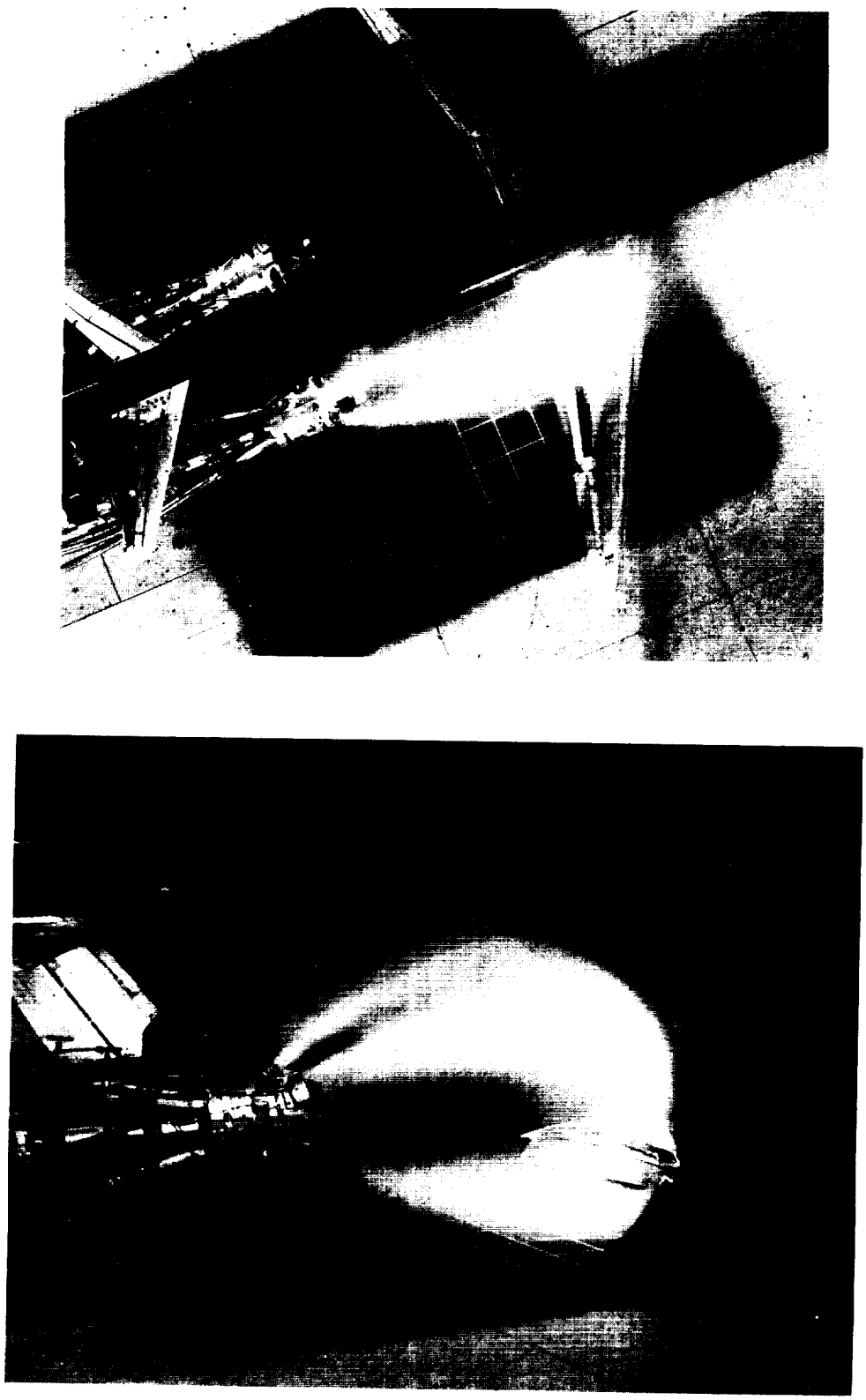

L-88-150

(c) $\dot{m}_R = 5.12$ lb/sec; $q_\infty = 1.4$ psf.

Figure 16. Continued.

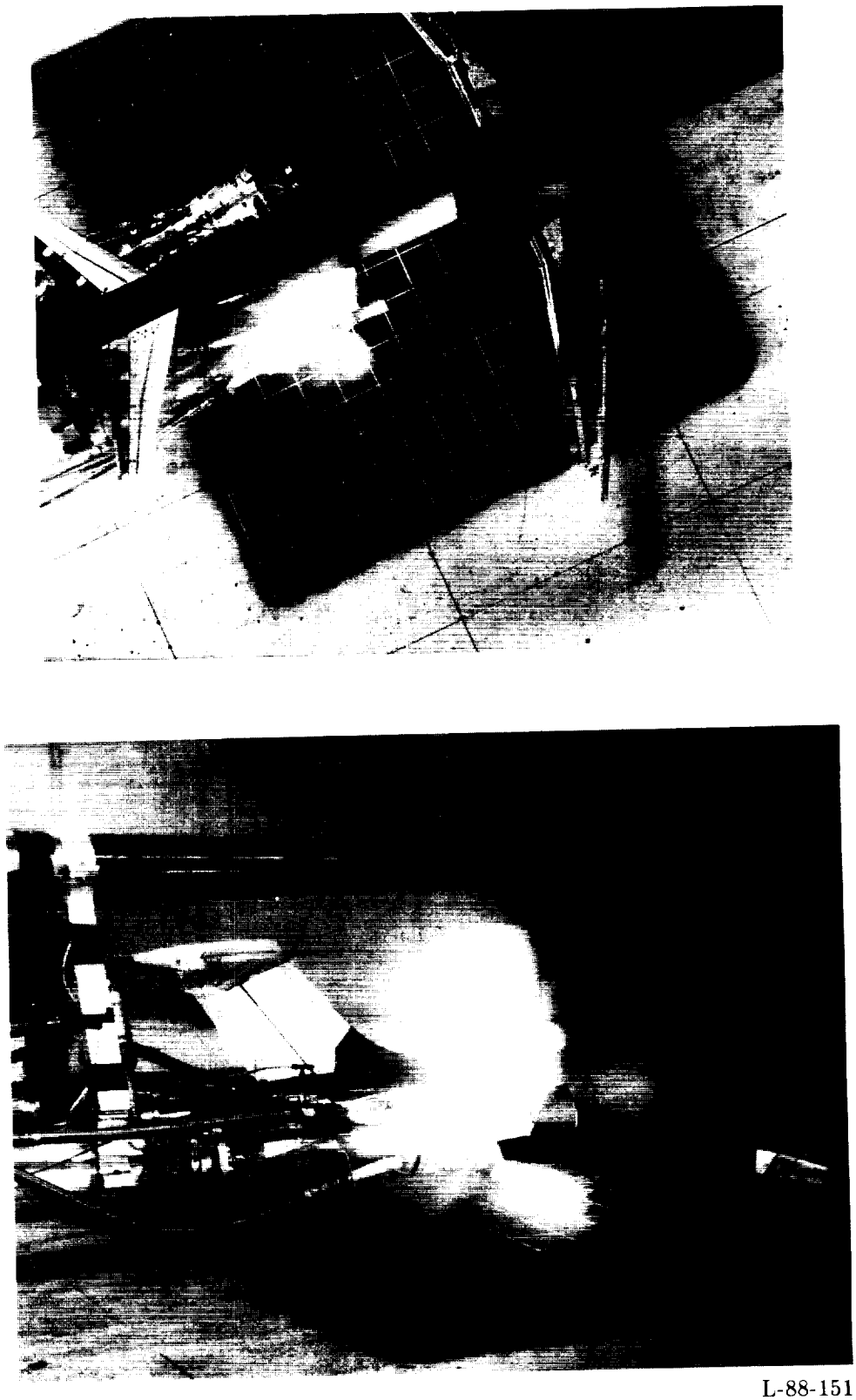

L-88-151

(d) $\dot{m}_R = 3.0$ lb/sec; $q_\infty = 12.2$ psf.

Figure 16. Continued.

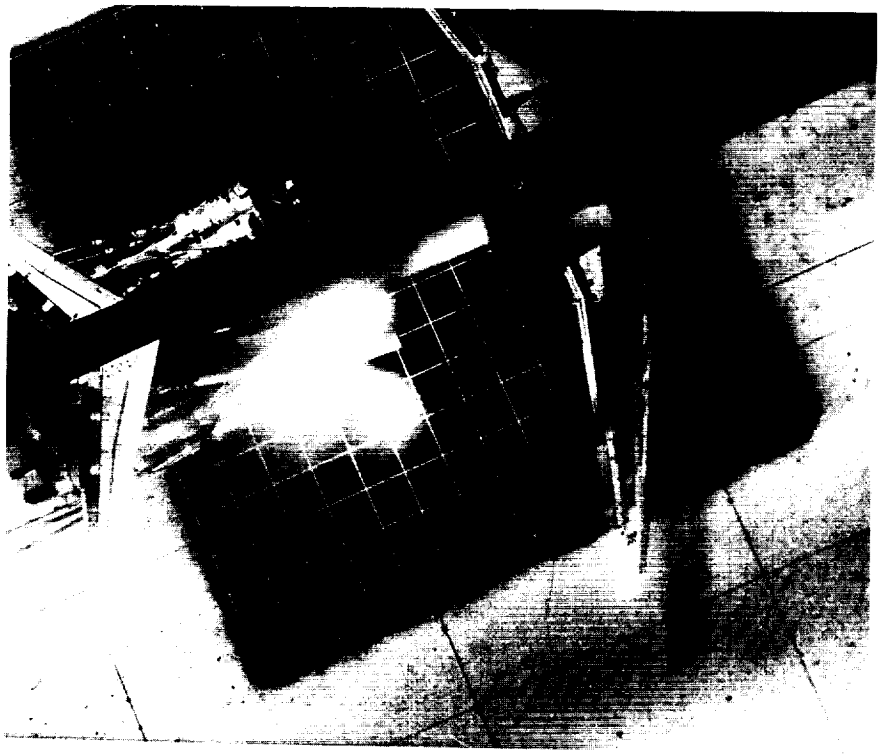

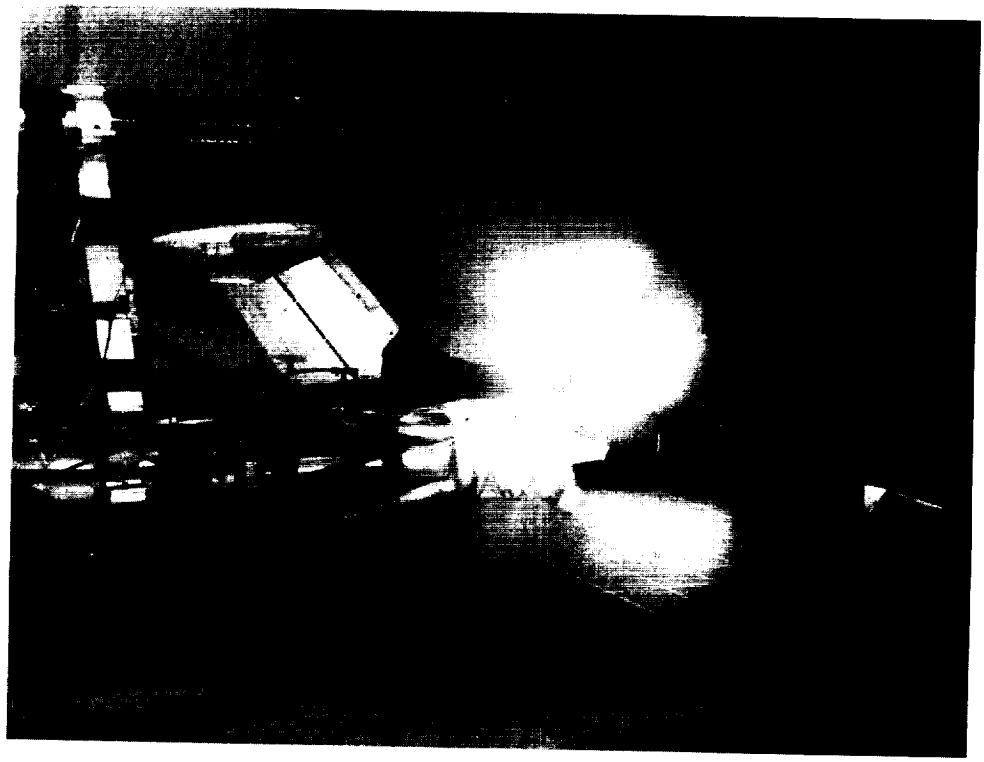

L-88-152

(e) $\dot{m}_R = 3.0$ lb/sec; $q_\infty = 5.4$ psf.

Figure 16. Continued.

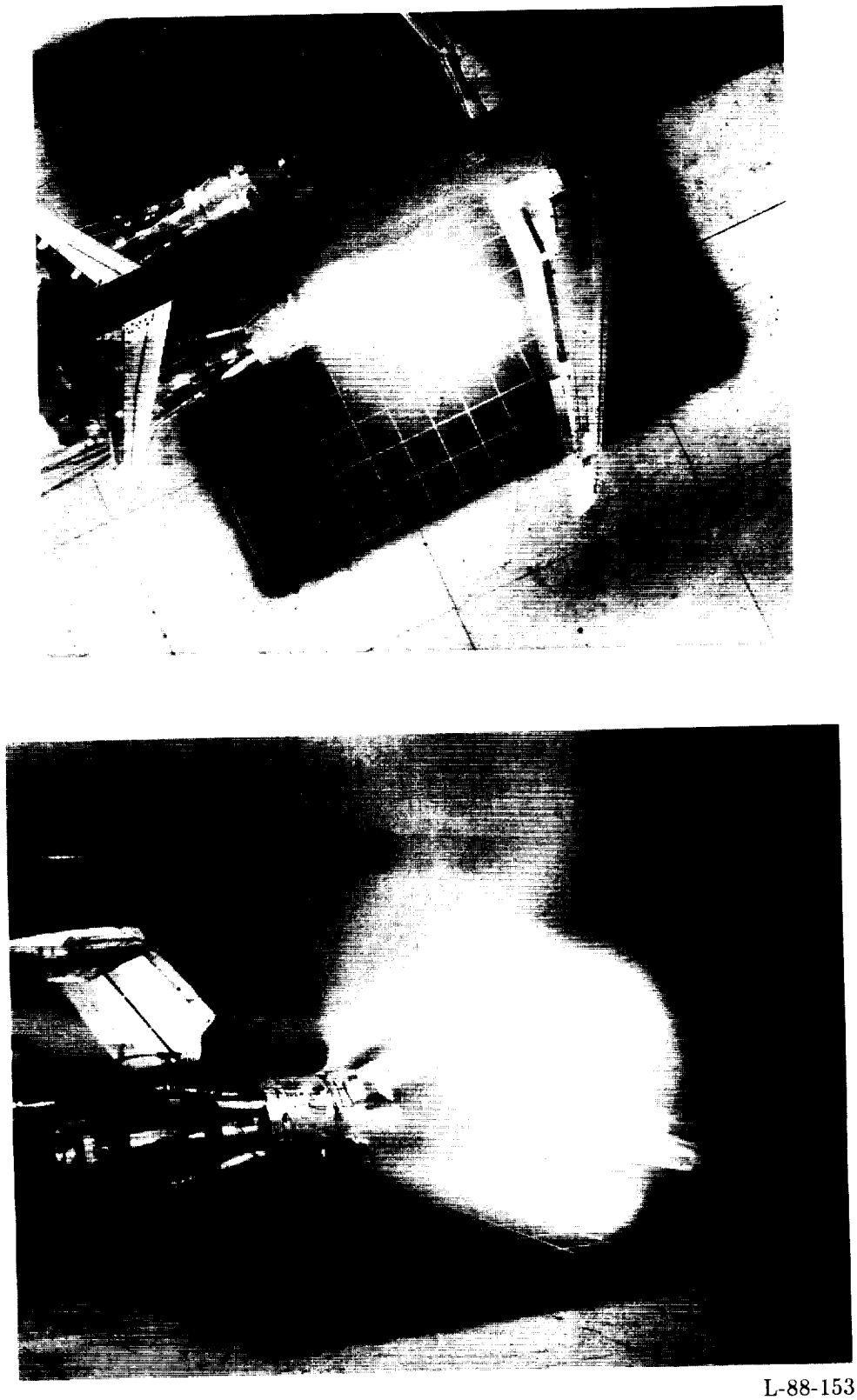

L-88-153

(f) $\dot{m}_R = 3.0$ lb/sec; $q_\infty = 1.4$ psf.

Figure 16. Continued.

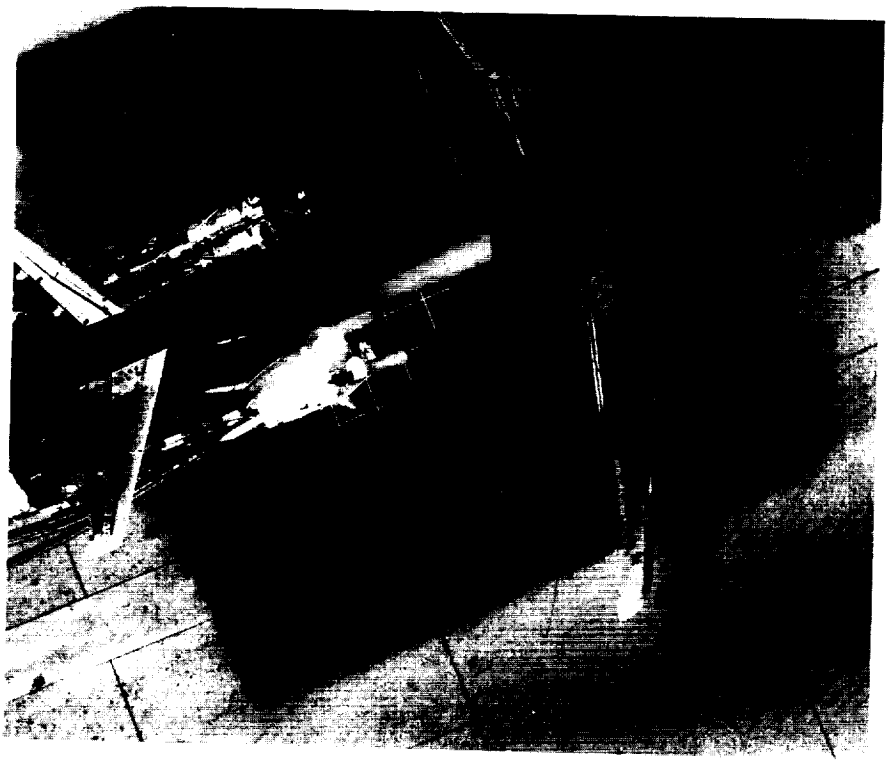

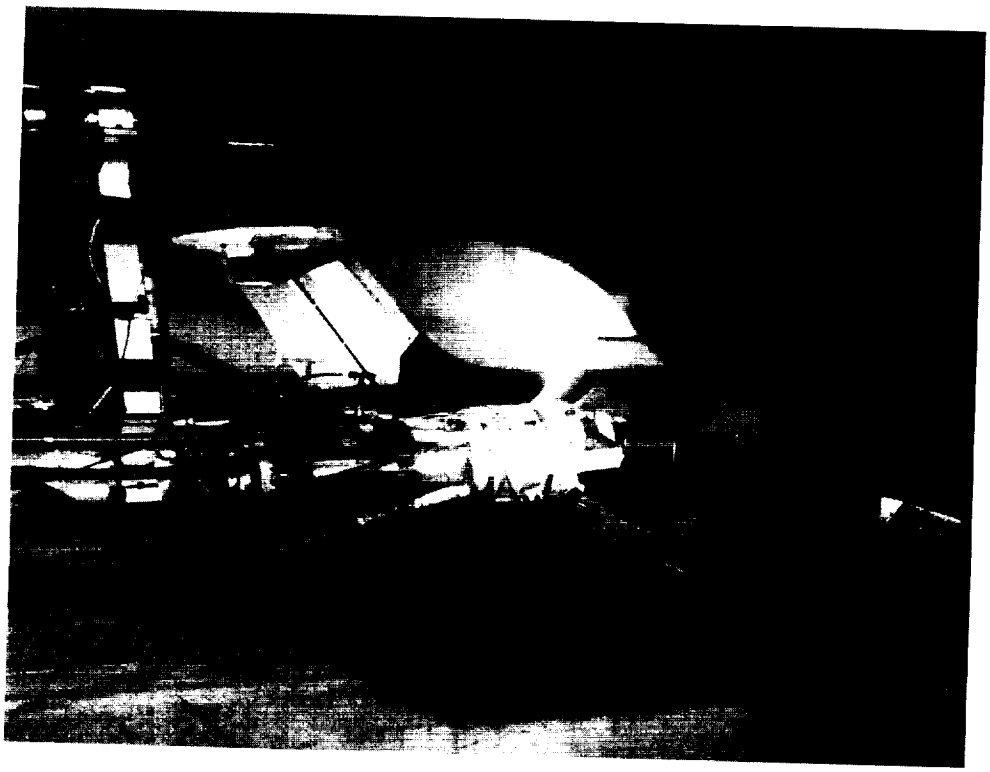

L-88-154

(g) $\dot{m}_R = 1.15$ lb/sec; $q_\infty = 12.2$ psf.

Figure 16. Continued.

L-88-155

(h) $\dot{m}_R = 1.15$ lb/sec; $q_\infty = 5.4$ psf.

Figure 16. Continued.

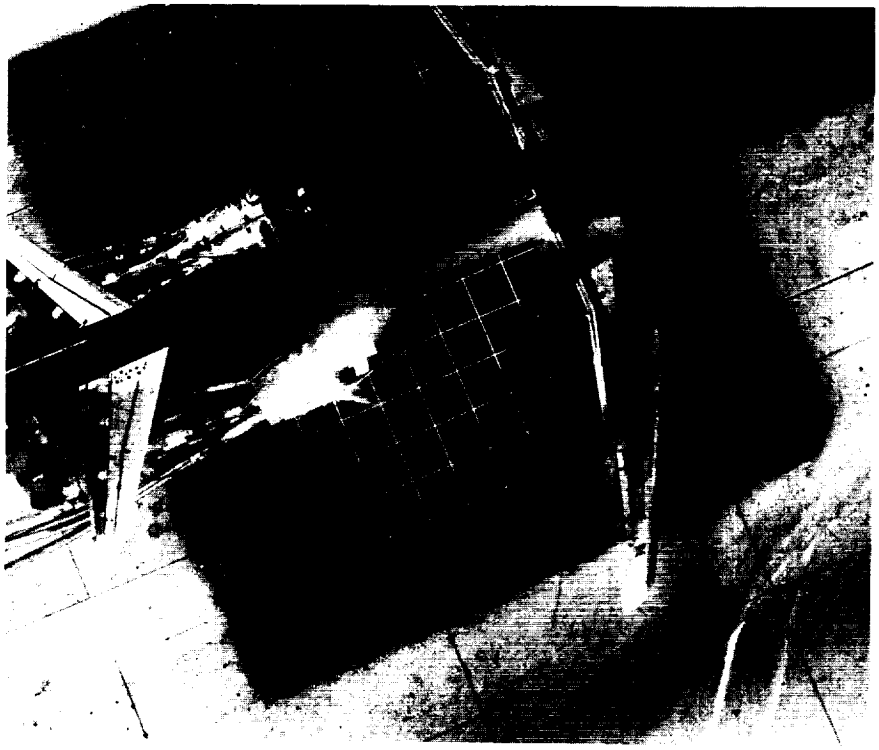

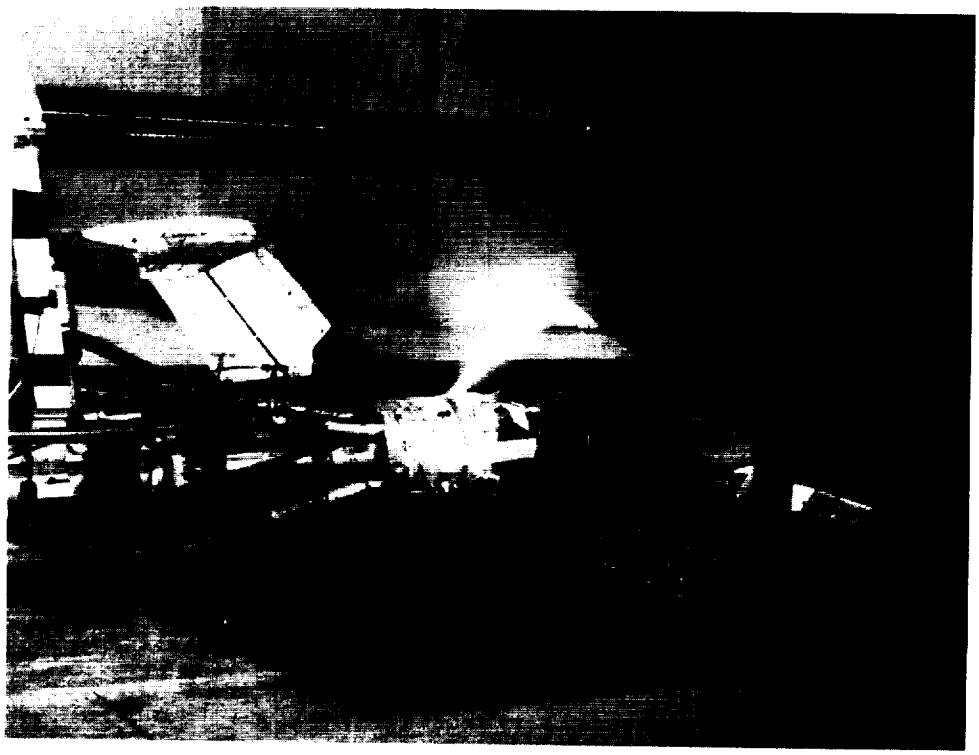

L-88-156

(i) $\dot{m}_R = 1.15$ lb/sec; $q_\infty = 1.4$ psf.

Figure 16. Concluded.

L-88-157

(a) $\dot{m}_R = 5.12$ lb/sec; $q_\infty = 12.2$ psf.

Figure 17. Water injection flow visualization for configuration III of four-door thrust reverser. $\delta_f = 40°$; $\delta_s = 60°$; IGE.

L-88-158

(b) $\dot{m}_R = 5.12$ lb/sec; $q_\infty = 5.4$ psf.

Figure 17. Continued.

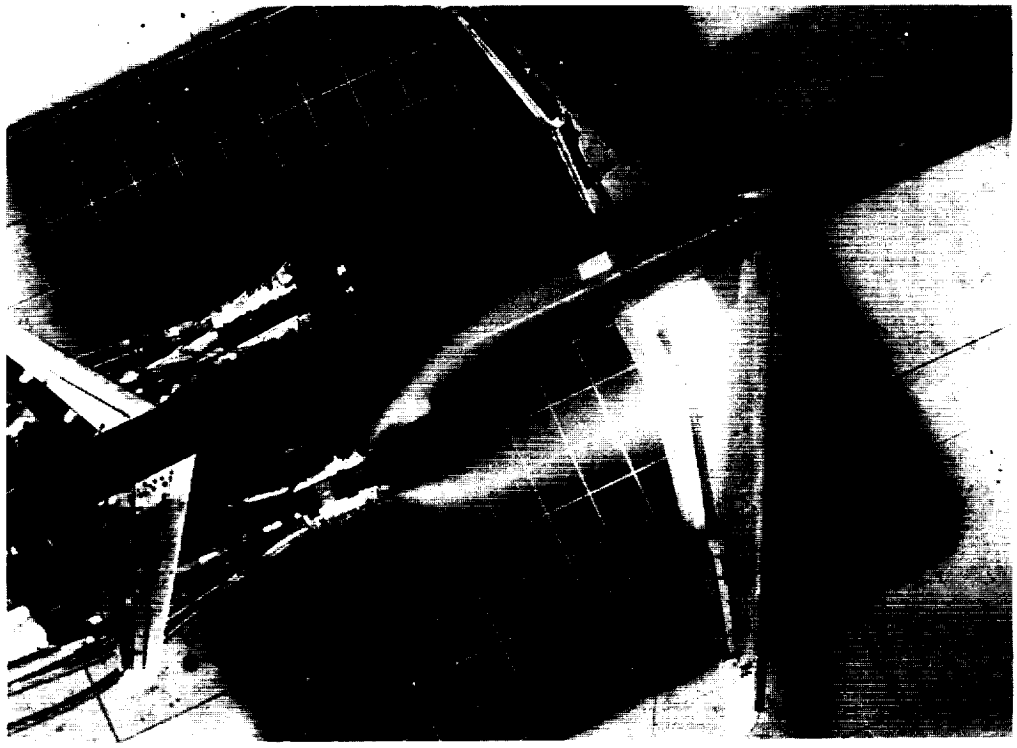

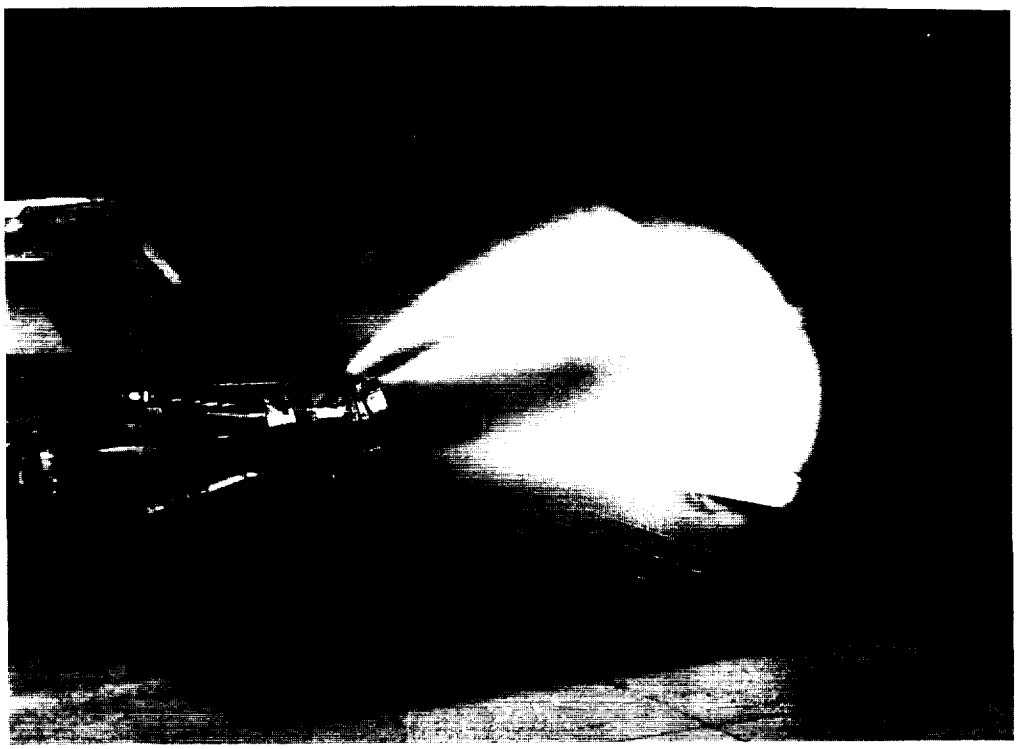

L-88-159

(c) $\dot{m}_R = 5.12$ lb/sec; $q_\infty = 1.4$ psf.

Figure 17. Continued.

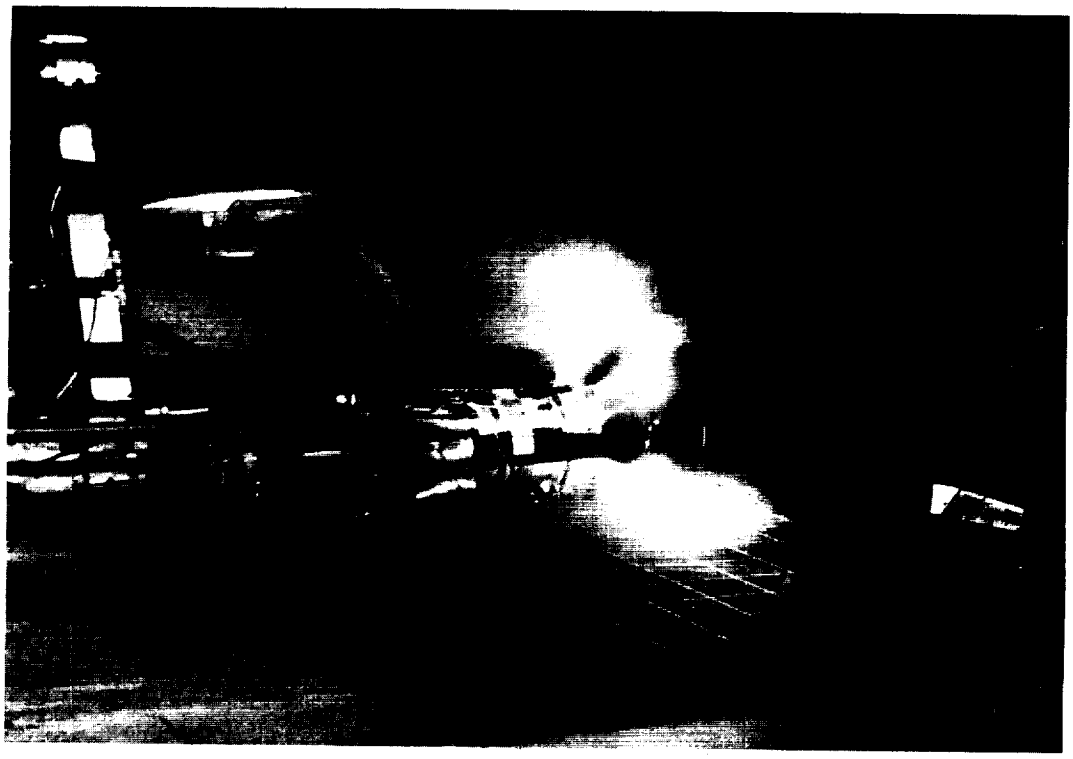

L-88-160

(d) $\dot{m}_R = 3.0$ lb/sec; $q_\infty = 12.2$ psf.

Figure 17. Continued.

L-88-161

(e) $\dot{m}_R = 3.0$ lb/sec; $q_\infty = 5.4$ psf.

Figure 17. Continued.

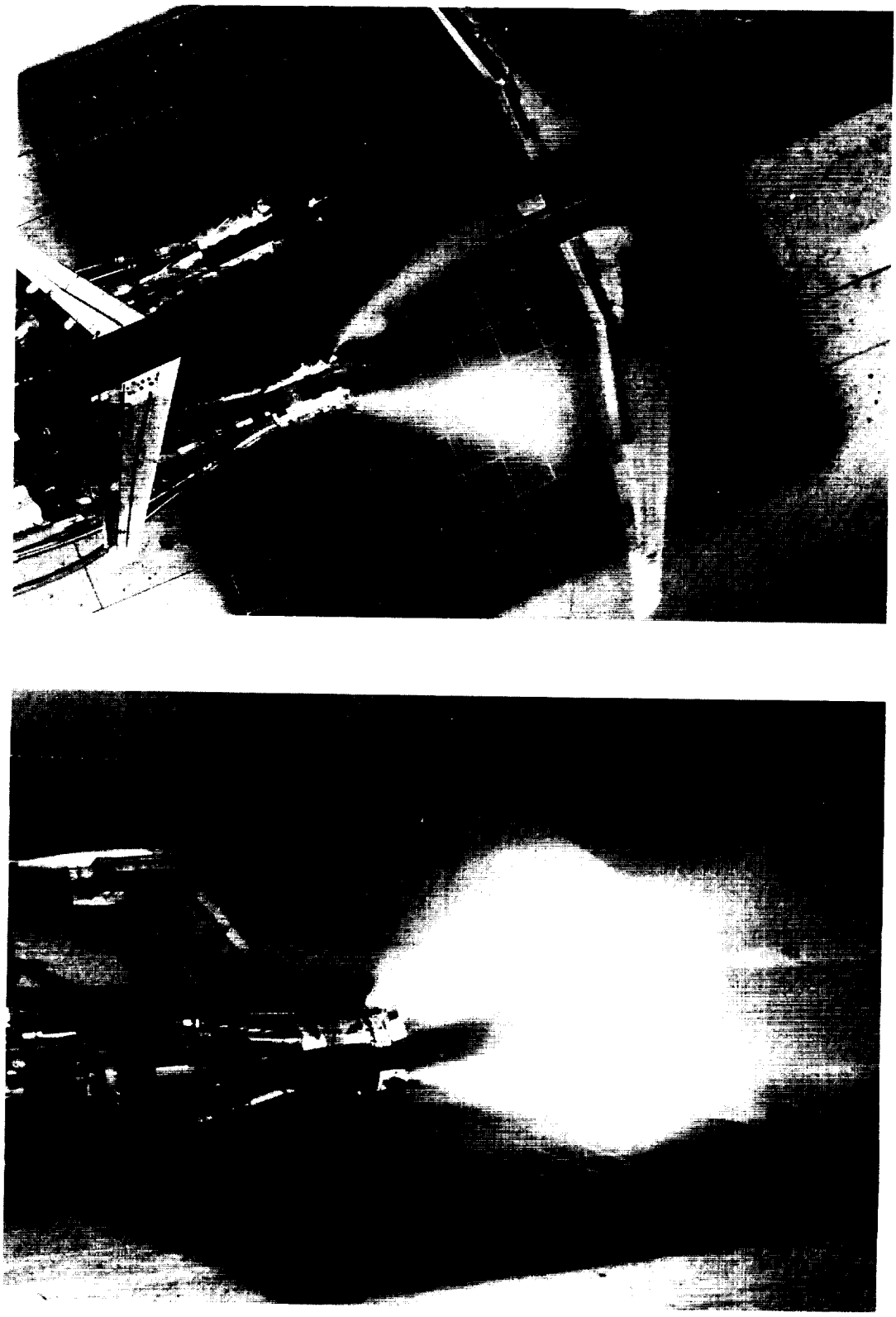

L-88-162

(f) $\dot{m}_R = 3.0$ lb/sec; $q_\infty = 1.4$ psf.

Figure 17. Continued.

L-88-163

(g) $\dot{m}_R = 1.15$ lb/sec; $q_\infty = 12.2$ psf.

Figure 17. Continued.

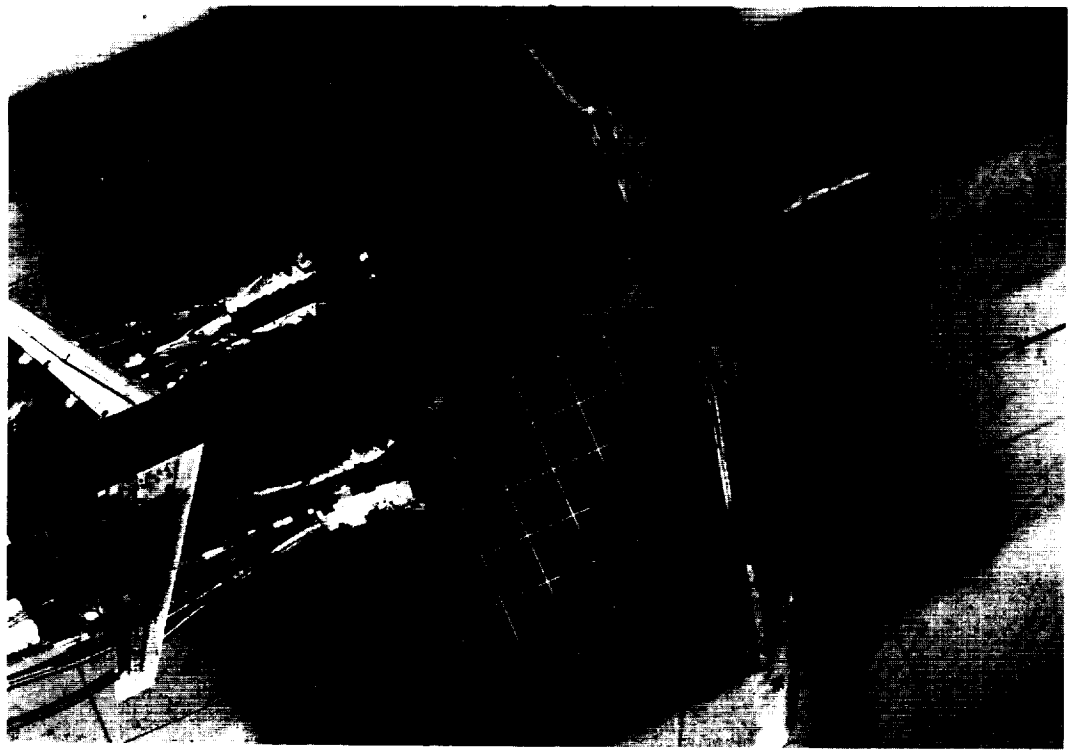

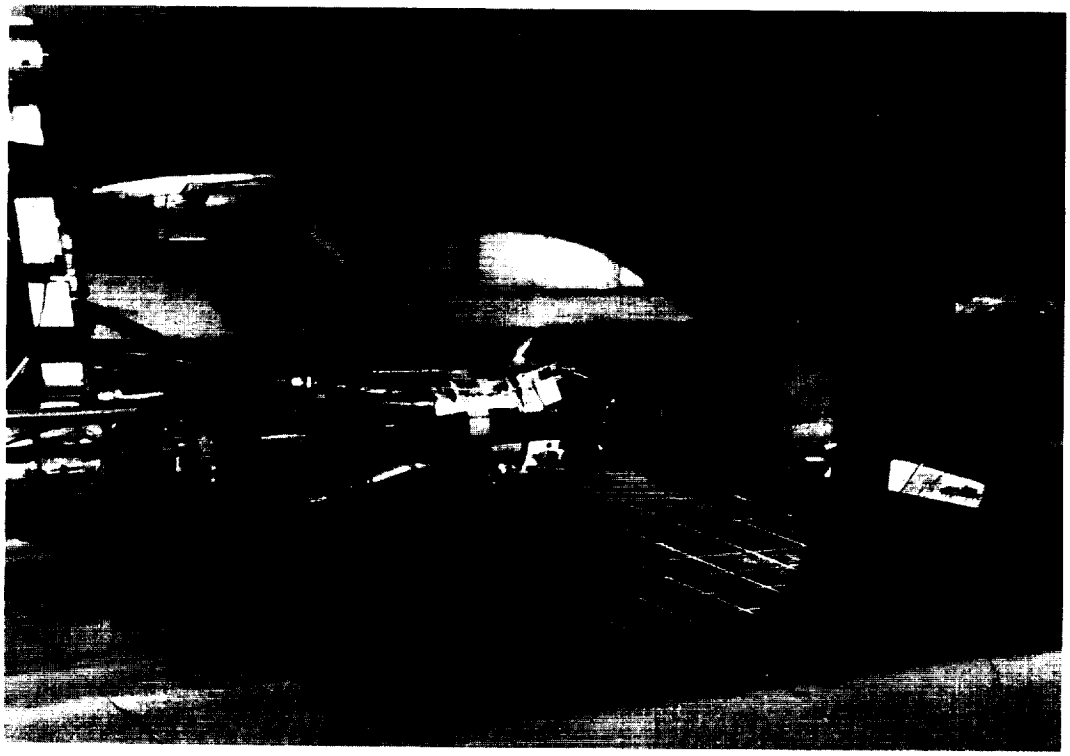

L-88-164

(h) $\dot{m}_R = 1.15$ lb/sec; $q_\infty = 5.4$ psf.

Figure 17. Continued.

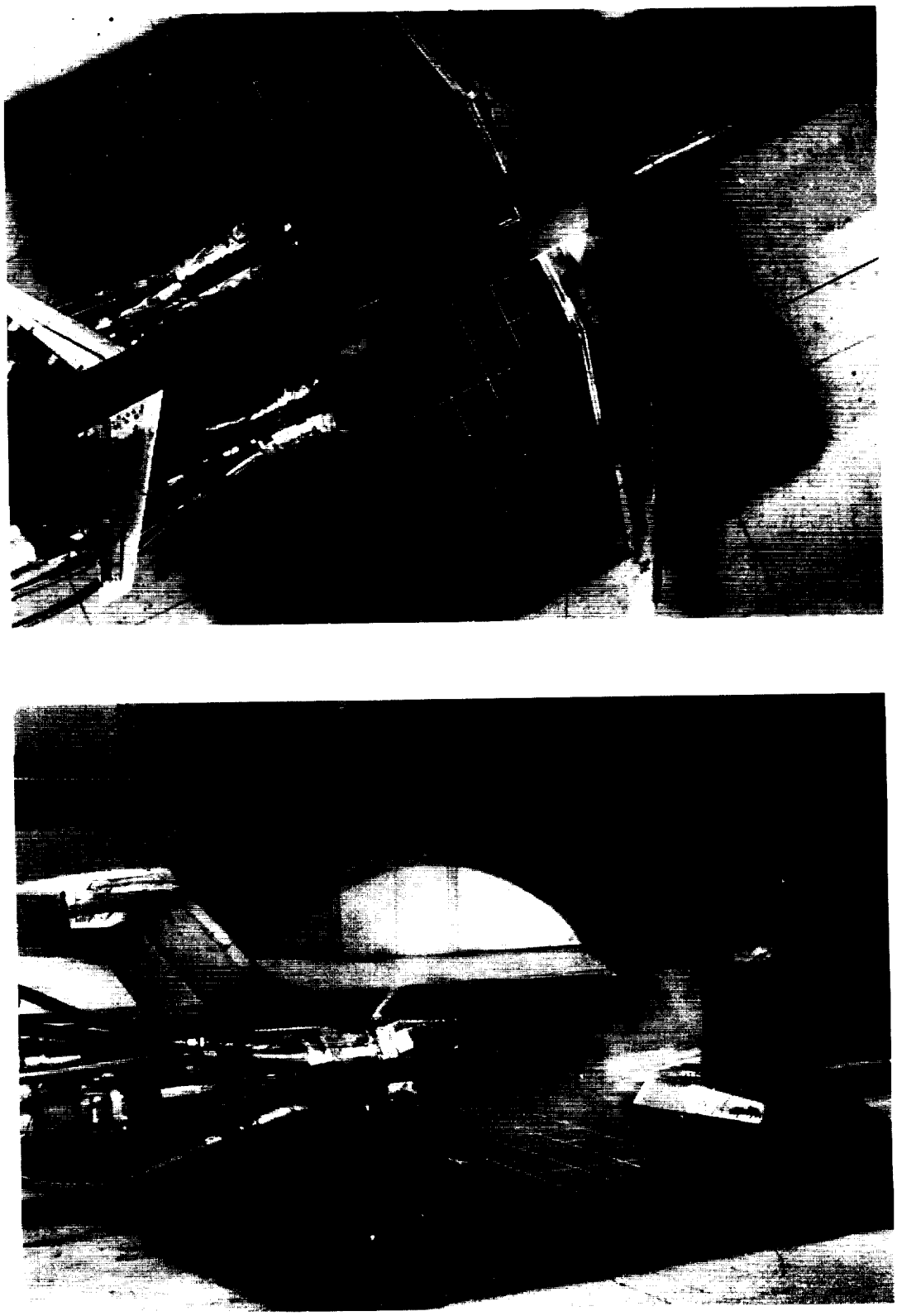

L-88-165

(i) $\dot{m}_R = 1.15$ lb/sec; $q_\infty = 1.4$ psf.

Figure 17. Concluded.

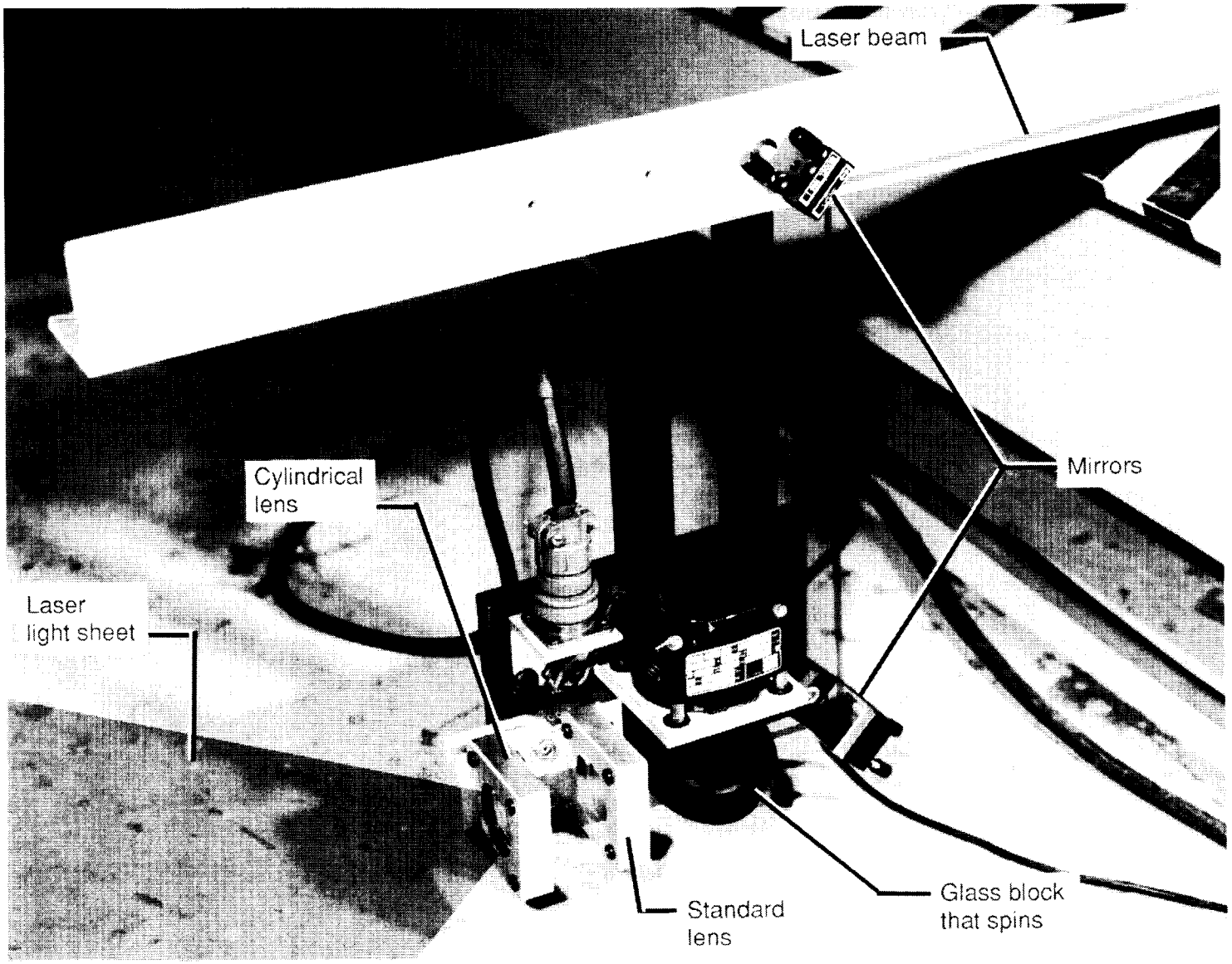


(a) Optics package used to generate horizontal laser light sheet.

Figure 18. Details of use of laser light sheet.

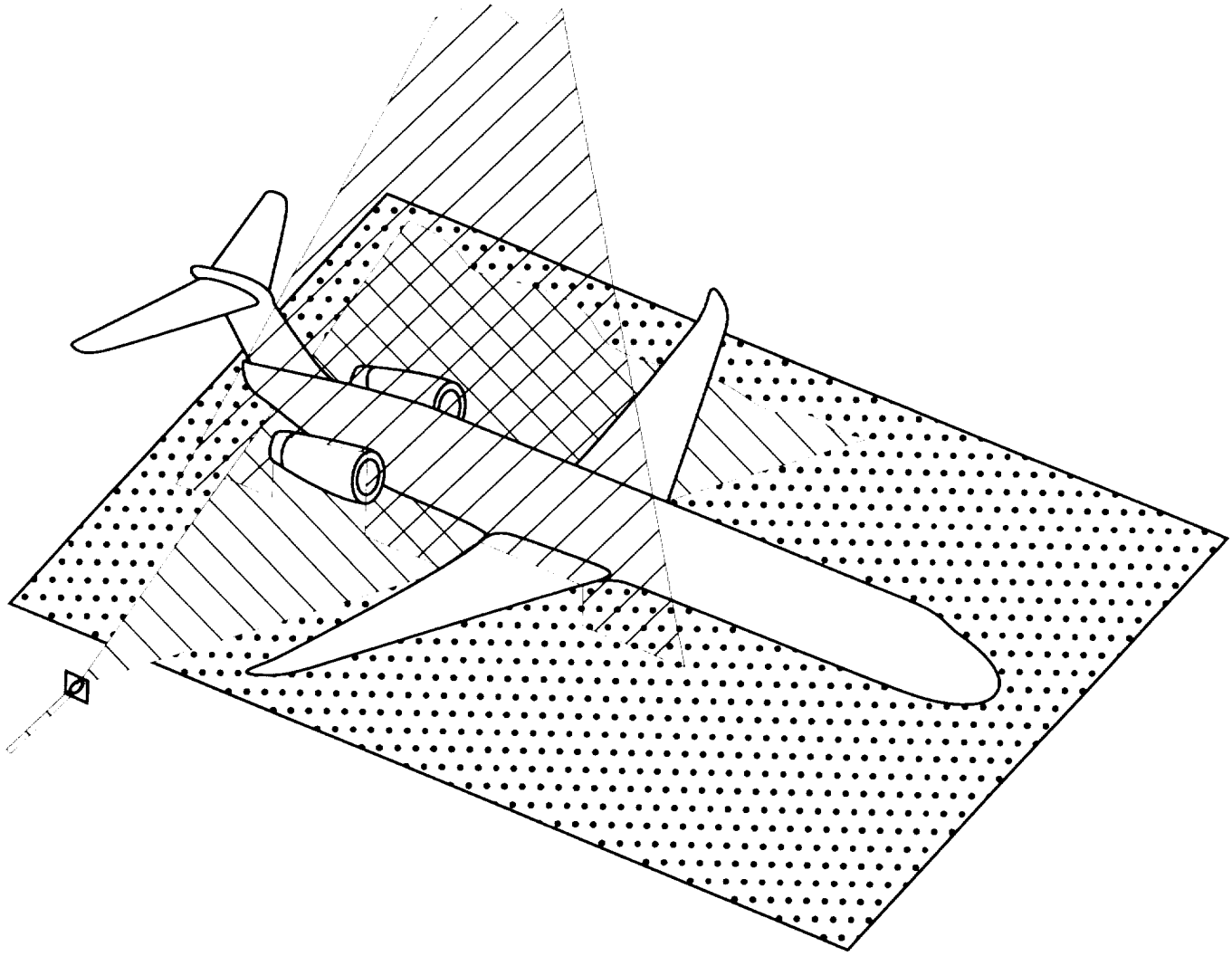

(b) Sketch illustrating position of both horizontal and vertical laser light sheets with respect to model.

Figure 18. Concluded.

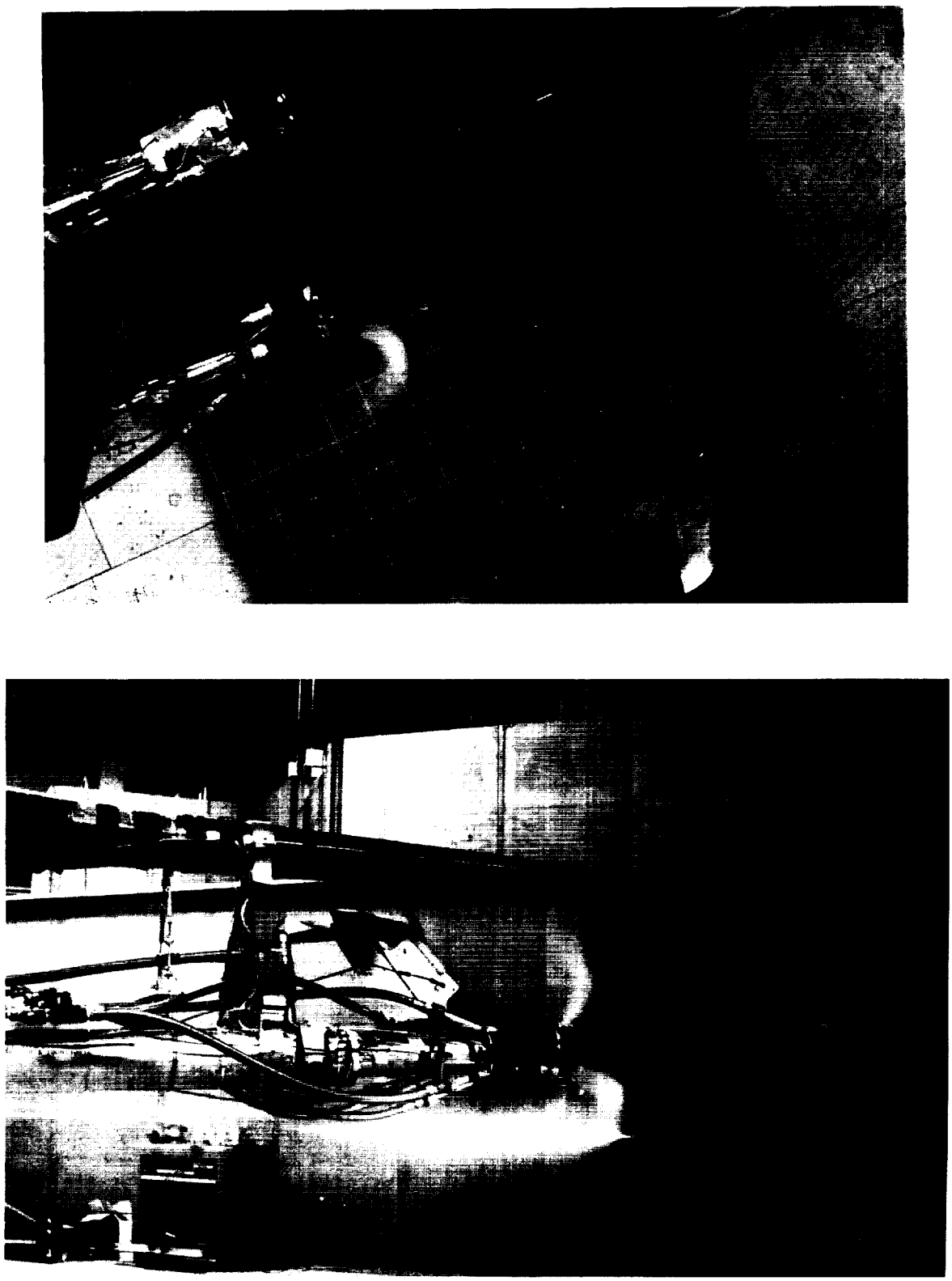

L-88-167

(a) $q_\infty = 12.2$ psf.

Figure 19. Horizontal laser light sheet with water injection flow visualization for cascade thrust reverser. $\dot{m}_R = 2.55$ lb/sec; $\delta_f = 0°$; $\delta_s = 0°$; $h = 48$ in.; OGE.

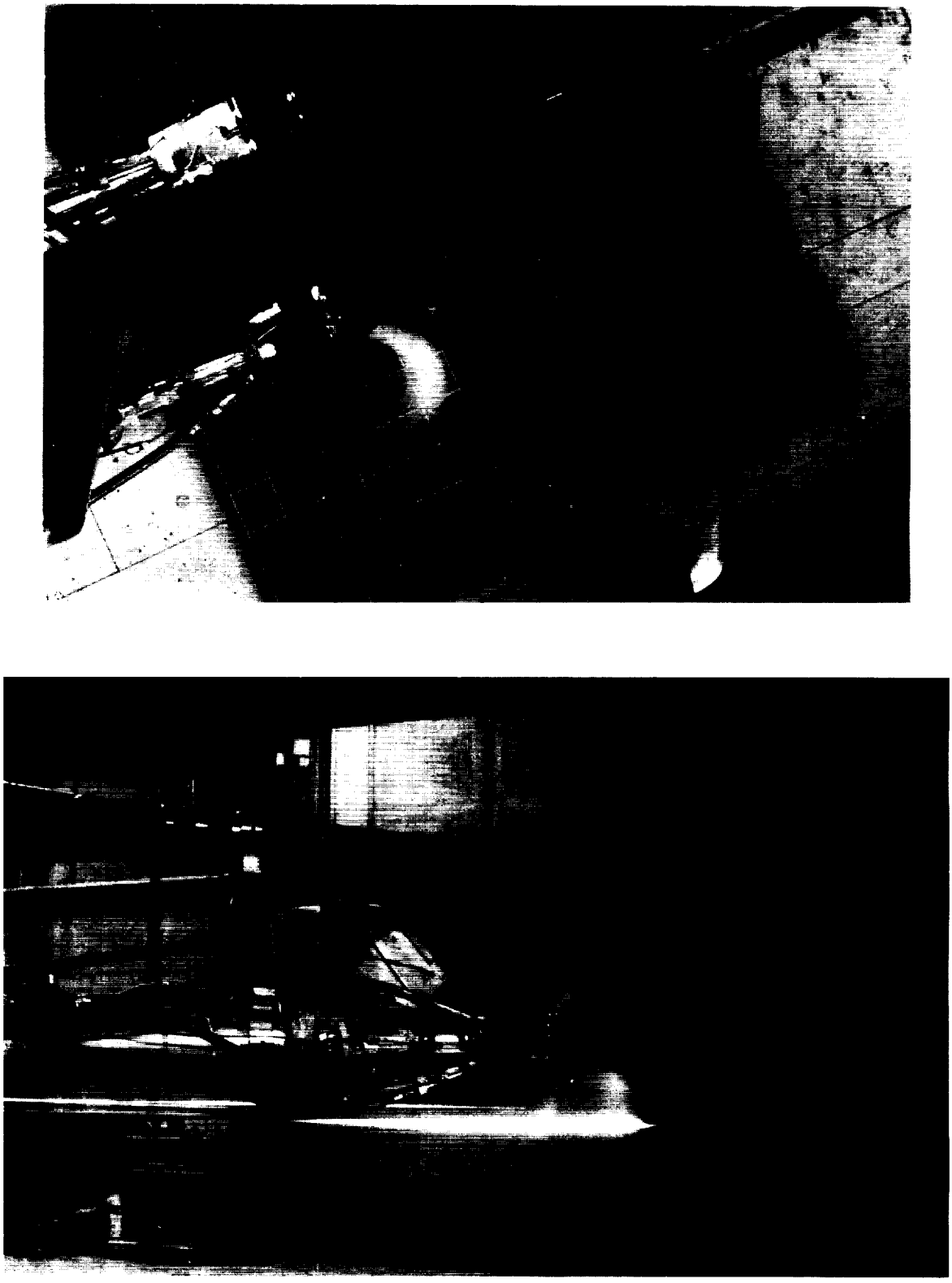

L-88-168

(b) $q_\infty = 5.4$ psf.

Figure 19. Continued.

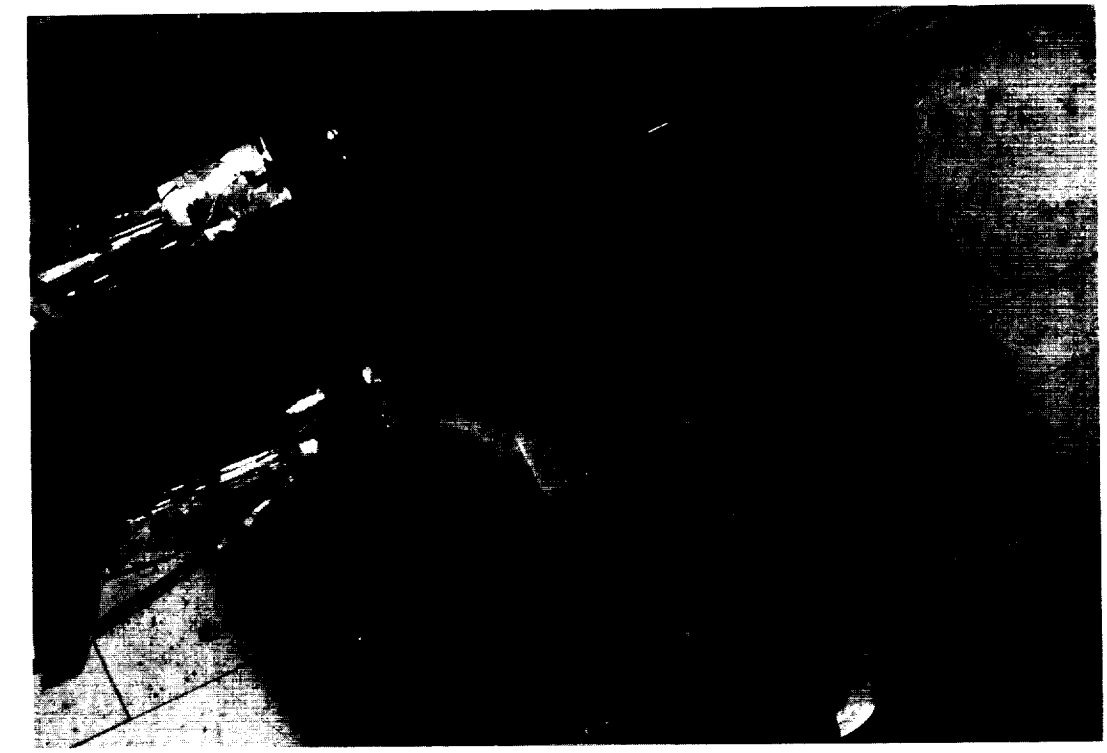

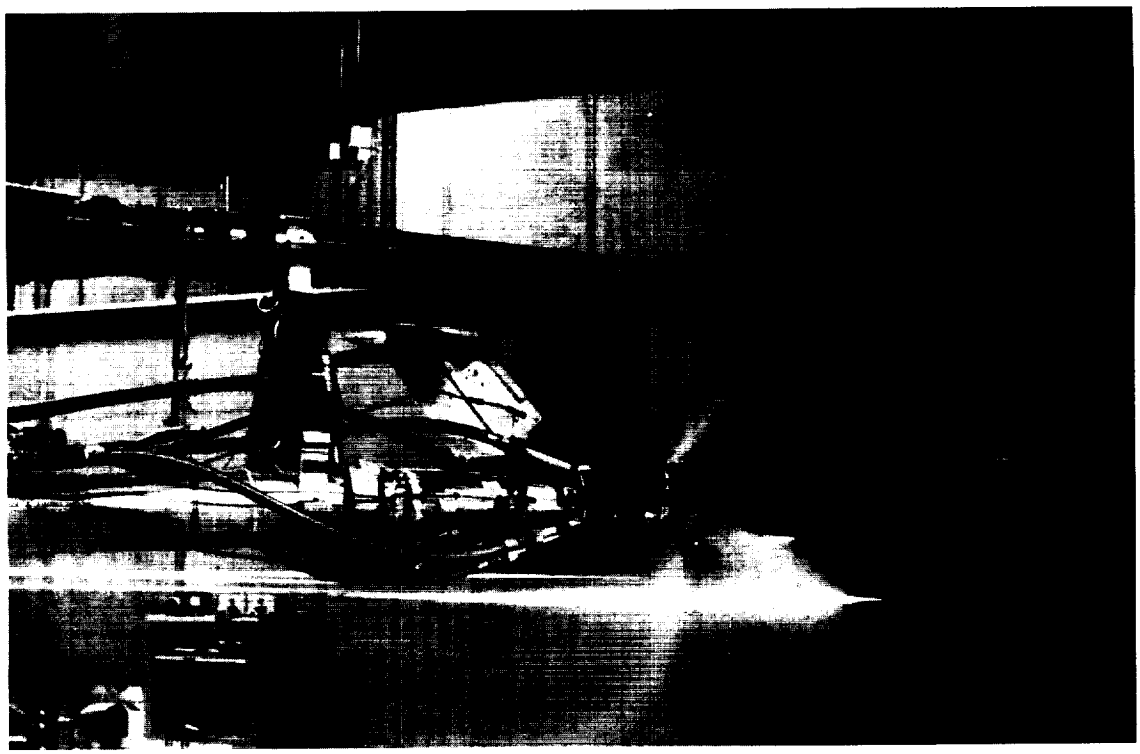

L-88-169

(c) $q_\infty = 1.4$ psf.

Figure 19. Concluded.

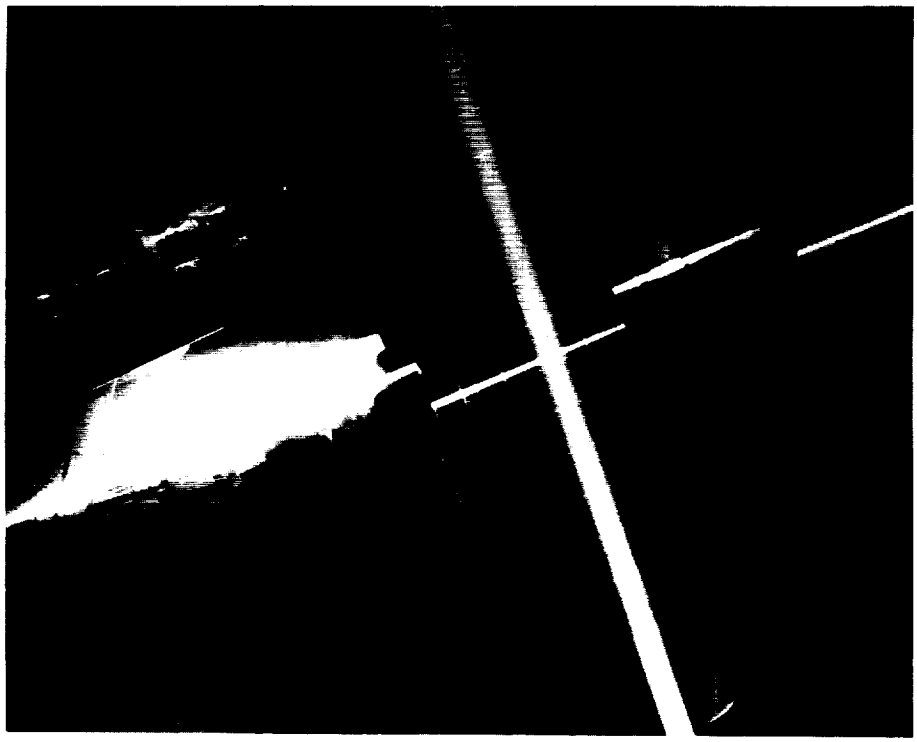

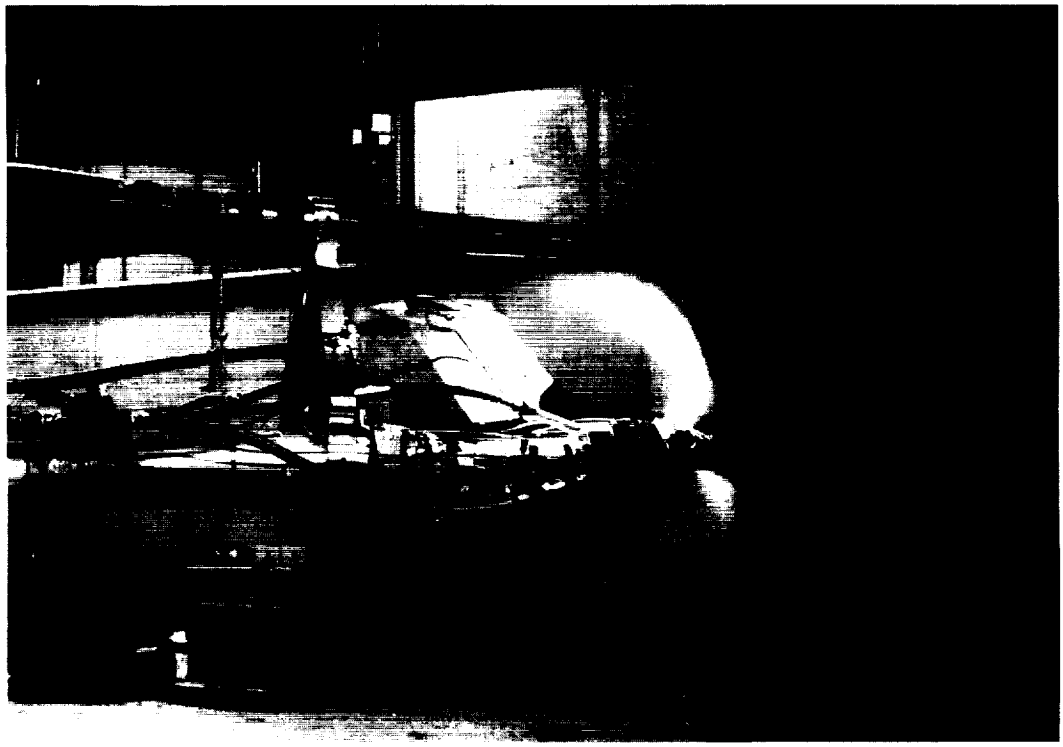

L-88-170

(a) $q_\infty = 12.2$ psf.

Figure 20. Vertical laser light sheet with water injection flow visualization for cascade thrust reverser. $\dot{m}_R = 2.55$ lb/sec; $\delta_f = 0°$; $\delta_s = 0°$; OGE.

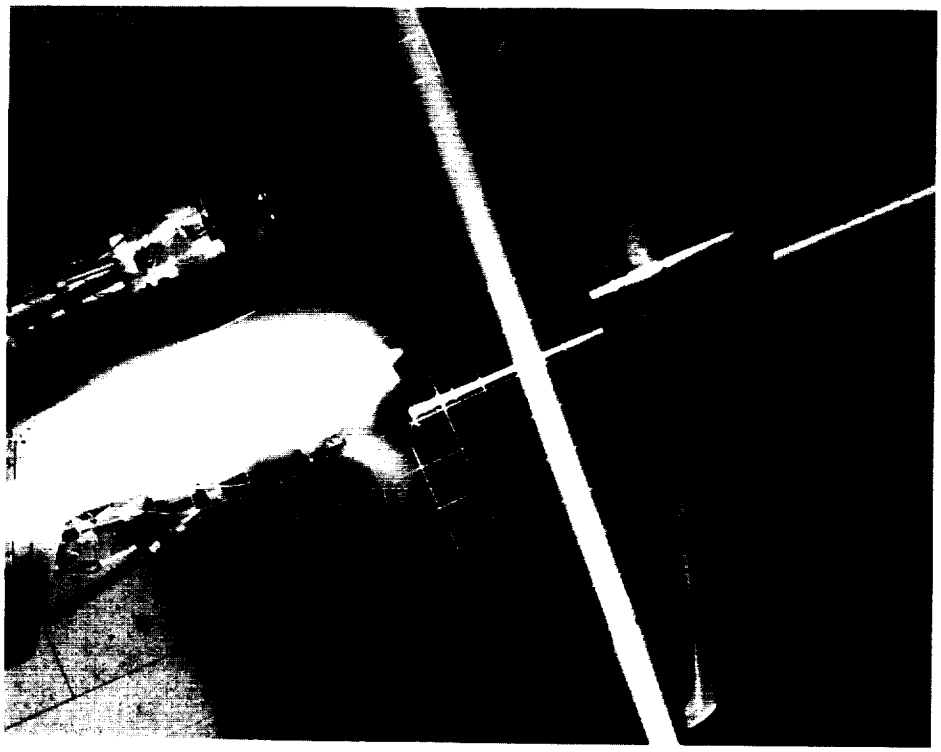

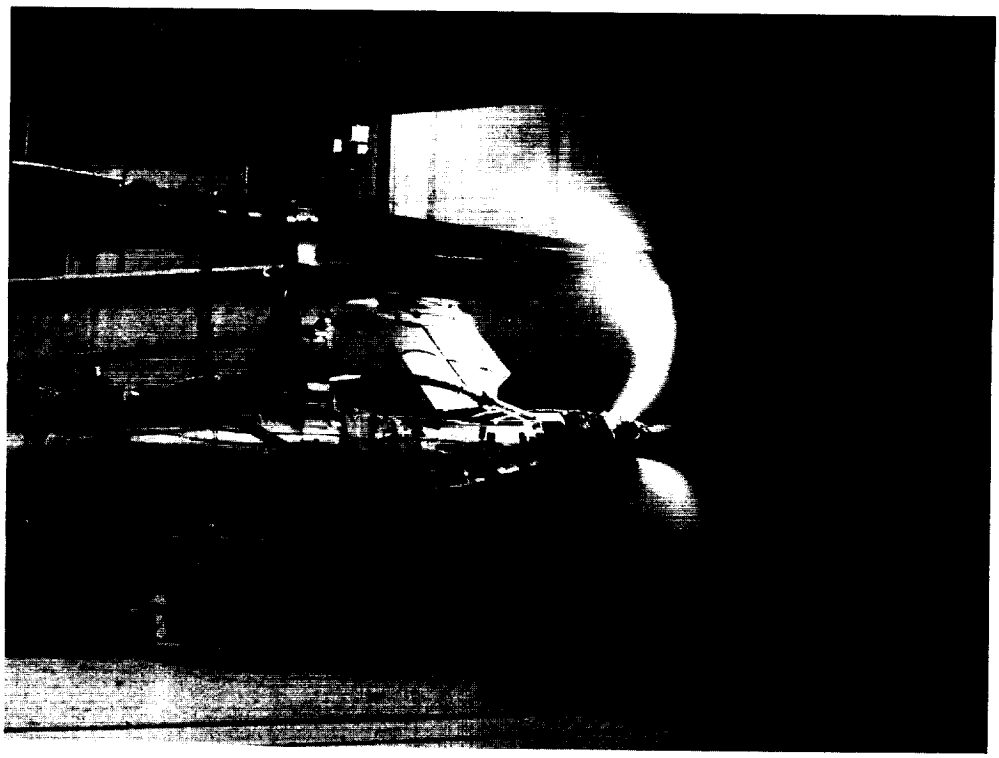

L-88-171

(b) $q_\infty = 5.4$ psf.

Figure 20. Continued.

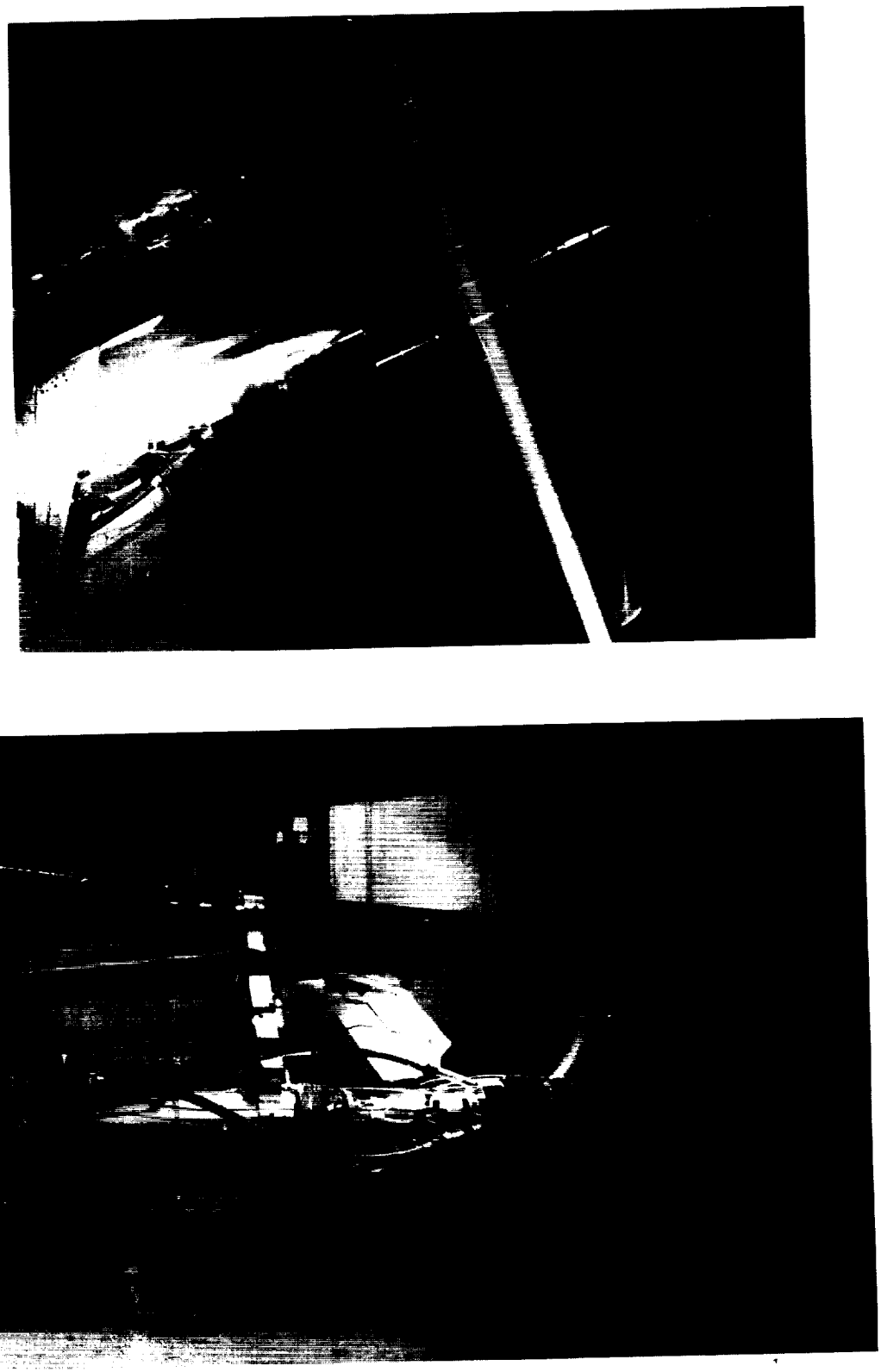

L-88-172

(c) Vertical laser light sheet at reduced power. $q_\infty = 5.4$ psf.

Figure 20. Continued.

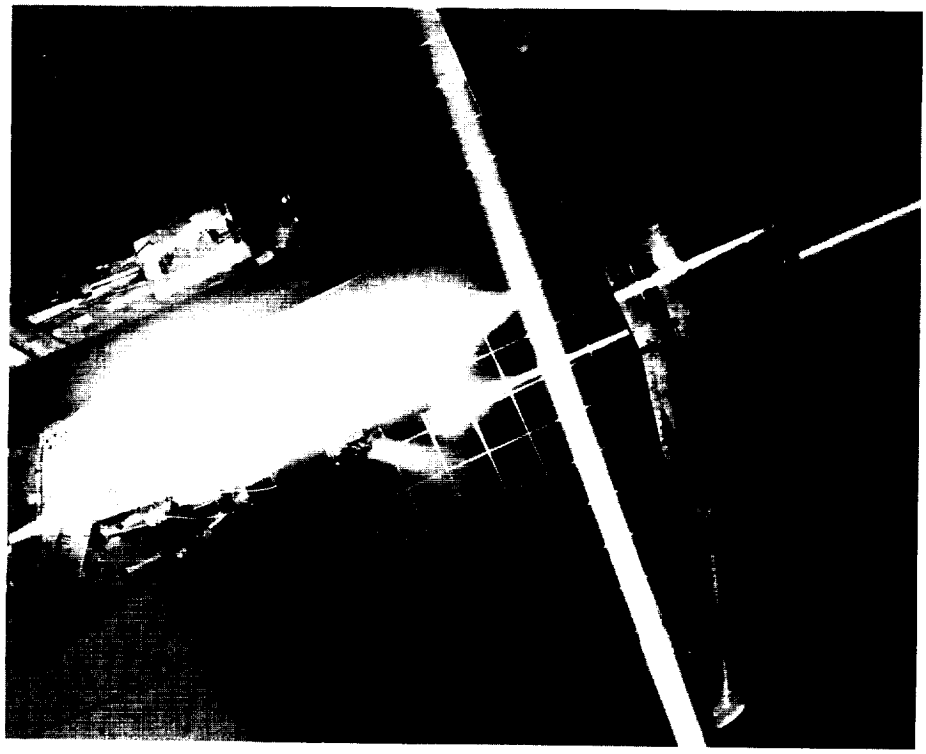

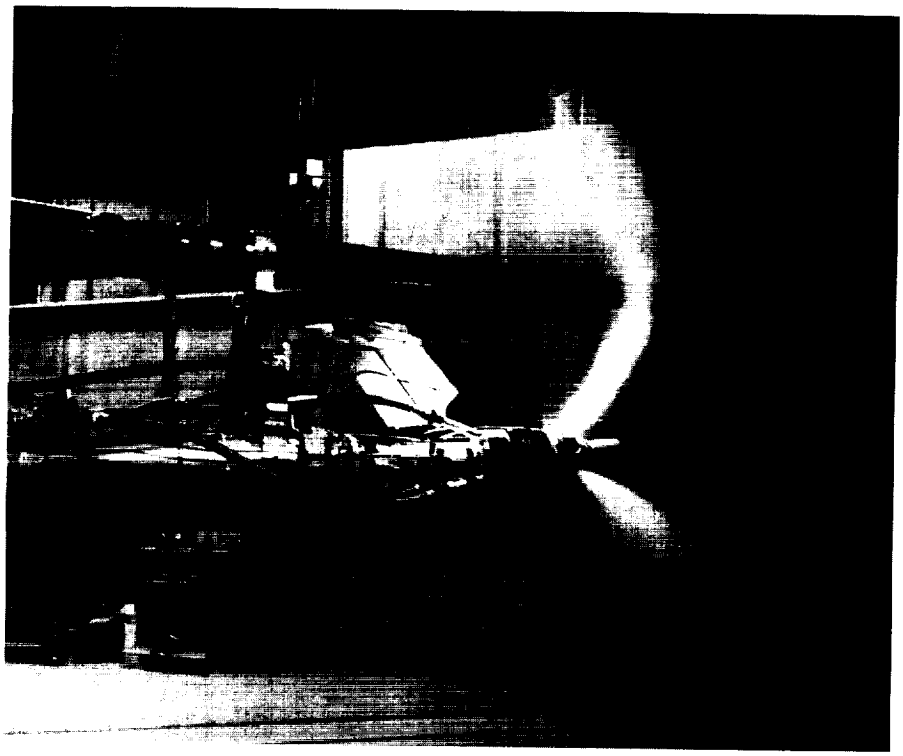

L-88-173

(d) $q_\infty = 1.4$ psf.

Figure 20. Concluded.

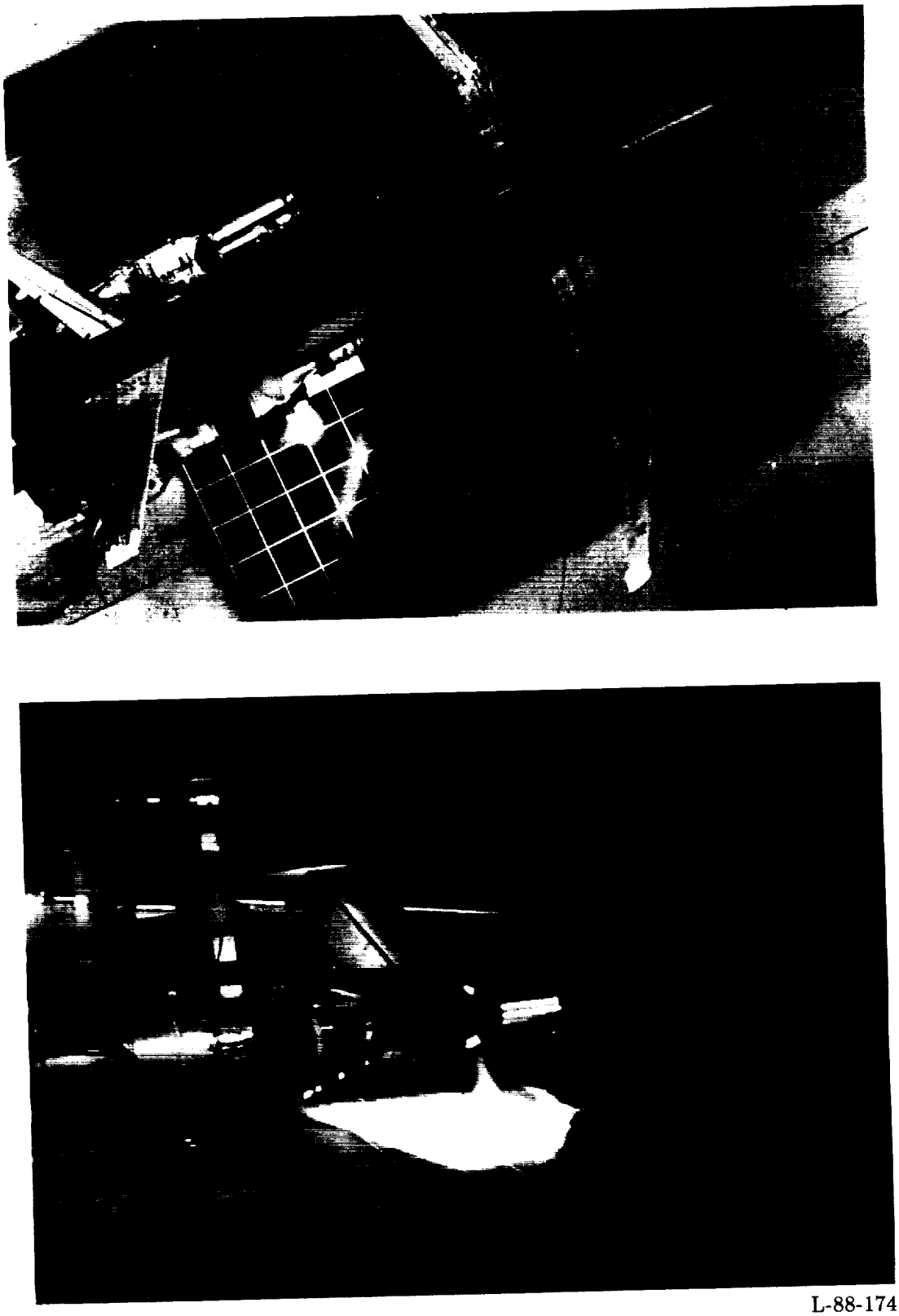

L-88-174

(a) $q_\infty = 12.2$ psf.

Figure 21. Horizontal laser light sheet with water injection flow visualization for 15° rotated target thrust reverser. $\dot{m}_R = 2.55$ lb/sec; $\delta_f = 0°$; $\delta_s = 0°$; $h = 1.5$ in.; IGE.

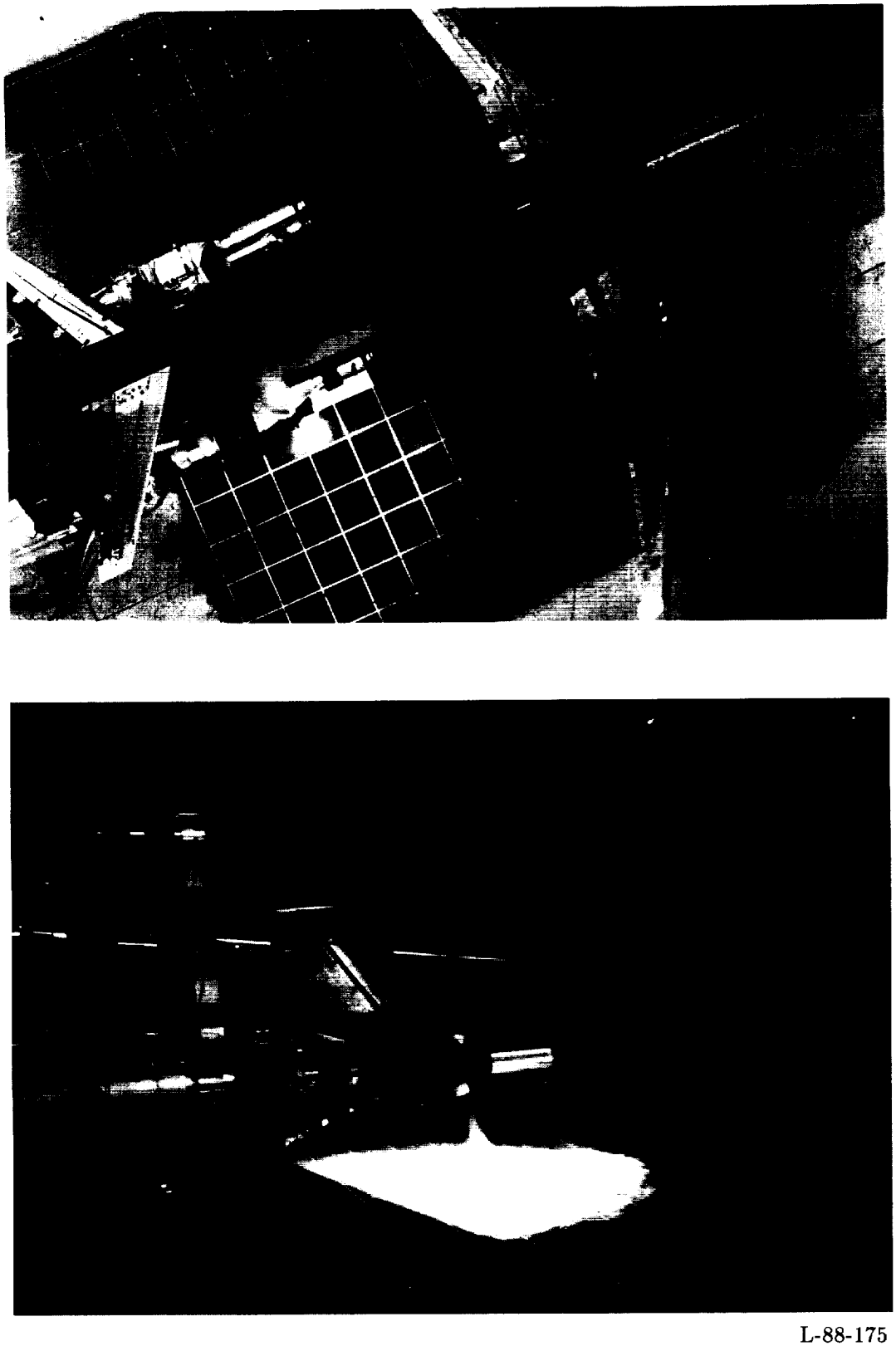

L-88-175

(b) $q_\infty = 5.4$ psf.

Figure 21. Continued.

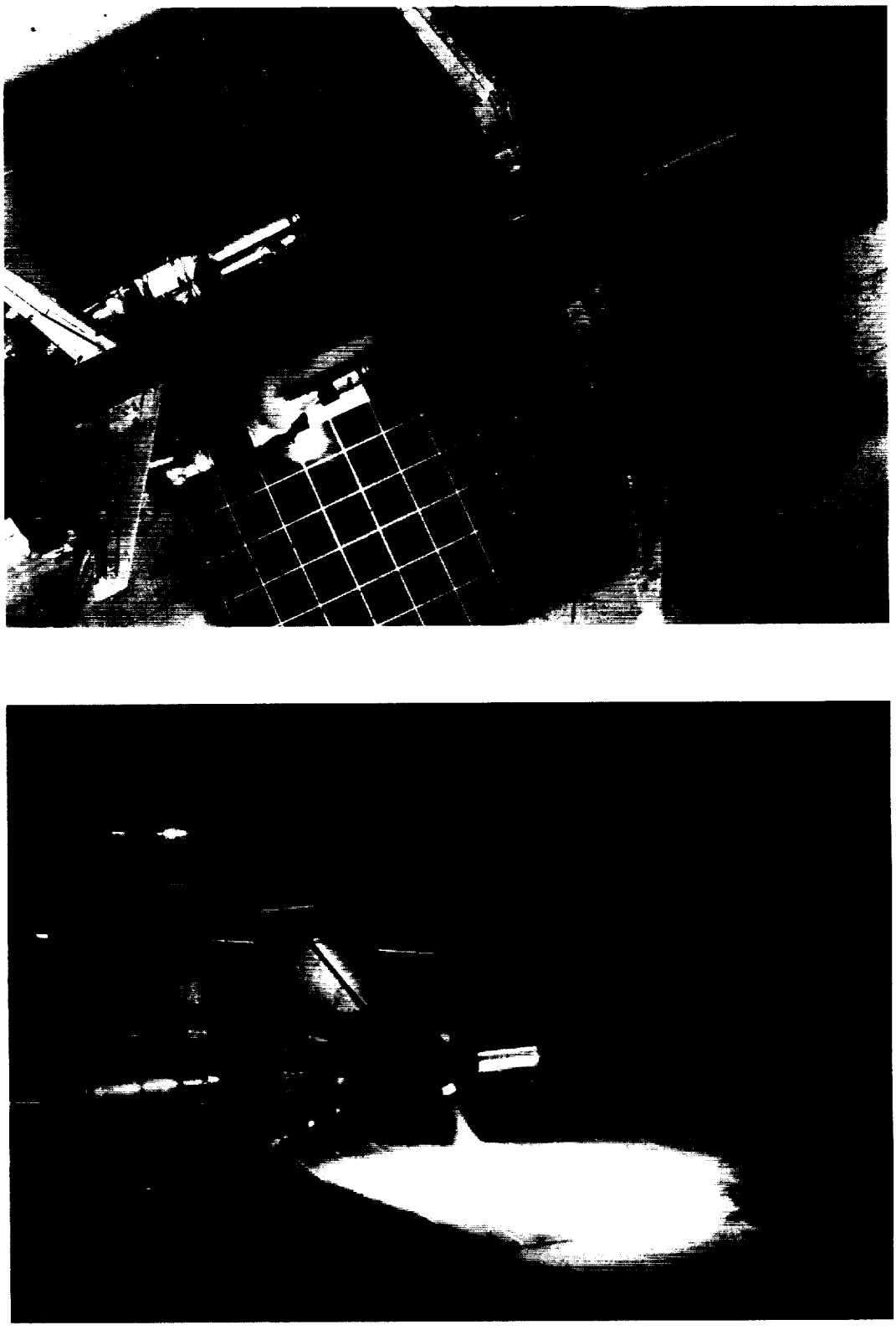

L-88-176

(c) $q_\infty = 1.4$ psf.

Figure 21. Concluded.

L-88-177

(a) $q_\infty = 12.2$ psf.

Figure 22. Vertical laser light sheet with water injection flow visualization for the 15° rotated target thrust reverser. $\dot{m}_R = 2.55$ lb/sec; $\delta_f = 0°$; $\delta_s = 0°$; IGE.

L-88-178

(b) $q_\infty = 5.4$ psf.

Figure 22. Concluded.

L-88-179

Figure 23. Horizontal laser light sheet with water injection flow visualization for configuration I of four-door thrust reverser. $\dot{m}_R = 3.0$ lb/sec; $q_\infty = 12.2$ psf; $\delta_f = 0°$; $\delta_s = 0°$; $h = 7$ in.; lights off; IGE.

L-88-180

(a) Lights off.

L-88-181

(b) Lights on.

Figure 24. Horizontal laser light sheet with water injection flow visualization for configuration I of four-door thrust reverser. $\dot{m}_R = 3.0$ lb/sec; $q_\infty = 5.4$ psf; $\delta_f = 0°$; $\delta_s = 0°$; $h = 7$ in.; IGE.

L-88-182

(a) Lights off.

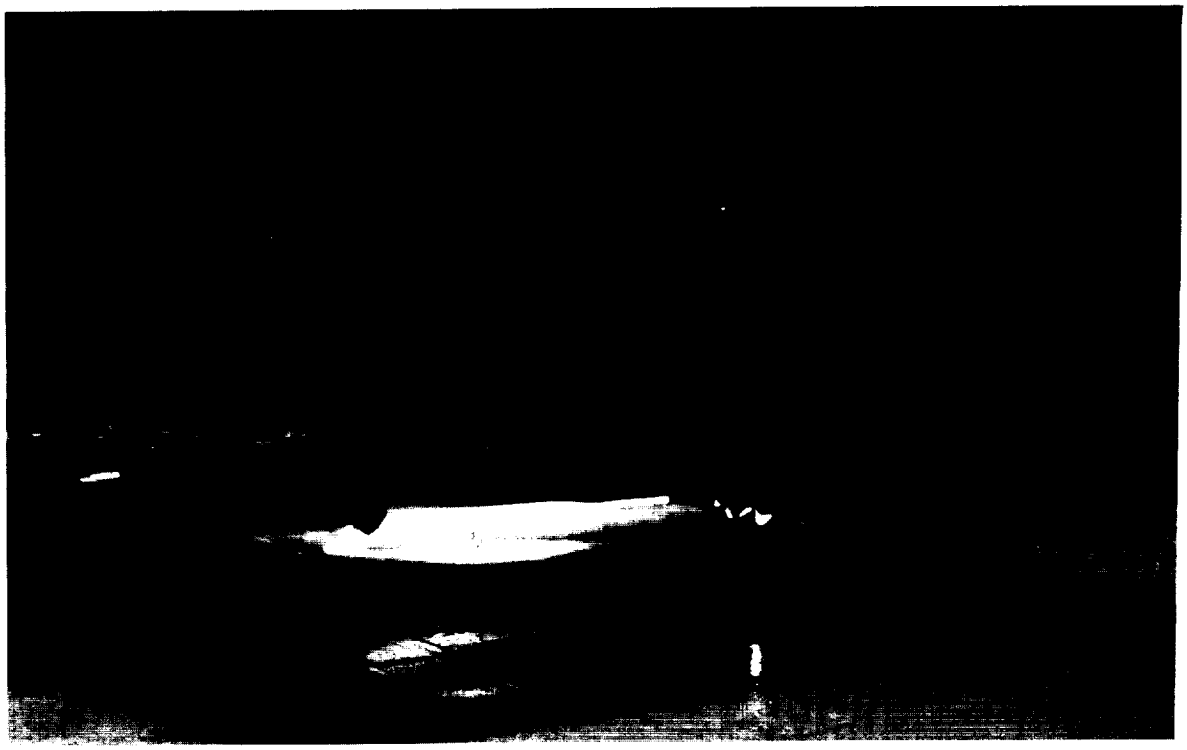

L-88-183

(b) Lights on.

Figure 25. Horizontal laser light sheet with water injection flow visualization for configuration I of four-door thrust reverser. $\dot{m}_R = 3.0$ lb/sec; $q_\infty = 1.4$ psf; $\delta_f = 0°$; $\delta_s = 0°$; $h = 7$ in.; IGE.

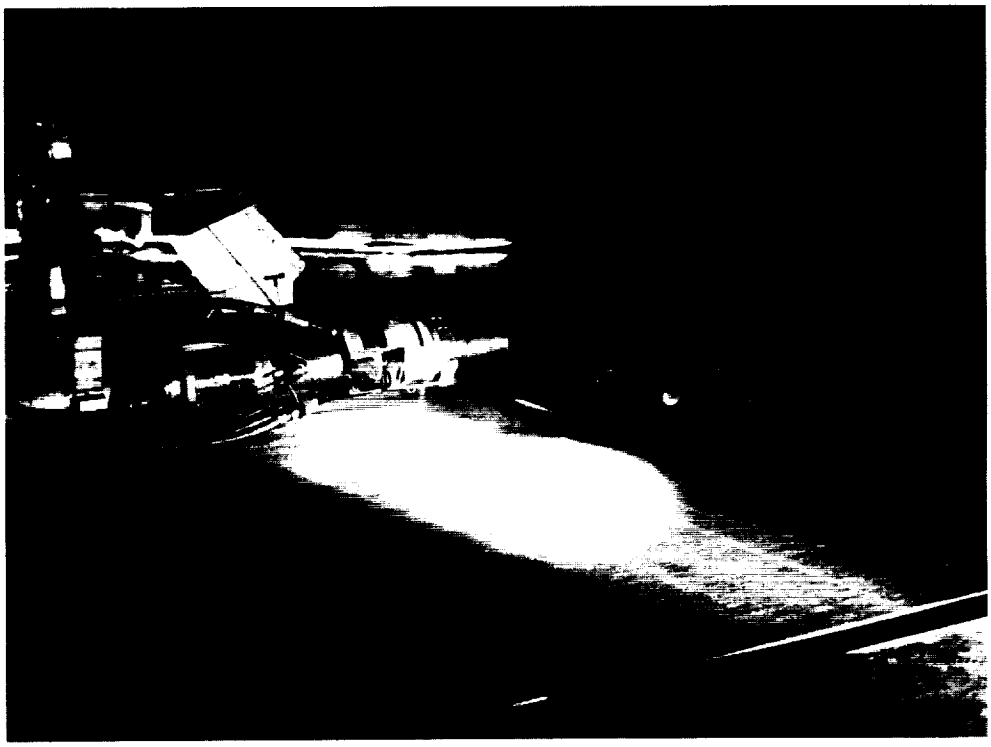

L-88-184

Figure 26. Horizontal laser light sheet with smoke injection flow visualization for cascade thrust reverser. $\dot{m}_R = 1.15$ lb/sec; $q_\infty = 0.7$ psf; $\delta_f = 40°$; $\delta_s = 60°$; $h = 1.5$ in.; IGE.

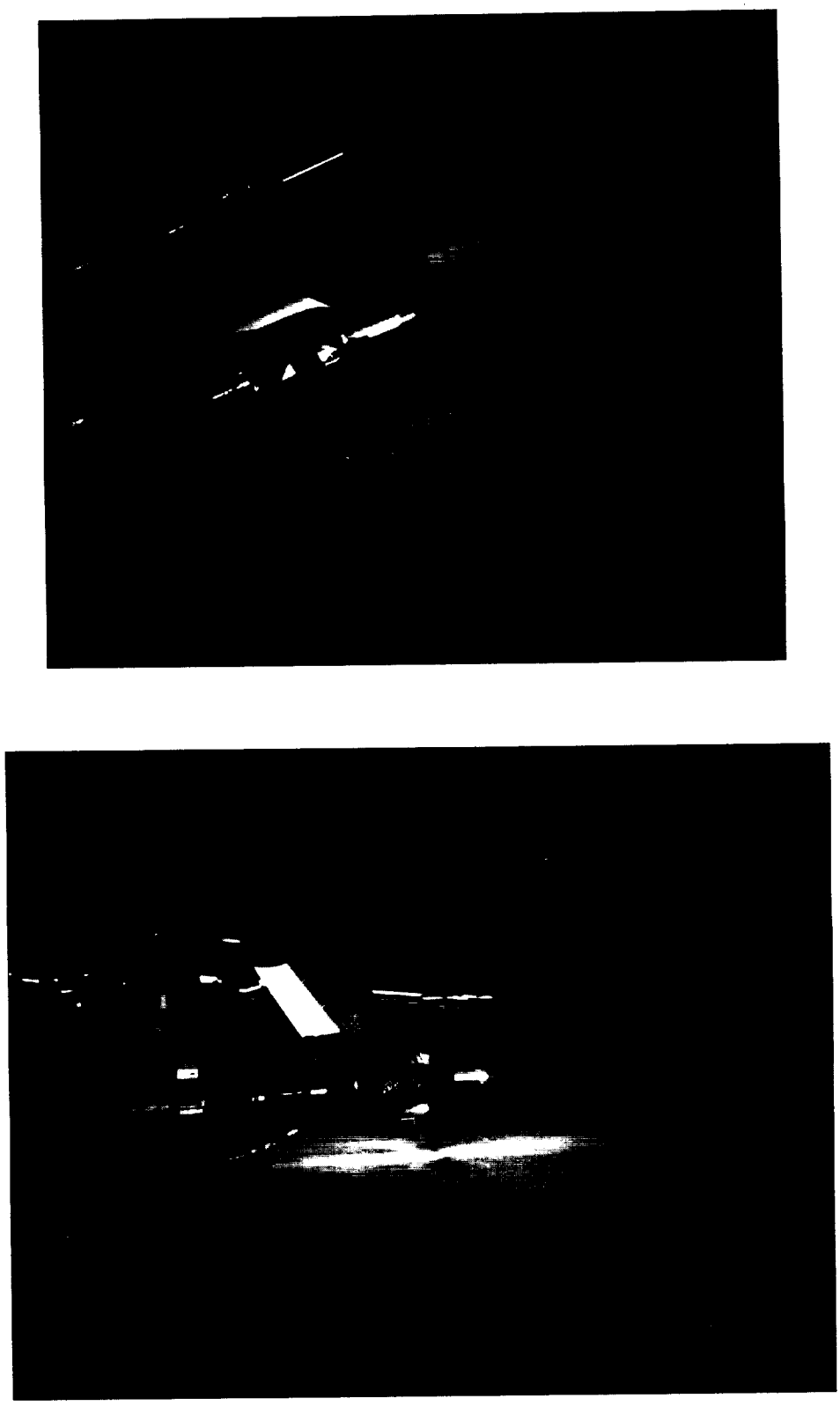

L-88-185

(a) $\dot{m}_R = 2.55$ lb/sec; $q_\infty = 1.4$ psf.

Figure 27. Horizontal laser light sheet with smoke injection flow visualization for 0° rotated target thrust reverser. $\delta_f = 40°$; $\delta_s = 60°$; $h = 1.5$ in.; IGE.

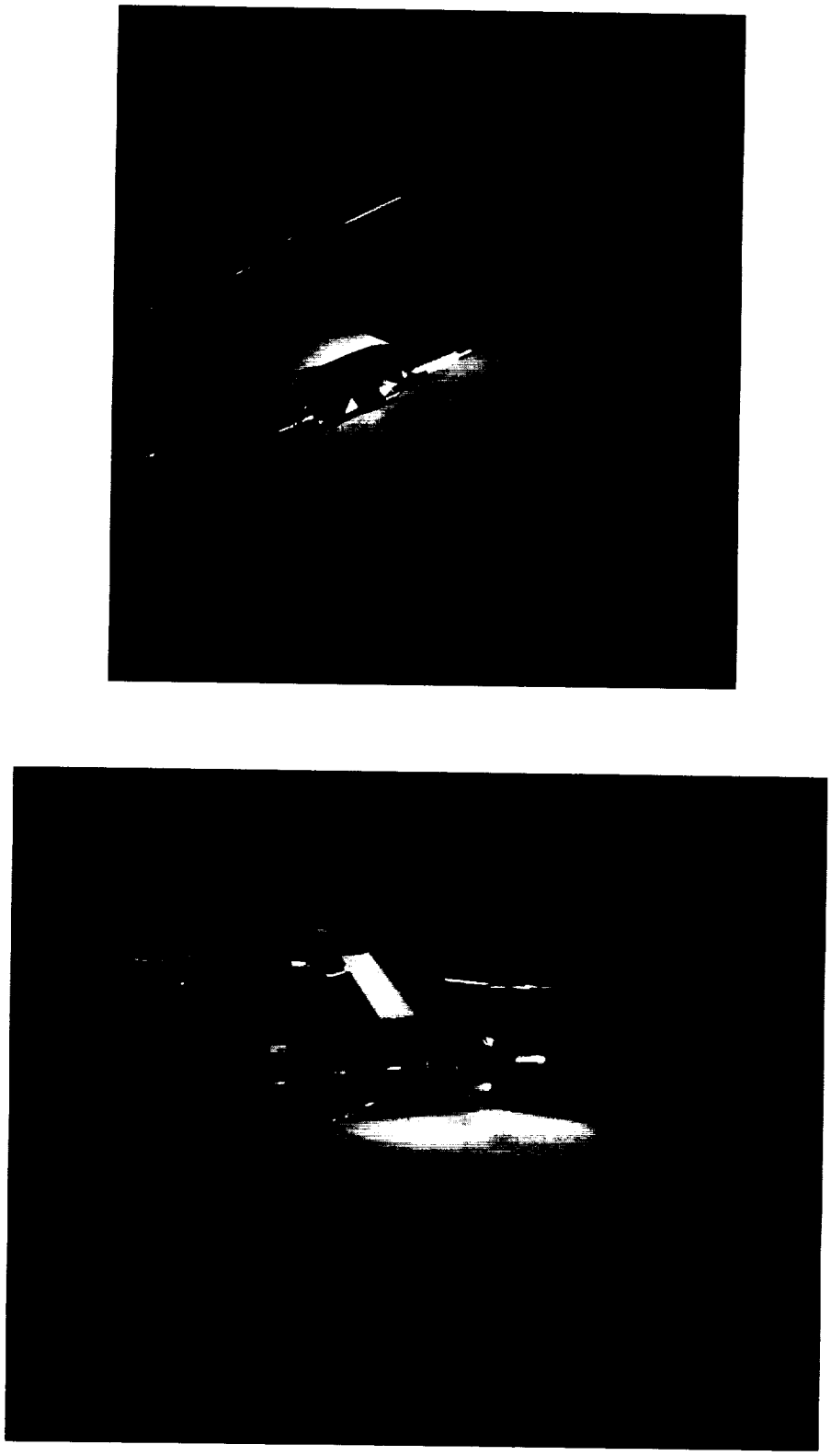

L-88-186

(b) $\dot{m}_R = 1.15$ lb/sec; $q_\infty = 1.4$ psf.

Figure 27. Continued.

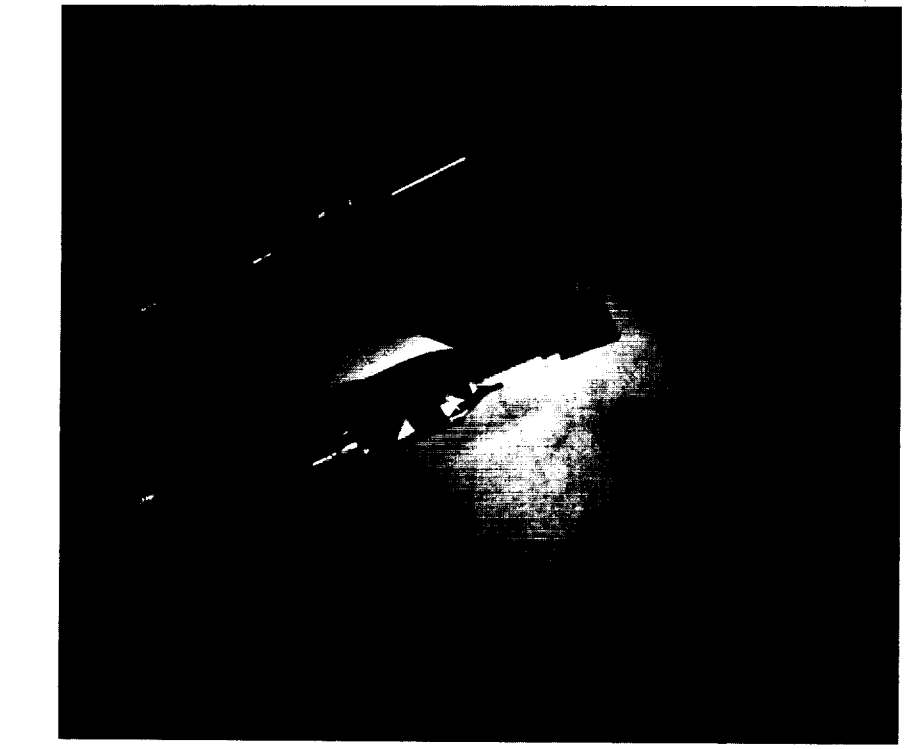

L-88-187

(c) $\dot{m}_R = 1.15$ lb/sec; $q_\infty = 0.7$ psf.

Figure 27. Continued.

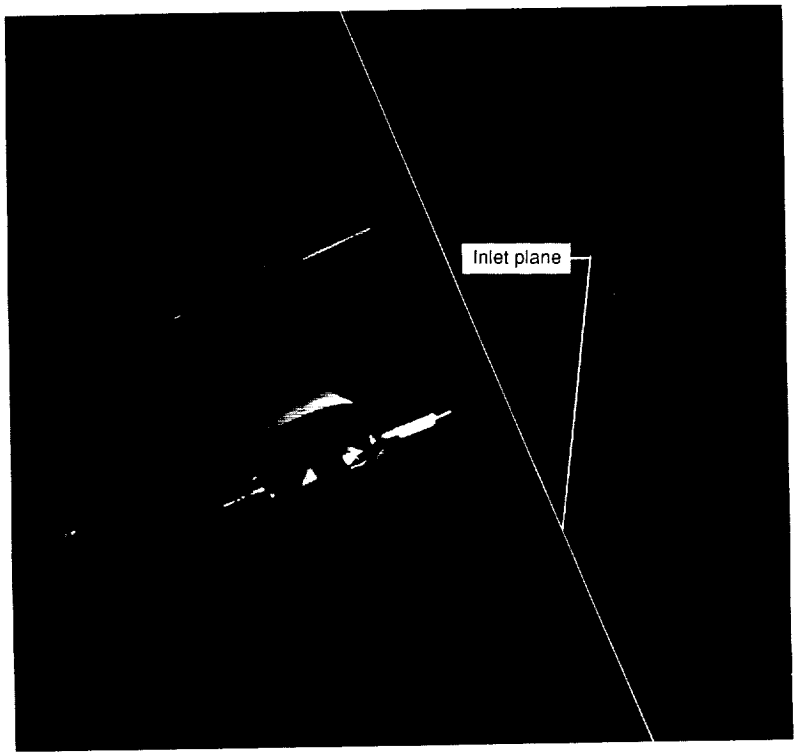


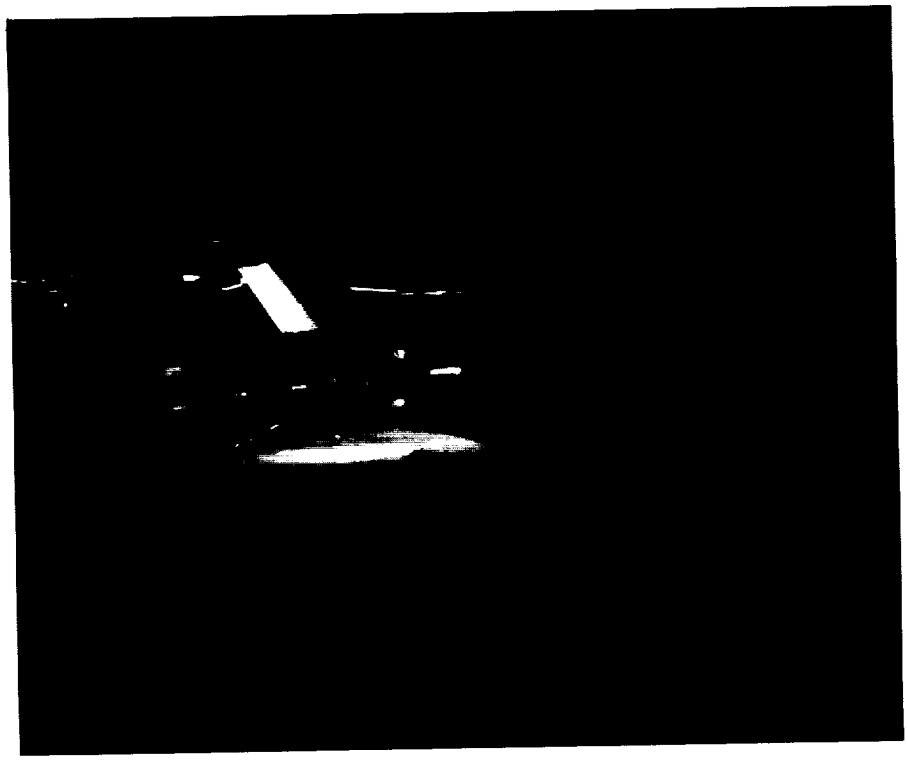

L-88-188

(d) $\dot{m}_R = 0.80$ lb/sec; $q_\infty = 1.4$ psf.

Figure 27. Continued.

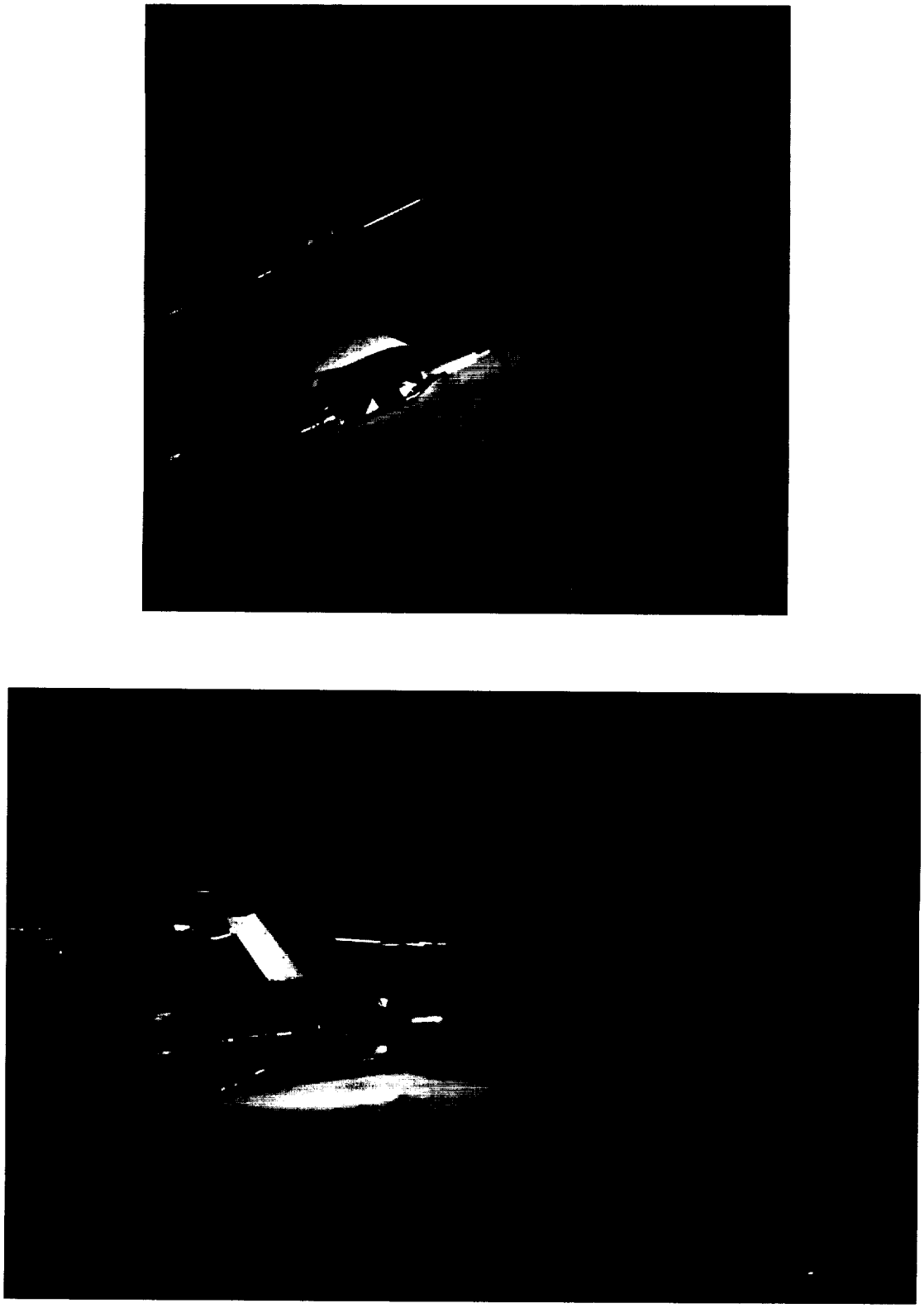

L-88-189

(e) $\dot{m}_R = 0.80$ lb/sec; $q_\infty = 0.7$ psf.

Figure 27. Concluded.

L-88-190

(a) $\dot{m}_R = 2.55$ lb/sec; $q_\infty = 1.4$ psf.

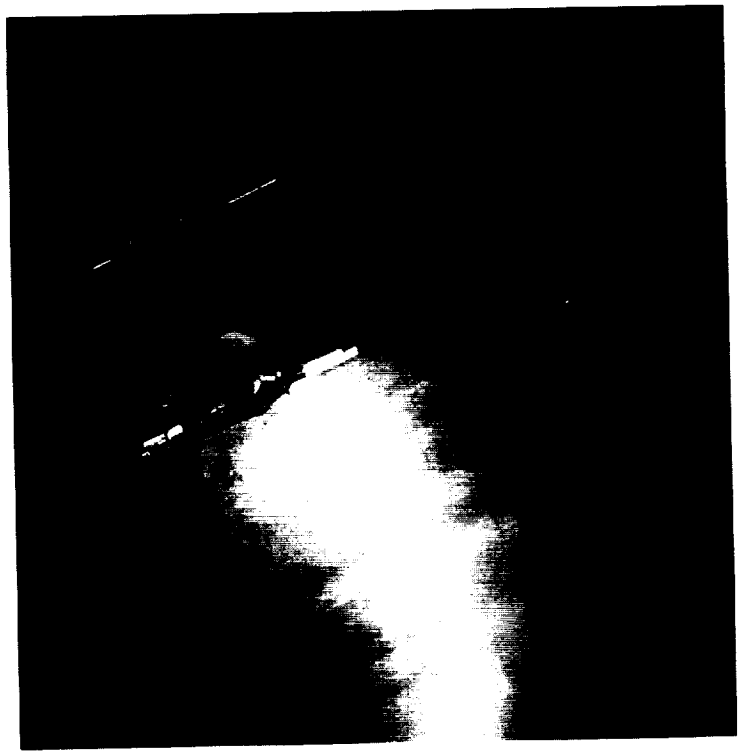

L-88-191

(b) $\dot{m}_R = 2.55$ lb/sec; $q_\infty = 0.7$ psf.

Figure 28. Horizontal laser light sheet with smoke injection flow visualization for 22.5° rotated target thrust reverser. $\delta_f = 40°$; $\delta_s = 60°$; $h = 1.5$ in.; IGE.

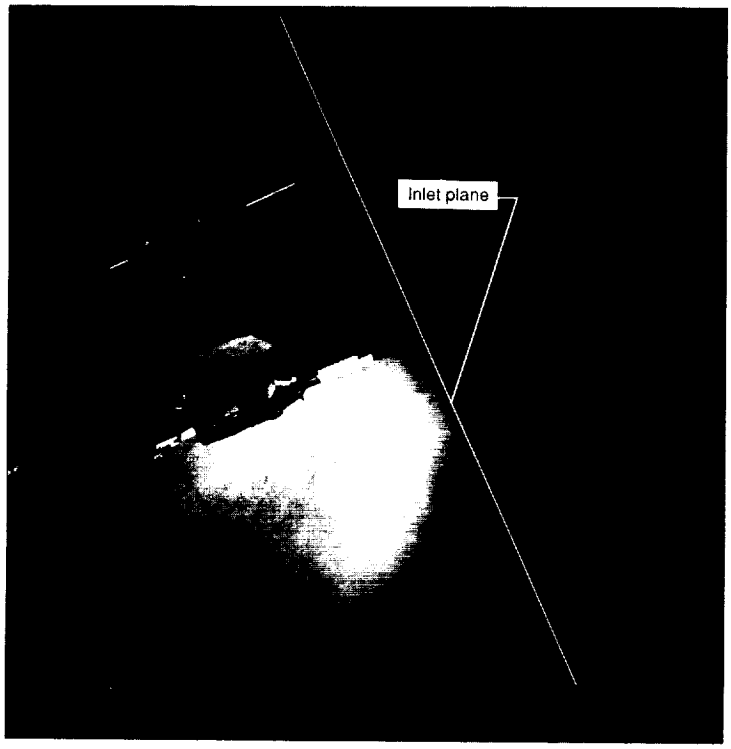


L-88-192

(c) $\dot{m}_R = 1.15$ lb/sec; $q_\infty = 1.4$ psf.

L-88-193

(d) $\dot{m}_R = 1.15$ lb/sec; $q_\infty = 0.7$ psf.

Figure 28. Continued.


L-88-194

(e) $\dot{m}_R = 0.80$ lb/sec; $q_\infty = 1.4$ psf.

L-88-195

(f) $\dot{m}_R = 0.80$ lb/sec; $q_\infty = 0.7$ psf.

Figure 28. Concluded.

L-88-196

Figure 29. Horizontal laser light sheet with smoke injection flow visualization for configuration III of four-door thrust reverser. $\dot{m}_R = 0.80$ lb/sec; $q_\infty = 0.7$ psf; $\delta_f = 40°$; $\delta_s = 60°$; $h = 1.5$ in.; IGE.

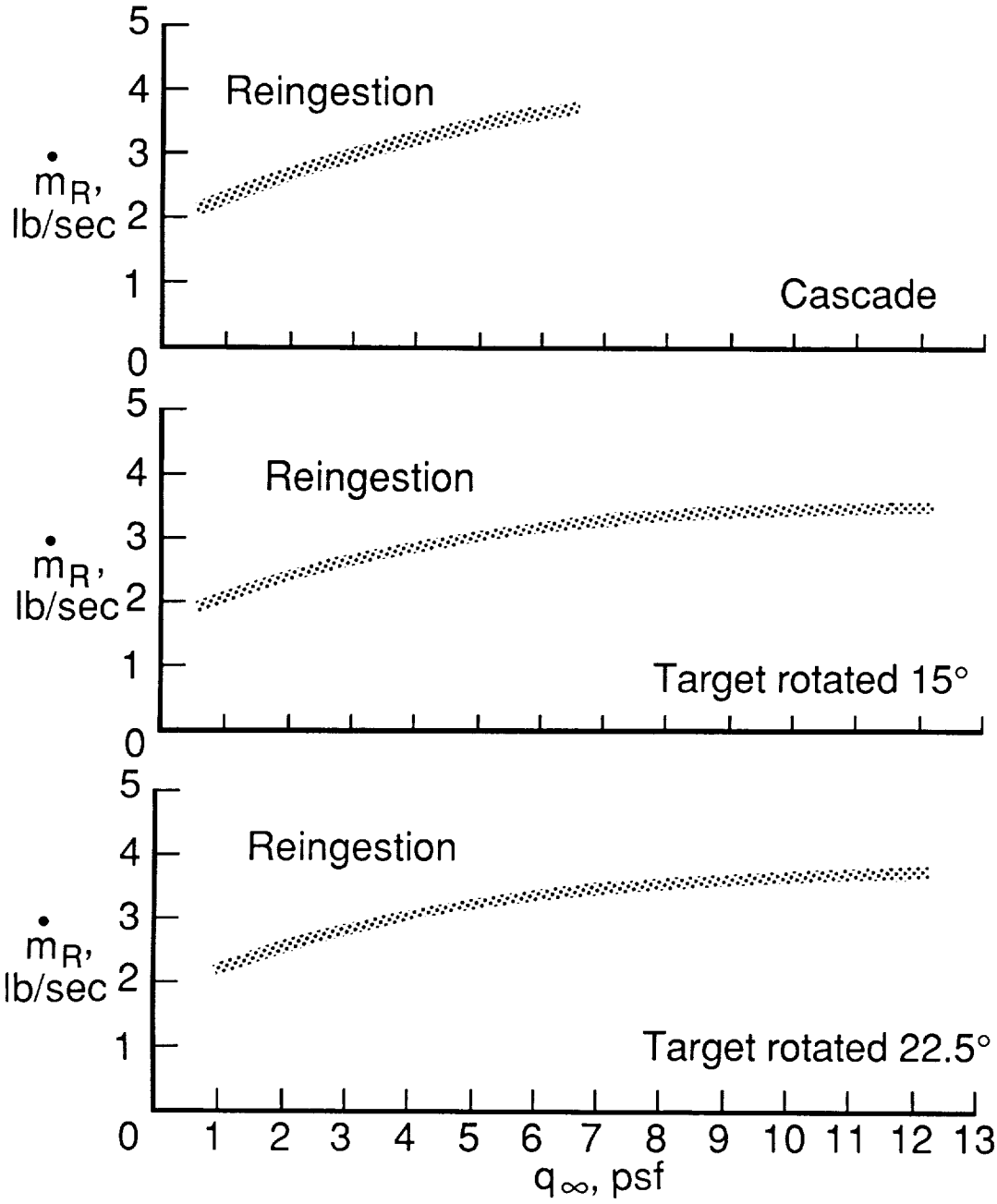


(a) Reingestion boundaries for cascade and target thrust reverser configurations with respect to $\dot{m}_R$ and $q_\infty$.

Figure 30. Boundaries representing onset of reingestion as based on flow visualization. $\delta_f = 40°$; $\delta_s = 60°$; IGE.

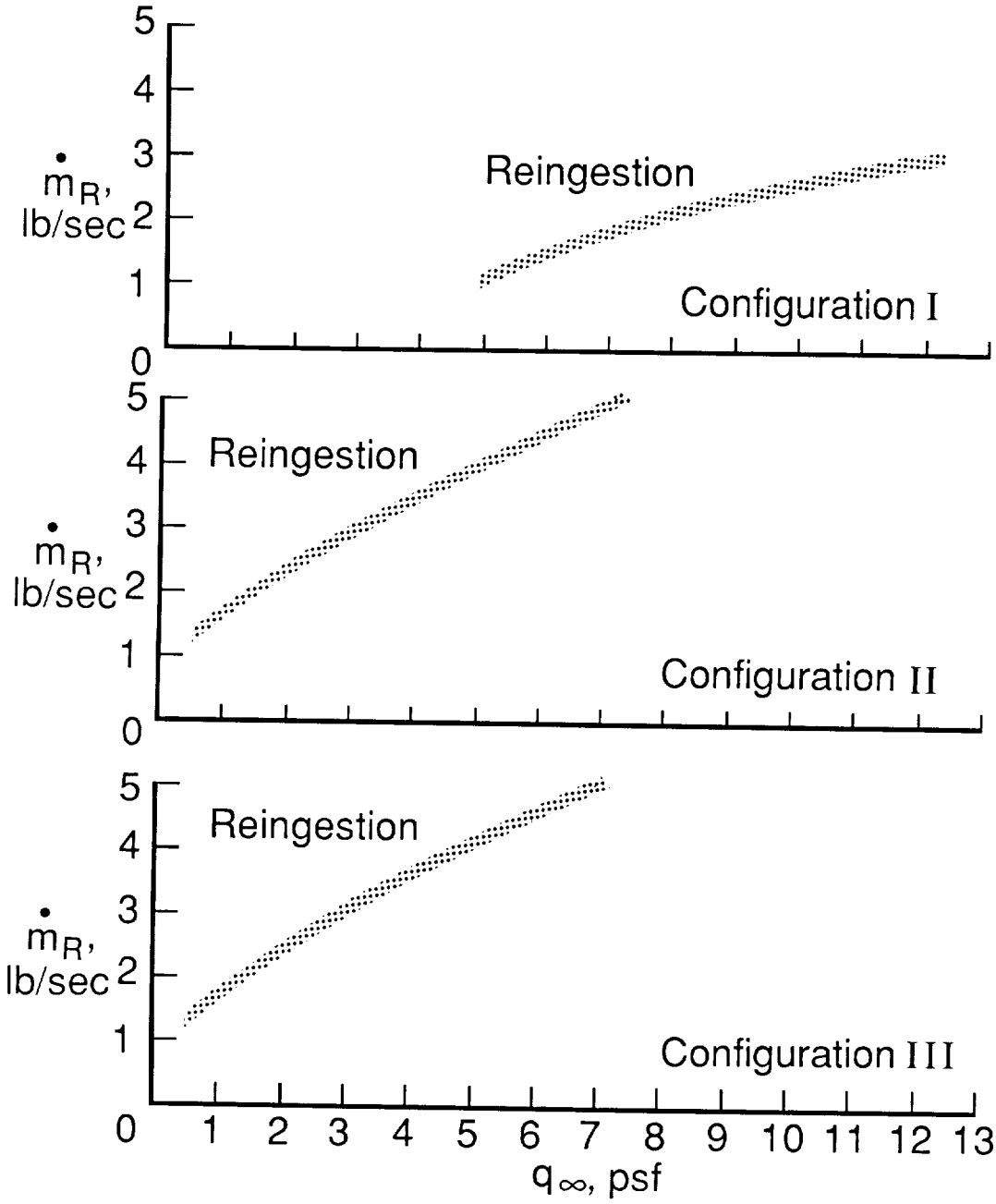


(b) Reingestion boundaries for four-door thrust reverser configurations with respect to $\dot{m}_R$ and $q_\infty$.

Figure 30. Concluded.

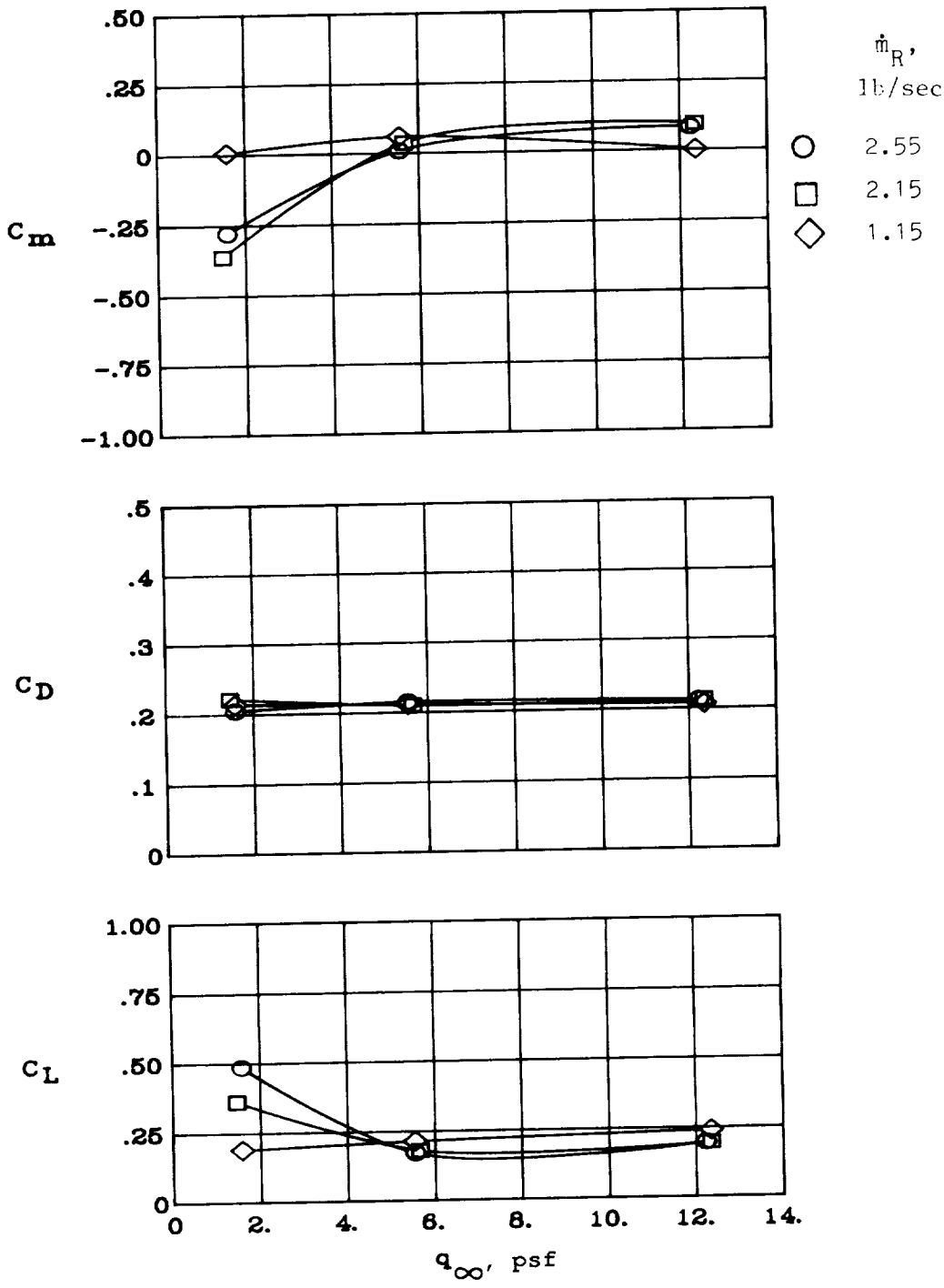


Figure 31. Variation of longitudinal aerodynamic coefficients with reverser flow rate and free-stream dynamic pressure for cascade configuration. $\delta_f = 40°$; $\delta_s = 60°$; IGE.

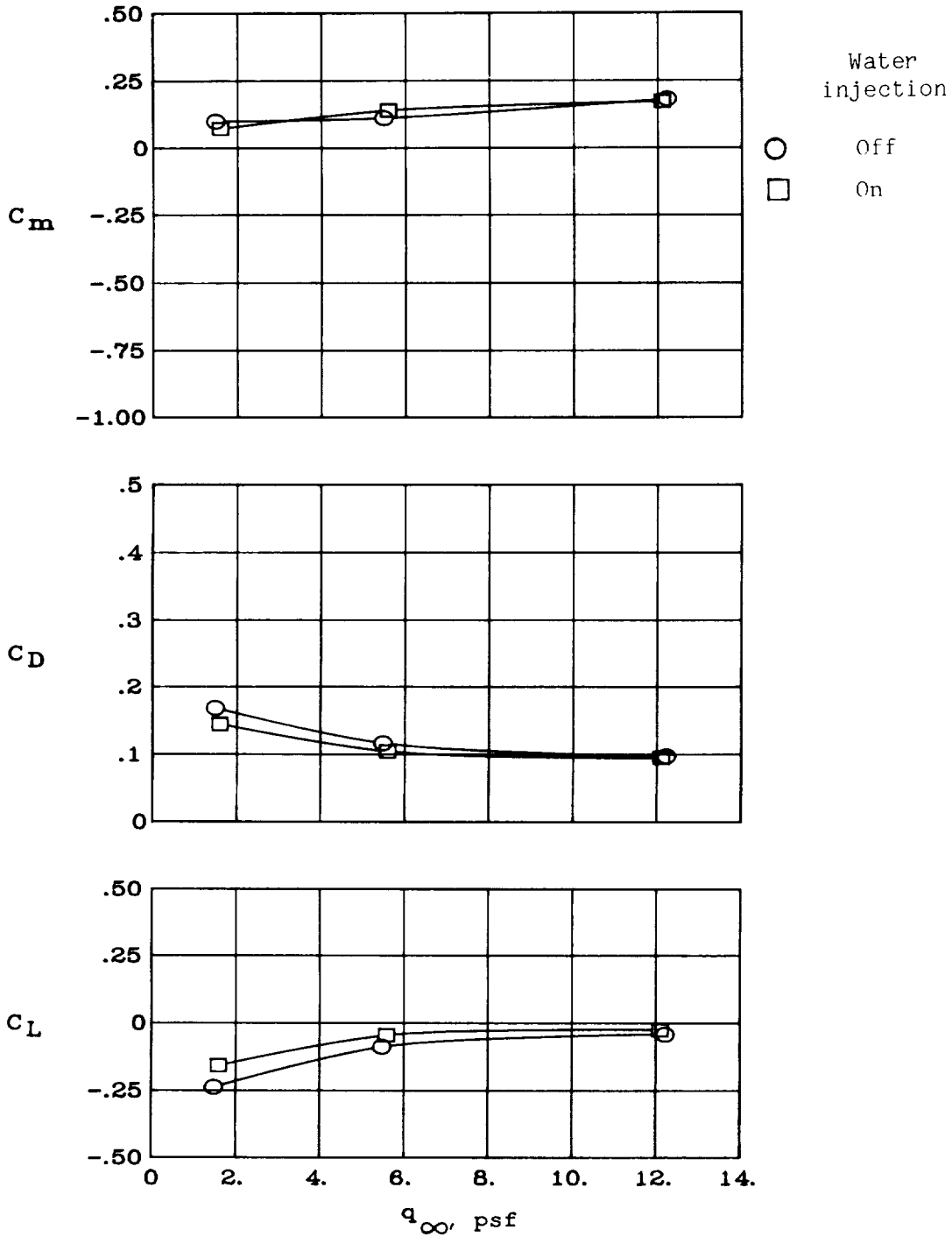


Figure 32. Effects of water injection into reversed flow on cascade configuration. $\dot{m}_R = 2.55$ lb/sec; $\delta_f = 40°$; $\delta_s = 60°$; OGE.

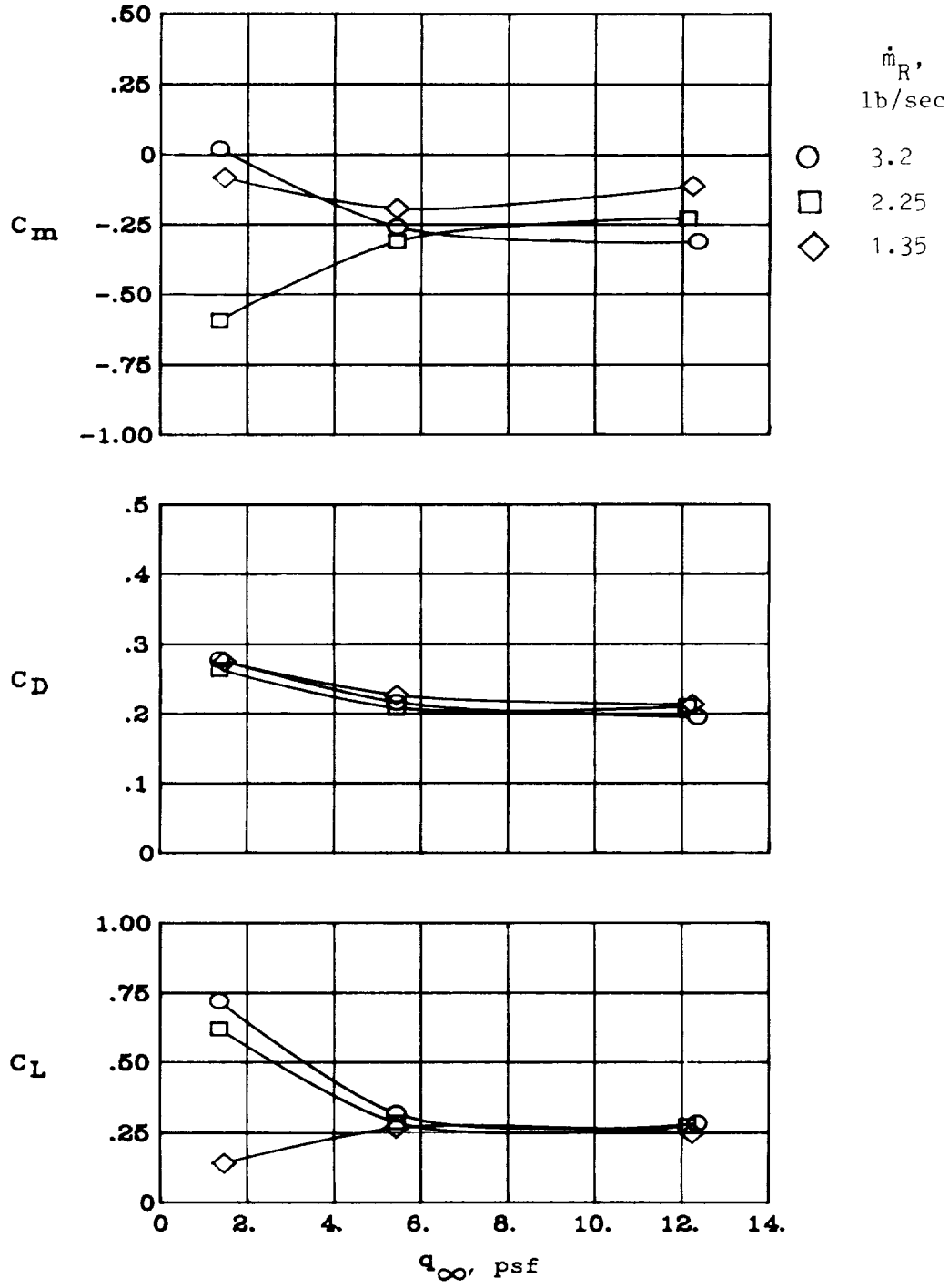


Figure 33. Variation of longitudinal aerodynamic coefficients with reverser flow rate and free-stream dynamic pressure for 22.5° rotated target configuration. $\delta_f = 40°$; $\delta_s = 60°$; IGE.

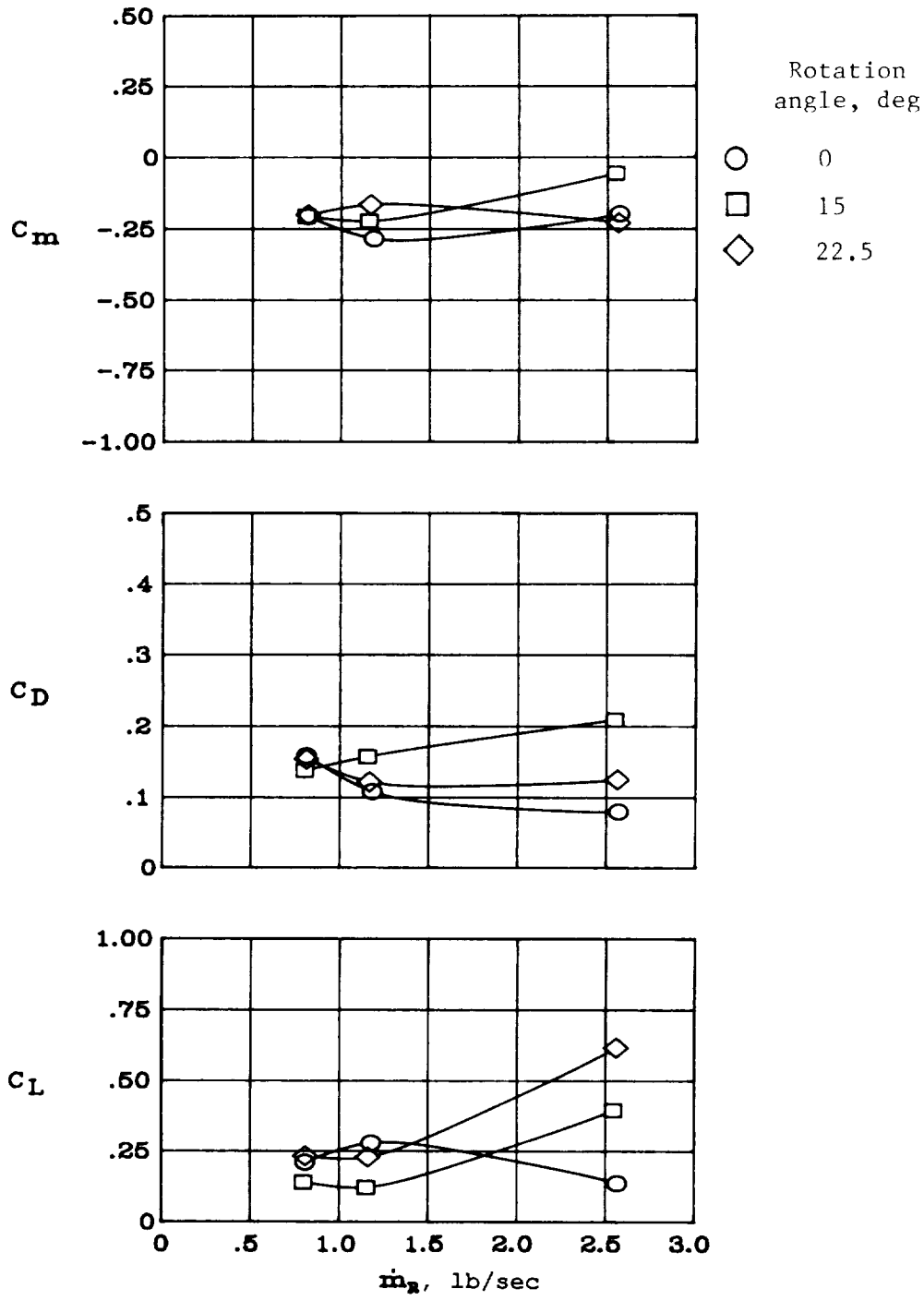


Figure 34. Effects of rotation angle on longitudinal aerodynamics of target configuration. $q_\infty = 1.4$ psf; $\delta_f = 40°$; $\delta_s = 60°$; IGE.

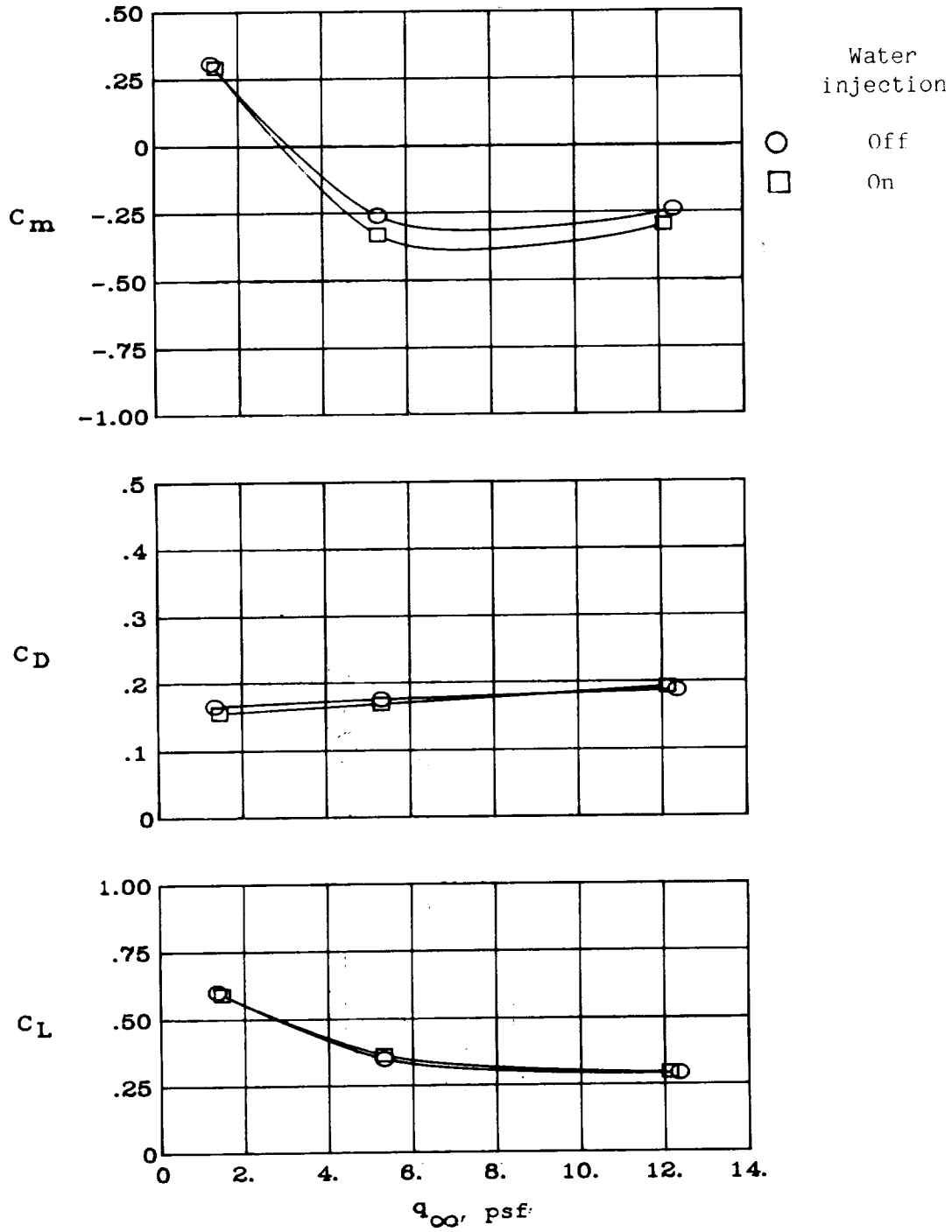


Figure 35. Effects of water injection into reversed flow on 15° rotated target configuration. $\dot{m}_R = 3.2$ lb/sec; $\delta_f = 40°$; $\delta_s = 60°$; IGE.

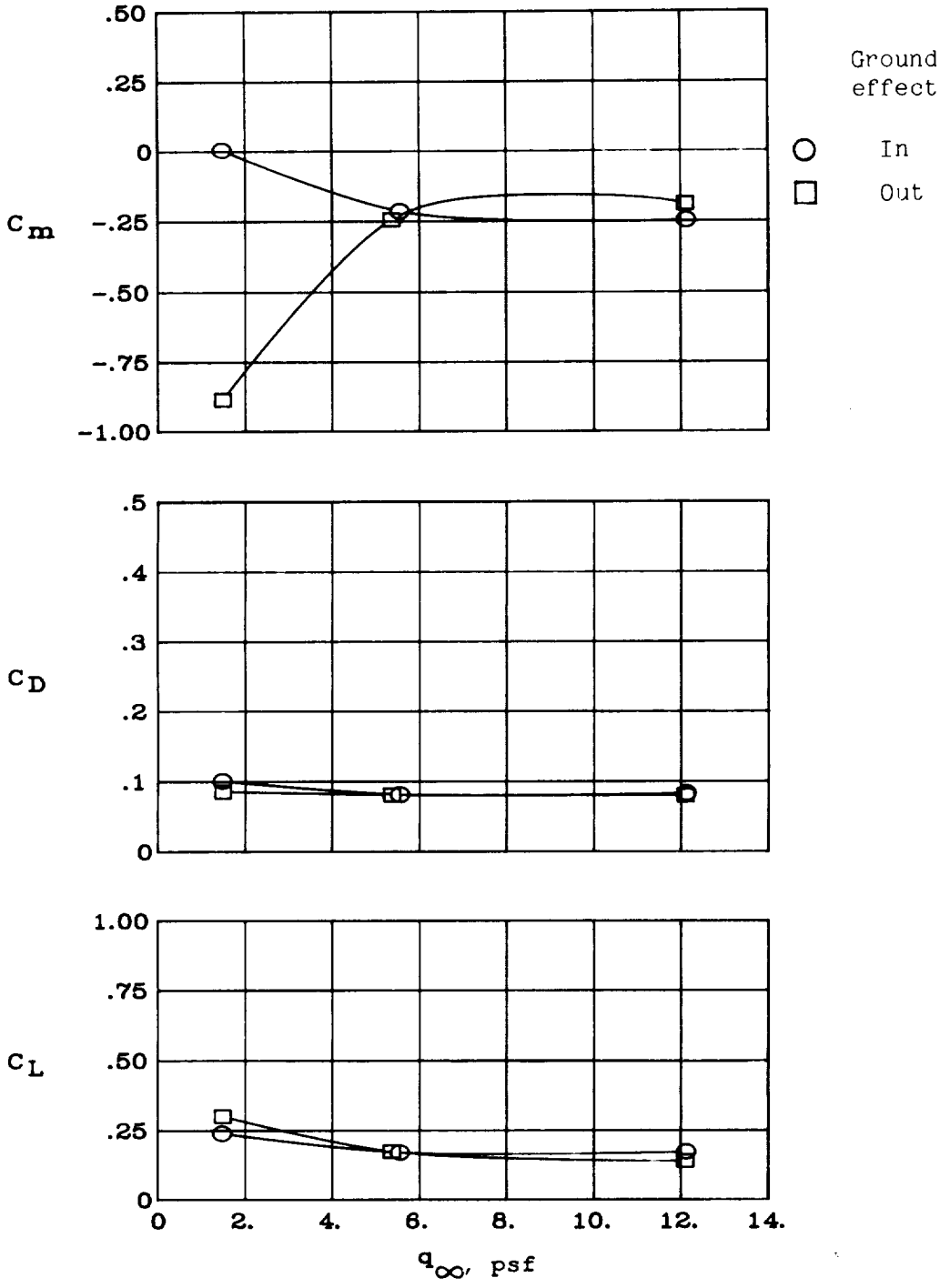


Figure 36. Variation of longitudinal aerodynamic coefficients in and out of ground effect for 15° rotated target configuration with $\dot{m}_R = 2.55$ lb/sec. $\delta_f = 40°; \delta_s = 60°$.

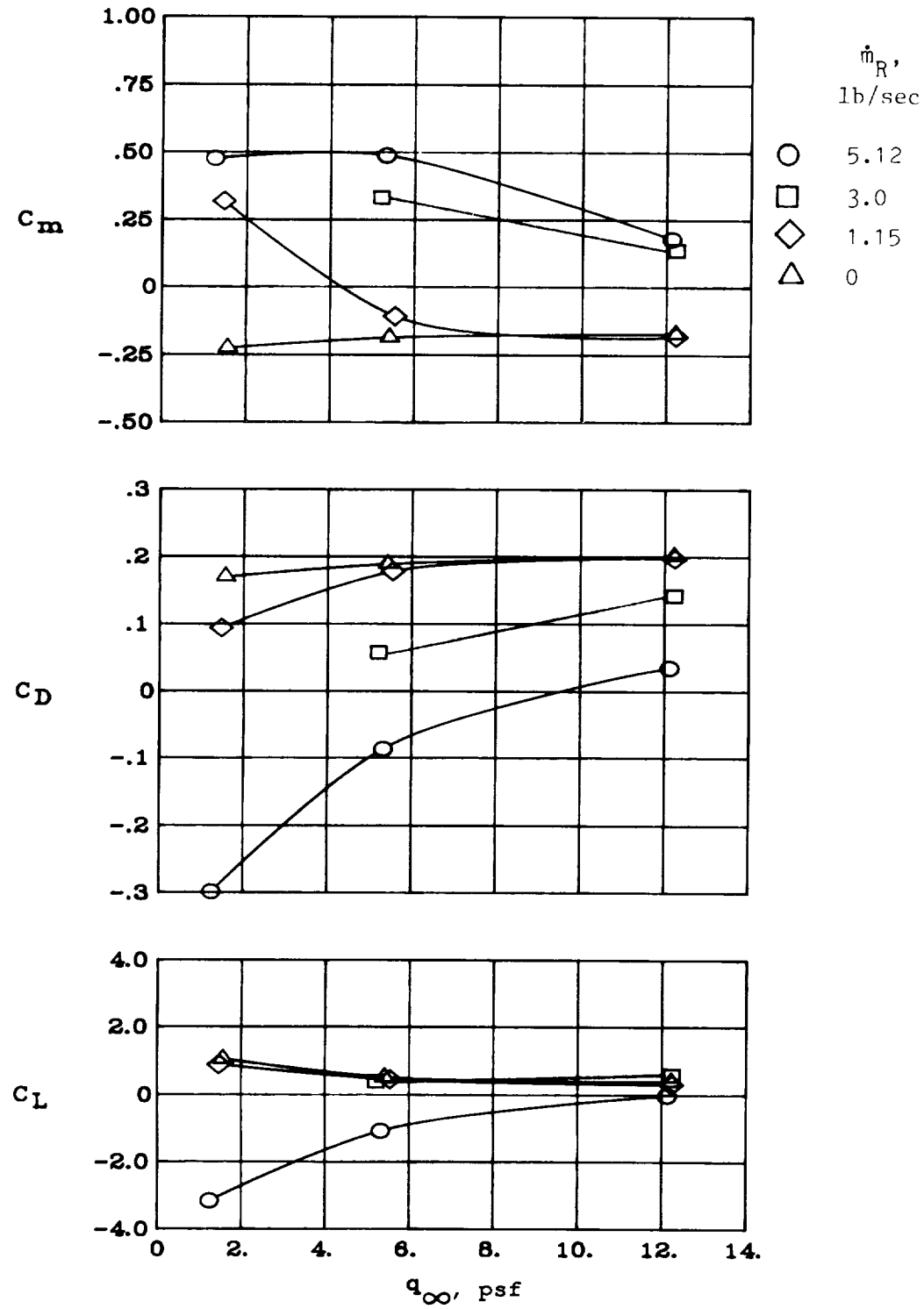


Figure 37. Variation of longitudinal aerodynamic coefficients with reverser flow rate and free-stream dynamic pressure for configuration I of four-door thrust reverser. $\delta_f = 40°$; $\delta_s = 60°$; IGE.

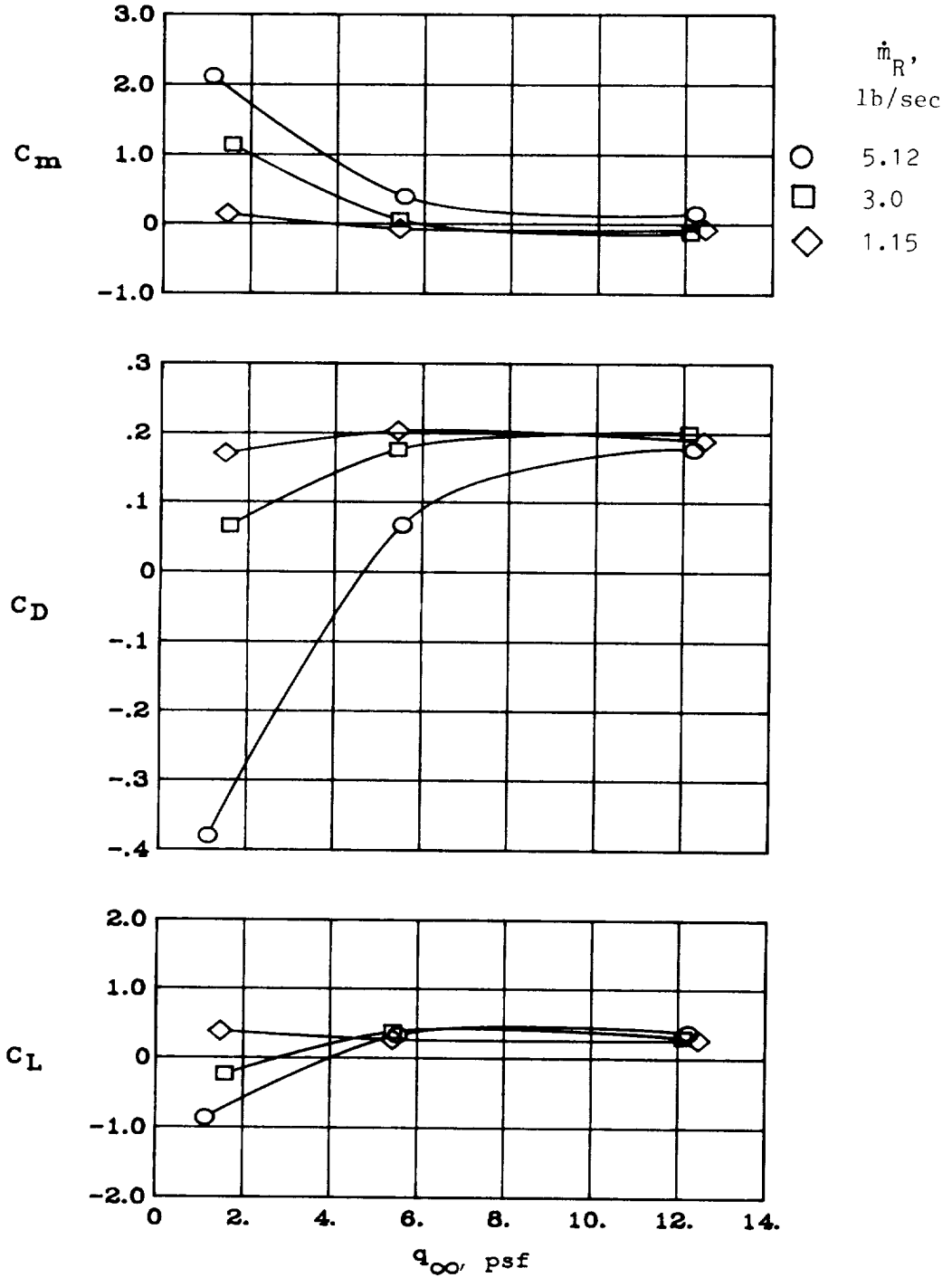


Figure 38. Variation of longitudinal aerodynamic coefficients with reverser flow rate and free-stream dynamic pressure for configuration II of four-door thrust reverser. $\delta_f = 40°; \delta_s = 60°$; IGE.

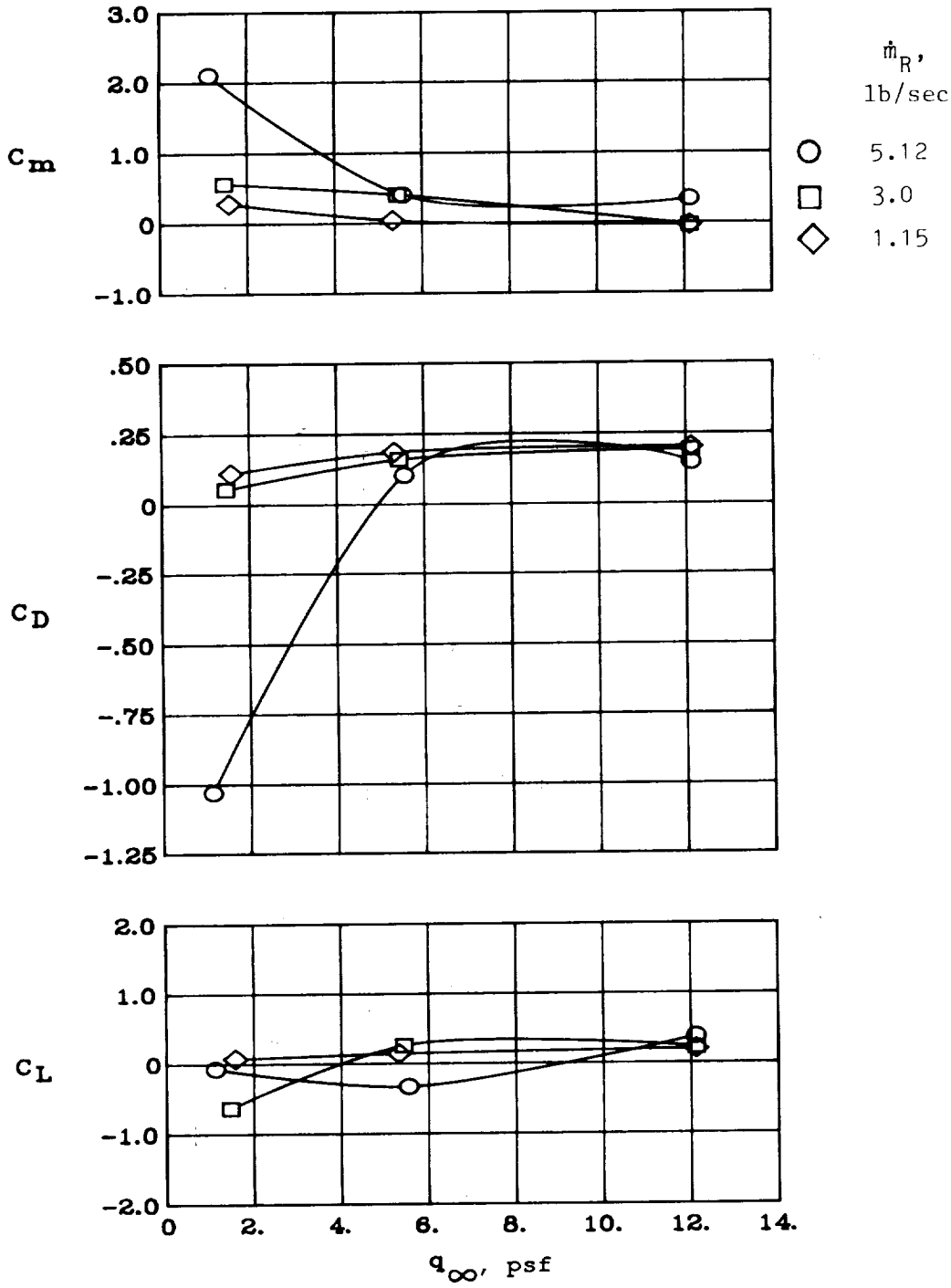


Figure 39. Variation of longitudinal aerodynamic coefficients with reverser flow rate and free-stream dynamic pressure for configuration III of four-door thrust reverser. $\delta_f = 40°$; $\delta_s = 60°$; IGE.

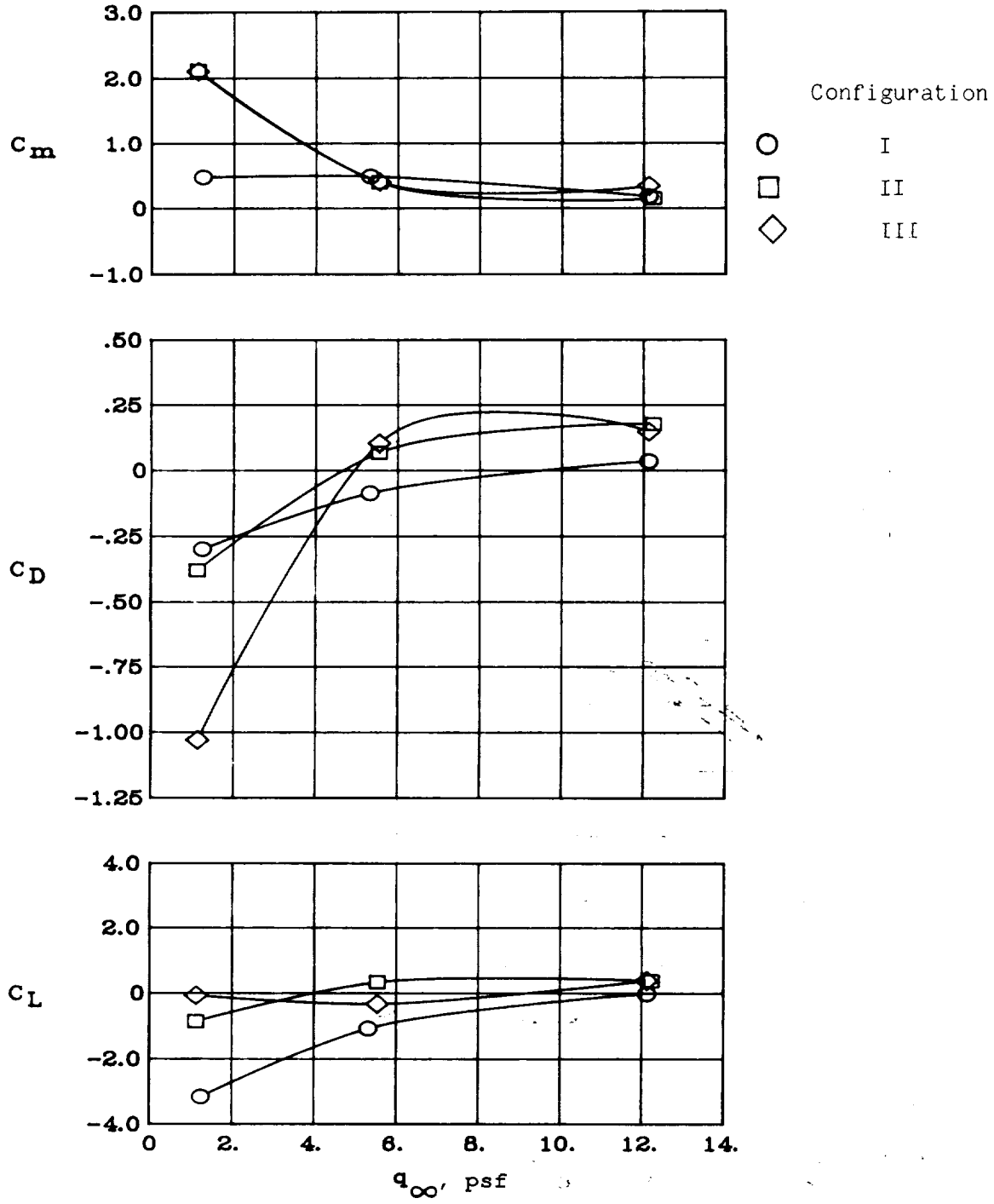


Figure 40. Comparison of four-door configurations. $\dot{m}_R = 5.12$ lb/sec; $\delta_f = 40°$; $\delta_s = 60°$; IGE.

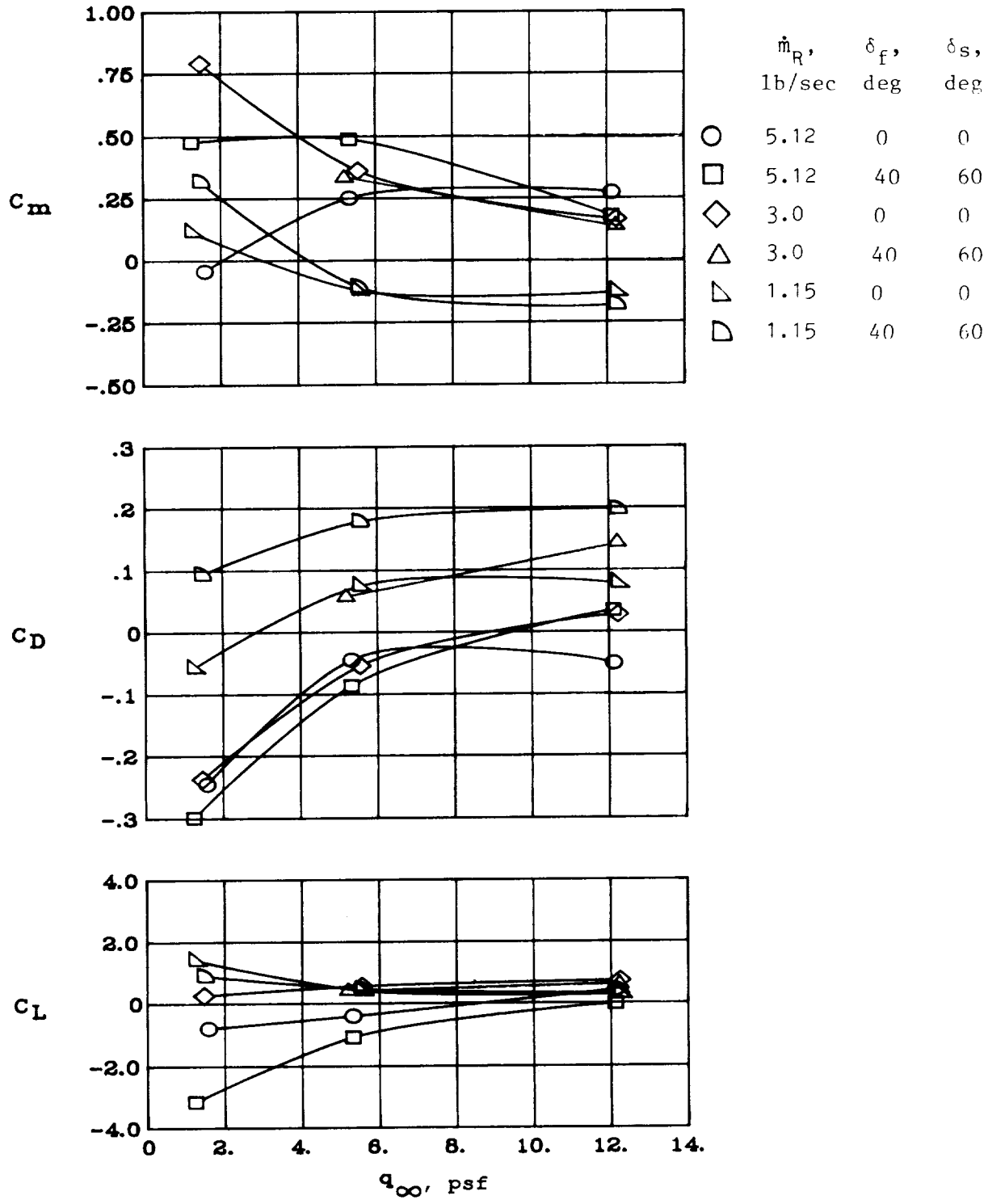


Figure 41. Effects of flaps and spoilers deflected on configuration I of four-door thrust reverser. IGE.

L-88-197

(a) Fixed ground plane.

L-88-198

(b) Moving-belt ground plane.

Figure 42. Horizontal laser light sheet with smoke injection flow visualization for cascade thrust reverser. $\dot{m}_R = 1.15$ lb/sec; $q_\infty = 0.7$ psf; $\delta_f = 40°$; $\delta_s = 60°$; $h = 1.5$ in.; IGE.

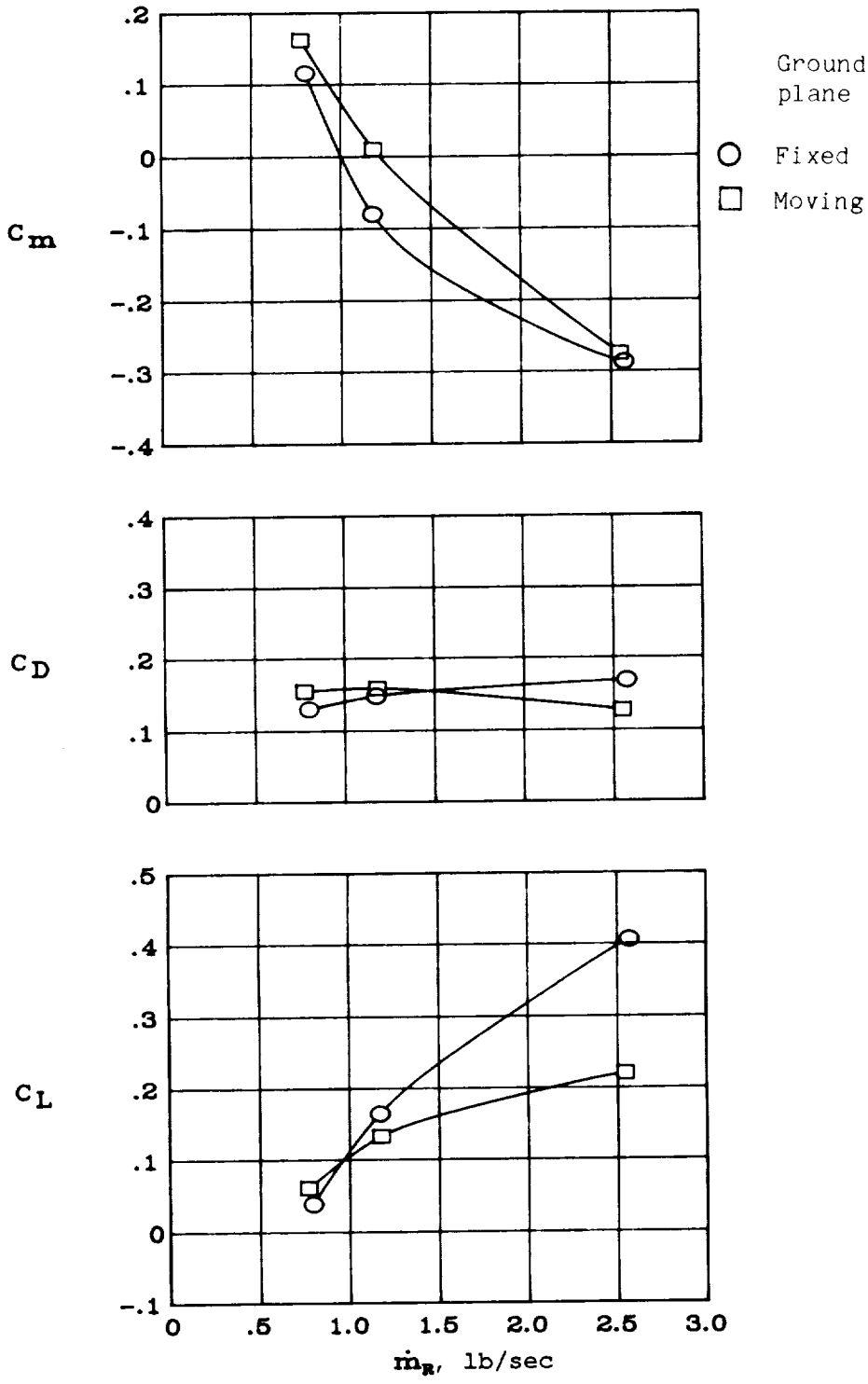


Figure 43. Fixed versus moving-belt ground plane for cascade thrust reverser. $q_\infty = 1.4$ psf; $\delta_f = 40°$; $\delta_s = 60°$; IGE.

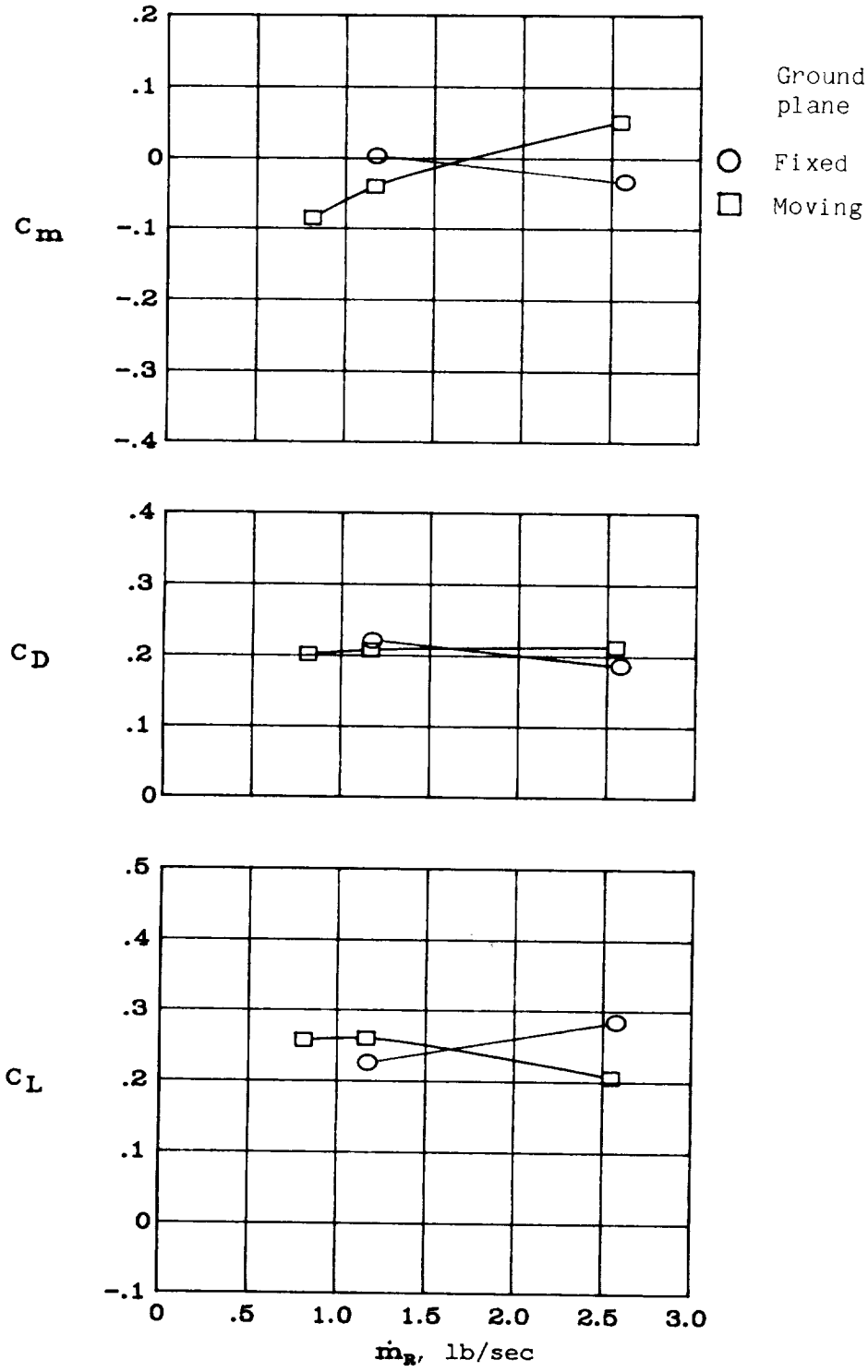


Figure 44. Fixed versus moving-belt ground plane for cascade thrust reverser. $q_\infty = 12.2$ psf; $\delta_f = 40°$; $\delta_s = 60°$; IGE.

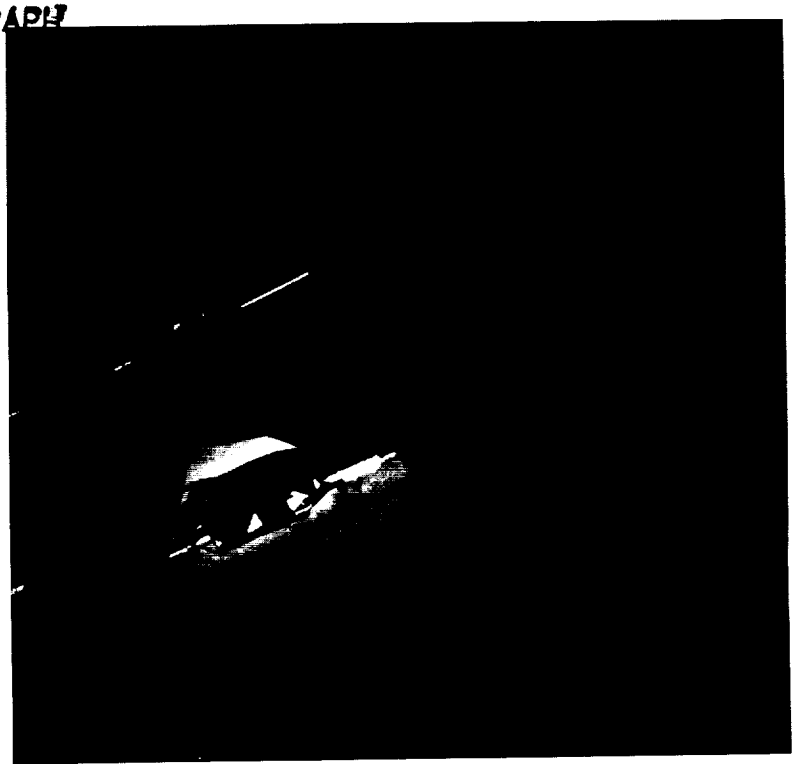

L-88-199

(a) Fixed ground plane.

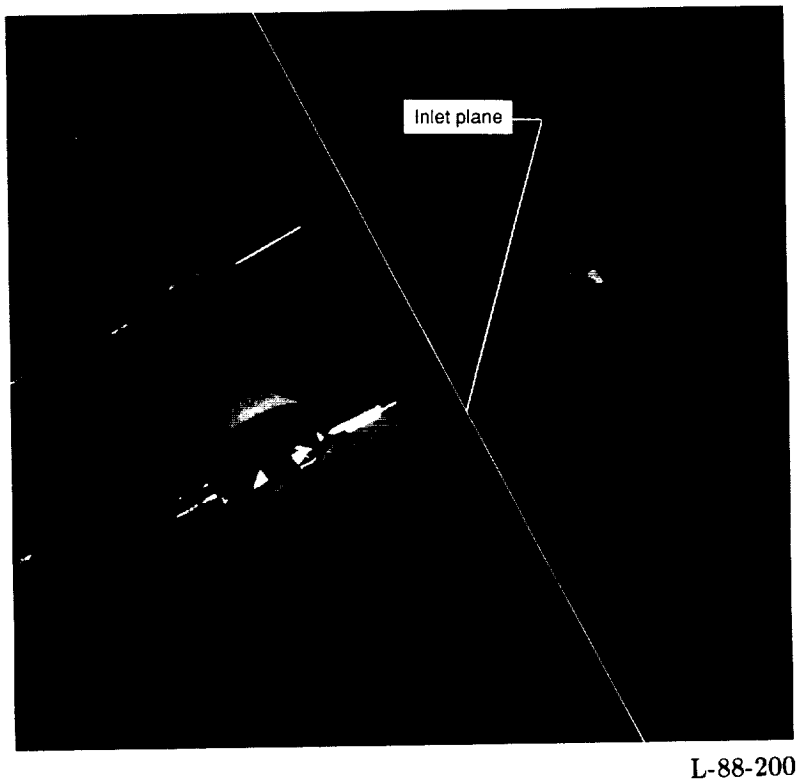


L-88-200

(b) Moving-belt ground plane.

Figure 45. Horizontal laser light sheet with smoke injection flow visualization for 0° rotated target thrust reverser. $\dot{m}_R = 0.80$ lb/sec; $q_\infty = 0.7$ psf; $\delta_f = 40°$; $\delta_s = 60°$; $h = 1.5$ in.; IGE.

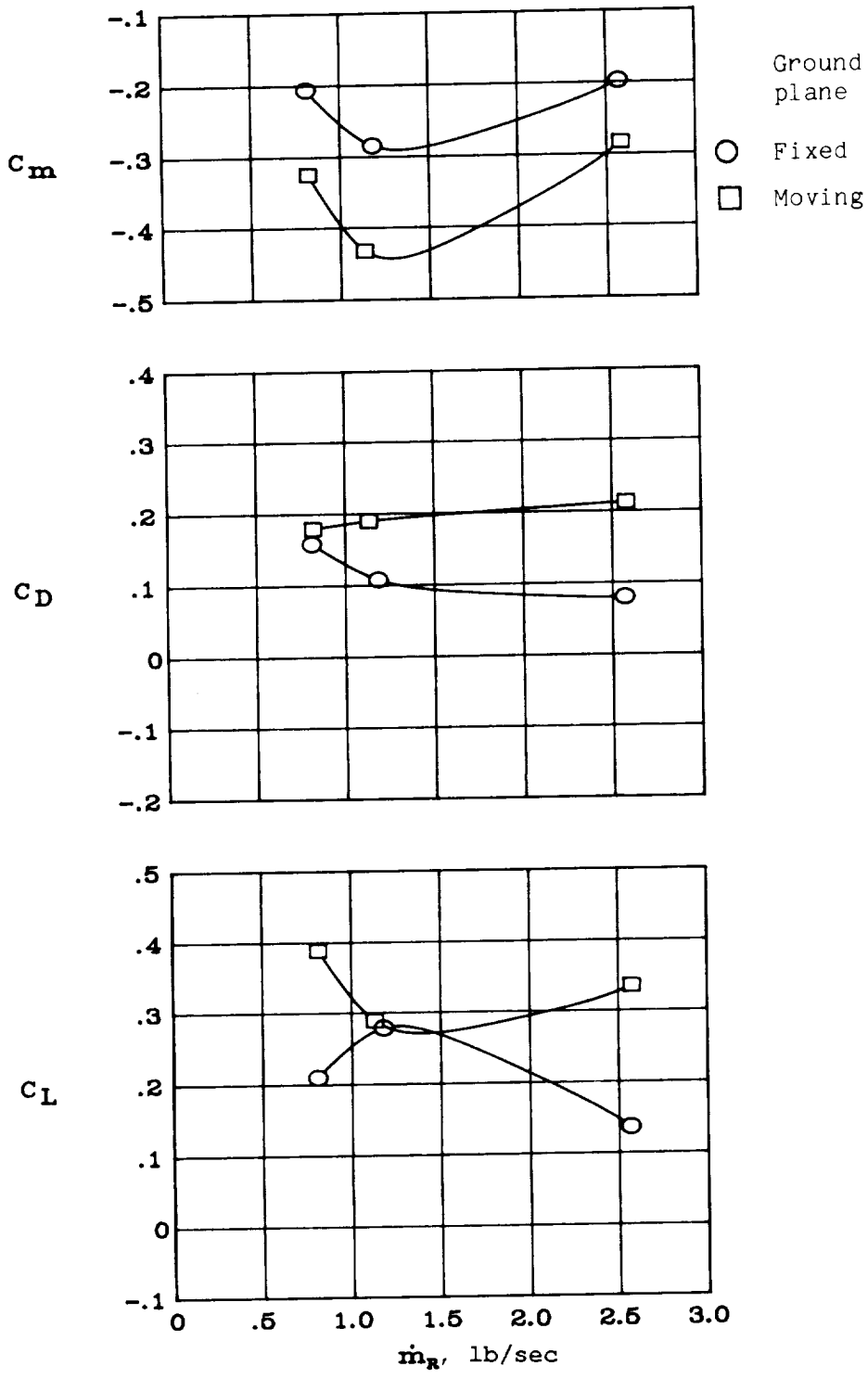


Figure 46. Fixed versus moving-belt ground plane for 0° rotated target thrust reverser. $q_\infty = 1.4$ psf; $\delta_f = 40°; \delta_s = 60°$; IGE.

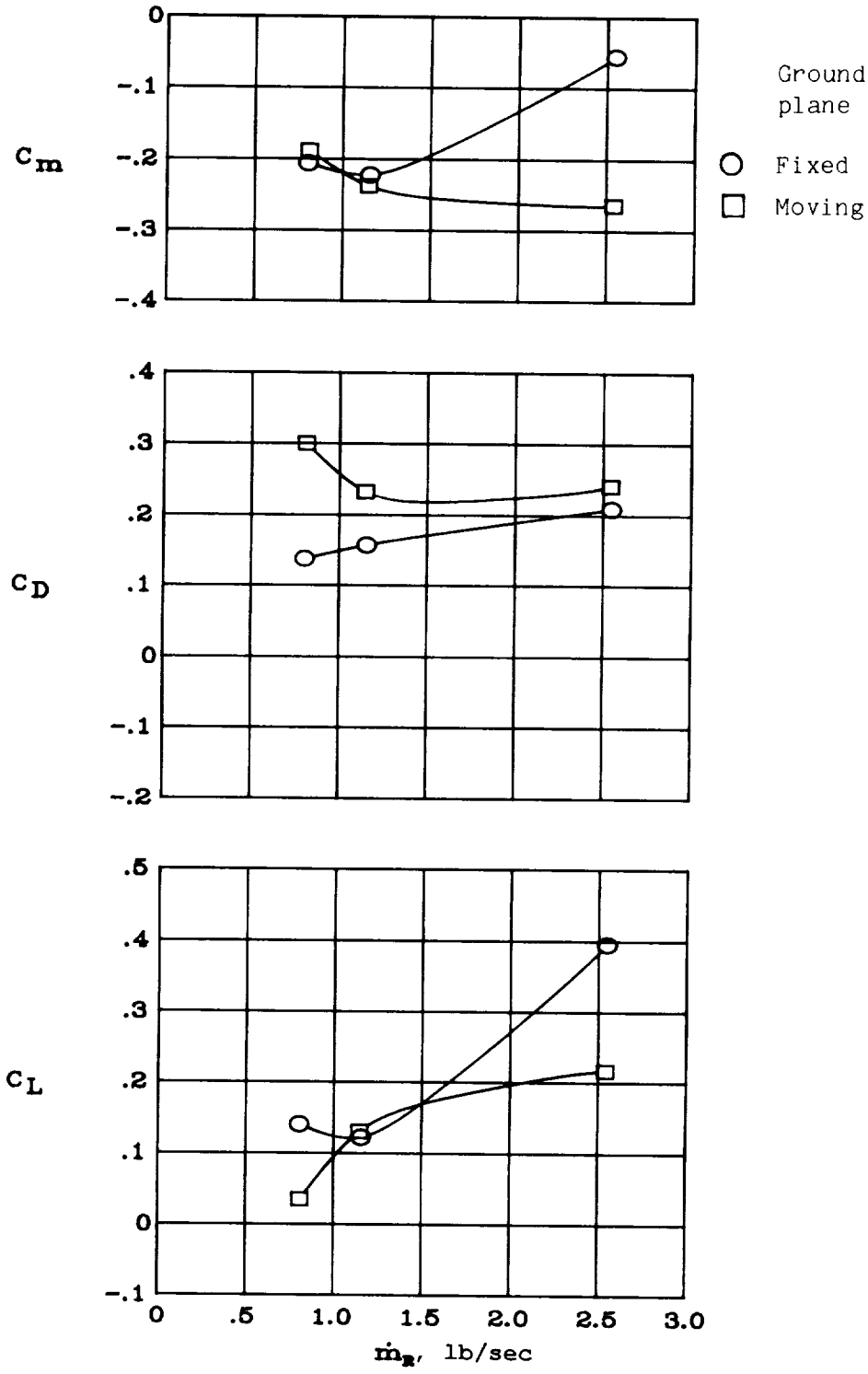


Figure 47. Fixed versus moving-belt ground plane for 15° rotated target thrust reverser. $q_\infty = 1.4$ psf; $\delta_f = 40°; \delta_s = 60°$; IGE.

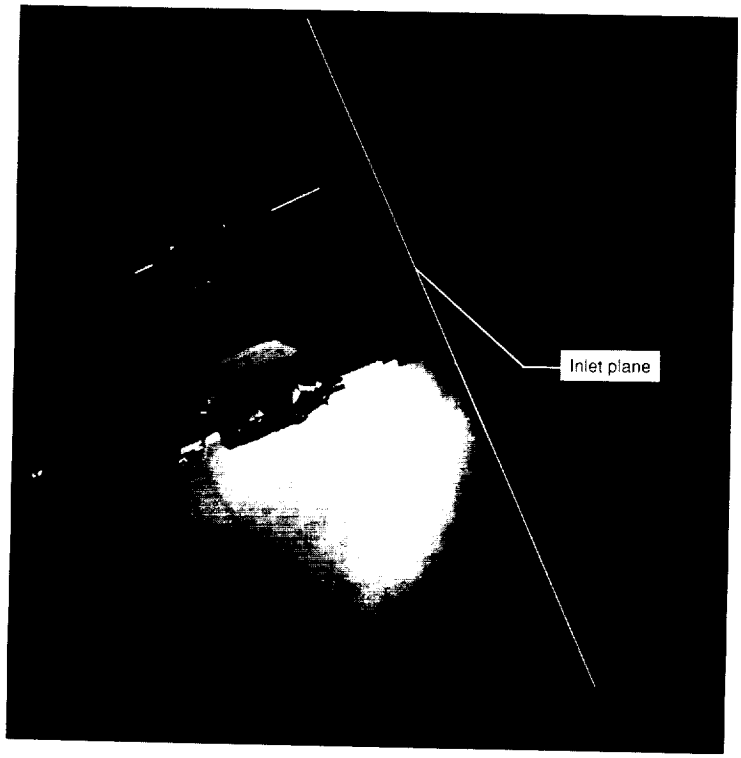


L-88-201

(a) Fixed ground plane.

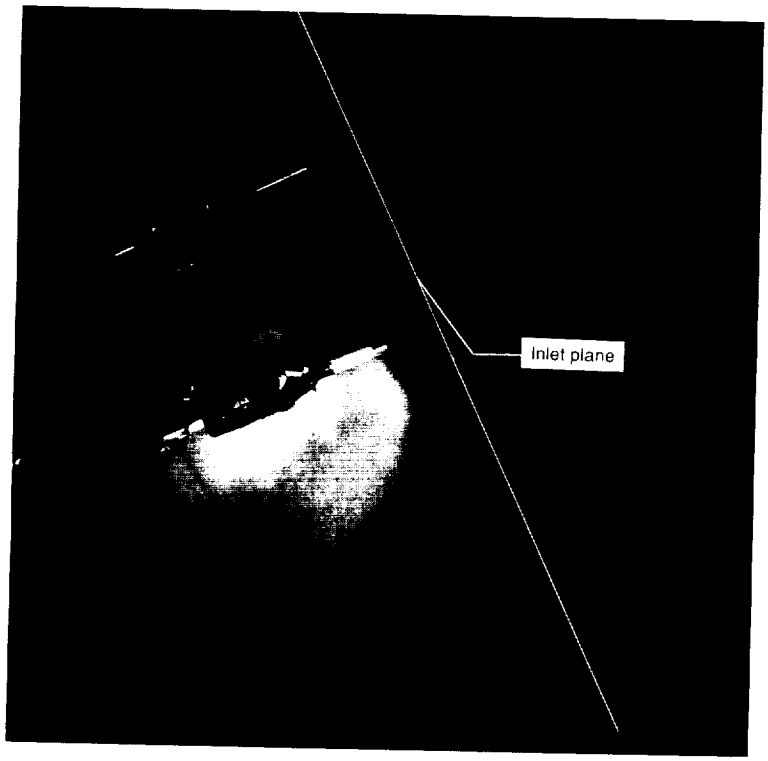


L-88-202

(b) Moving-belt ground plane.

Figure 48. Horizontal laser light sheet with smoke injection flow visualization for 22.5° rotated target thrust reverser. $\dot{m}_R = 1.15$ lb/sec; $q_\infty = 1.4$ psf; $\delta_f = 40°$; $\delta_s = 60°$; $h = 1.5$ in.; IGE.

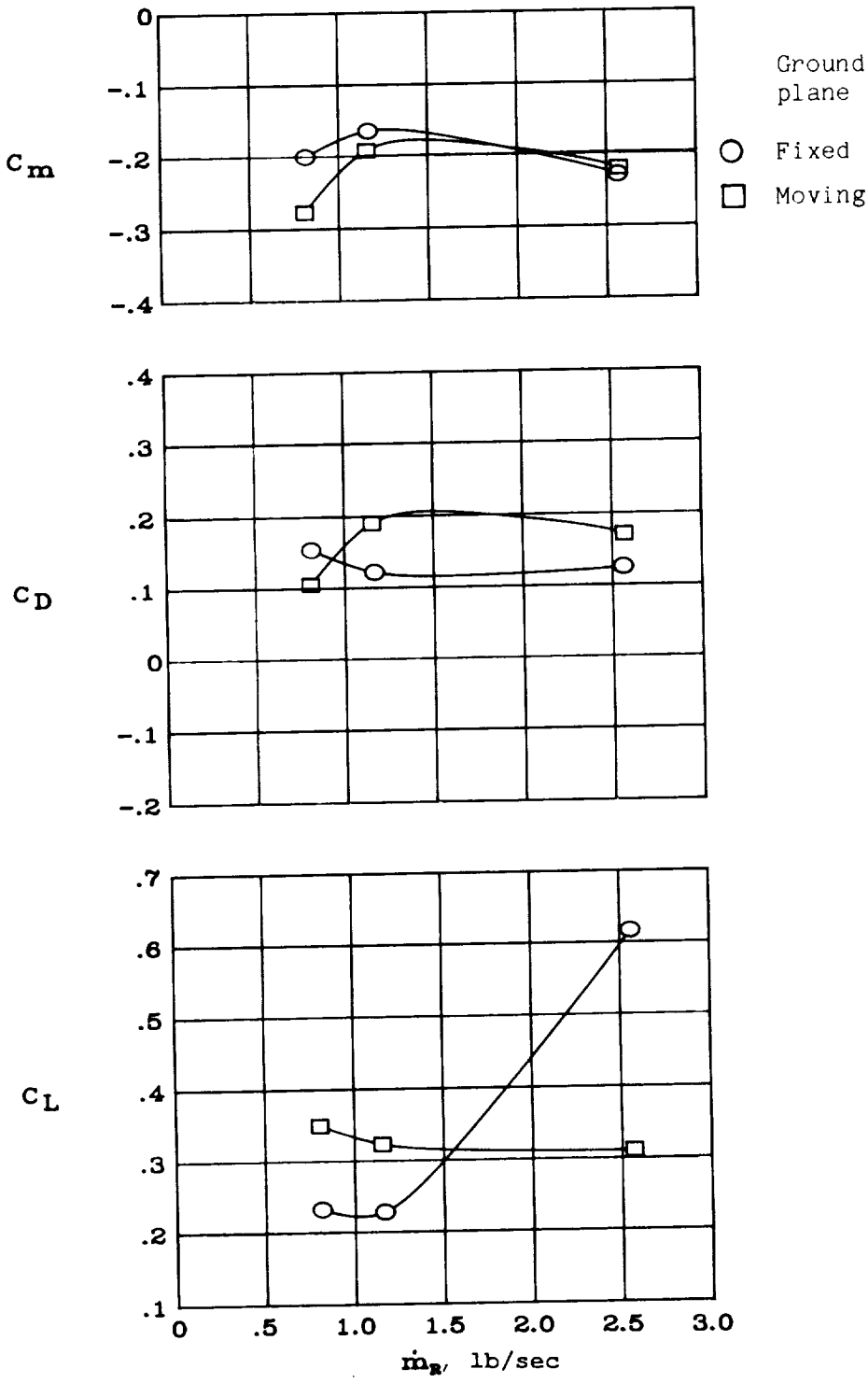


Figure 49. Fixed versus moving-belt ground plane for 22.5° rotated target thrust reverser. $q_\infty = 1.4$ psf; $\delta_f = 40°$; $\delta_s = 60°$; IGE.

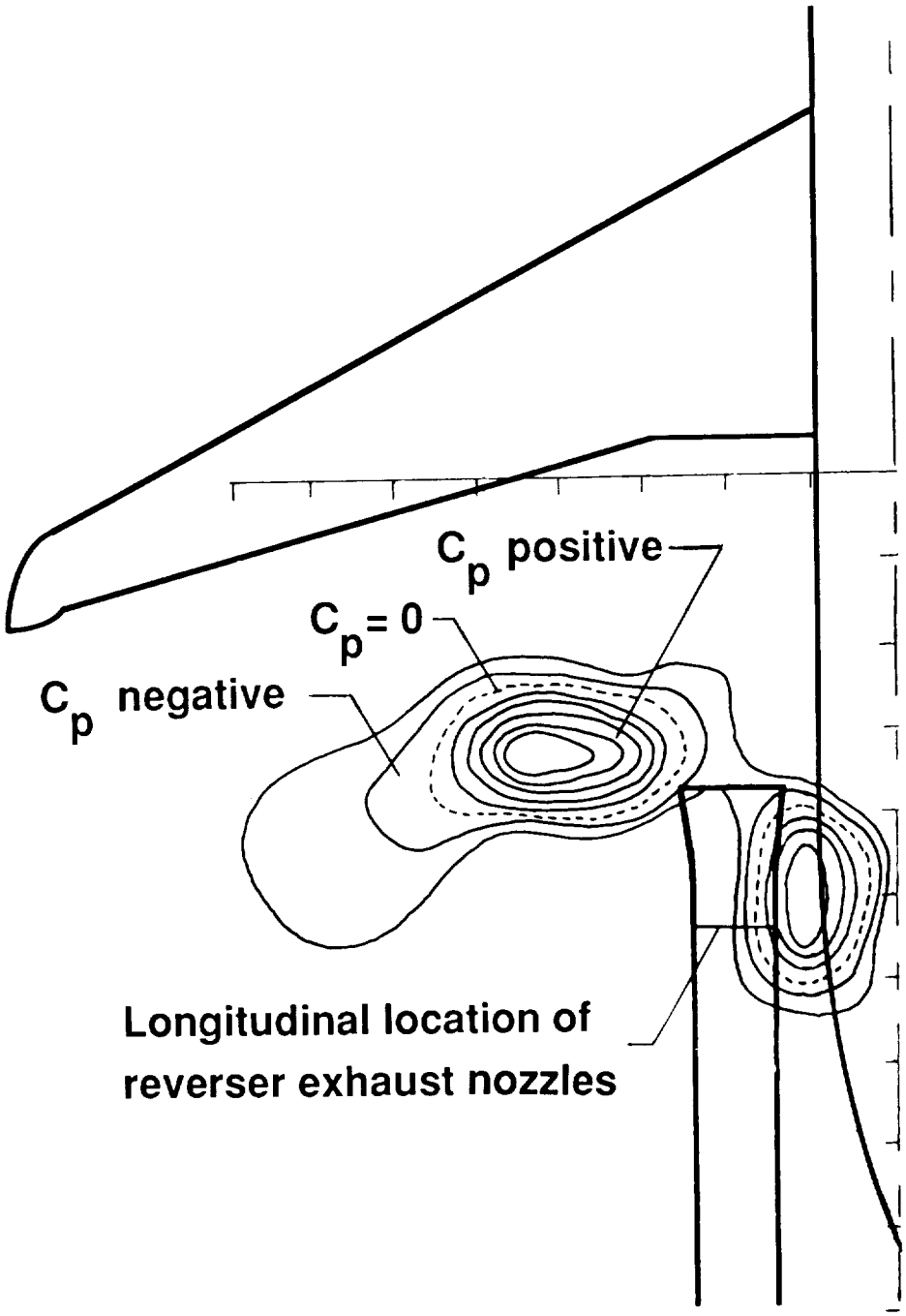


(a) $\dot{m}_R = 2.55$ lb/sec; $\Delta C_p = 0.3266$.

Figure 50. Pressure contours for cascade thrust reverser. $q_\infty = 1.4$ psf; $\delta_f = 40°$; $\delta_s = 60°$; IGE.

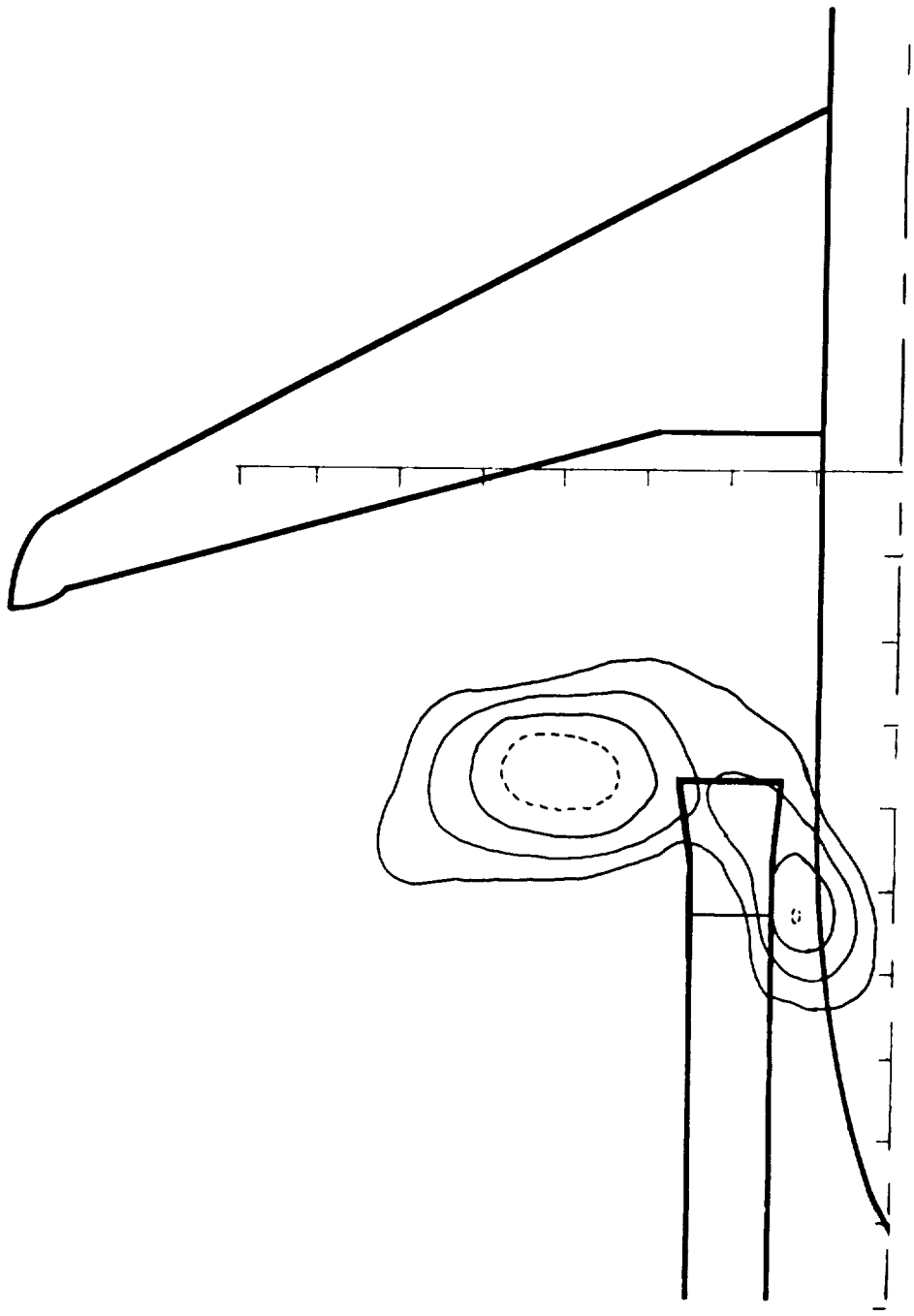

(b) $\dot{m}_R = 2.15$ lb/sec; $\Delta C_p = 0.3817$.

Figure 50. Concluded.

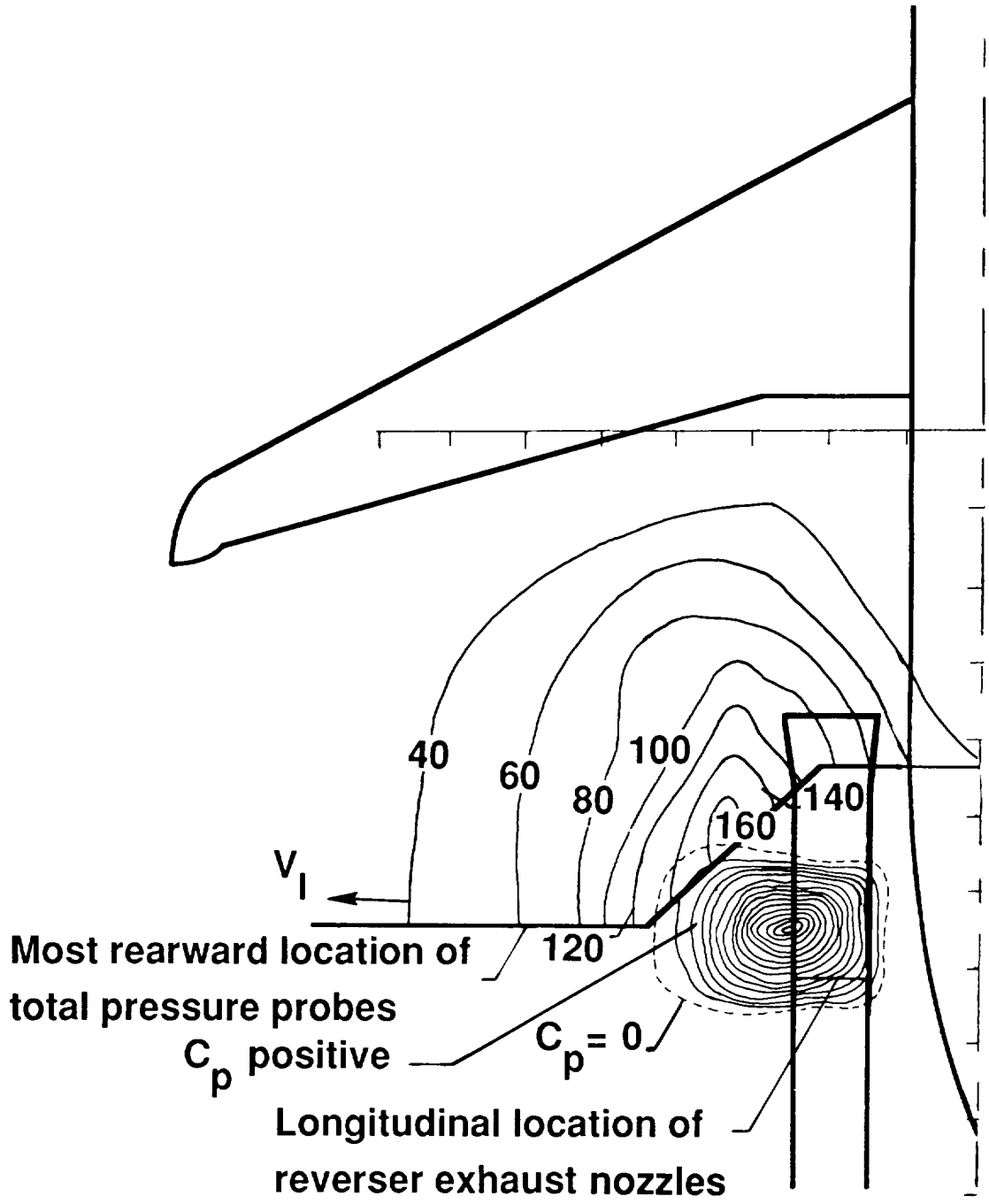


(a) $\dot{m}_R = 3.2$ lb/sec; $\Delta C_p = 1.60$.

Figure 51. Pressure and velocity contours for 15° rotated target thrust reverser. Velocity contours are in feet per second; $q_\infty = 1.4$ psf; $\delta_f = 40°$; $\delta_s = 60°$; IGE.

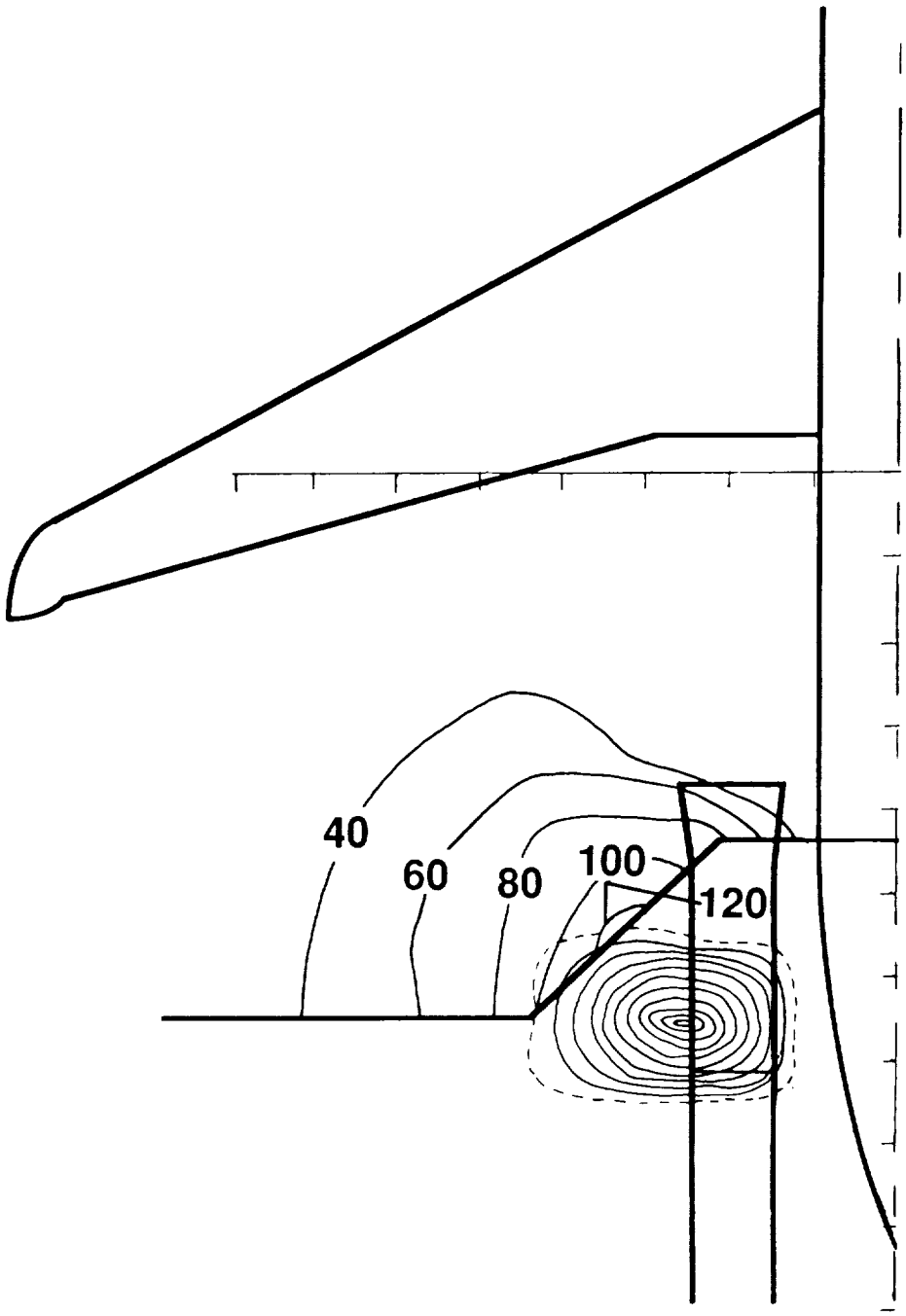


(b) $\dot{m}_R = 2.25$ lb/sec; $\Delta C_p = 1.60$.

Figure 51. Continued.

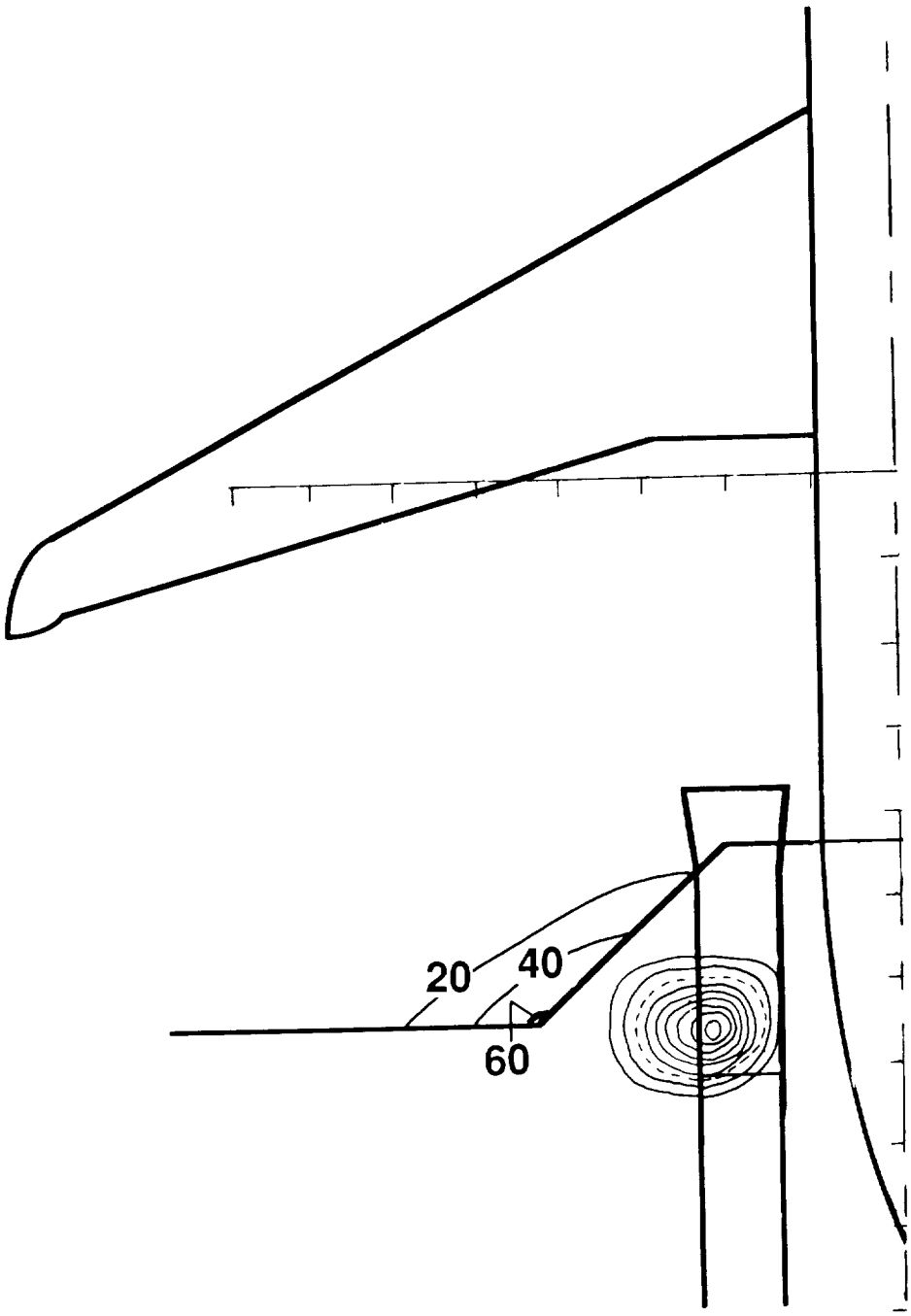


(c) $\dot{m}_R = 1.35$ lb/sec; $\Delta C_p = 0.20$.

Figure 51. Concluded.

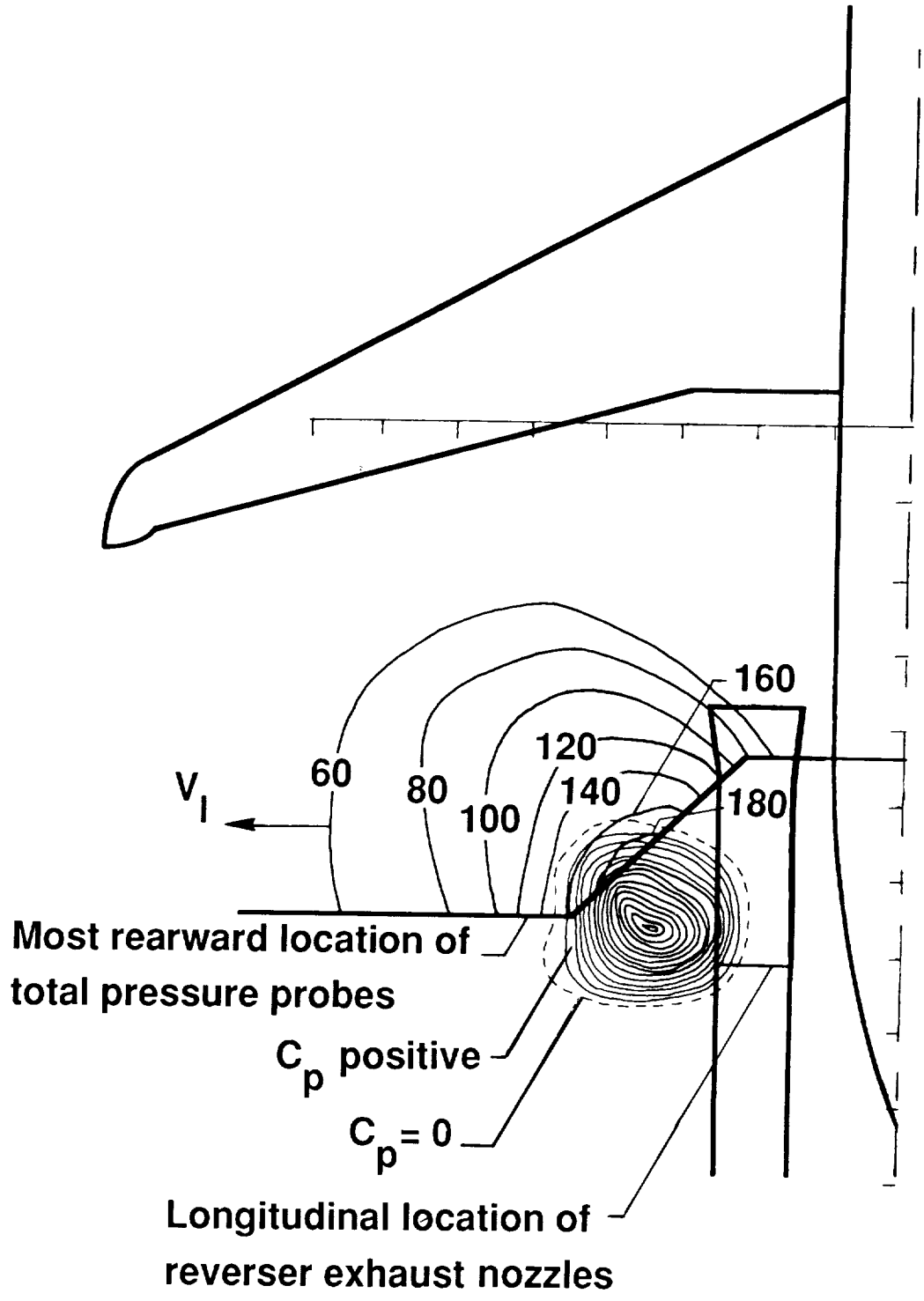


(a) $\dot{m}_R = 3.2$ lb/sec; $\Delta C_p = 1.0$.

Figure 52. Pressure and velocity contours for 22.5° rotated target thrust reverser. Velocity contours are in feet per second; $q_\infty = 1.4$ psf; $\delta_f = 40°$; $\delta_s = 60°$; IGE.

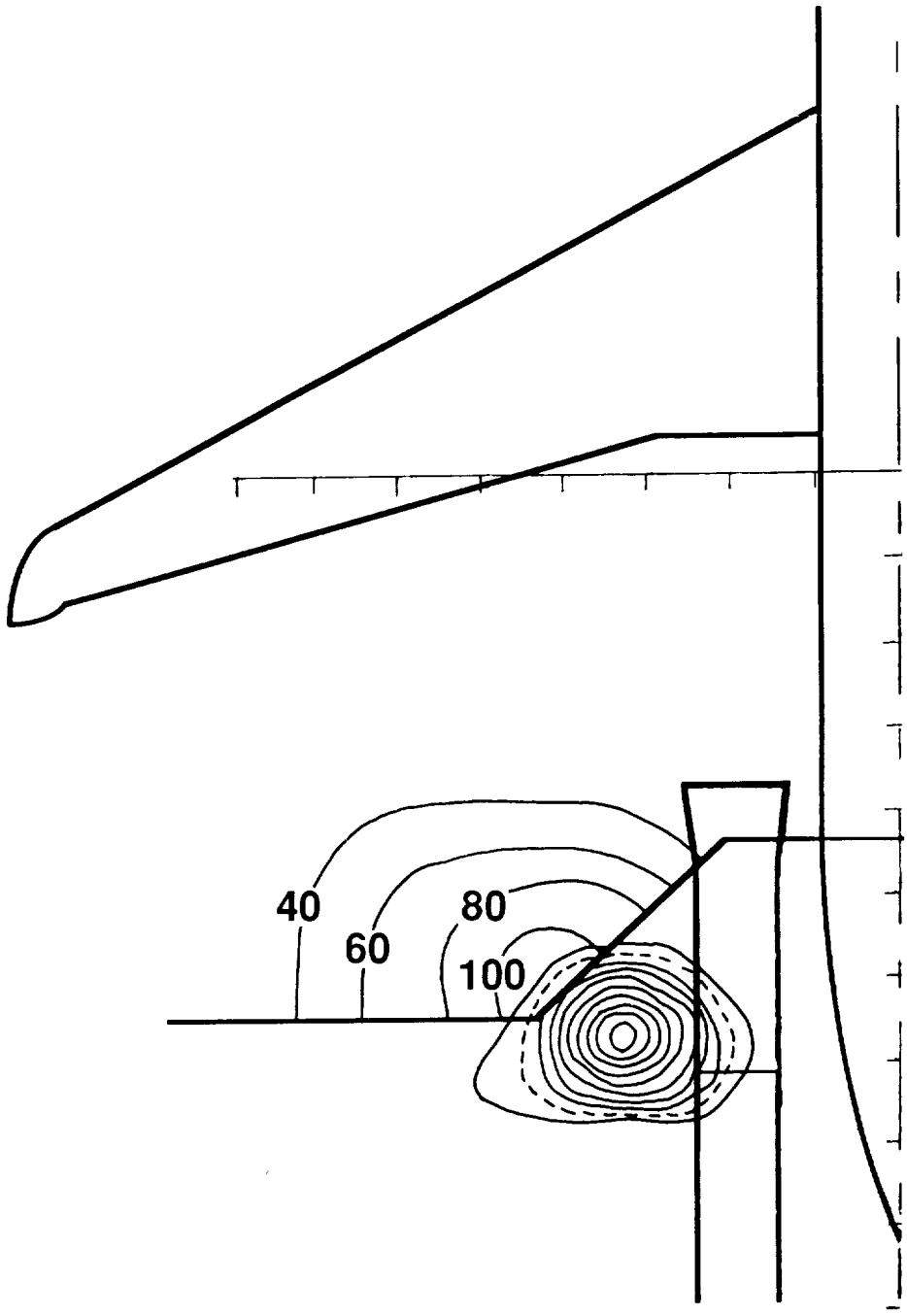


(b) $\dot{m}_R = 2.25$ lb/sec; $\Delta C_p = 0.5$.

Figure 52. Continued.

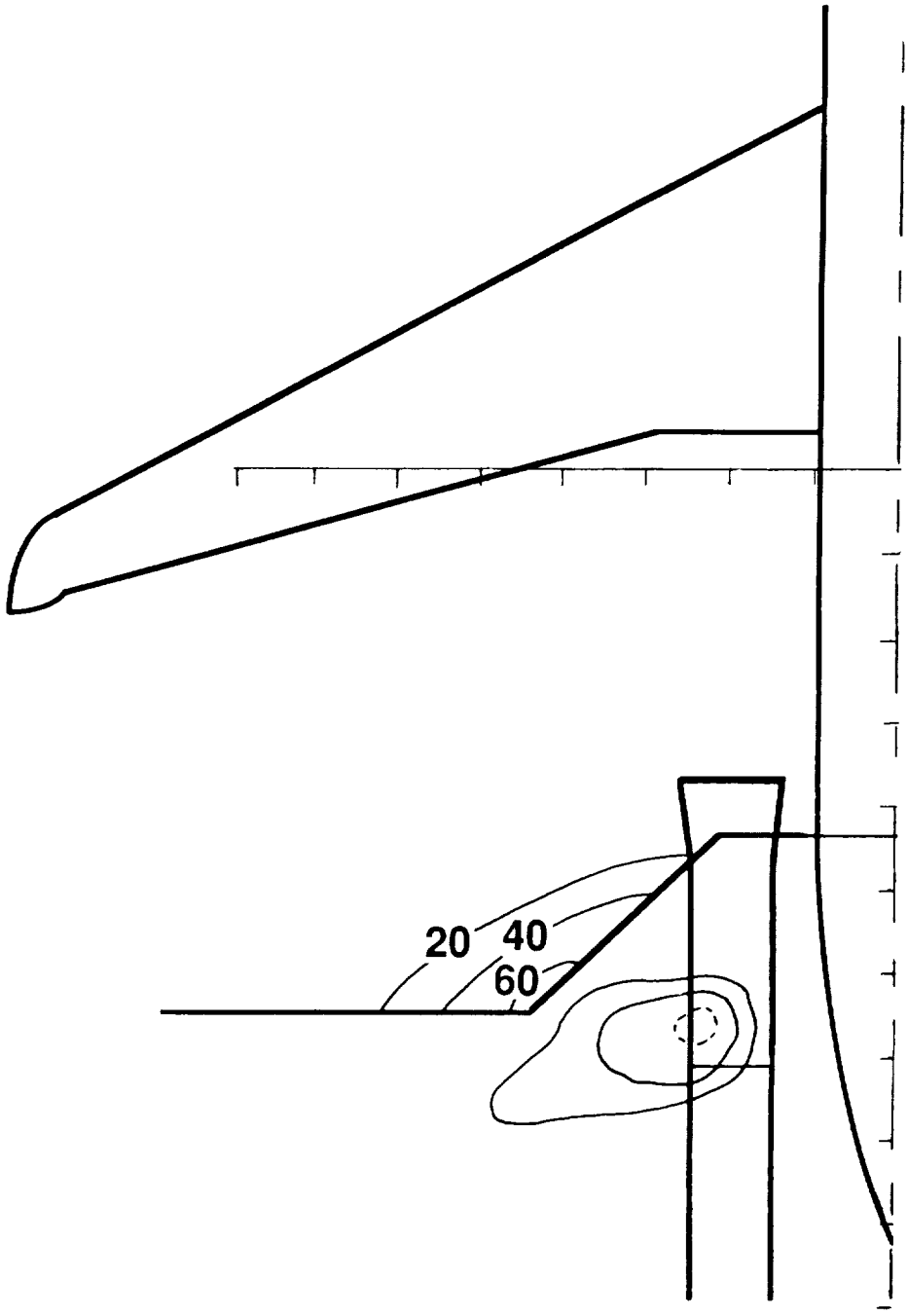


(c) $\dot{m}_R = 1.35$ lb/sec; $\Delta C_p = 0.5$.

Figure 52. Concluded.

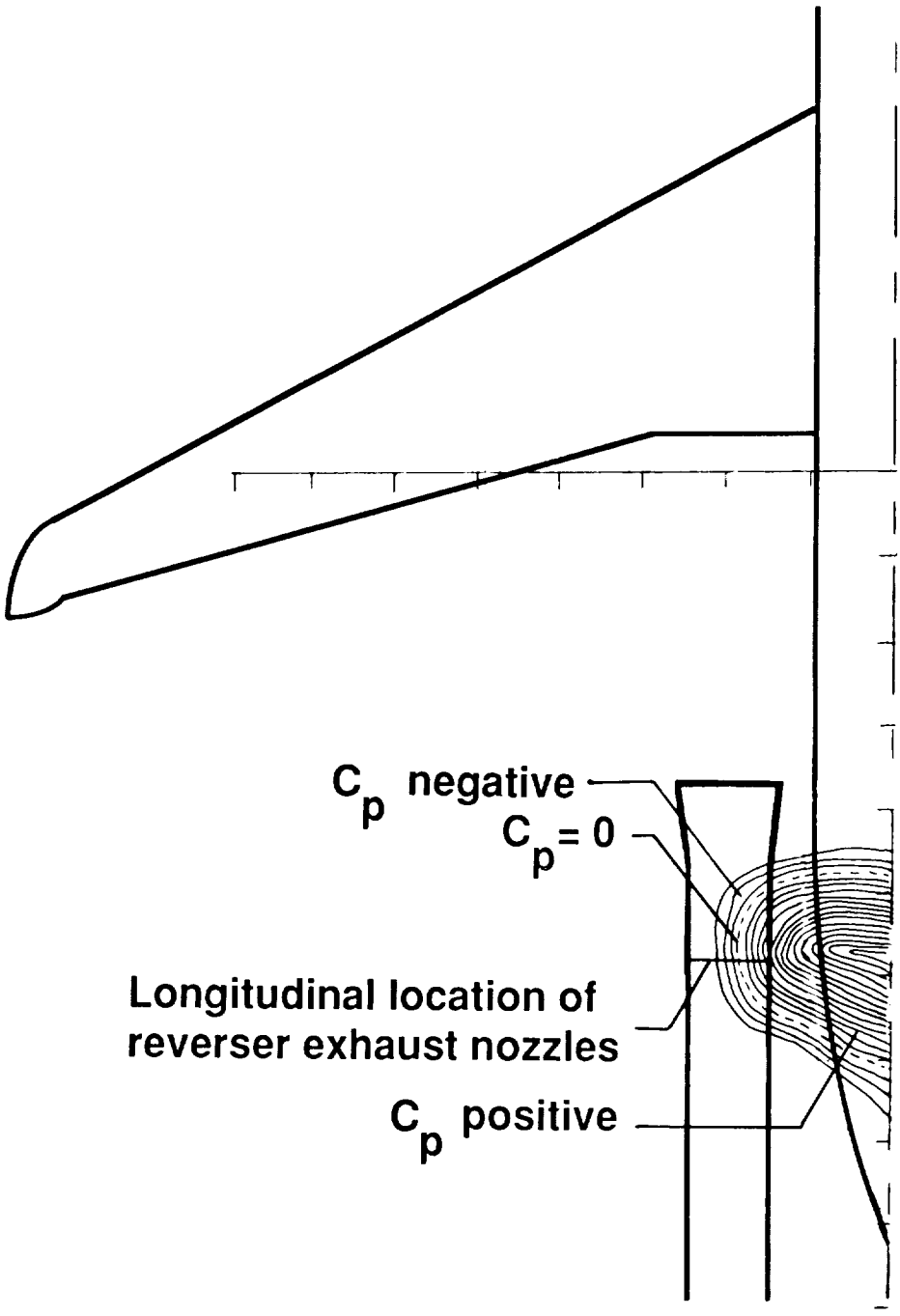


(a) $\dot{m}_R = 2.55$ lb/sec; $\Delta C_p = 0.5564$.

Figure 53. Pressure contours for configuration II of four-door thrust reverser. $q_\infty = 1.4$ psf; $\delta_f = 40°$; $\delta_s = 60°$; IGE.

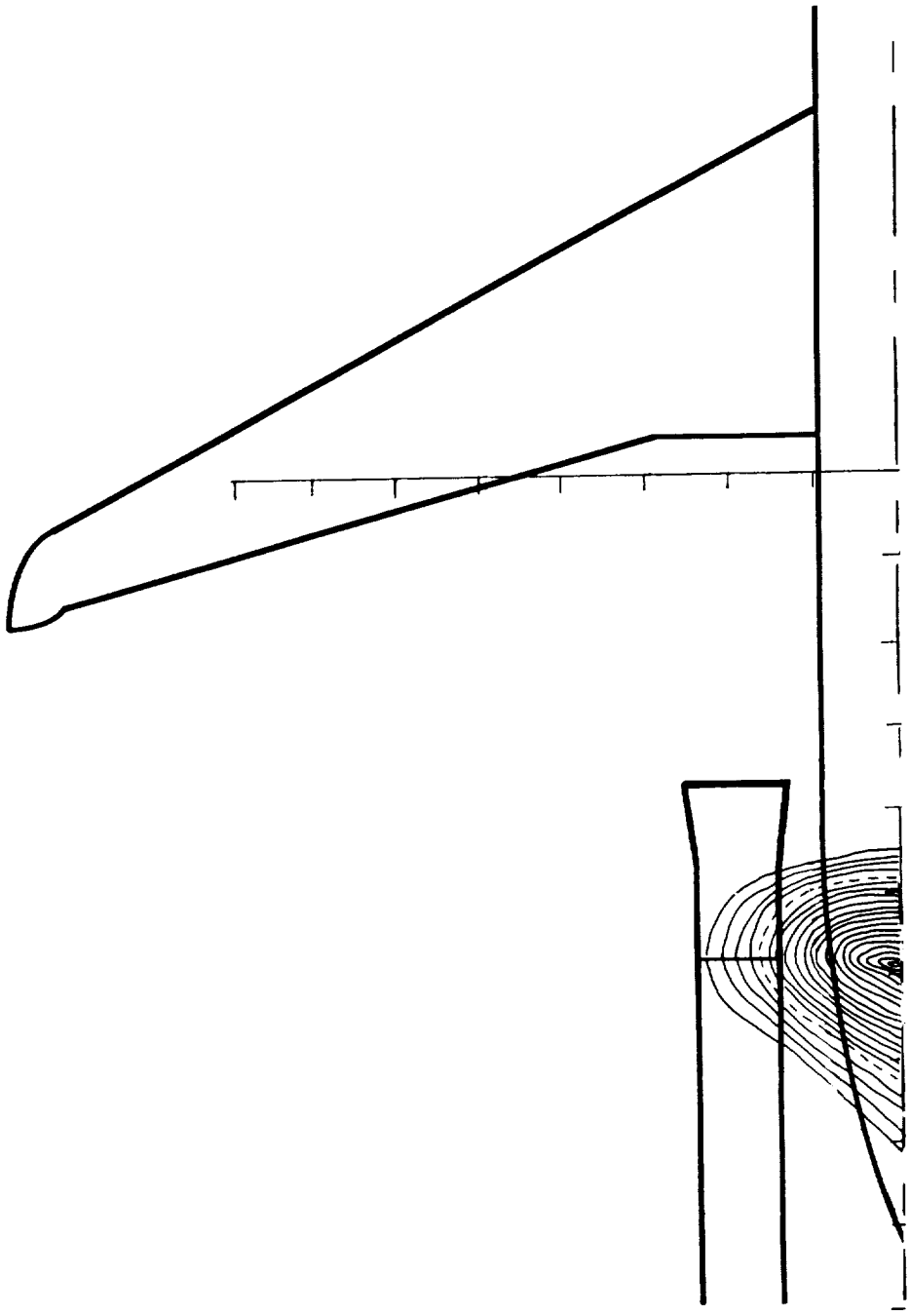

(b) $\dot{m}_R = 2.0$ lb/sec; $\Delta C_p = 0.3160$.

Figure 53. Continued.

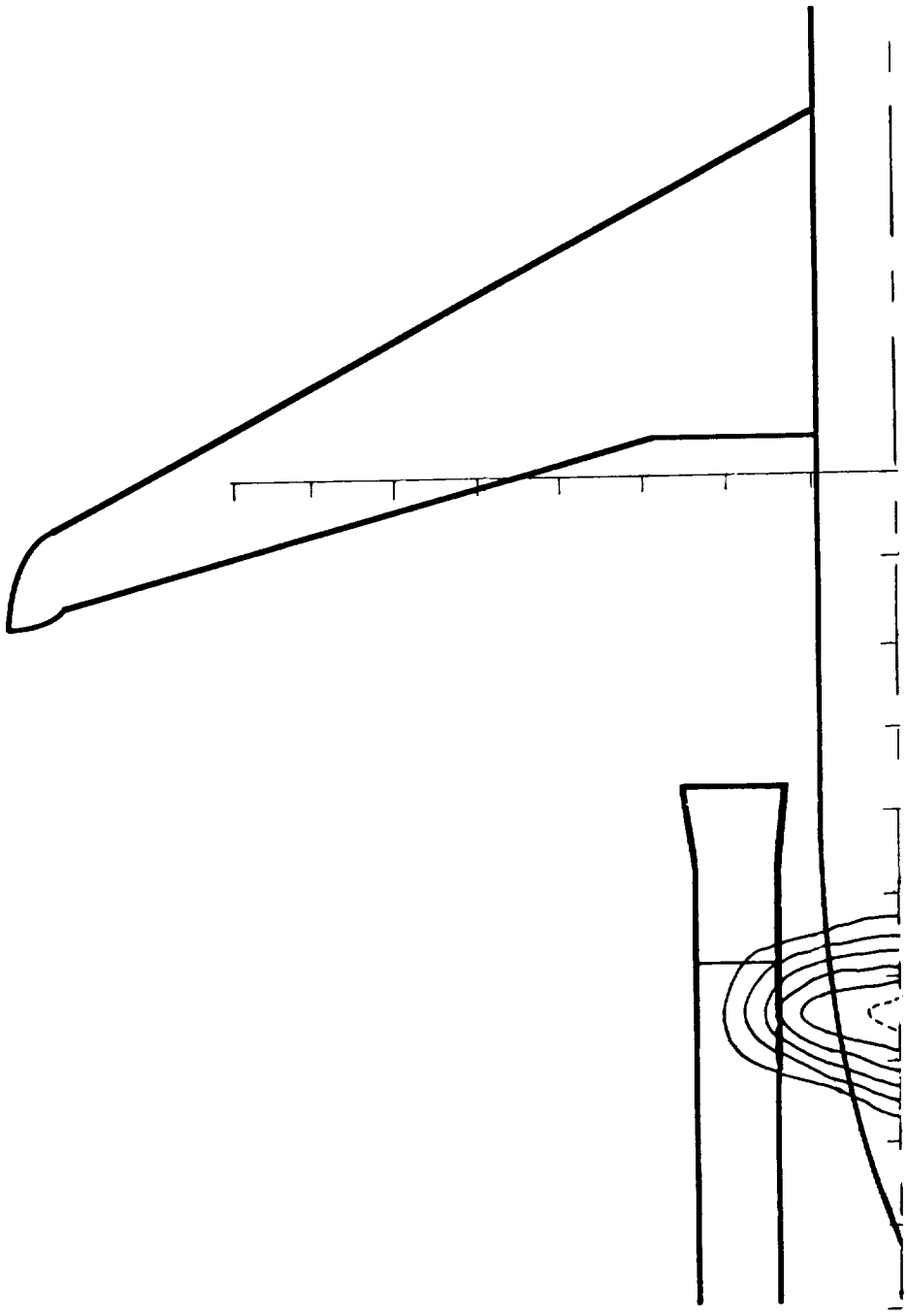

(c) $\dot{m}_R = 1.15$ lb/sec; $\Delta C_p = 0.1582$.

Figure 53. Concluded.

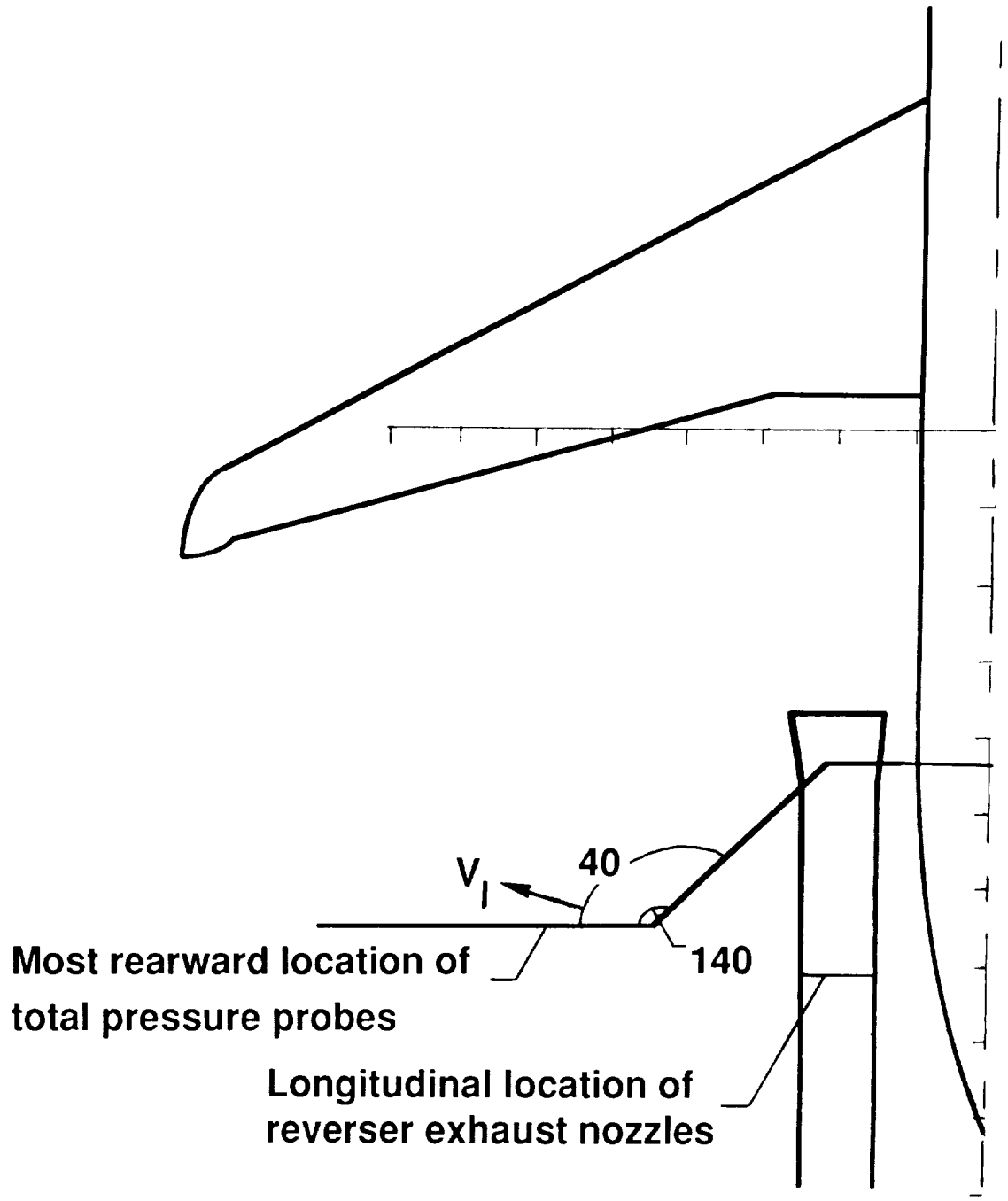


(a) $q_\infty = 12.2$ psf.

Figure 54. Velocity contours for 15° rotated target thrust reverser. Velocity contours are in feet per second; $\dot{m}_R = 3.2$ lb/sec; $\delta_f = 40°$; $\delta_s = 60°$; IGE.

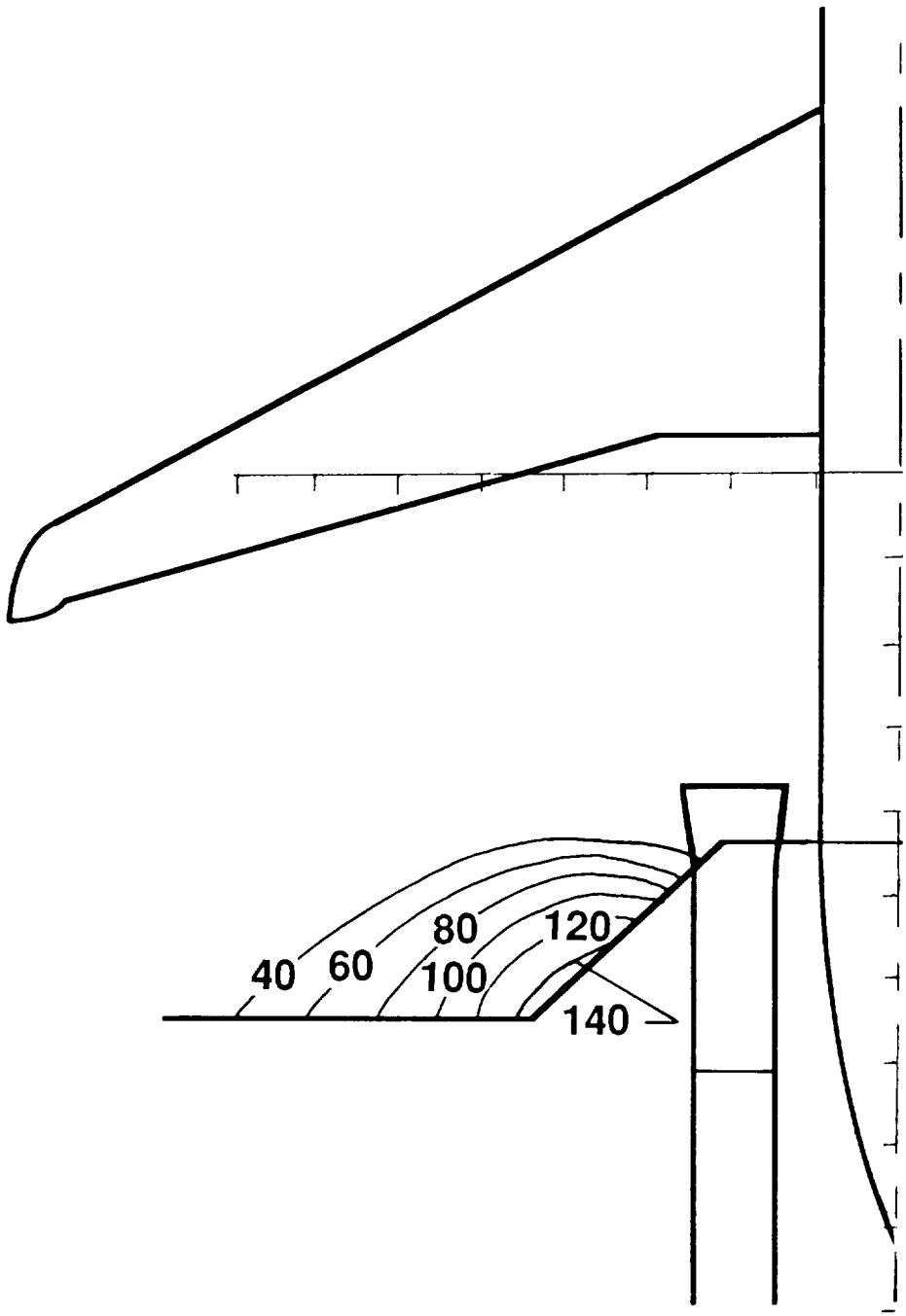


(b) $q_\infty = 5.4$ psf.

Figure 54. Continued.

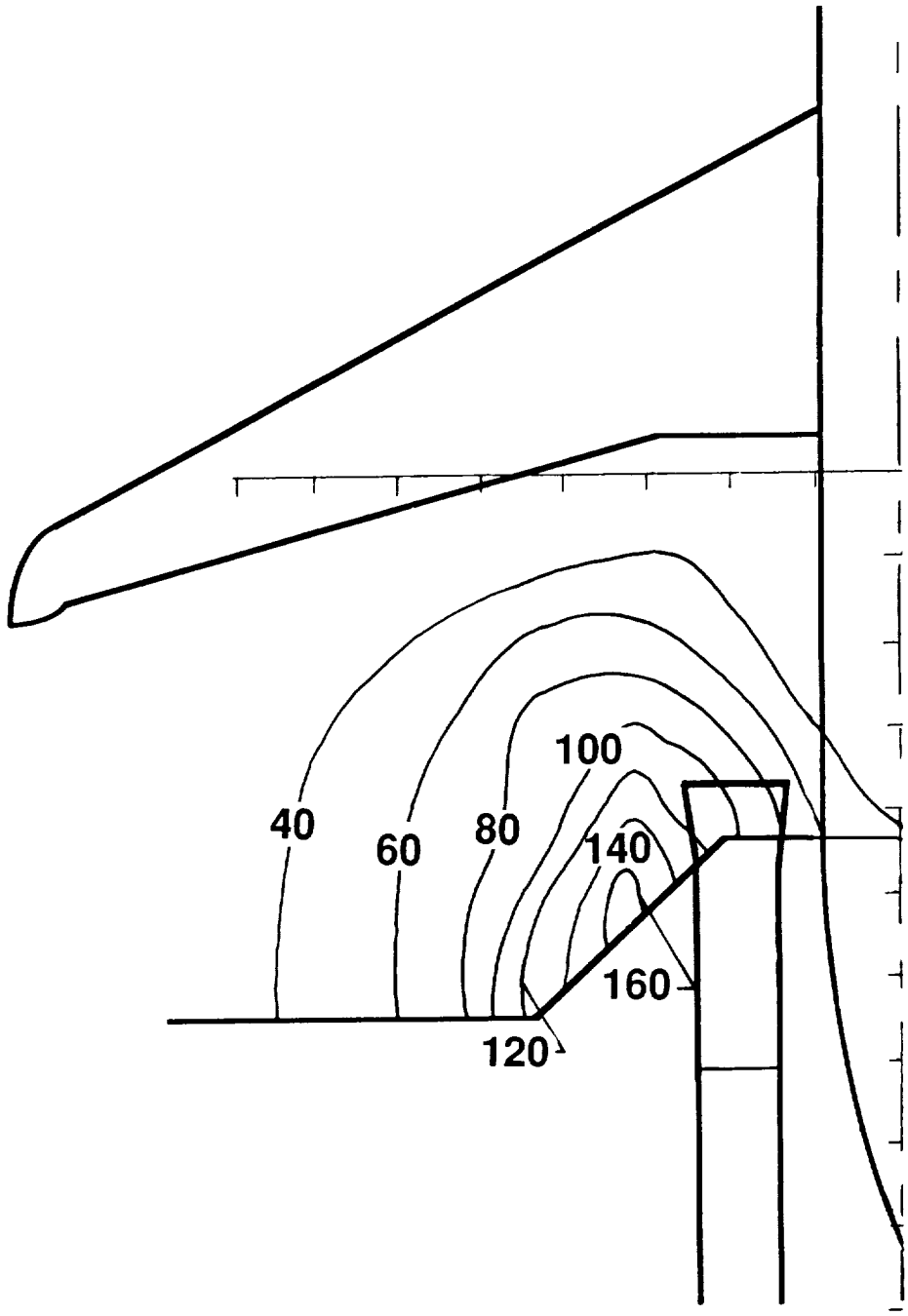


(c) $q_\infty = 1.4$ psf.

Figure 54. Concluded.

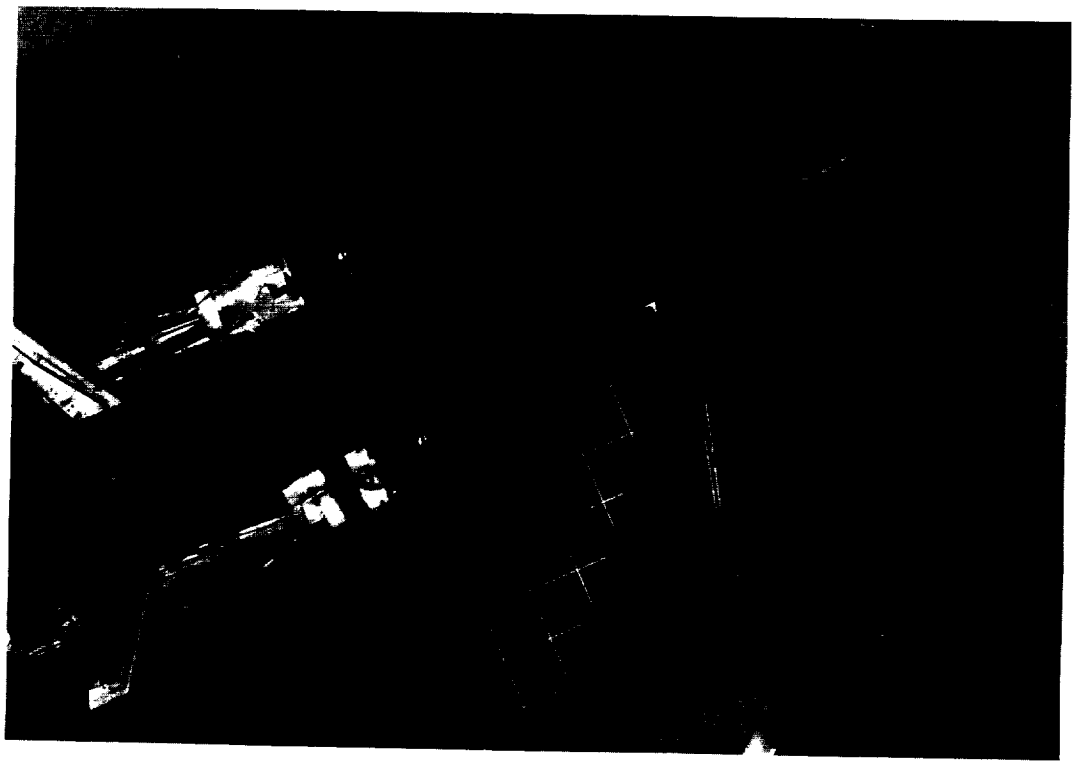

L-88-203

(a) Full inlet flow.

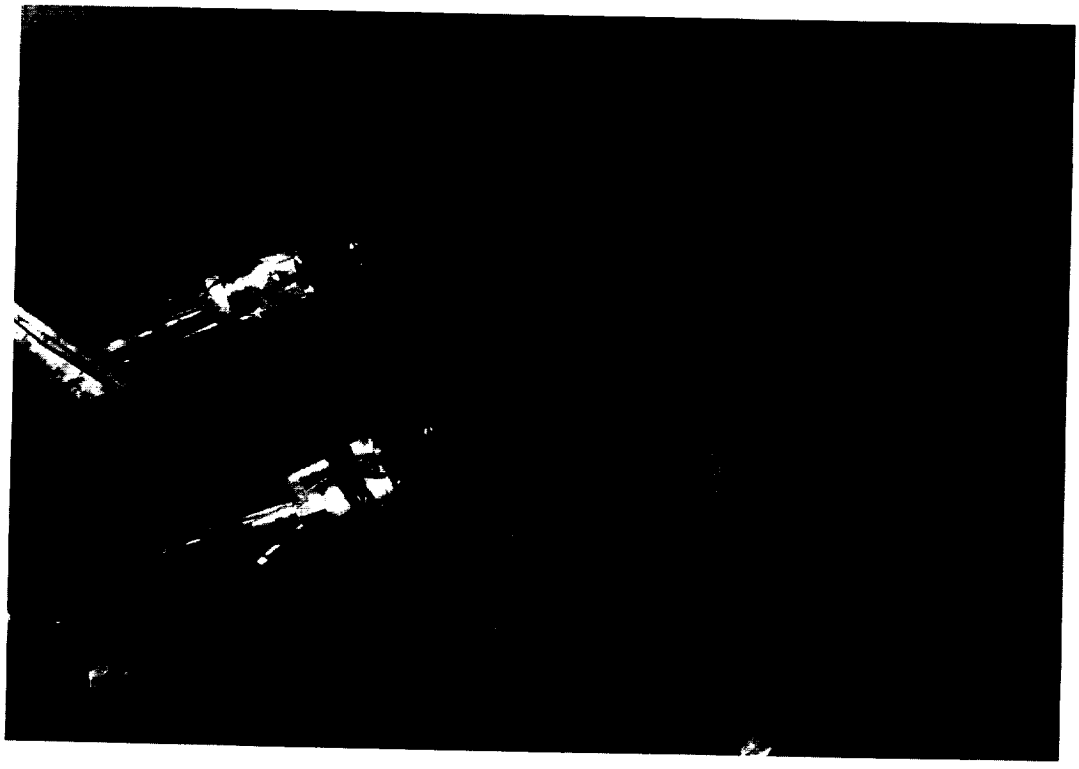

L-88-204

(b) Flow-through inlet.

Figure 55. Flow visualization photographs of full inlet flow versus flow-through inlet flow for cascade thrust reverser. $\dot{m}_R = 1.15$ lb/sec; $q_\infty = 12.2$ psf; $\delta_f = 40°$; $\delta_s = 60°$; IGE.

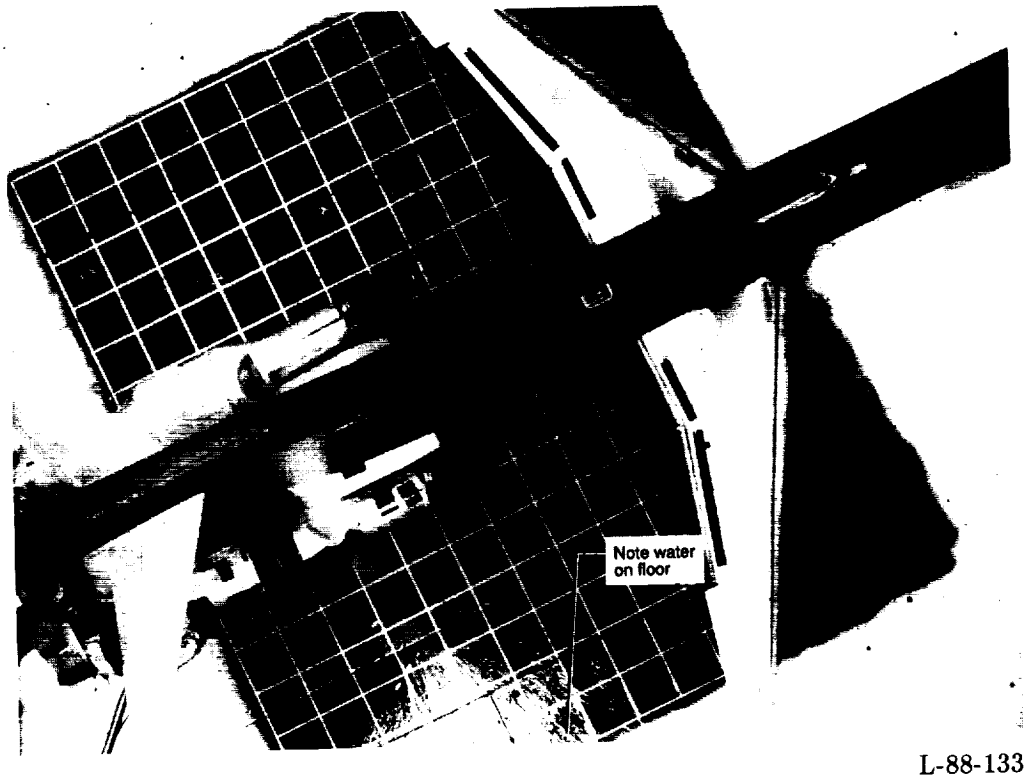


L-88-133

(a) Full inlet flow.

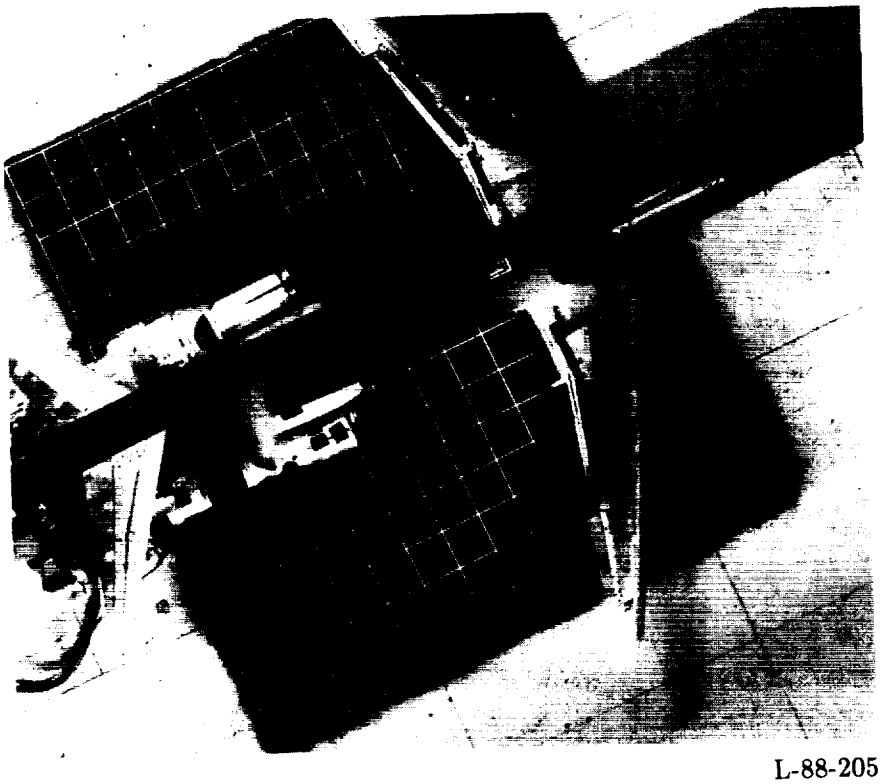

L-88-205

(b) Flow-through inlet.

Figure 56. Flow visualization photographs of full inlet flow versus flow-through inlet flow for 22.5° rotated target thrust reverser. $\dot{m}_R = 3.2$ lb/sec; $q_\infty = 1.4$ psf; $\delta_f = 40°$; $\delta_s = 60°$; IGE.

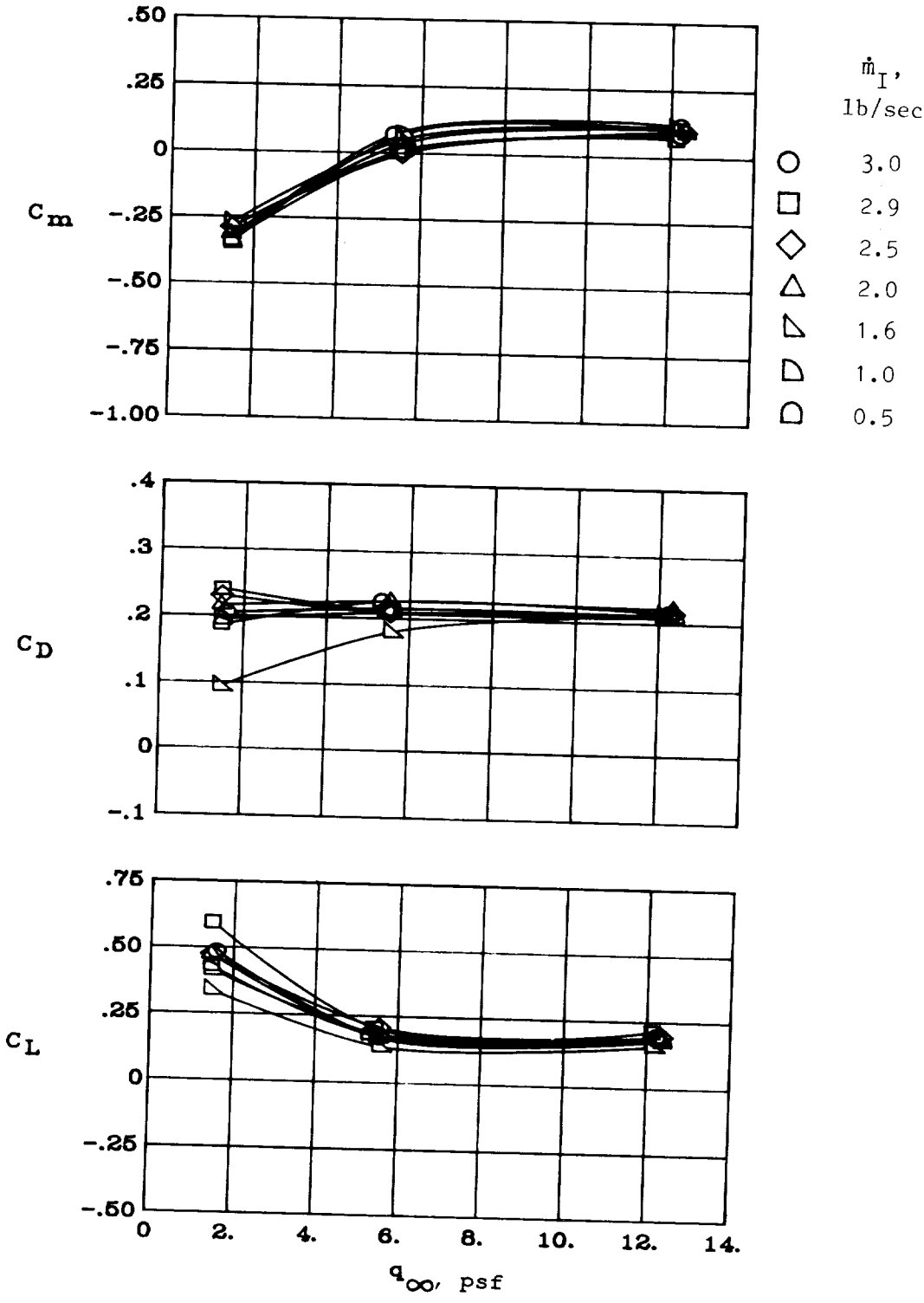


(a) In ground effect.

Figure 57. Effects of reduced inlet flow on longitudinal aerodynamics of cascade configuration. $\dot{m}_R = 2.55$ lb/sec; $\delta_f = 40°$; $\delta_s = 60°$.

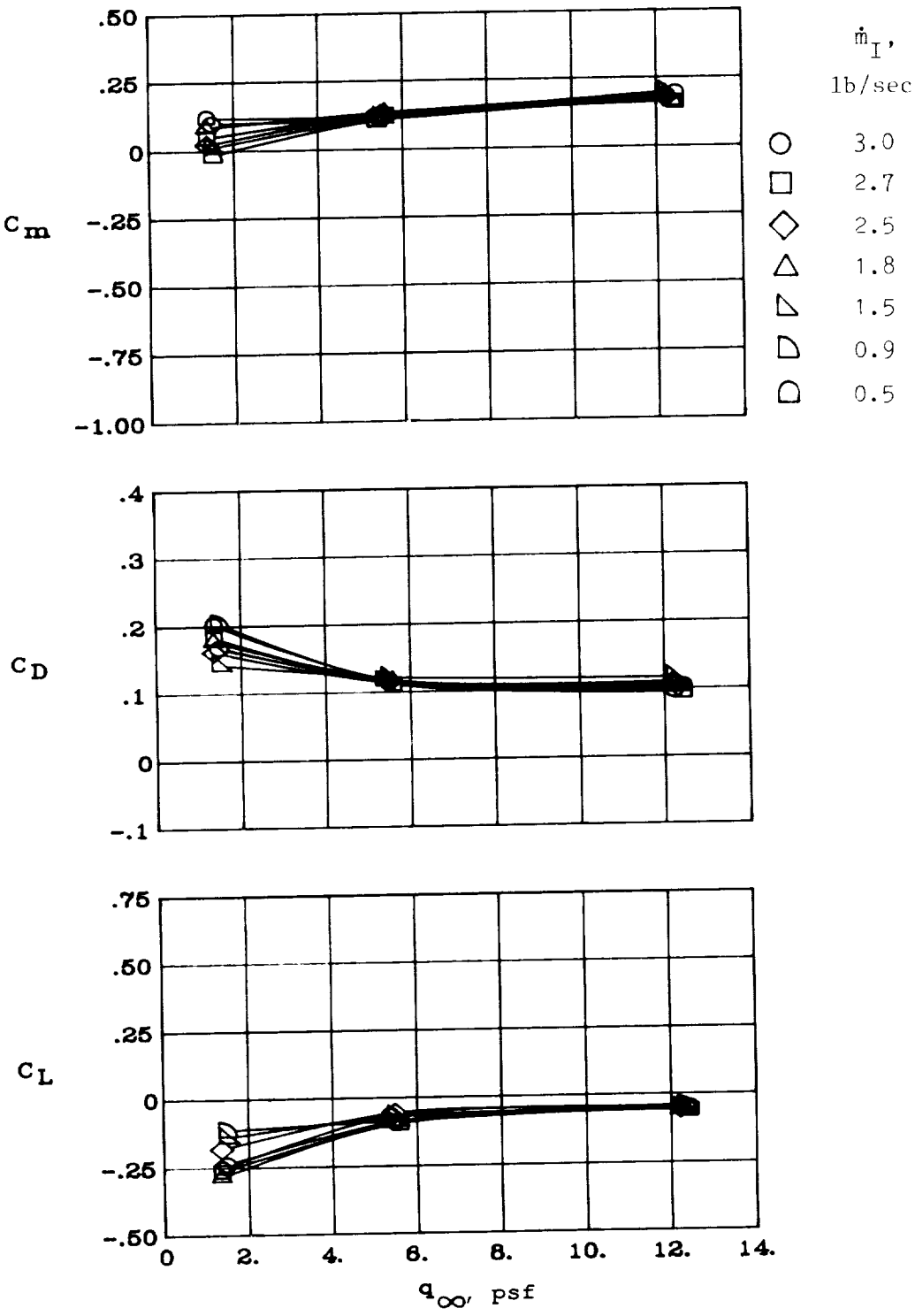


(b) Out of ground effect.

Figure 57. Concluded.

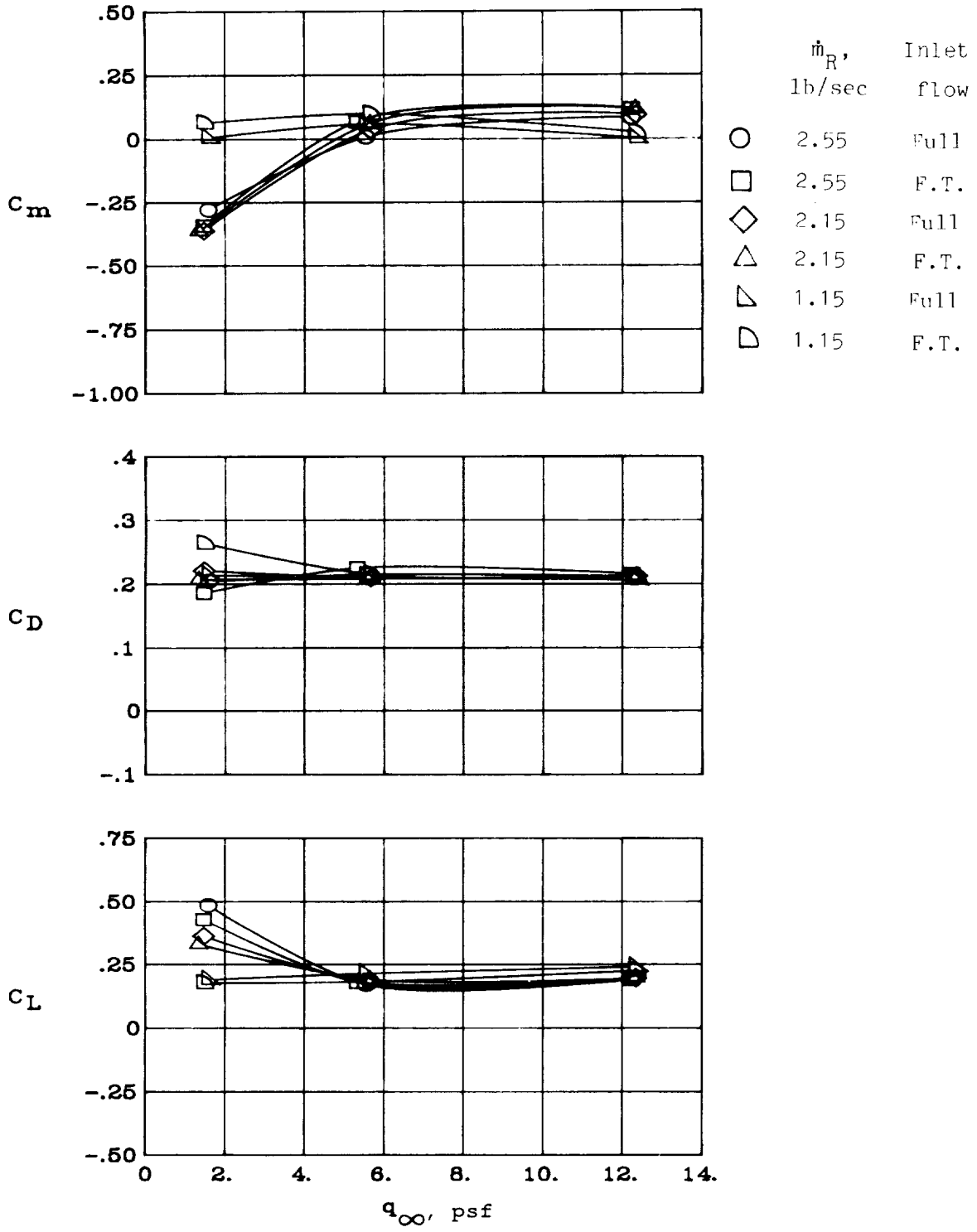


Figure 58. Effects of full inlet flow versus flow-through inlet flow and variations in $\dot{m}_R$ on longitudinal aerodynamics of cascade configuration. $\delta_f = 40°$; $\delta_s = 60°$; IGE.

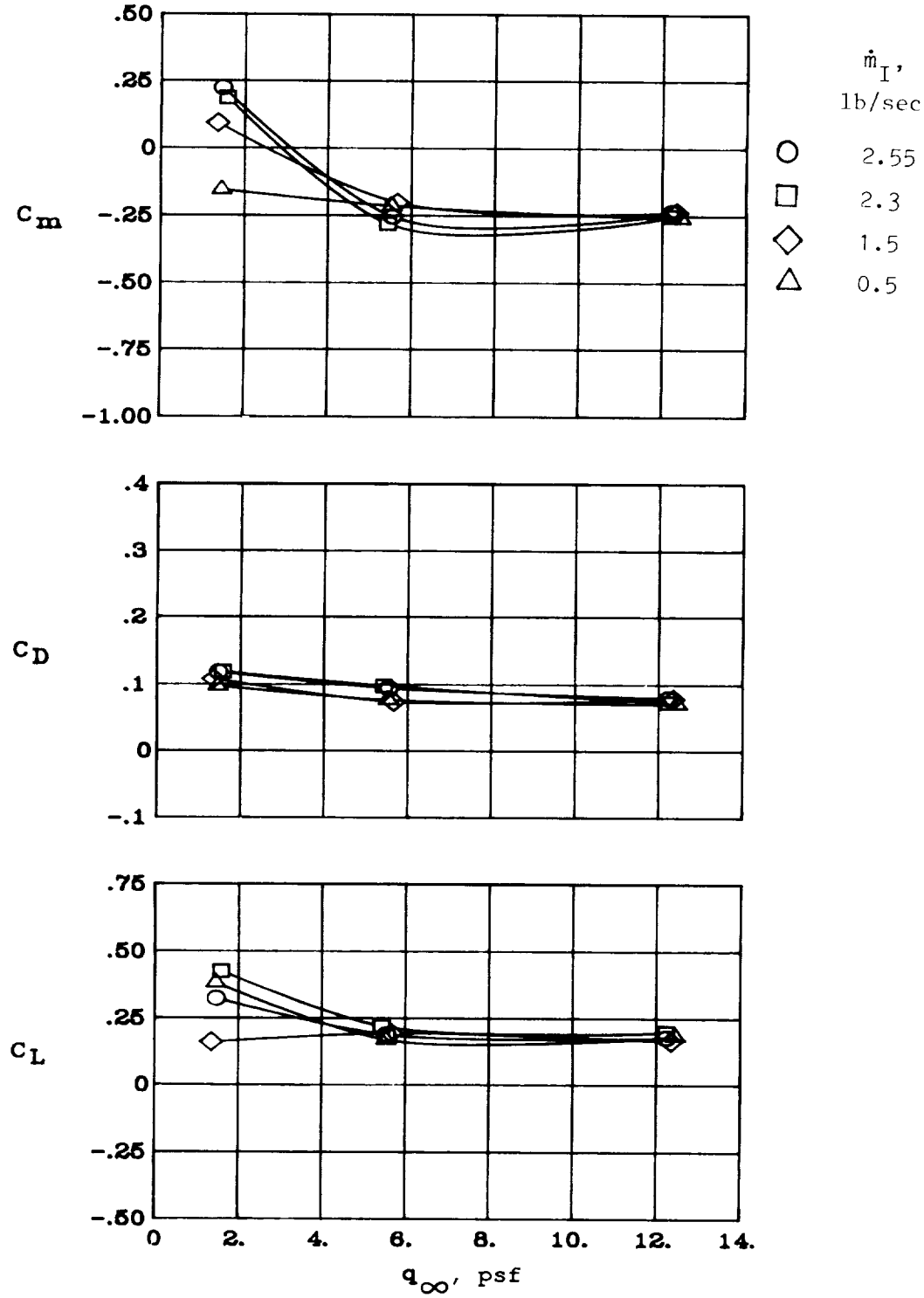


(a) In ground effect.

Figure 59. Effects of reduced inlet flow on longitudinal aerodynamics of 15° rotated target configuration $\dot{m}_R = 2.55$ lb/sec; $\delta_f = 40°$; $\delta_s = 60°$

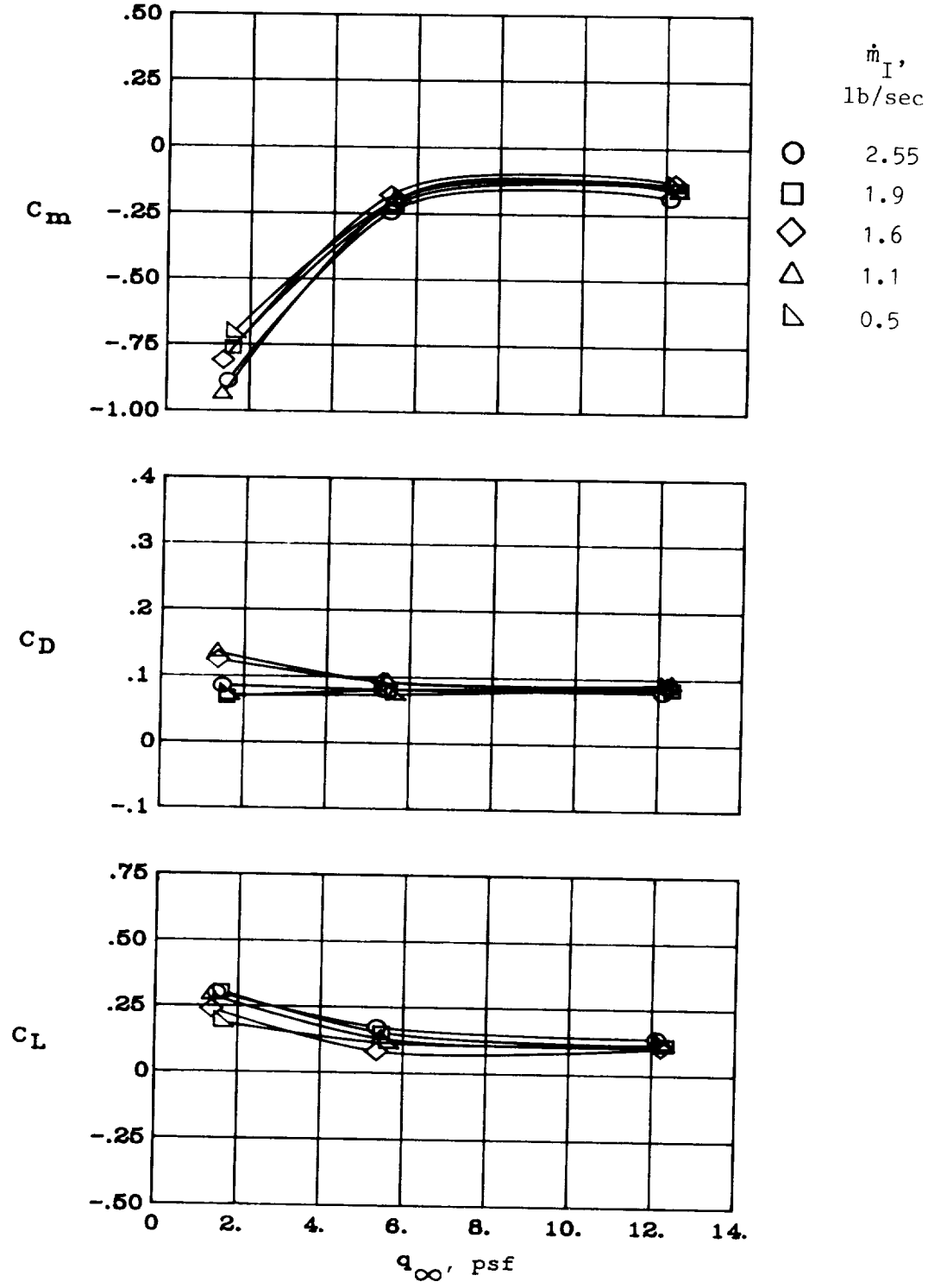


(b) Out of ground effect.

Figure 59. Concluded.

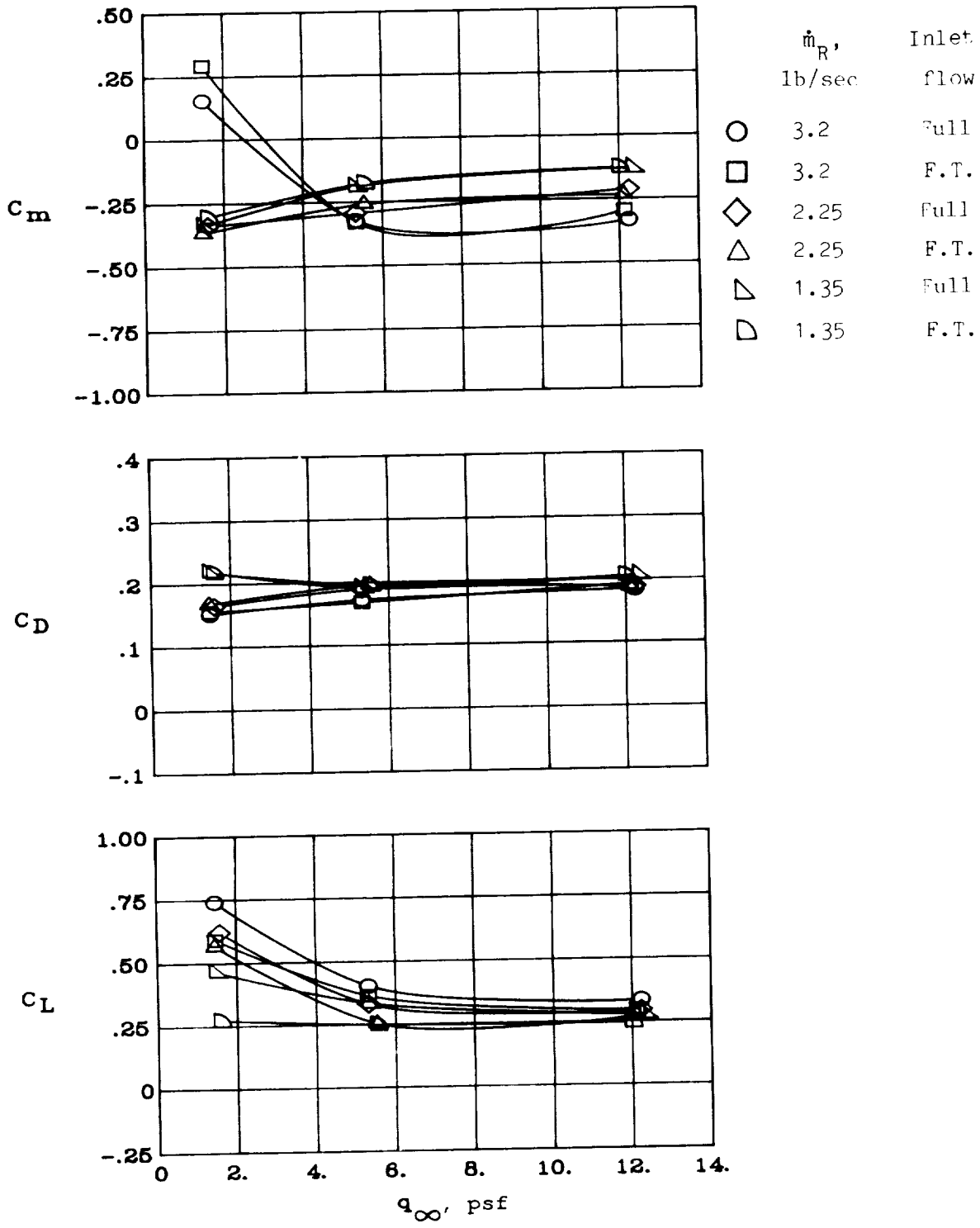


(a) 15° rotated target thrust reverser.

Figure 60. Effects of full inlet flow versus flow-through inlet flow and variations in $\dot{m}_R$ on longitudinal aerodynamics of rotated target configurations. $\delta_f = 40°$; $\delta_s = 60°$; IGE.

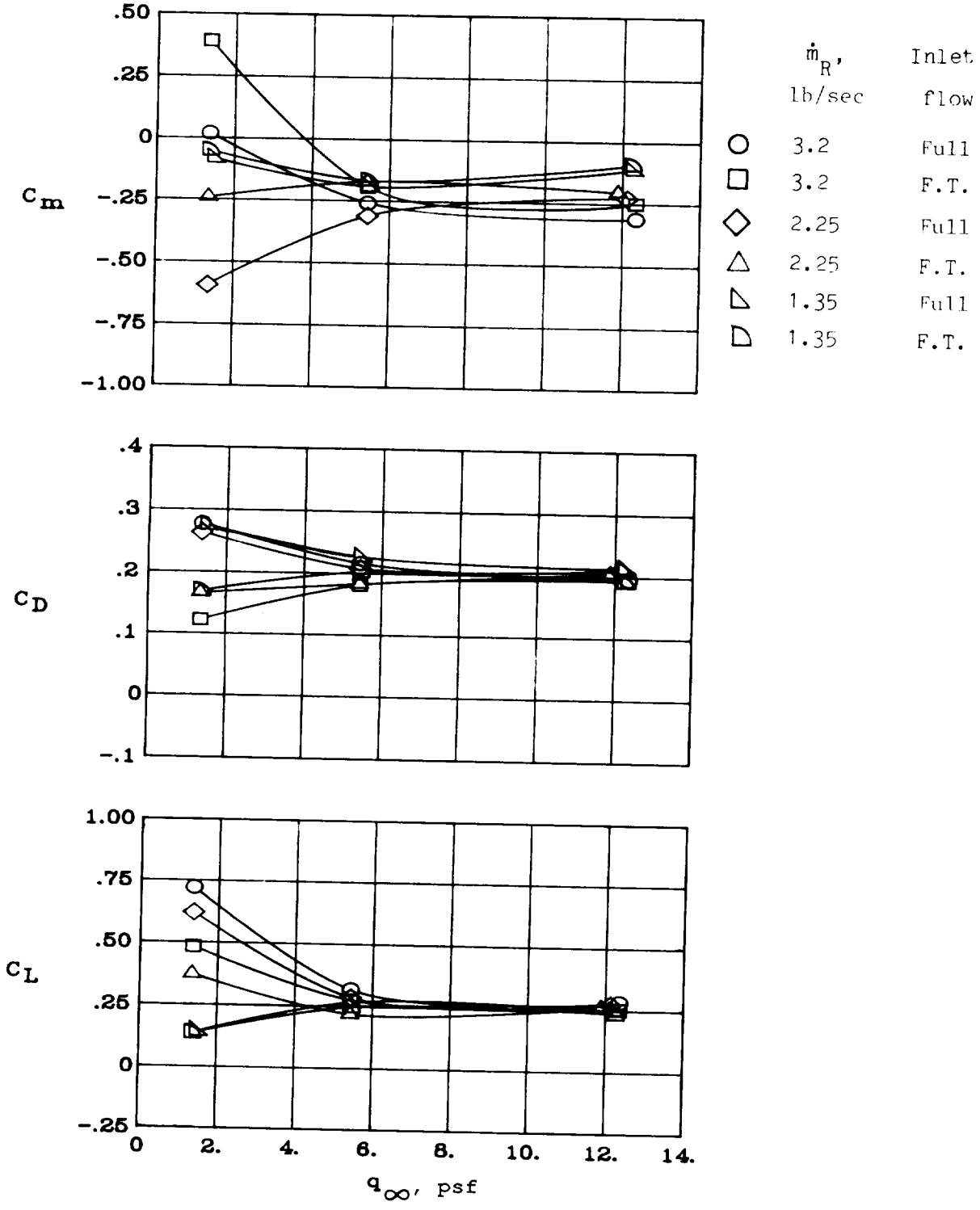


(b) 22.5° rotated target thrust reverser.

Figure 60. Concluded.

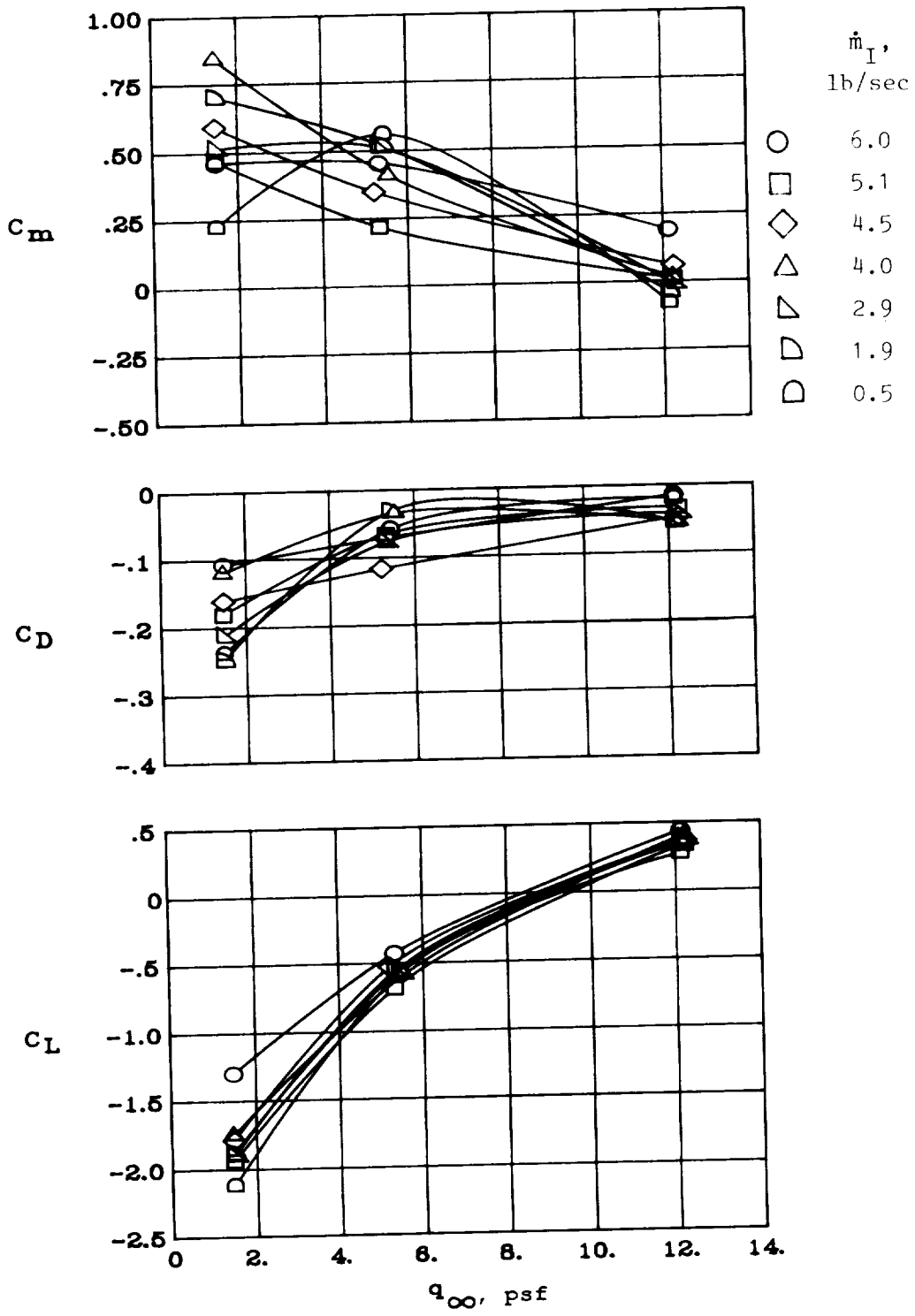


(a) Configuration I; $\dot{m}_R = 5.12$ lb/sec.

Figure 61. Effects of reduced inlet flow on longitudinal aerodynamics of configurations I and III of four-door thrust reverser. $\delta_f = 40°$; $\delta_s = 60°$; IGE.

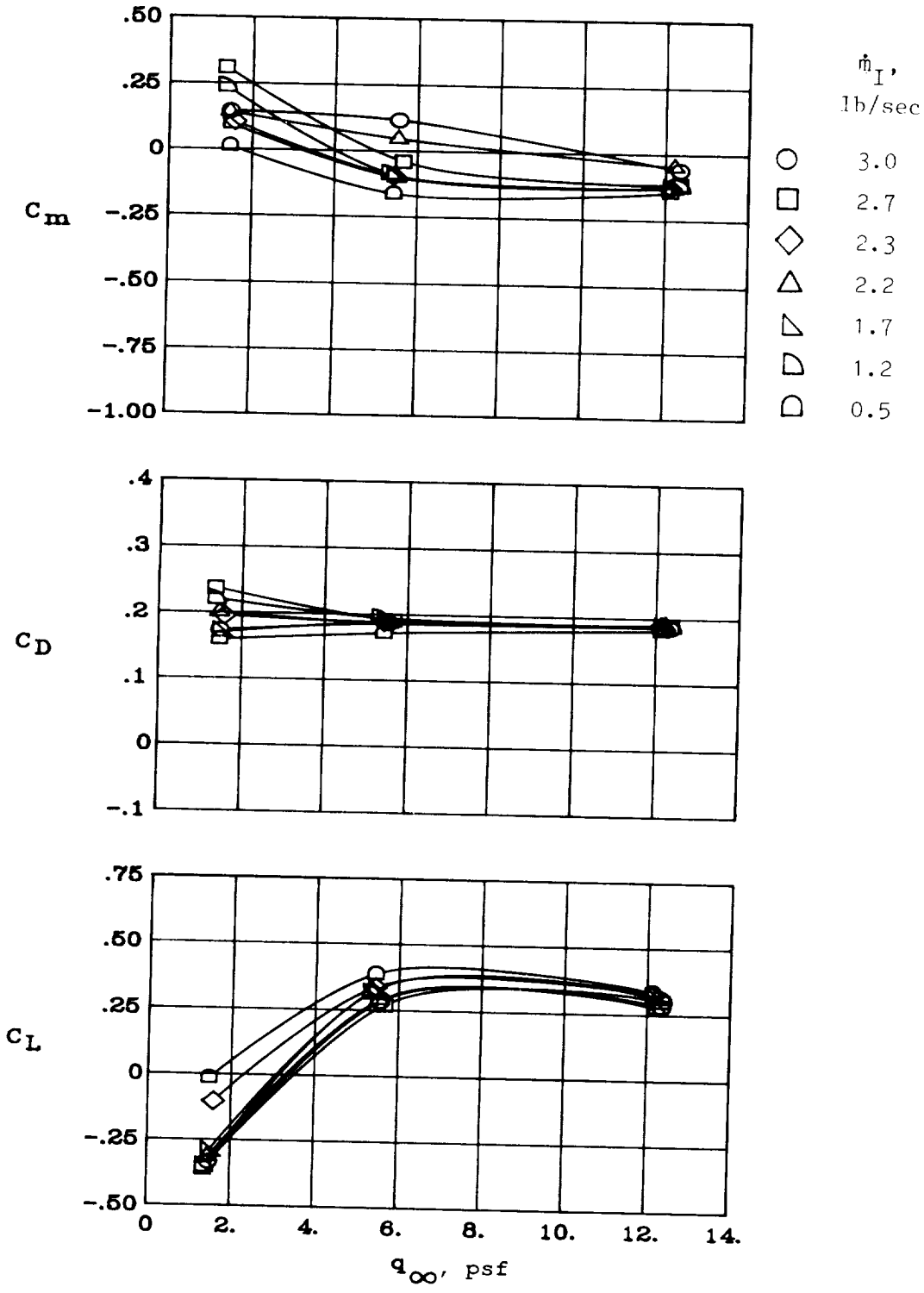


(b) Configuration III; $\dot{m}_R = 2.55$ lb/sec.

Figure 61. Concluded.

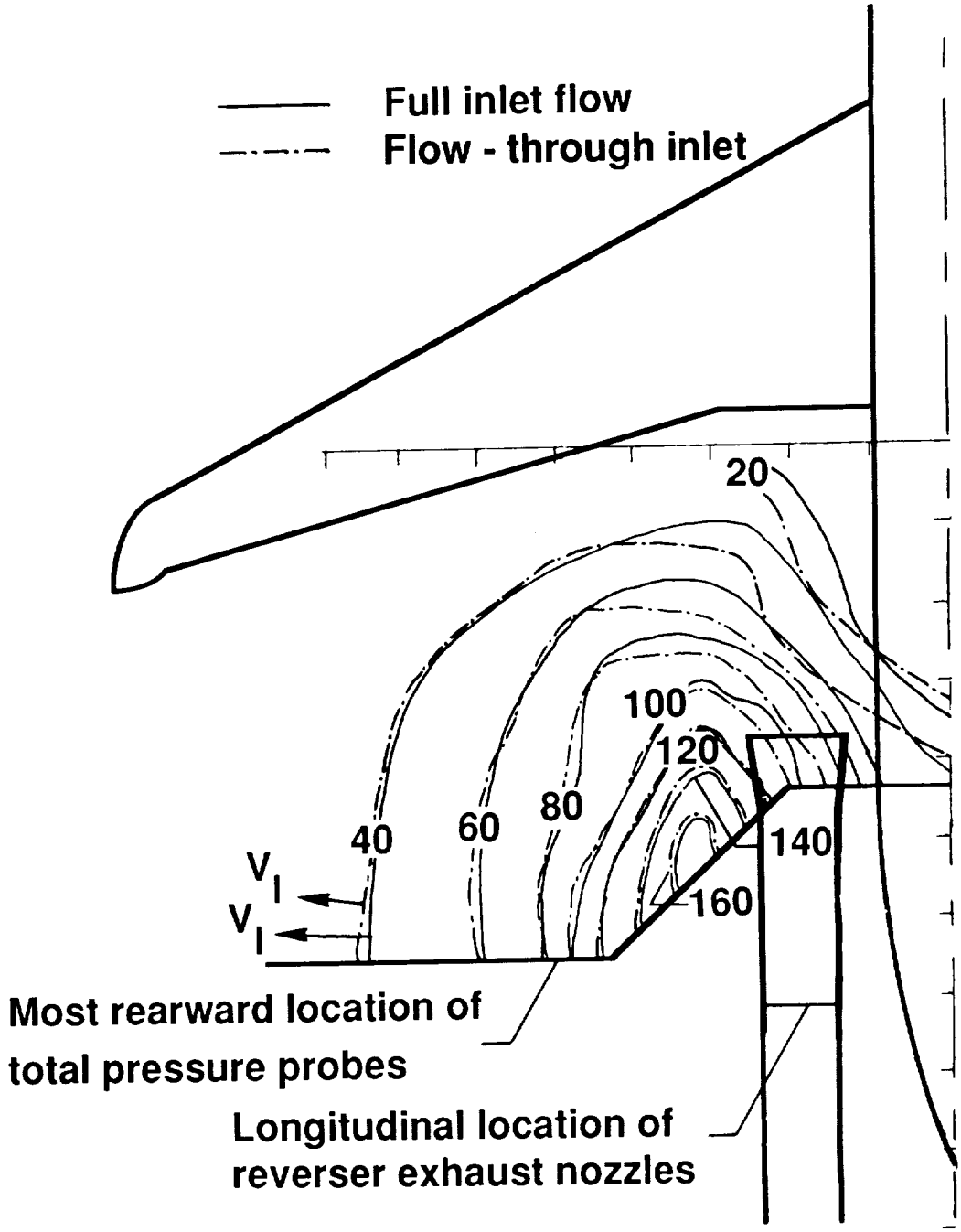


(a) 15° rotated target thrust reverser.

Figure 62. Velocity contour comparison of full inlet flow versus flow-through inlet flow for target thrust reverser. $\dot{m}_R = 3.2$ lb/sec; $q_\infty = 1.4$ psf; $\delta_f = 40°$; $\delta_s = 60°$; IGE.

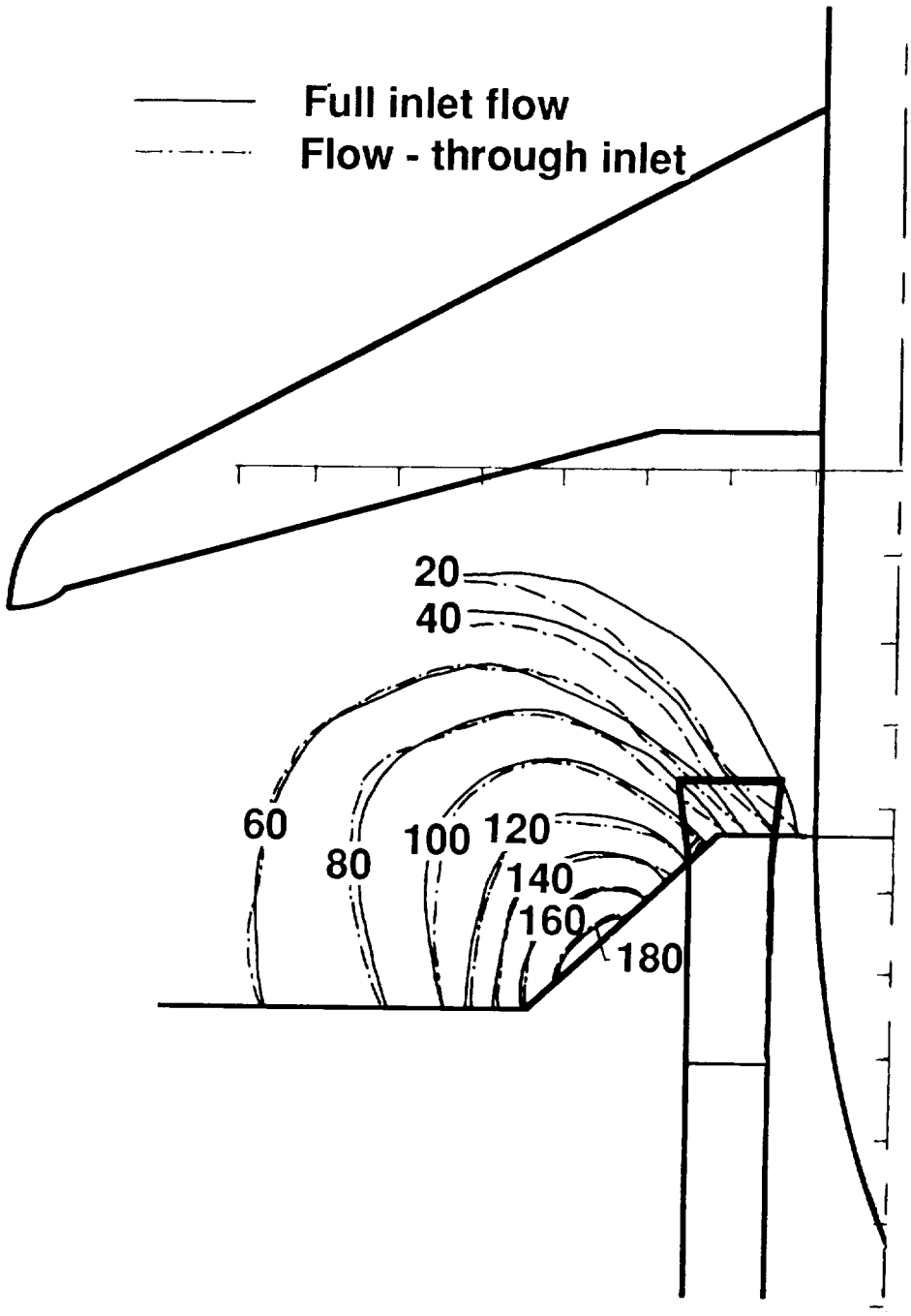


(b) 22.5° rotated target thrust reverser.

Figure 62. Concluded.

NASA
National Aeronautics and Space Administration

# Report Documentation Page

| 1. Report No. | 2. Government Accession No. | 3. Recipient's Catalog No. |
|---|---|---|
| NASA TP-2856 | | |

| 4. Title and Subtitle | 5. Report Date |
|---|---|
| Thrust-Reverser Flow Investigation on a Twin-Engine Transport | December 1988 |
| | 6. Performing Organization Code |

| 7. Author(s) | 8. Performing Organization Report No. |
|---|---|
| Gregory M. Gatlin and P. Frank Quinto | L-16426 |
| | 10. Work Unit No. |
| | 505-68-71-04 |

| 9. Performing Organization Name and Address | 11. Contract or Grant No. |
|---|---|
| NASA Langley Research Center<br>Hampton, VA 23665-5225 | |
| | 13. Type of Report and Period Covered |
| | Technical Paper |

| 12. Sponsoring Agency Name and Address | 14. Sponsoring Agency Code |
|---|---|
| National Aeronautics and Space Administration<br>Washington, DC 20546-0001 | |

15. Supplementary Notes

16. Abstract

An investigation was conducted in the Langley 14- by 22-Foot Subsonic Tunnel to study the effects of engine thrust reversing on an aft-mounted twin-engine transport and to develop effective testing techniques. Testing was done over a fixed and a moving-belt ground plane and over a pressure-instrumented ground board. Free-stream dynamic pressure was set at values up to 12.2 psf, which corresponded to a maximum Reynolds number based on mean aerodynamic chord of $7.65 \times 10^5$. The thrust reversers examined included cascade, target, and four-door configurations. The investigation focused on the range of free-stream velocities and engine thrust-reverser flow rates that would be typical for landing ground-roll conditions. Flow visualization techniques were investigated, and the use of water or smoke injection into the reverser flow proved effective to determine the forward progression of the reversed flow and reingestion limits. When testing over a moving-belt ground plane, as opposed to a fixed ground plane, forward penetration of the reversed flow was reduced. The use of a pressure-instrumented ground board enabled reversed flow ground velocities to be obtained, and it provided a means by which to identify the reversed flow impingement point on the ground.

| 17. Key Words (Suggested by Authors(s)) | 18. Distribution Statement |
|---|---|
| Thrust reverser<br>Reingestion<br>Flow visualization<br>Ground effects<br>Engine simulation | Unclassified—Unlimited<br><br>Subject Category 02 |

| 19. Security Classif.(of this report) | 20. Security Classif.(of this page) | 21. No. of Pages | 22. Price |
|---|---|---|---|
| Unclassified | Unclassified | 154 | A08 |

NASA-Langley, 1988

NASA FORM 1626 OCT 86

For sale by the National Technical Information Service, Springfield, Virginia 22161-2171

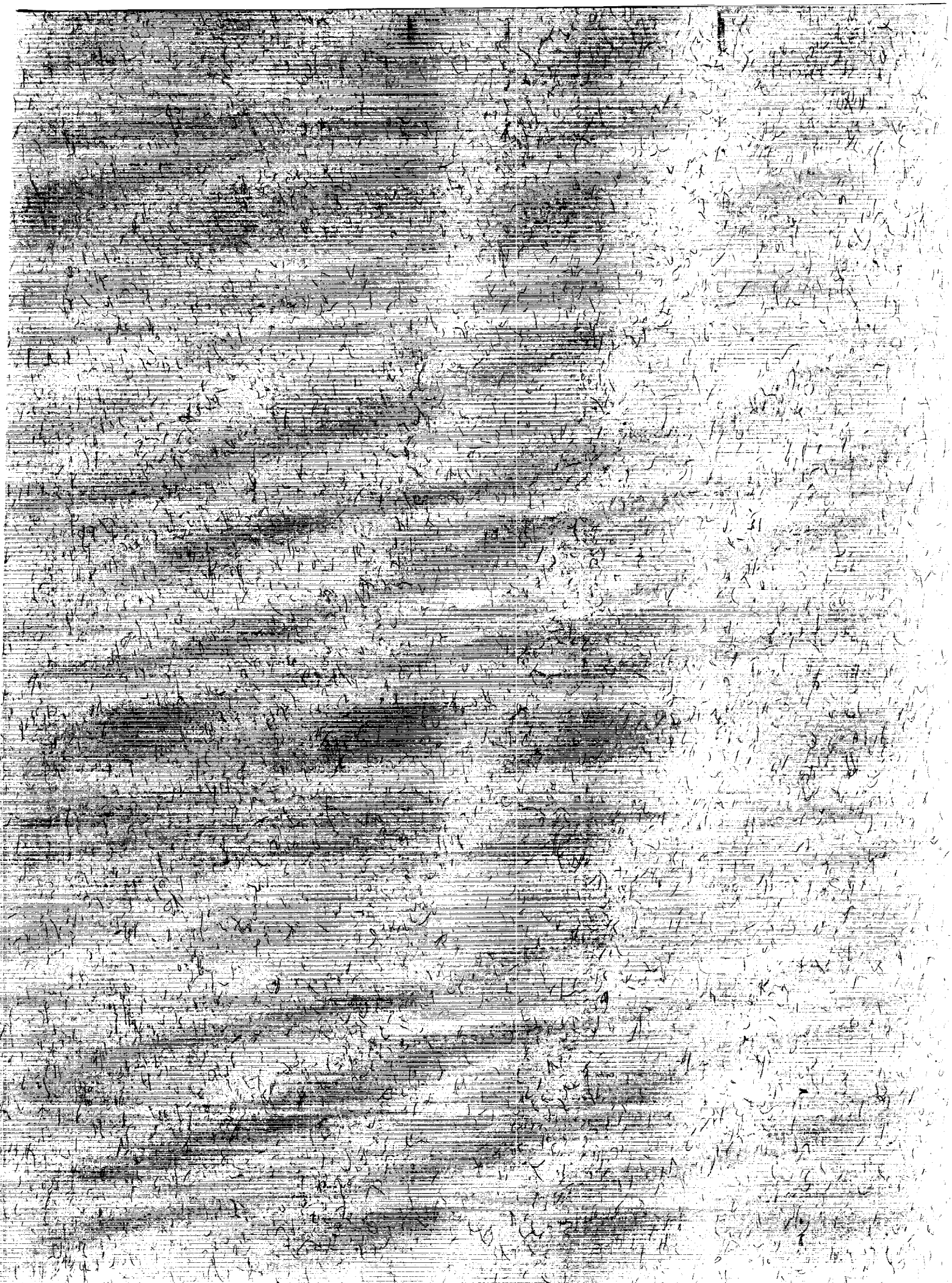

National Aeronautics and
Space Administration
Code NTT-4

Washington, D.C.
20546-0001



SPECIAL FOURTH-CLASS RATE
POSTAGE & FEES PAID
NASA
Permit No. G-27

NASA